INSTITUTE OF CHEMICAL TECHNOLOGY, PRAGUE

Faculty of Chemical Engineering

Department of Physical Chemistry

Dissertation

PREPARATION, CHARACTERIZATION AND STUDY OF ELECTRON TRANSFER IN SELF-ORGANIZED STRUCTURES ON SOLID ELECTRODES

Author: Mgr. Viliam Kolivoška

Supervisor: Mgr. Magdaléna Hromadová, Ph.D.

Study program: Chemistry

Field of study: Physical Chemistry

Prague 2011

VYSOKÁ ŠKOLA CHEMICKO-TECHNOLOGICKÁ V PRAZE

Fakulta chemicko-inženýrská

Ústav fyzikální chemie

Disertační práce

PŘÍPRAVA, CHARAKTERIZACE A STUDIUM PŘENOSU ELEKTRONU V SAMOORGANIZOVANÝCH STRUKTURÁCH NA PEVNÝCH ELEKTRODÁCH

Autor: Mgr. Viliam Kolivoška

Školitel: Mgr. Magdaléna Hromadová, Ph.D.

Studijní program: Chemie

Studijní obor: Fyzikální chemie

Praha 2011

Declaration

The thesis was worked out at the Department of Physical Chemistry, Faculty of Chemical Engineering, Institute of Chemical Technology, Prague from September 2008 to January 2011.

„I hereby declare that I have worked out the thesis independently while noting all the resources employed as well as co-authors. I consent to the publication of the thesis under Act No. 111/1998, Coll., on universities, as amended by subsequent regulations.“

Prague 2011

Viliam Kolivoška

Acknowledgements

I thank all members of Department of Physical Chemistry, Faculty of Chemical Engineering, Institute of Chemical Technology, Prague for giving me the opportinity to be enrolled as a Ph.D student. My special thank belongs to my supervisor Mgr. Magdaléna Hromadová, Ph.D. for a tireless guidance in the work. I also thank to all my colleagues, especially Doc. RNDr. Lubomír Pospíšil, CSc. and RNDr. Bc. Miroslav Gál, Ph.D. for fruitful discussions. I am deeply indepted to my parents, Ing. Viera Kolivošková and Ing. Jozef Kolivoška, CSc, for the financial assistance during my studies. Last but not least, I would like to thank Jan Kmínek and Adéla Singerová for the support during writing the thesis.

The presented thesis focuses on electrochemical, spectroelectrochemical, adsorption, complexation and conductivity properties of extended viologens of variable length (the compounds **1** to **6**). In the future, their molecules could serve as conducting molecular wires in the devices of molecular electronics. At the mercury/electrolyte interface, all studied compounds were found to form a compact monolayer with flat-lying molecules with the diffusion as the rate-determining step. The presence of adsorbed molecules on Au(111) surface was confirmed by STM and PM IRRAS techniques. The extended viologen molecule consisting of one repeating unit (the compound **1**) was found to reversibly transfer four electrons, behaving as a fully delocalized system. On the other hand, the molecule of the compound **2** transfers two electrons independently, having thus two noncommunicating centers. The molecules containing higher number of repeating units (*n*) transfer *2(n-1)* electrons in the first two closely-positioned reduction steps (with *n-1* electrons being independently consumed in each of them). Chemical stability of reduced forms of the compounds **1** to **6** was confirmed by UV/VIS/NIR in-situ spectroelectrochemical techniques. Electric conductance of junctions containing extended viologen molecules (scrutinized by Tao's method) was found to exponentially decrease with the molecular length.

In other types of the extended viologen molecules (the compounds **1'** and **4'**), the presence of homogenous disproportionation was found to have a significant impact on their electrochemical behavior. In the case of extended viologen molecule consisting of four repeating units (the compound **4'**), the oscillations and bifurcations were found in the current transients. They allowed the value of Feigenbaum constant to be experimentally verified.

Besides the extended viologens, the thesis focuses also on the electrochemical behavior of other types of N-heteroaromatic cations, namely on benzothiazolium and quinolinium cations.

A design of a non-covalent molecular switch based on the ferrocene:cyclodextrin interactions is proposed. The complexation behavior of ferrocene and cyclodextrin molecules of various cavity sizes and side groups is investigated in DMSO:H_2O mixtures by cyclic voltammetry. Self-assembly of host molecules (fully methylated beta-cyclodextrin) on Au(111) surface is inspected by scanning tunneling microscopy and atomic force microscopy.

Predkladaná dizertačná práca sa zameriava na elektrochemické, spektroelektrochemické, adsorpčné, komplexačné a vodivostné vlastnosti predĺžených viologénov rôznej dĺžky (zlúčeniny **1** až **6**). Ich molekuly by v budúcnosti mohli slúžiť ako vodivé molekulové drôty v prístrojoch molekulovej elektroniky. Všetky študované zlúčeniny vytvárajú na rozhraní ortuť/elektrolyt kompaktnú monovrstvu paralelne ležiacich molekúl s difúzne riadeným vznikom. Prítomnosť adsorbovaných molekúl na povrchu Au(111) bola potvrdená technikami STM a PM IRRAS. Molekula predĺženého viologénu obsahujúca jednu opakujúcu sa jednotku (zlúčenina **1**) reverzibilne prijíma štyri elektróny, chovajúc sa ako plne delokalizovaný system. Molekula zlúčeniny **2** však prijíma dva elektróny nezávisle a má preto dve nekomunikujúce centrá. Molekuly obsahujúce väčší počet jednotiek (*n*) prijímajú v prvých dvoch redukčných krokoch *2(n-1)* elektrónov (*n-1* v každom). Chemická stabilita redukovaných foriem zlúčenín **1** až **6** bola potvrdená pomocou in-situ UV/VIS/NIR spektroelektrochemických techník. Vodivosť elektrických spojov obsahujúcich molekuly predĺžených viologénov (meraná Taovou metódou) klesá exponenciálne s dĺžkou molekuly.

V prípade iných typov predĺžených viologénov (zlúčeniny **1'** a **4'**) sa zistilo, že na ich elektrochemické chovanie má výrazný vplyv homogénna disproporcionácia. U molekuly zloženej zo štyroch jednotiek (zlúčenina **4'**) boli v prúdových záznamoch objavené oscilácie a bifurkácie. Tie umožnili experimentálne overenie hodnoty Feigenbaumovej konštanty.

Okrem predĺžených viologénov sa dizertačná práca tiež zameriava na electrochemické chovanie iných typov N-heteroaromatických katiónov, konkrétne na benzothiazoliový a chinolídiový katión.

V dizertačnej práci je tiež navrhnutá konštrukcia molekulového prepínača založeného na interakcii medzi molekulami ferocénu a cyklodextrínov. Komplexácia ferocénu a cyklodextrínov s rôznou veľkosťou dutiny a postrannými skupinami je študované pomocou cyklickej voltametrie v zmesi DMSO:voda. Samoorganizované štruktúry hostiteľských molekúl (plne metylovaný beta-cyklodextrín) na povrchu Au(111) boli študované pomocou rastrovacej tunelovej miktroskopie a mikroskopie atómových síl.

List of abbreviations used

AAC-AFM	Acoustic Alternating Contact Atomic Force Microscopy
AC	Alternating Current, Alternating Contact
AC-AFM	Alternating Contact Atomic Force Microscopy
AFM	Atomic Force Microscopy
AN	Acetonitrile
ATR FTIR	Attenuated Total Reflection Fourier Transform Infrared Spectroscopy
BP	4,4' - Bipyridine, 4,4' - Bipyridinium
BzTfO	Benzothiazolium Triflate
Cc, Cc^+	Cobaltocene, Cobaltocenium
CD	Cyclodextrin
CM-AFM	Contact Mode Atomic Force Microscopy
Cp	Cyclopentadienyl
CP-AFM	Conductive Probe Atomic Force Microscopy
CS-AFM	Current Sensing Atomic Force Microscopy
CV	Cyclic Voltammetry
DC	Direct Current
DCE	1,2-Dichloroethane
DFT	Density Functional Theory
DME	Dropping Mercury Electrode
DMF	Dimethylformamide
DMSO	Dimethylsulfoxide
EMAC	Extended Metal Atom Chain
EPR, ESR	Electron Paramagnetic Resonance, Electron Spin Resonance
ESCA	Electron Spectroscopy for Chemical Analysis
Fc, Fc^+	Ferrocene, Ferrocinium
FFT	Fast Fourier Transform
FI	Fluorescence Intensity
HMDE	Hanging Mercury Drop Electrode
HOMO	Highest Occupied Molecular Orbital
HOPG	Highly Oriented Pyrolytic Graphite
HPLC	High Performance Liquid Chromatography
IC-AFM	Intermittent Contact Atomic Force Microscopy
IR	Infrared Radiation, potential loss in an electrochemical cell
LDOS	Local Density of States
LST	Linear Sweep Techniques
LUMO	Lowest Unoccupied Molecular Orbital
MAC-AFM	Magnetic Alternating Contact Atomic Force Microscopy
$Me_2\beta CD$	Heptakis(2,6-di-O-methyl)-beta-cyclodextrin
$Me_3\beta CD$	Heptakis(2,3,6-tri-O-methyl)-beta-cyclodextrin

Me_3βCDCys-SH	Heptakis(2,3,6-tri-O-methyl)-beta-cyclodextrin modified by cystein
MS	Mass Spectroscopy
MV	Methyl Viologen
MW	Molecular Wire
NADPH	Nicotinamide Adenine Dinucleotide Phosphate
NIR	Near Infrared Radiation
NMR	Nuclear Magnetic Resonance
O	Oxidized form of an electroactive species
OPE	Oligo-(phenylene-ethynylene)
OPV	Oligo-(phenylene-vinylene)
OTTLE	Optically Transparent Thin Layer Electrode
PEM	Photoelastic Modulator
Ph	Phenyl, 1,4-Phenylene
PM IRRAS	Polarization Modulated Infrared Reflection Absorption Spectroscopy
PTTF	Pyrrolo-Tetrathiafulvalene
Py, Py^+	Pyridine, Pyridinium
QnTfO	Quinolinium Triflate
R	Reduced form of an electroactive species
ROS	Reactive Oxygen Species
SECM	Scanning Electrochemical Microscopy
SMDE	Static Mercury Drop Electrode
SMS	Single-Molecule Spectroscopy
SNOM	Scanning Near-Field Optical Microscopy
SPM	Scanning Probe Microscopy
STM	Scanning Tunneling Microscopy
STS	Scanning Tunneling Spectroscopy
$TBAPF_6$	Tetrabutylammonium Hexafluorophosphate
THF	Tetrahydrofuran
TM-AFM	Tapping Mode Atomic Force Microscopy
TOP-MAC-AFM	Top Magnetic Alternating Contact Atomic Force Microscopy
TOF SIMS	Time-of-Flight Secondary Ion Mass Spectroscopy
TTF	Tetrathiafulvalene
UV	Ultraviolet Radiation
V	Viologen
VIS	Visible Radiation
αCD	Alpha-cyclodextrin
βCD	Beta-cyclodextrin
γCD	Gamma-cyclodextrin

Table of contents

1 AIMS OF THE THESIS

Extended viologens are pyridinium-based N-heteroaromatic cations containing conjugated structures inserted between the pyridinium rings. They could be one day used as molecular wires in the devices of molecular electronics.

The presented thesis is aimed at the investigation of adsorption, electrochemical, spectroelectrochemical and conductivity properties of the extended viologens. Furthermore, their inclusion complexes with the cyclodextrin host molecules are studied with the aim to isolate individual molecular wires.

Electrochemical and spectroelectrochemical techniques will be employed to investigate the electron transfer in the molecules of extended viologen.

To the best of our knowledge, there is no study on the adsorption of extended viologen molecules. The adsorption properties will be scrutinized by electrochemical and scanning probe techniques.

The electric conductance of single-molecule junctions containing extended viologens will be examined. Such studies are necessary as the extended viologens are designed to serve as conducting molecular wires in the devices of molecular electronics.

Inclusion complexes of extended viologens with cyclodextrin hosts will be investigated by electrochemical and spectroscopis techniques. In the circuits of molecular electronic devices, the electric conductors will need to be separated by non-conductive molecules. The cyclodextrin complexes of extended viologens may serve as the models of insulated molecular wires.

The curent oscillations of extended viologen molecules will be inspected by electrochemical techniques. The oscillatory behavior allows the extended viologens to be used as single-molecule oscillators.

Electrochemical properties of other N-heteroaromatic cations (benzothiazolium and quinolinium) will be inspected as well.

Besides the molecular wires, molecular switches are other elements needed to be incorporated into circuits of devices of molecular electronics. They may utilize the electrochemically controlled host-guest interactions. The molecular switches based on the ferrocene:cyclodextrin complexes will be scrutinized by cyclic voltammetry. Electrochemical as well as the scanning probe techniques will be applied to investigate the self-assembly of the host cyclodextrin molecules on the metallic surfaces.

2 THEORETICAL PART

2.1 Present state of knowledge

2.1.1 Molecular wires

Molecular wires (MWs) are conductive objects of molecular dimensions. Their typical diameter is on the order of nanometers, with the length being usually much higher, exceeding even to micrometers or millimeters. The MWs may be either organic or inorganic. According to their origin, MWs are divided into natural, modified natural and artificial. A typical example of a natural organic wire is DNA [1]. The DNA may be coated by noble metal atoms, yielding a modified natural MW [2]. Examples of artificial organic MWs are oligo-(phenylene-ethynylene)s (OPEs), oligo-(phenylene-vinylene)s (OPVs) and viologens. Typical artificial inorganic MWs are carbon nanotubes [3]. Other well-known inorganic artificial MWs are molybdenum-based structures such as $Mo_6S_{9-x}I_x$ [4–6] and $Li_2Mo_6Se_6$ [7] and the extended metal atom chains (EMACs) [8]. The EMACs are defined as molecules containing directly bonded transition metal atoms (Co, Ni or Cr) aligned in a linear string 3 – 9 atoms long [9]. In EMACs, the six-coordinate metallic atoms are surrounded by four organic ligands (dipyridyl amide moieties). The presence of protecting organic ligands prevents EMACs from aggregation and allows them to serve as distinct molecular entities.

The MWs consist of repeating units. In case of DNA, the repeating unit is a nucleotide, with a backbone composed of the alternating sugar and phosphate groups, with a base being attached to each sugar group [10,11]. In an EMAC, the repeating unit is made of one metallic atom surrounded by four organic ligands [9,12]. The terminal groups of molecular wires are usually low-mass moieties such as –OH groups (DNA), halogen atoms (EMACs) [8,9] or other groups, allowing the wires to be protected from aggregation and allow them to assemble on various surfaces.

2.1.2 Molecular electronics

Molecular electronics is a branch of nanotechnology that studies the application of molecular building blocks for the preparation of electronic components [13,14]. Molecular electronics is probably the only way to extend the validity of Moore's law, which says that the number of transistors placed inexpensively on a certain area of an integrated circuit doubles every two

years [15]. With existing silicon technologies, the Moore's law is believed to be obeyed for 10 – 20 years from today. With the aid of technologies based on molecular electronics, the Moore's law could hold longer [16].

In the future technologies, molecular electronics will need both active (transistors [17], molecular switches [18,19]) and passive (conductors [20,21]) building blocks. MWs will serve as electric conductors (i.e. passive elements) in the electronic devices. Several inevitable conditions have to be simultaneously satisfied when considering a molecule or group of molecules to serve as MW:

- The MWs should be able to reproducibly bind to the metal surfaces (Au, Ag) to ensure the connection to the "outside world". Covalent bonds are highly desirable in order to arrange a proper contact.
- The MWs must be available in various lengths.
- The MWs must be able to self-assemble on the surfaces by a defined way.
- In some cases, branched MWs will be necessary.
- The MWs have to withstand the electron transfer through their molecules.
- High electric conductivity of the molecular backbone is desired.

2.1.3 Viologens and viologen-based molecular wires

Viologens are 1,1'-di(hydrocarbyl)-4,4'-bipyridinium salts [22]. The term comes from their color upon reduction by one electron. Viologen dication V^{2+} is known to accept two electrons in two subsequent steps to produce a radical cation $V^{+\cdot}$ and a neutral form V^0, respectively. According to the conditions, the $V^{+\cdot}$ form may undergo the dimerization [23,24], with the dimeric form being further reduced. The best known viologen is 1,1'-dimethyl-4,4'-bipyridinium dichloride also known as methyl viologen (MV) or Paraquat. It is used as a quickly acting, non-selective herbicide. It was first synthesized in 1882, but its herbicidal properties were first recognized in 1955 [25]. It was first sold by Imperial Chemical Industries in Great Britain, in 1962. Paraquat is one of the most used weed-killers in the world.

When present in a light-exposed plant cell, a paraquat molecule MV^{2+} may accept an electron (liberated from the photosystem I) to generate the radical cation, $MV^{+\cdot}$. The $MV^{+\cdot}$ form is very reactive and transfers the gained electron further to a dioxygen molecule [26]. Reactive oxygen species (ROS), such as superoxides and peroxides, come into existence and the parent (MV^{2+}) form of paraquat is regenerated. It may accept electron again, serving thus as an

electron mediator. Generated ROS were proven to be harmful to both plant and animal cells, causing defects in the DNA and protein molecules [27,28]. In scientific research, paraquat is intentionally used to induce the formation of ROS [29]. In this case, paraquat molecules are reduced by electron donors such as NADPH, with an electron being transferred further to dioxygen molecule to produce ROS.

Paraquat is highly toxic to mammals, including humans [26]. The ingestion may cause liver, heart, lung and kidney failure [30]. Paraquat was also linked to an increased incidence of Parkinson's disease in rats [31]. In the United States, paraquat may be used with some restrictions. However, since 2007, it is completely forbidden in the European Union [32].

Paraquat may also be employed in electrochromic devices [33,34]. The applications include electrochromic displays and so called smart windows. In both cases, viologen may change the opacity of a supporting material from transparent to blue depending on the redox state of molecules ($MV^{2+}/MV^{+\cdot}$).

Paraquat, along with homologues containing longer alkyl side chains (i.e. 1,1'-dialkyl-4,4'-bipyridinium salts, for brevity denoted as C_nVC_n) are often regarded as the models of organic molecular wires. Haiss et al. [35] formed an STM junction containing 1,1'-di(6-sulfanylhexyl)-4,4'-bipyridinium (HSC_6VC_6SH) molecular wires. The authors found the single-molecule conductivity to be dependent on the redox-state of the viologen moiety. The conductivity significantly increased (from 0.5 to 2.8 nS) upon the one-electron electrochemical reduction. In a related study [36], the conductance behavior of gold|HSC_6VC_6SH|gold molecular junctions was compared to that of gold|HSC_6(PTTF)C_6SH|gold and gold|HSC_6PhC_6SH|gold junctions (PTTF = pyrrolo-tetrathiafulvalene, Ph = 1,4-phenylene). The different conductance-overpotential behavior was rationalized in terms of the conformational dynamics of the respective systems. The presence of various conformations was also confirmed in gold|Py-$(C\equiv C)_n$-Py|gold systems [37] (with Py = 4-pyridyl and n = 1, 2, 4). The conductance histogram revealed multiple peaks attributed to different contact geometries between the pyridyl head groups and gold electrodes. The obtained experimental results were further supported by DFT calculations. The gold|HSC_6VC_6SH|gold junction was also scrutinized by Li at al. [38]. Besides the STM technique, the self-assembled monolayer of HSC_6VC_6SH molecules was also investigated by cyclic voltammetry and surface enhanced infrared spectroscopy. Three different types of adlayers were found: a low-coverage disordered, a low-coverage stripped (with parallel-lying molecules) and a high-coverage phase, composed of tilted molecules. Similarly to Heiss et al. [35], an in-situ electrochemical STM technique was employed to explore the electron transfer

in the junction and a sigmoidal dependence of conductance on the electrode potential was found. Pobelov at al. [39] focused on asymmetric junctions formed of 1-hexyl-1'-(6-sulfanylhexyl)-4,4'-bipyridinium dibromide (HSC_6VC_6H) molecules in the electrochemical environment. The experiments focused on the one-electron transfer reaction between the dication and the radical cation. A transistor-like behavior was observed. Lee at al. [40] employed an ultra high vacuum scanning tunneling microscopy study to investigate the charge transfer in self-assembled monolayers composed of both symmetric (HSC_nVC_nSH) and asymmetric (HC_1VC_nSH) molecules. For both series of molecules, the resistance of the monolayers was found to increase exponentially with the length of the molecules. Bagrets at al. [41] provided the calculations of electric conductivities for both methyl viologen as well as for symmetrical viologen-based MWs HSC_nVC_nSH (with n = 4, 5 and 6). The calculations showed that the single-molecule conductance values of viologen-containing junctions may differ by two orders of magnitude depending on the geometrical arrangement of the MV molecules between the electrodes. For the viologen-based, SH- terminated symmetrical MWs, an exponential decay of the conductance with the length of the molecule was obtained, being in agreement with experiments.

Adsorption properties of 4,4'-bipyridyl (BP) were investigated by Heyrovský and Novotný in water solutions of Na_2SO_4 and H_2SO_4 [42]. In the neutral solution, BP was found to be strongly adsorbed. On the other hand, the doubly protonated form (4,4'-bipyridynium dication, BPH_2^{2+}) present in the acidic solutions, is only weakly adsorbed. Gómez at al. [43,44] studied the formation of a 2D phases during the electrochemical reduction of BP. The work also suggests a mathematical model explaining the chronoamperometric behavior observed during the formation of adsorbed phases. Sanchez-Maestre et al. [45] provided a detailed study of the adsorption of BPH_2^{2+} in the acidic solutions. The influence of experimental variables, such as bulk concentration of BP, temperature and the type of anion, was scrutinized in detail.

Heyrovský and Novotný [23] investigated the adsorption properties of MV. The molecules of the parent compound, MV^{2+}, were found to lay parallel to the electrode surface. The electron transfer in the adsorbed layer was found to take place at more positive potential values than that of the molecules from the bulk of the solution (forming thus an adsorption prewave). The singly reduced form of methyl viologen, $MV^{+\cdot}$, was found to dimerize in the vicinity of the electrode. The dimeric form was also adsorbed on the electrode surface. This behavior was confirmed by Kobayashi et al. [46], who showed that MV^{2+} adsorbs on the mercury electrode in the parallel-lying orientation at potential values more positive than the potential of zero

charge. The reduced form $MV^{+\bullet}$ adsorbs, however, with a vertical orientation, at the potentials more negative than the formal potential of the $MV^{2+}/MV^{+\bullet}$ redox couple. The reorientation of molecules upon electrochemical reduction was also confirmed by Pospíšil and Kůta [47]. The same behavior (reorientation of adsorbed molecules upon electrochemical reduction) was also observed for viologens with longer chains (C_nVC_n, n > 1). Millán et al. [48–50] studied the reorientation of diheptyl viologen molecules (C_7VC_7) on mercury electrode. The same behavior was also observed on polycrystalline silver electrode for C_7VC_7 [51] and monocrystalline gold electrode for dialkylviologens of variable chain length [52–54].

The adsorption properties of thiolated derivatives of alkyl viologens were also investigated. As mentioned above, Li at al. [38] performed a detailed study of the adsorption of HSC_6VC_6SH molecule on the monocrystalline gold surface. De Long and Buttry [55] investigated the adsorption properties of the compounds with asymmetric molecules, namely $C_1VC_{12}SH$, $C_{10}VC_3SH$ and $C_{10}VC_{10}SH$. Electrochemical as well as quartz crystal microbalance techniques were employed. All three compounds were found to form well-ordered self-assembled monolayers on Au electrode, with the electrochemical reversibility of the viologen moiety being retained. Tang at al. [56] compared the self-assembly of thiol and disulfide derivatives of alkyl viologens. In particular, the compounds $C_1VC_{12}SH$ and $(C_1VC_{12}S)_2$ were scrutinized. The monolayers formed on Au and Ag surfaces were investigated by cyclic voltammetry and Raman spectroscopy. In contrast to the behavior of alkane thiols (C_nSH) and dialkyl disulfides (C_nSSC_n), which adsorb to give nearly the same surface coverage and interfacial properties, these two viologen derivatives were found to exhibit different surface coverages. The differences were attributed to lateral interactions between the viologen moieties. Haiss at al. [57] studied the self-assembly of viologen-based symmetrical MWs HSC_6VC_6SH and $HSC_{10}VC_{10}SH$. It was observed that the surface coverage increased with the time of the adsorption, with a concomitant change in the orientation of adsorbed molecules changing from parallel to perpendicular. The MWs were further self-assembled in a matrix composed of the electrochemically silent alkanethiol molecules, in order to isolate the redox-active viologen-based MWs. Gold nanoparticles were further attached to the viologen-based wires and their single-molecule conductivity was probed by the scanning tunneling spectroscopy (STS) method. In a related study [58], the single-molecule conductivity was measured directly by forming a molecular junction between the STM probe and the sample surface similarly to that mentioned in [35].

2.1.4 Extended viologens

In extended viologens, conjugated structures such as 1,4-phenylene, ethene-1,2-diyl and thiophene-2,5-diyl are inserted between the pyridinium rings. Volke et at. [59] investigated the electrochemical behavior of the compounds, the general formula of which may be written as $R_1R_2R_3Py^+XPy^+R_1R_2R_3$ $(ClO_4^-)_2$, with R_1, R_2, R_3 (substituents) and X (the linker) being either an aliphatic or an aromatic moiety. The compounds contain two pyridinium rings separated by either 1,4-phenylene (phen) or a 4,4‘-biphenylene (biphen) moiety as well as those separated by aliphatic chains (X = C_n with n = 2, 3, 4 and 6). A full delocalization was found in the compounds with aromatic linkers, with correspondingly less negative potentials of the first reduction wave. On the other hand, in compounds with aliphatic linkers, the electrons were not found to be fully delocalized. The electrochemical measurements confirmed that the molecules possess two non-communicating redox-active centers (i.e. two separated π-electron systems). In a related study [60] Volke et al. employed a combination of electrochemical and EPR methods to study the reduction of compounds $R_1R_2R_3Py^+XPy^+R_1R_2R_3$ $(ClO_4^-)_2$ with $R_1 = R_2 = R_3$ = -Ph and X = $-C_2-$, $-C_6-$, phen and biphen as well as the mononucleic pyridinium compounds Ph_3Py^+Y ClO_4^- with Y = $-C_1$, $-C_4$ and -Ph. In both classes of compounds, the EPR measurements confirmed that the electrochemical behavior is complicated by the presence of conproportionation reactions between the parent and doubly reduced species. On the other hand, the dimerization was not observed. Its absence was explained by the presence of three bulky phenyl substituents on the pyridinium rings in both classes of compounds. Porter et al. [61] synthesized and characterized the compound di-octyl bis(4-pyridyl)biphenyl dibromide ($HC_8Py^+PhPhPy^+C_8H$ $2Br^-$). The redox behavior was scrutinized by electrochemical as well as by redox titration methods. The compound was found to accept two electrons to yield a neutral form, being an extremely strong reducing agent. Valášek et al. [62] synthesized the first five members of an oligomeric series built from the alternating *p*-connected 1,4-phenylene and 1,4-pyridinium rings. The repeating unit is *p*-phenylene-bis-4,4‘-(1-aryl-2,6-diphenylpyridinium). The compounds were denoted as **1'** to **5'** according to the number of repeating units in the molecule. The electrochemical behavior of the compound **1'** was studied by Funston et al. [63] and Pospíšil et al. [64]. The compound **1'** (initially a dication) reduced by one electron yielded a red radical cation $(1')^{+\cdot}$ with a strong NIR band. The form was generated by electrochemical, pulse radiolysis and redox titration methods. The results of all used methods suggested a fully delocalized structure of the radical cation $(1')^{+\cdot}$.

2.1.5 Cyclodextrins

Cyclodextrins (CDs) are cyclic oligosaccharides [65], first described in 1891 by Villiers [66]. Their hydrophobic cavity allows them to serve as host molecules for various compounds [67–70]. The driving forces for the complexation of CD with guest molecules are hydrophobic interactions, electronic effects and van der Waals forces [71]. CDs are used in the pharmaceutical industry [72] and in the production of HPLC columns for enantioselective separation [73]. The methods of capillary electrophoresis also often rely on the presence of CD molecules adsorbed on a separation capillary wall [74,75]. CDs were also found to bind cholesterol molecules [76,77] and are therefore considered as possible weight loss supplements [78].

2.1.6 Inclusion complexes of viologens with cyclodextrins

Yasuda et al [79] investigated the complex formation of tetramethylene bis-4(1-benzylpyridine-4′-yl)pyridinium ($PhC_1PyPyC_4PyPyC_1Ph$) and diheptyl viologen (C_7VC_7) dications with βCD. In both cases, the structure of the inclusion complex was found to be dependent on the redox states of the guest molecules. Sivagnanam and Palaniandavar [80] investigated the inclusion complexes of methyl viologen with αCD, βCD and γCD by cyclic voltammetry. While the presence of αCD and γCD did not significantly affect the shape of voltammograms, βCD was found to bind methyl viologen molecules, with a 1:1 complex being formed. The calculated equilibrium constants suggest that the singly reduced form, $MV^{+\cdot}$, binds βCD much stronger than MV^{2+} and MV^0. Similarly, Mirzoian and Kaifer [81] used cyclic voltammetry to investigate the complexation behavior of three viologen-based guest molecules with βCD and heptakis(2,6-di-O-methyl)-β-cyclodextrin (Me_2βCD). In particular, the guests $HOC_2OC_2OC_2VC_2OC_2OC_2OH$, $HOOCC_5VC_5COOH$ and $HO_3SC_3VC_3SO_3H$ were employed, with the side chains being chosen intentionally to improve the solubility in water. Digital simulation techniques were employed to calculate the complex formation constants. In the case of all three guests, both host molecules were found not to bind the oxidized (parent) forms. On the other hand, singly and doubly reduced species were found to form intermediately ($\approx 10^2$ M^{-1}) and very strong ($\approx 10^3 - 10^4$ M^{-1}) inclusion complexes, respectively. It was also found that Me_2βCD forms stronger complexes than βCD. Kitamura at al. [82] investigated the adsorption behavior of symmetric dialkyl viologens (C_nVC_n, n = 1,2,…,8) in the presence of αCD and βCD on HMDE, by cyclic voltammetry.

Both hosts were found to bind the alkyl viologen molecules in the bulk of the solution. However, only αCD binds the molecules adsorbed on the surface. In the presence of αCD, the reduction wave of adsorbed molecules with n > 4 shifted to potentials more negative than in the absence of αCD. This suggests that the alkyl chain portion of the viologen molecule is included in the cavity of αCD. The complex with a singly reduced viologen group was found to release αCD molecule into the solution, forming a compact layer of dialkyl viologen molecules being identical to that observed in the absence of αCD. Lee at al. [83] performed a spectroelectrochemical study of dimerization of 1-methyl-1′-alkylviologen molecules (C_1VC_n, with n = 1, 6, 7, 8, 9 and 10) in the absence and presence of αCD. The absorption spectra in the absence of αCD upon the acceptance of one electron show that the extent of dimerization does not significantly change for $n \leq 8$. On the other hand, marked preference for the dimerization was observed for C_1VC_9 and C_1VC_{10}. The effect of αCD on the dimerization of the viologen cation radicals was further investigated for C_1VC_8 and C_4VC_4. In the presence of αCD, the dimerization of C_4VC_4 was strongly supressed, suggesting the formation of a a strong complex between C_4VC_4 and αCD. On the other hand, for C_1VC_8 the dimerization was not affected by the presence of αCD, which was explained by a sterical hindrance. In a related study, [84], the authors investigated the effect of γCD on the dimerization of the full series of 1-methyl-1′-alkylviologen radical cations ($C_1V^{+\cdot}C_n$, with n = 1, 2,...,10). Electrochemical and spectroelectrochemical techniques were employed. The dimerization is enhanced upon the addition of γCD for the molecules with n = 1,2,...,8 with the maximum effect being observed for n = 4. This was explained by stabilization of dimer molecules by the inclusion of the dimer in the large cavity of γCD. However, the dimerization of $C_1V^{+\cdot}C_9$ and $C_1V^{+\cdot}C_{10}$ (the both exhibiting a strong tendency towards the dimerization in the absence of host molecules, see [83]) was found to be suppressed in the presence of γCD. The two studies [83,84] show how the dimerization equilibrium may be shifted by the presence of host molecules of different cavity sizes (αCD and γCD). Yasuda and Seto [85] investigated the electrochemical behavior of viologens with non-alkyl substituents. In particular, the compounds dibenzyl viologen (PhC_1VC_1Ph) and dicyanophenyl viologen (NCPhVPhCN) were scrutinized by cyclic voltammetry and spectroelectrochemical techniques, both in the absence and presence of αCD, βCD and γCD, respectively. The molecule of PhC_1VC_1Ph was found to form an inclusion complex with αCD and γCD only in the singly reduced state, whereas both singly reduced and parent species were included in the cavity of βCD. On the other hand, NCPhVPhCN forms the complex in both reduced and oxidized state, with all three CDs.

2.1.7 Inclusion complexes of molecular wires with cyclodextrins

Data on the complex formation between the extended viologens and cyclodextrin molecules do not exist. Instead, we review the complex formation of other kinds of molecular wires, such as those based on OPE, OPV, poly(1,4-phenylene), poly(4,4'-diphenylene vinylene) and polyaniline.

Taniguchi and Kawai [86] theoretically investigated the effect of αCD coating on the electronic states and electric conduction of OPE- and OPV-based MWs. The first-principles calculation as well as Green's function method was employed. When the wires were coated, the energy of molecular orbitals was stabilized and the molecular structure changed due to a steric hindrance (although the HOMO–LUMO gap did not change). Consequently, the αCD coating was found to reduce the electronic transmission. The corresponding electric conductance of the molecular wires therefore decreased.

Cacialli et al. [87] investigated the properties of conjugated macromolecules poly(1,4-phenylene), poly(4,4'-diphenylene vinylene) and polyfluorene threaded through the cavities of αCD and βCD. The intermolecular interactions (aggregation of wires) were found to be reduced, with the charge-transfer abilities of the wires being largely retained.

Shimomura et al. [88] prepared a series of insulated molecular wires composed of polyaniline coated by a molecular nanotube formed by αCD molecules. The molecules were found to form a symmetric junction i.e. without the rectification of the electric current. The conductivity of the assembly was determined, yielding a value 4×10^{-2} S/cm. In a related study [89] the same inclusion complex was scrutinized by the AFM technique. The atomic force micrographs revealed a presence of a long uniform rod-like structure of height being almost equal to the outside diameter of the αCD molecule. The same αCD:polyaniline complex was also studied by the STM technique and the frequency-domain electric birefringence spectroscopy [90]. The latter method showed that polyaniline changes its conformation from coil to rod in the presence of αCD. The STM technique confirmed the presence of rod-like structures on the gold surface. The authors also showed that the presence of αCD also improves the stability of polyaniline with respect to oxidation.

2.1.8 Inclusion complexes of ferrocene and its derivatives with cyclodextrins

Ferrocene (bis(cyclopentadienyl) iron, Cp-Fe-Cp, abbreviated as Fc) is one of the most used redox mediators [91] and is recommended as a standard, to which the redox potentials are referenced [92]. Fc exchanges one electron in a reversible process [93]. Though the presence of water has no impact on the reversibility, the solubility of Fc is limited in water/organic solvent mixtures. Fc is practically insoluble in pure water [94].

Fc is known to form complexes with the cyclodextrin molecules [95]. In 1975, Siegel and Breslow were the first to report that βCD forms a 1:1 adduct with Fc [96]. Matsue et al. [97] performed a comprehensive study of the inclusion of Fc into the cavity of βCD in the aqueous medium. Ferrocenecarboxylic acid was employed instead of a native ferrocene in order to increase the solubility in water. UV-VIS absorption spectroscopy, circular dichroism and cyclic voltammetry methods were employed. The formation of a 1:1 adduct was confirmed, with the Cp-Fe-Cp axis being oriented parallel to the axis of βCD cavity. The corresponding complex formation constant value, K = 2200 M^{-1}, suggests a very strong complex. The orientation of ferrocenecarboxylic acid and its anion in βCD (in aqueous solutions) was further inspected by circular dichroism in a related study [98]. The inclusion of Fc to the cavities of all three cyclodextrins (αCD, βCD and γCD) was also studied by Wu at al. [99] by measurements of Fc solubility changes. βCD and γCD hosts were found to form 1:1 complexes with Fc, whereas Fc-$(\alpha CD)_2$ complex was observed. Harada and Takahashi [100] studied the complex formation of Fc with βCD and γCD in alcohol solutions. Matsue at al. [101,102] investigated the complex formation between βCD and Fc in pure DMSO and its 80 % water solution, finding the complex formation constants 60 and 320 M^{-1}, respectively.

In conclusion, βCD and γCD were found to form strong 1:1 complexes with Fc [95–99], while αCD forms a rather weak complex with 2:1 stoichiometry Fc-$(\alpha CD)_2$ [71,95,99]. The complex formation strongly depends on the redox state of the Fc molecule [97]. The reduced (neutral) Fc molecule may interact with the hydrophobic cavity of a cyclodextrin molecule. On the other hand, the oxidized form of Fc, ferrocenium Fc^+, is positively charged and therefore, its inclusion into the hydrophobic cavity is much less energetically favorable. As a consequence, the K values of Fc are much higher than those obtained for Fc^+ [97]. The Fc^+ form is, on the other hand, more soluble in polar solvents.

Several approaches were applied for the study of complex formation between Fc and CDs. The spectroscopic (combined circular dichroism and absorption spectroscopy [96–

98,100,103]), electrochemical [96,97,101,102,104–111], calorimetric [112,113], NMR [106] and MS [114] techniques as well as solubility [99] and thermogravimetric measurements [115,116] were used. The Fc was dissolved directly in a solvent of interest [97] or a solid complex was first prepared and then dissolved [108]. The problems could arise in the latter approach as the complex may dissociate upon dissolution, which may lead to a partial precipitation of Fc molecules. This leads to unknown Fc concentration, which causes erroneous results. One may also dissolve Fc in the Fc^+ form to overcome the solubility problems [117]. The Fc may be then generated by the electrochemical reduction of Fc^+.

Schönherr et al. [118] and Zapotoczny et al. [119] performed an AFM study in order to measure the interaction force in the Fc:βCD complex. Chemically modified βCD was self-assembled on the gold substrate, serving thus as a sensoric layer for the guest (Fc) molecules. The Fc molecules (in the form of FcC_nSH, with n = 6 or 16) were adsorbed on the gold-coated AFM tip. The single-molecule spectroscopy (SMS) was then employed to study the rupture of single host-guest complexes. The fundamental force quantum was determined as 55 ± 10 pN.

OPEs serving as linkers between the electrode and the Fc moiety are also available [120,121]. Creager et. al [122] investigated the electron transfer in diluted self-assembled monolayers of Fc-terminated OPEs of six different lengths. The OPEs were attached to a gold substrate via the –SH group. AC voltammetry was employed to study the kinetics of electron transfer. The work lists the electron transfer rate constants for all six lengths of OPE linkers employed. The logarithm of the electron transfer rate was found to linearly decrease with the length of the OPE linker.

2.2 Methods

2.2.1 Electrochemical methods

2.2.1.1 Basic principles of electrochemical methods

Electrochemistry is a part of physical chemistry that studies chemical reactions (and related phenomena) taking place at an interface of an electron conductor (an electrode) and an ionic conductor (an electrolyte), with an electron transfer involved. A metallic electrode can easily provide or withdraw electrons, serving thus as a redox partner with continuously tunable strength depending on its potential. The electrode at which a process of interest takes place is called the working electrode. A common arrangement of an electrochemical experiment involves, besides the working electrode, also a reference and a counter electrode the former one having a fixed potential value, to which a potential of the working electrode is being referred. The counter electrode, usually of a sizeable area, serves as an interface, at which the counter-process takes place, allowing thus the reference electrode to be alleviated from the passage of the electric current that could possibly change its potential. Some applications need oxygen to be removed from the tested solution. Therefore, a stream of an inert gas is passed through the electrochemical cell Figure 1 shows a basic arrangement of an electrochemical experiment.

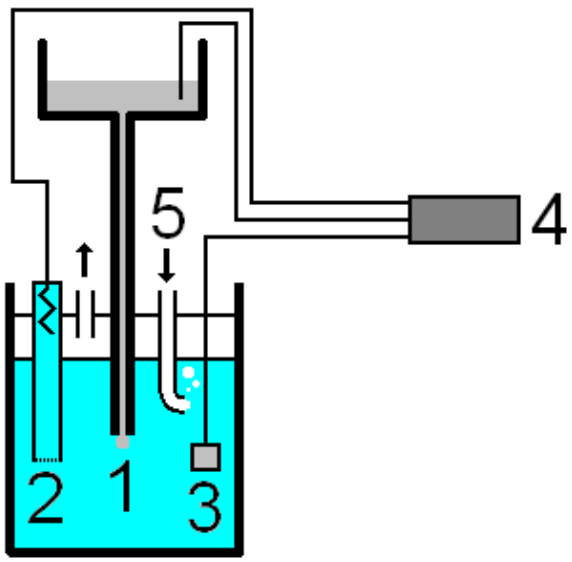

Figure 1: Basic arrangement of an electrochemical experiment. The potentials of the three electrodes: working (1), reference (2) and counter (3) electrode are controlled by a potentiostat (4). Inlet for an inert gas (5).

German physicist and physical chemist Walther Nernst derived the equation relating the solution composition and the potential of the electrode *E* being in contact with that solution [123]. For solution containing electroactive species undergoing a reversible electrochemical reaction

$$O(aq) + n\,e^- \varsigma R(aq) \qquad (1)$$

the Nernst equation takes the shape

$$E = E_0 + \frac{RT}{nF} \ln \frac{c_O(x=0)}{c_R(x=0)} \qquad (2)$$

where $c_O(x=0)$ and $c_R(x=0)$ is the surface concentration of oxidized and reduced form of the electroactive species and *n* is the number of transferred electrons. The standard potential, E^0, of the redox pair O/R is the one at which $c_O(x=0) = c_R(x=0)$. The variables *R*, *T* and *F* are the gas constant, absolute temperature and Faraday's constant, respectively. Changing the potential of the working electrode is a way to control the surface concentrations of electroactive species. The surface concentrations may considerably differ from those in the bulk of the solution, c_O^* and c_R^*, creating thus concentration gradients exploited in the most of the electrochemical techniques.

If O is initially present in the solution, while R is not ($c_R^*=0$), only the electrochemical reduction of O may take place, provided that the potential of the working electrode is set to a sufficiently negative value. The R form, initially absent, is generated at the electrode, with O form being consumed, creating thus concentration gradients for both forms. According to the first Fick's law [123–125] the concentration gradients induce the diffusion movement of the species

$$J_O = D_0 \frac{c_O^* - c_O(x=0)}{\delta_O} \qquad J_R = D_R \frac{c_R(x=0) - c_R^*}{\delta_R} \qquad (3)$$

where D_O and D_R are the diffusion coefficients of the oxidized and reduced form of the electroactive species, respectively. The quantities δ_O and δ_R (called reaction layer thicknesses) characterize the extent to which the solution is altered by the electrode process. The molar diffusion fluxes (J_O and J_R) are the quantities of main interest as they are related to the electric current being a principal observable quantity in electrochemistry. Figure 2 shows the typical concentration profiles of both oxidized and reduced form of the electroactive species in the course of the electrochemical reduction.

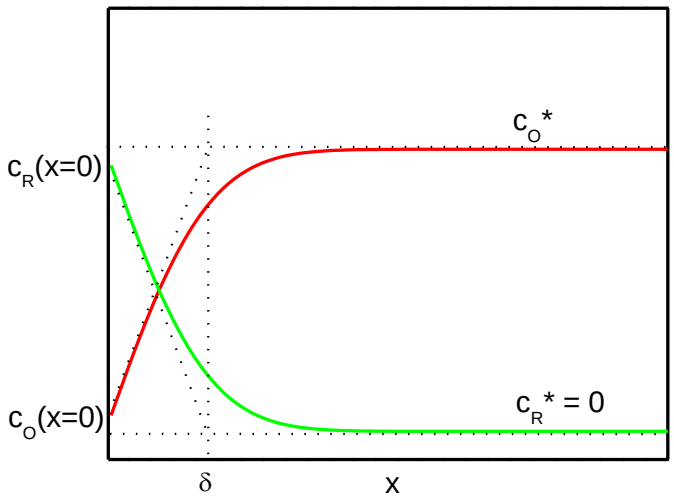

Figure 2: Characteristic concentration profiles of oxidized and reduced forms of electroactive species during the electrochemical reduction of O (with R initially absent). Electrode surface is positioned at x = 0.

2.2.1.2 Classical and sampled DC polarography

In 1922, Czech physical chemist Jaroslav Heyrovský invented the dropping mercury electrode (DME), a device of enormous importance in both physical and analytical electrochemistry [126,127]. The DME was originally devised to measure the surface tension of mercury/electrolyte interface under the potential control. However, Heyrovský quickly realized that the DME could be also used as a working electrode in an electrochemical cell, inventing thus a form of voltammetry which he called the polarography. Heyrovský was recognized with the Nobel Prize in Chemistry in 1959.

In a classical DME, mercury flows from a large reservoir through a capillary of a defined diameter. The height difference between the mercury level in the reservoir and the top of the capillary is well-defined, applying thus a certain constant hydrostatic pressure. The flow rate of the mercury through the capillary is given by the Hagen-Poiseuille equation [128]. The nearly spherical, constantly growing mercury drops at the bottom of the capillary serve as the working electrode. The drop grows until its own gravity can no longer be balanced by the electrolyte/mercury interfacial tension. A leaving drop largely stirs the solution around the working electrode, allowing thus a new drop to be born in a fresh solution.

The potential of the working electrode is slowly swept (or, actually, stepped in very small intervals) with respect to the reference electrode and the current flowing through the working electrode is recorded. It comprises both capacitive and faradaic components, the former one arising due to the presence of an electric double-layer at the mercury/electrolyte interface. The latter one originates from the heterogeneous electron transfer between the electrode and the electroactive species dissolved in the solution. In most cases, the DME is designed for electrochemical reductions, serving thus as the cathode of an electrochemical cell, with the electric current flowing from the solution to the electrode. The current transients recorded at the DME account for both drop growth ($i \sim t^{2/3}$) and the depletion of an electroactive species in the vicinity of the electrode ($i \sim t^{-1/2}$). If the capacitive contribution is neglected, the current transients are governed by the Ilkovič equation [129,130] with $i \sim t^{1/6}$.

Though frequently used in many electrochemical experiments, the DME suffers from some drawbacks:

- Constantly changing area complicates the mathematical treatment in the mass-transport governing continuity equation.
- Unlike stationary electrodes, new surface area created during the drop lifetime creates an additional charging current.
- Considerable disadvantage is a limited mercury flow rate causing thus a limited range of drop lifetimes and final sizes.

The lifetime of the drop can be reduced by a drop knocker, providing the defined drop time and final area. In this case, sampled current measurement (τ being the sampling time of the measurement) can be used instead of a cumbersome continuous recording.

The static mercury drop electrode (SMDE) was invented to overcome the above mentioned disadvantages and limitations of DME [131,132]. In SMDE, the mercury flow is valve-operated, the valve being opened usually for tens of milliseconds, allowing a defined amount of mercury to be extruded through the capillary. The static mercury drop of constant area remains at the outlet of the capillary during a trial and is dislodged by the drop knocker afterwards. The SMDE is used in a repetitive mode, retaining the important benefits of DME:

- working electrode of reproducible surface area
- solution stirring
- atomically flat interface

Mercury electrode may also be used in the form of hanging mercury drop electrode, HMDE, e.g. cyclic voltammetry or differential capacity - time measurements, still retaining important

the advantages over the polycrystalline solid electrodes. In the case of HMDE, the respective method should be called "voltammetry" rather than "polarography" as the working electrode is not renewed anymore.

If the potential of the working electrode is sufficiently positive, no electrochemical reduction takes place and the current flowing through the electrode originates only from the double-layer charging. For sufficiently negative potential values, the charging current is superimposed by the faradaic one, forming a plateau, the height of which is called the limiting diffusion current, i_L. It is proportional to the concentration of the electroactive species in the solution. The half wave potential, $E_{1/2}$, is defined as the potential at which $i=i_L/2$. The value of $E_{1/2}$ provides the information about the chemical identity of the electroactive species and is very close to E^0 for reversible systems. In the region, where the electric current attains the i_L value, the rate of the electrochemical reaction is limited by the mass transfer (diffusion). whereas at less negative potentials (in a capacitive area and at $E_{1/2}$) it is governed by both diffusion and charge transfer kinetics.

Figure 3 shows a typical (simulated) sampled DC polarogram (with SMDE as the working electrode) of electrochemical reduction of an electroactive species.

The exact behavior the electroactive species with R initially absent in the solution in sampled DC polarography is given by the equation

$$E = E_{1/2} + \frac{RT}{nF} \ln \frac{i_d(\tau) - i(\tau)}{i(\tau)} \qquad (4)$$

which may easily be derived by combining the Nernst equation (Eq. 2) and the first Fick's law (Eq. 3) for the diffusion (τ being a chosen sampling time, kept constant during entire experiment). The equation 4 can be rearranged to the shape [133,134]

$$\ln \frac{i_d - i}{i} = \frac{nF}{RT}(E - E_{1/2}) \qquad (5)$$

frequently used in what is called the "log-plot" analysis. The log-plot analysis offers the number of electrons transferred in an electrochemical reduction to be determined by plotting the term $ln(i_d-i)/i$ (or alternatively $log(i_d-i)/i$) against the electrode potential and calculating the slope, which is proportional to the number of accepted electrons.

The other procedure to determine the electron consumption is a direct comparison of a wave height to that of a standard obtained at the very same conditions (concentration, sampling time, electrode area, solvent, temperature).

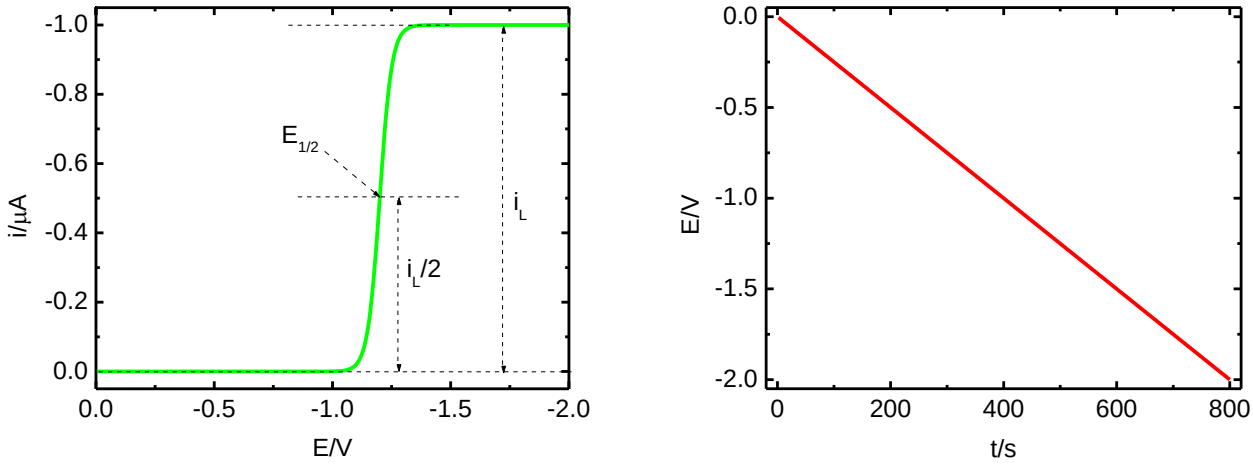

Figure 3: Simulated sampled DC polarogram (left panel) for an electroactive species consuming 1e⁻. Simulation conditions: τ = 1s, $E_{1/2}$ = -1.20 V and $i_L(\tau)$= 1.0 μA. Respective potential program for the working electrode is shown in the right panel.

2.2.1.3 Cyclic voltammetry

Unlike in the techniques of the sampled DC and classical polarography, in the cyclic voltammetry (CV) the electrode has a constant surface area, *A*, and is not renewed during the entire experiment [123]. Both solid (Au, Pt and others) and liquid (HMDE) working electrodes may be used. The CV belongs to what is collectively called the as linear sweep techniques (LST). As in the sampled DC polarography, the potential is swept within the potential window of the electrode/electrolyte system, at various scan-rates, *v*. The use of solid electrodes offers the possibility to study both oxidations and reductions at once. As the electrode is not renewed, the electroactive response of the reaction intermediates and products may also be investigated. The current response has a peak shape rather than reaching a plateau as in sampled DC and classical polarography.

Even for the simplest case (i.e. reversible electron transfer with reduced form initially absent, without complications such as adsorption and follow-up reactions), the mathematics involved in deriving the current response in CV are rather complicated. The peak current, i_p, is given by the Randles-Ševčík equation [123,135,136].

$$i_p = k\left(\frac{F^3}{RT}\right)^{1/2} n^{3/2} A D_O^{1/2} c_O^* v^{1/2} \qquad (6)$$

with the constant k = 0.4463 (for i_p being in μA). The cathodic current peaks (with the height $i_{p,c}$) at the potential $E^0 - 30/n$ (in mV, E^0 being the standard redox potential of a respective electroactive species and n is the number of electron transferred). The general advantage of CV is that the reaction products may be turned back into the parent species when the electrode potential is swept back, giving rise to the anodic current peak (with the height $i_{p,a}$) at the potential $E^0 + 30/n$. Thus, for reversible systems, the difference between the cathodic and anodic peak is $E_a - E_c = 60/n$, the peaks being symmetrically positioned around the E^0 value. Another sign of the reversibility is the equal peak height $i_p = i_{p,a} = i_{p,c}$ for all v values being proportional to $v^{1/2}$. Figure 4 shows a typical cyclic voltammogram for a reversible one-step one-electron transfer.

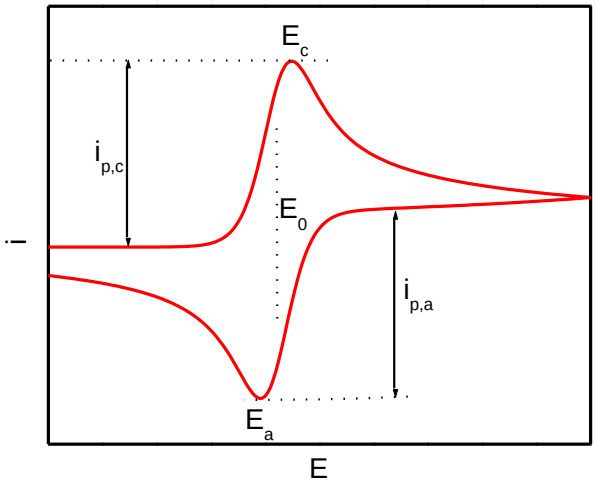

Figure 4: Simulated cyclic voltammogram for a reversible one-step, one-electron transfer. Simulating conditions: scan-rate 0.1 V/s, c_O = 1 mM, with R initially absent.*

CV is also able to probe quasi-reversible and irreversible systems [123]. For electrochemically quasi-reversible systems, the peak separation is $E_a - E_c > 60/n$, being dependent on the scan-rate. Electrochemically irreversible systems lack the presence of a backward peak (either cathodic or anodic, depending on the scan direction and accessible potential values). The reason for an increased peak separation is the need to provide an additional overvoltage for the electron transfer to occur.

A characteristic sign of chemically quasi-reversible/irreversible systems is a voltammogram having diminished/vanished backward peak(s), caused by a partial/total deactivation of the electro-generated species by a follow-up process like decomposition, dimerization or the reaction with solvent or electrolyte molecules. However, new peaks may arise when the products of the follow-up processes are electroactive.

If two or more electroactive species are present in the solution and/or an electroactive species accepts two or more electrons in subsequent steps, several voltammetric peaks will arise. Figure 5 shows the cyclic voltammograms for fully reversible (left panel) and chemically irreversible (right panel) two-step electron transfer.

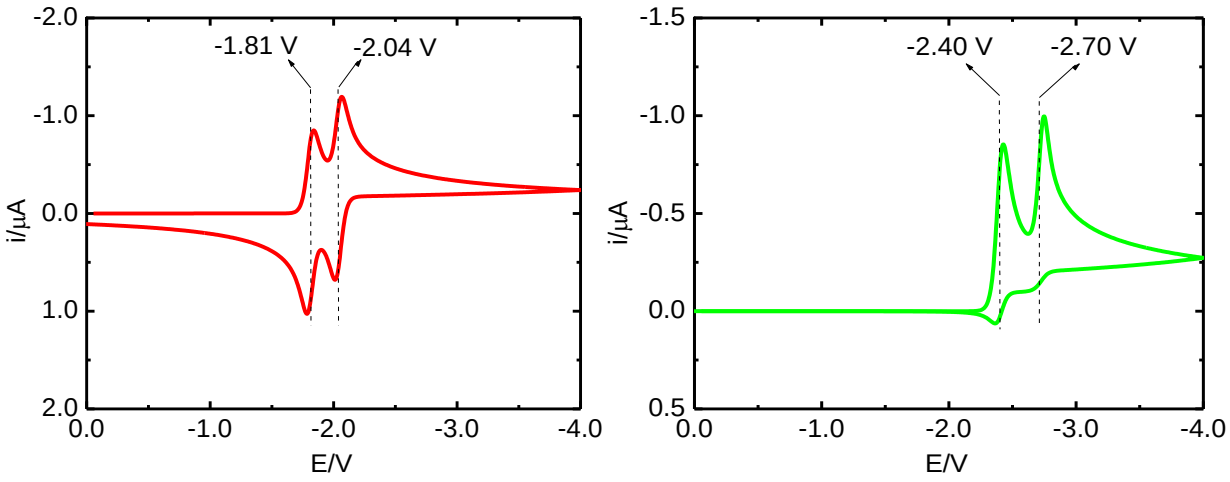

$A + e^- \varsigma A^-$

$A^- + e^- \varsigma A^{2-}$

no homogenous reactions

$A + e^- \varsigma A^-$

$A^- + e^- \varsigma A^{2-}$

$A^{2-} \varsigma B$ (not electroactive)

Figure 5: Simulated cyclic voltammograms of chemically reversible (left panel) and irreversible (right panel) electron transfer of an electroactive species with E_1^0 = -1.81 V and E_2^0 = -2.04 V (left panel) and E_1^0 = -2.40 V and E_2^0 = -2.70 V (right panel). The electroactive species consumes 1 electron in each step, with the electron transfer being electrochemically reversible. Simulation conditions: c = 1 mM, v = 0.1 V/s.
The reaction mechanism is described by the schemes below the panels.

Cyclic voltammetry can also reveal the presence of adsorbed species on the electrode surface [123]. If an electrode is modified by an adsorbed layer, new features originate in CV:

- An adsorbed layer modifies the structure of the electric double-layer of the electrode and therefore, changes the value of its differential capacity. The capacity changes (caused by the adsorption, desorption or phase transitions) may be traced by CV technique, showing the tensammetric peaks.
- Adsorbed layers may block the electrode, hindering thus the mass-transfer and/or charge-transfer of an electroactive species (form the bulk of the solution).
- Certain molecules, such as cyclodextrins and calixarenes, may adsorb on the electrode surface and selectively control the electron transfer of electroactive species.

- If an adsorbed layer is electroactive itself, peaks arise in cyclic voltammograms, due to the charge-transfer in the layer. If electroactive species areabsent in the bulk of the electrolyte (or are of a negligible concentration), the adsorbed molecules provide the response alone. In that case, sharp, bell-shaped peaks originate, with no cathodic/anodic peak separation, as there is no mass-transfer limitation within the electroactive monolayer. The peak current is proportional to the scan-rate and surface concentration of molecules forming the electroactive layer.
- If an electroactive species are present both in the bulk of the electrolyte and on the electrode, the response of bulk molecules is superimposed by that of adsorbed ones.

Figure 6 shows the overview of the mentioned adsorption situations.

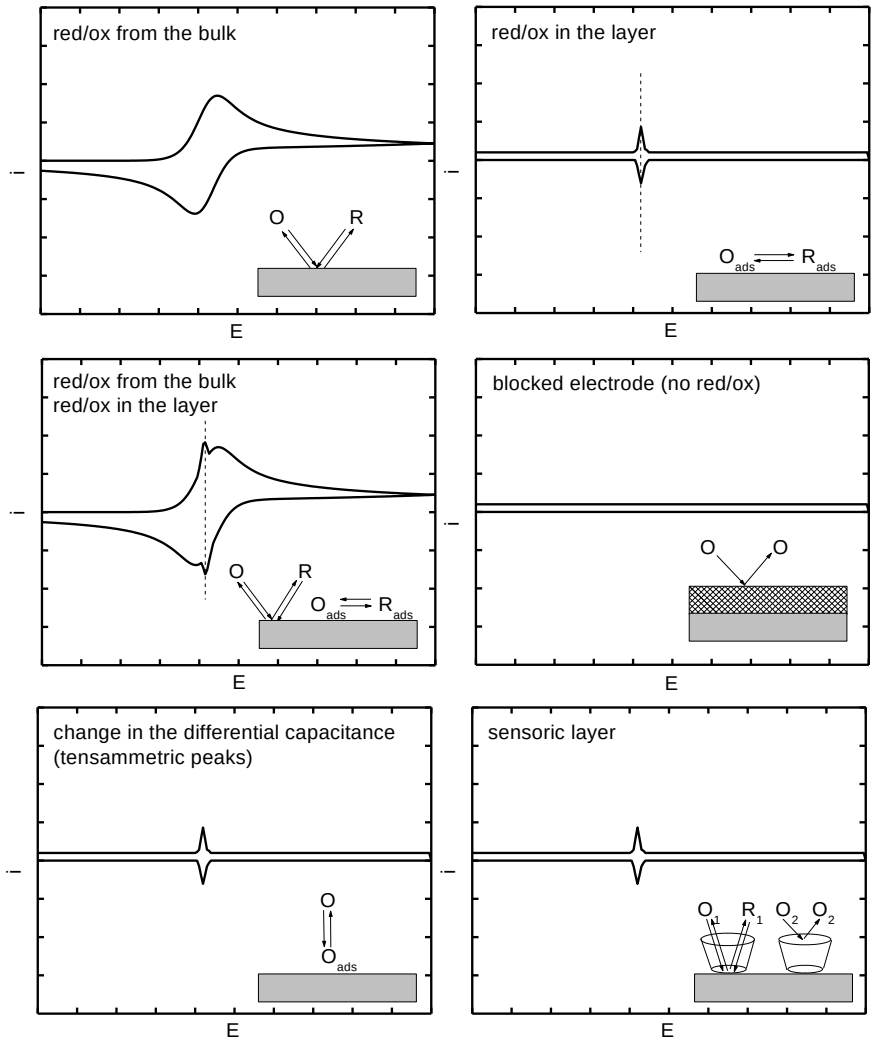

Figure 6: Cyclic voltammograms for: (A) reversible charge transfer of species from the bulk of the solution without adsorption, (B) reversible charge transfer of species adsorbed on the electrode, (C) simultaneous charge-transfer of a species both from bulk of the solution and adsorbed on the electrode, (D) blocked electrode with no current response, (E) adsorption and desorption of non-electroactive species, (F) an electrode with sensors adsorbed.

2.2.1.4 Potentiostatic methods

The potentiostatic methods exploited in this thesis are divided into two groups:

- bulk electrolysis methods, in which the entire solution is electrochemically altered in the course of the electrolysis [123].
- methods employing optically transparent thin layer electrode (OTTLE), in which only part of the scrutinized solution (that close to working and counter electrode) is electrochemically modified [123,137,138].

The common denominator of the two methods is that (unlike CV, classical polarography and sampled DC polarography) the entire experiment is accomplished at a constant potential of the working electrode. The bulk electrolysis is suitable to determine the electron consumption, but lacks the opportunity to obtain in-situ absorption spectra. The OTTLE-based methods are also applicable to electron consumption studies and, moreover, offer the in-situ spectra to be acquired. These may be done in order to confirm the chemical stability of electro-generated species. If some follow-up reactions are present, one may employ the in-situ spectroelectrochemistry to study the kinetics and/or determine the side-reaction extent under various conditions.

Though having considerably different effective reaction volumes and time scales, the both families of methods have some similar features. In both cases, the potential is stepped from a capacitive region (i.e. from the region in which no faradaic reaction occurs) to the potential, at which the charge-transfer is diffusion-limited. After a certain time during which the electric current and absorption UV-VIS-IR spectra are recorded, the potential is stepped back to a value in a capacitive region, with the backward electron transfer being investigated.

The difference between the the bulk and OTTLE-employing electrolysis lies in the mass-transfer of the electroactive species.

In the bulk electrolysis methods, the solution is agitated by a stirrer and/or stream of an inert gas and therefore, the convection (besides the diffusion) plays a role in the mass transport of both reactant and product. Under such conditions, the entire solution of volume V is assumed to be of constant composition (due to the convection), except for the reaction layer of a thickness δ in the vicinity of the working electrode of area A, where the mass-transfer is largely controlled by the diffusion. If R form is initially absent, the current-time dependence takes the form [123]

$$i(t) = i(0)e^{-D_O At/\delta V} \qquad (7)$$

with *i(0)* being the initial current flowing through the working electrode. At any chosen time, *T*, the electric charge can be calculated by the integration of the current transient

$$Q(T) = \int_0^T i(t)dt \tag{8}$$

For fast bulk electrolysis, a large *A/V* ratio as well as the intense agitation (small δ) is necessary. The mass-transfer in OTTLE-based electrolysis is controlled exclusively by diffusion. Therefore, the current-time behavior is governed by the Cottrell equation [123,139]

$$i(t) = \frac{nFAD_O^{1/2}c_O^*}{\pi^{1/2}t^{1/2}} \tag{9}$$

The conditions assumed in derivation of the Cottrell equation (namely the constant concentration c_O^* in the bulk of the solution) are, however, not met in the late stages of the OTTLE electrolysis as the entire amount of an electroactive species within the space of the OTTLE working electrode of a volume *V* is assumed to be altered. The current transient shape is therefore somewhat experimental and a calibration using a standard is necessary to determine the electron consumption. The way of current integration is identical to that for the bulk electrolysis (Eq. 8).

Figure 7 shows a typical potential program for the potentiostatic experiment and a resulting current transient.

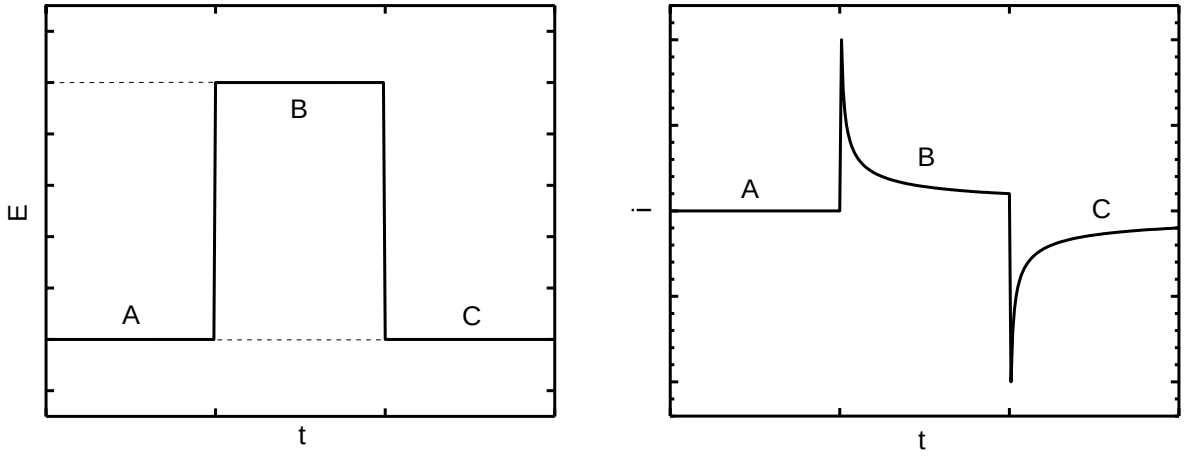

Figure 7: Typical potential (left panel) and current (right panel) profiles during potentiostatic electrolysis: (A) potential set to a value in a capacitive area, (B) potential stepped to a value at which the process of interest is diffusion-limited, (C) a step back to the capacitive area. The two methods differ in their i-t transient shapes (exponential for bulk vs. inverse square-root for OTTLE-employing electrolysis).

2.2.1.5 Impedance techniques

2.2.1.5.1 Basic principles of impedance techniques

The methods described in this chapter have a common denominator: a periodical perturbation (usually sine wave oscillations in the working electrode potential) imposed in the electrochemical cell [123,140]. The resulting oscillating current flowing through the working electrode is used to gain information about the investigated system. The both quantities i.e. alternating voltage and alternating current are analyzed by a lock-in amplifier, with the cell admittance (an inverse of the cell impedance) being the main output of the measurements.

The electrochemical impedance techniques employ the cell design in which the impedance of the working electrode prevails over that of the counter electrode and the solution. The counter electrode impedance can largely be eliminated by using an electrode of considerably larger area than that of the working electrode. The solution resistance can be suppressed either by a high concentration of the supporting electrolyte or by the IR compensation.

The frequency of perturbation signal may attain a very broad range of values, allowing thus both slow and fast electrochemical reactions to be investigated. Moreover, impedance techniques may also help to probe the electric double-layer of the working electrode. As the double-layer differential capacity sensitively reflects the interfacial properties, the impedance techniques are indispensable for studies of adsorption and phase transitions at interfaces.

2.2.1.5.2 Adsorption and impedance techniques

The simplest electrochemical system, an ideally polarizable working electrode immersed in an electrolyte solution containing no electroactive species, can be replaced by a serial RC equivalent circuit. The differential capacity of the electric double-layer of the working electrode changes with the electrode potential and sensitively reflects the double-layer properties [140]. If an adsorbable species is added to the solution, the value of the differential capacity will decrease in a certain range of electrode potentials (Figure 8). This decrease is a consequence of the double-layer structure changes, namely the replacement of the solvent by the absorbable species (having different dielectric properties). The adsorption region has usually sharp maxima on both its edges (Figure 8). This may be explained by desorption of molecules.

Besides being studied as a function of the electrode potential, the capacity transients may also be investigated (at a constant electrode potential).

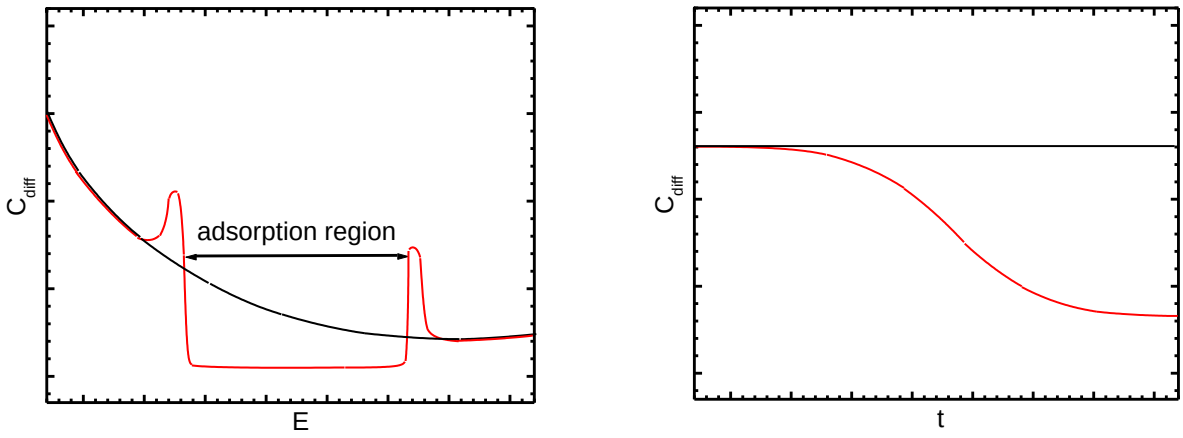

Figure 8: Double-layer differential capacity of a pure electrolyte (black lines) and a solution of an adsorbate (red lines). Differential capacity as a function of the electrode potential (left panel) and capacity transients (right panel) at a constant potential in the adsorption region.

2.2.1.5.3 Redox reactions and impedance techniques

Faradaic processes may also be investigated by the aid of impedance techniques [123]. Depending on the electrode potential, the species in the solution may participate in the charge transfer reactions. In terms of the equivalent circuits, the charge transfer may be modeled by a resistor (with the charge-transfer resistance, R_{ct}) being parallel to the double layer capacity, C. The reactions with fast electron transfer have small R_{ct} values and *vice versa*. At fast rates of faradaic processes (with R_{ct} being small), the mass-transport becomes a rate-limiting step. Therefore, a circuit element accounting for the mass-transport is also necessary. This element is called the Warburg impedance, Z_W, and is positioned in the series with the charge transfer resistance. Though rather complicated mathematical treatment is involved when dealing with both R_{ct} and Z_W, the results are well understandable in single frequency measurements. The both real and imaginary components (Y_F' and Y_F'') of the faradaic impedance

$$Y_F = Y_F' + jY_F'' = 1/Z_F \qquad Z_F = R_{ct} + Z_W \tag{10}$$

depend on the applied potential and form peak-shaped functions, both being superimposed on the real and imaginary part of the "electrode baseline", respectively. For electrochemically reversible systems, the both components are equal $Y_F' = Y_F''$ at all potentials and the peak potentials coincide with E^0. For quasi-reversible systems, the both maxima are shifted (with respect to E^0) and $Y_F' > Y_F''$. For irreversible systems, $Y_F'' = 0$. However, the division to

reversible, quasi-reversible and irreversible processes is only relative, as, in principle, any reversible process may become quasi-reversible or even irreversible at sufficiently high perturbation frequency values and *vice versa*. Figure 9 shows a typical AC polarogram of a reversible (left panel), quasi-reversible (middle panel) and irreversible (right panel) electrochemical process.

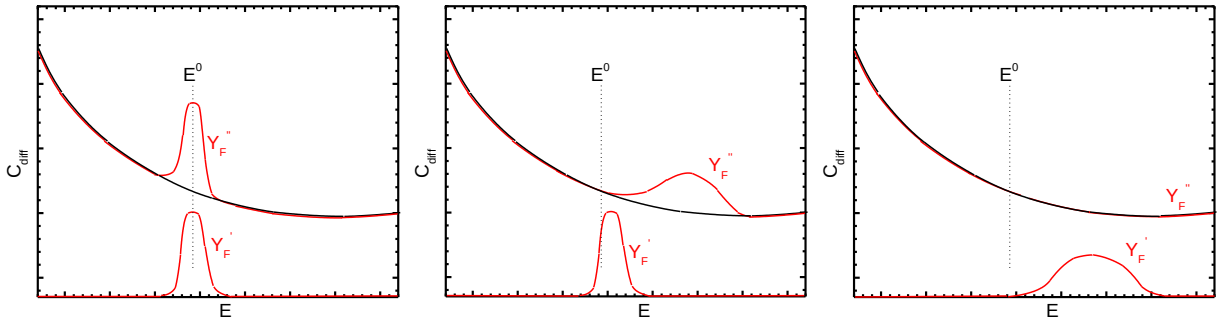

Figure 9: Typical AC polarograms of a reversible (left panel), quasi-reversible (middle panel) and irreversible (right panel) electrochemical process. The faradaic responses (red lines) are superimposed on the "electrode baseline" (black lines).

2.2.1.5.4 Electrochemical impedance spectroscopy

The AC techniques may investigate the electrochemical processes of a very broad range of rate constants, *k* [123,140]. Besides being used at a constant frequency *f* (with the electrode potential being varied), the impedance spectroscopy (sweeping of the perturbation frequency through a certain range of values) may also be employed. The frequency response of an electrochemical cell accounts for the presence of all circuit elements in its equivalent circuit. The solution resistance, modeled by a simple resistor (with a resistance *R*), and the capacity of the electric double-layer of the working electrode, modeled by a capacitor (with the potential-dependent capacity *C*), are the simplest circuit elements.

The charge-transfer at the working electrode is modeled by the above mentioned charge transfer resistance R_{ct}, being dependent on the electrode potential

$$\frac{1}{R_{ct}} = nFA\left(c_R \frac{\partial k_f}{\partial E} - c_O \frac{\partial k_b}{\partial E} \right) \qquad (11)$$

where *n* is the number of electrons transferred in an electrochemical reaction taking place at an interface of area *A*. The rate of the reaction depends on the electrode potential *E* in both its directions, with the rate constants k_f and k_b for reduction and oxidation process, respectively.

The surface concentrations of both oxidized, c_O, and reduced, c_R, forms of an electroactive species depend on the electrode potential according to the Nernst equation (4).

The mass-transfer at the working electrode is modeled by the Warburg impedance, defined as

$$Z_W = \zeta R_{ct}(1 - j) \tag{12}$$

having therefore the two components equal, $Z_W' = Z_W''$, with the parameter ζ defined as

$$\zeta = \frac{k_f}{\sqrt{2\omega D_R}} + \frac{k_b}{\sqrt{2\omega D_O}} \tag{13}$$

here, D_O and D_R are the diffusion coefficients of the oxidized and reduced form, respectively, and $\omega = 2\pi f$. The faradic impedance (accounting for both charge-transfer and mass-transfer contributions) may, therefore, be expressed as

$$Z_F = R_{ct} + Z_w = (1 + \zeta)R_{ct} - j\zeta R_{ct} \tag{14}$$

One can show that for sufficiently large values of frequency, the faradaic admittance, $Y_F = 1/Z_F$, becomes purely resistive

$$\omega \to \infty: \quad Y_F' \to \frac{1}{R_{ct}} \quad Y_F'' \to 0 \tag{15}$$

The overall imaginary part of the cell admittance will, however, not vanish completely as the double-layer capacity term, $Y'' = \omega C$, is left unaffected (see Figure 9). For low-frequency measurements, another simplification is obtained, in which the two components of the faradaic admittance become equal

$$\omega \to 0: \quad Y_F' = Y_F'' \to \frac{1}{2\zeta R_{ct}} \tag{16}$$

In a very fast electrochemical process ($R_{ct} \to 0$), the mass-transfer (i.e. diffusion) becomes a rate-limiting step, the faradaic impedance being therefore equal to the Warburg impedance, for which $Z_W' = Z_W''$. A slanted line (with the angle 45°) represents, therefore, a diffusion-limited electrochemical process in the complex plane plot (lower left panel in Figure 10).

For a slow electrochemical process, on the other hand, the R_{ct} term becomes dominant and the circle (with the radius of $R_{ct}/2$) is the representation of charge-transfer limited process in the complex plane plot (lower right panel in Figure 10).

For moderate rate constants of the electrochemical process, both R_{ct} and Z_W are relevant (each in a certain range of frequencies) and therefore, both circle (characteristic for a charge-transfer limited process) and a slanted straight line (typical for a mass-transfer limited process) are observed (upper right panel in Figure 10).

A straight vertical line, typical for an RC equivalent circuit, is observed in the complex impedance plot when no electrochemical process takes place (upper left panel in Figure 10).

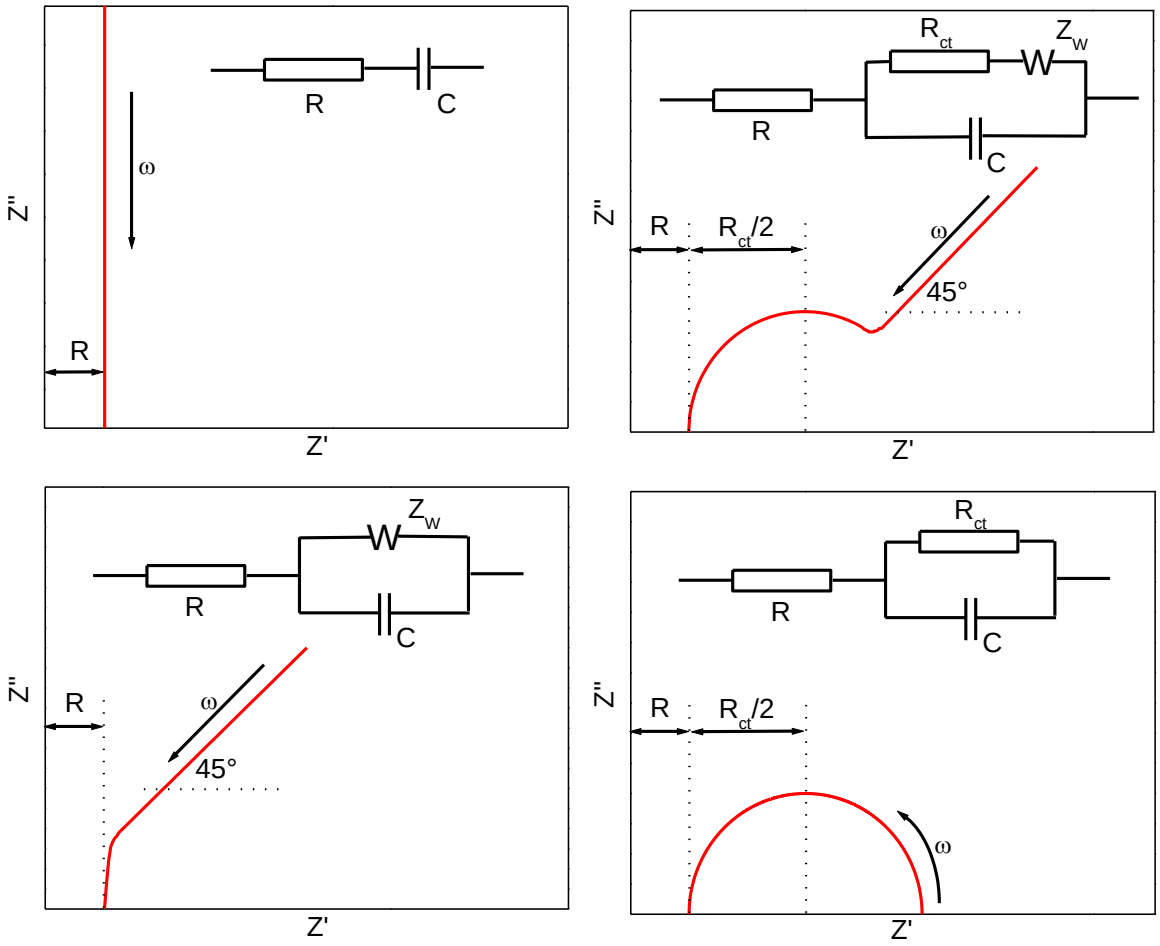

Figure 10: Simulated complex plane representation of an electrochemical cell with (A) no, (B) moderately facile, (C) fast and (D) slow charge-transfer process. The respective equivalent circuits are shown in the panels.

2.2.2 Scanning probe techniques

Scanning probe microscopy (SPM) techniques offer significant benefits over conventional optical and electron microscopic techniques (higher resolution, no need to use conductive substrates, advanced surface analysis and a probe-induced particle movement). There are four families of SPM techniques:

- Atomic force microscopy (AFM)
- Scanning tunneling microscopy (STM)
- Scanning near-field optical microscopy (SNOM)
- Scanning electrochemical microscopy (SECM)

The former two mentioned methods are frequently used throughout this thesis.

2.2.2.1 Atomic force microscopy

2.2.2.1.1 Principles of atomic force microscopy

British physicist and chemist Robert Hooke was the first to discover, in 1676, the principle behind the action of elastic deformations [141] today called in his honour the Hooke's law. Though Hooke originally derived the law for dilation/contraction of linear and circular springs (the balance wheel for pocket watches he has constructed as a student in 1660 [142]), the Hooke's law applies to many other types of bodies e.g. beams and cantilevers and deformations, such as bending, torsion and shear. When applied to bending of an end-loaded cantilever, Hooke's law becomes the underlying principle of atomic force microscopy (AFM) techniques [143,144].

The force F, which is the result of the interaction between the AFM probe and the sample surface causes a cantilever to deflect from its equilibrium position, with the deflection δ being proportional to F, provided that δ is sufficiently small

$$F = -k\delta \tag{17}$$

with k being the proportionality constant, called the spring constant (in the case of springs) or cantilever stiffness (for the cantilevers). For the former case, it is given by the equation

$$k = E\frac{A}{l_0} \tag{18}$$

with E being Young modulus [145] and A and l_0 the effective area and length of the resting spring. For a rectangular cantilever (Figure 11), the equation takes the form [146]

$$k = E\frac{wh^3}{4L^3} \tag{19}$$

with *w*, *h* and *L* being the cantilever width, height (i.e. thickness) and length, respectively.

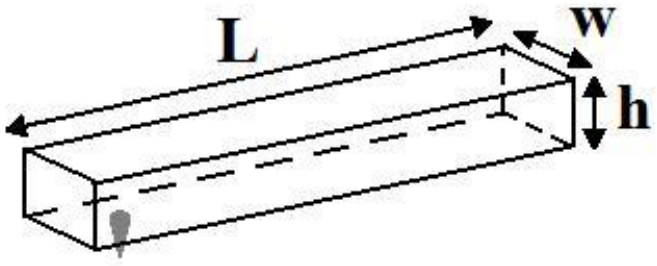

Figure 11 Schematic representation of a resting rectangular cantilever with a probe installed (grey tip). The letters refer to the dimensions.

A clear analogy can be seen between springs and cantilevers, as the material property *E* multiplies the fraction, in which the dimensions of a body are grouped. The relations for triangular cantilevers (frequently used in AFM measurements) are more complicated, but both rectangular and triangular share the most important properties.

The cantilever deflection may be expressed in two ways: (1) as a change of the z-position ($\delta = \Delta z$) of its end upon load with respect to its resting position and (2) as a deflection angle φ, for which tg φ = Δz/L. The former option is chosen throughout this thesis. The cantilever deflection is, however, never measured directly and the deflection of the laser beam reflecting off the cantilever back is traced instead. The laser coming from a suitable steady laser source is reflected from the back of the cantilever and hits the photomultiplier four-quadrant detector. It allows to trace the changes of laser trajectory exactly. When no sample-probe interactions are present i.e. with the probe retracted from the sample surface, the laser position in the detector is set to zero. After bringing them into contact, the cantilever deflects due to the interaction forces and the change in the laser position i.e. its deflection *D* is traced. The *D* value is proportional to the cantilever deflection, $D = S\,\Delta z$, with the proportionality constant *S* called the deflection sensitivity. For each probe used, the *S* value have to be found by a calibration using a rigid, non-sticky surface (e.g. Au(111) or freshly cleaved HOPG). Knowing *S* and *k* values, one can calculate the force acting between the sample and the probe. The *k* value may be calculated theoretically or found experimentally by measuring the resonant frequency $f_0 = \omega_0/2\pi$ of the cantilever. The cantilever stiffness is then given by

$$k = m\omega_0^2 \tag{20}$$

with *m* being the effective cantilever mass.

Figure 12 shows a general scheme of the measurements in the AFM technique.

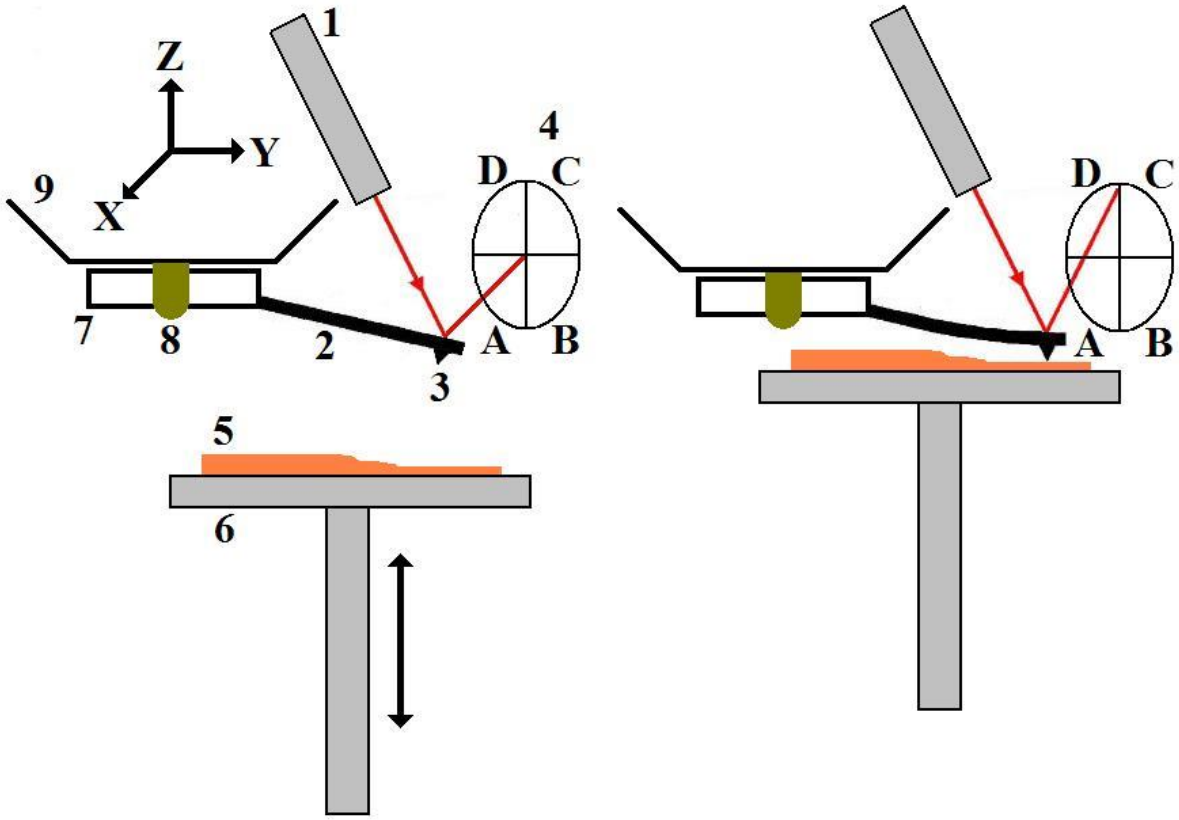

Figure 12: Basic working principle of AFM. The laser source (1) is used to provide a beam shining on the back of the cantilever (2) with a sharp probe (3) attached, being deflected due to interaction forces. The laser position is traced using the four-quadrant photomultiplier detector (4). For rough approach of the sample (5) to the probe, a step motor connected to the sample holder (6) is used. The cantilever is mounted to the platform (7) attached by a clip (8) to the piezo-electric actuators (9). AFM setup with retracted (left pannel) and approached (right pannel) sample is shown.

A step motor connected to the sample holder is used for rough approach of the sample to the probe. Scanning of the probe over the sample is accomplished by precise piezo-electric actuators.

2.2.2.1.2 Contact mode atomic force microscopy

In the contact mode AFM (CM-AFM), the probe is scanned without being oscillated. In principle, two modes are possible:

- Constant force CM-AFM
- Constant height CM-AFM

In the former one, the interaction force is maintained constant by the feedback electronics. Actually, the laser deflection is kept constant rather than the interaction force itself, the two quantities being proportional to each other through the deflection sensitivity and the Hooke's law (17). The feedback electronics changes the *z* position of the probe with respect to the sample surface in order to maintain the pre-defined interaction force called the setpoint force, creating thus the topographic image of the sample surface z = z(x,y). The important parameter to be set for the feedback electronics is the feedback gain *G*, a quantity usually stated in % and controlling the rate, at which the probe reacts to changes in the surface topography. Higher feedback gain values are required for rough surfaces, making them somewhat difficult to be analysed as the noise level of the measurement is proportional to the feedback gain.

In the constant height CM-AFM, the feedback electronics is completely disabled (*G = 0* and *z = const.*). The interaction force is the observed quantity and no information about the sample surface topography is gained. As there is a risk of sample and probe damage when rough surfaces are analysed, this mode is suitable only for extremely flat sample surfaces.

Both constant force and constant height mode CM-AFM are of use only for stiff surfaces. In the case of surfaces containing weakly interacting structures, there is a risk of an undesirable tip-induced particle movement, which leads to the imaging of the underlying substrate rather than of the structures of interest. Figure 13 shows the schematic depiction of both constant force and constant height CM-AFM.

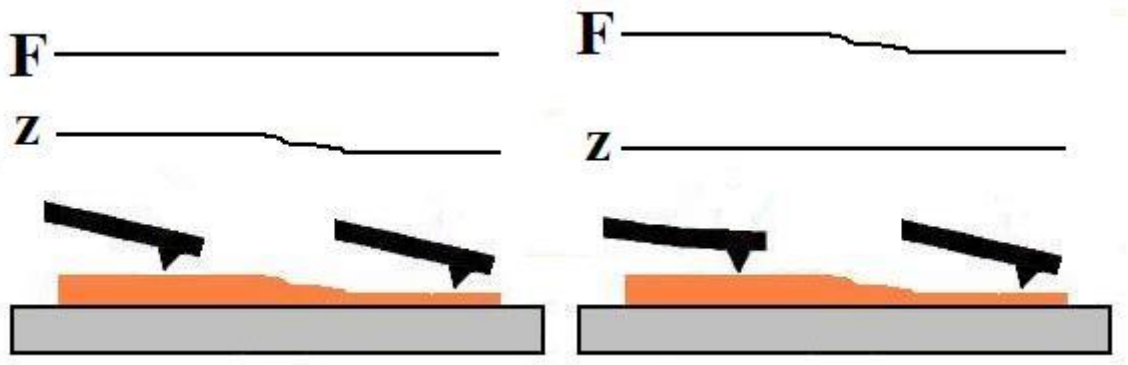

Figure 13: Schematic representation of constant force CM-AFM (left pannel) and constant height CM-AFM (right pannel).

2.2.2.1.3 Alternating contact atomic force microscopy

In the alternating contact AFM, AC-AFM (also called tapping-mode AFM, TM-AFM or intermittent contact AFM, IC-AFM), the probe is oscillated, while scanning the sample surface. As in CM-AFM, two operating modes are possible:

- Constant amplitude AC-AFM
- Constant height AC-AFM

The former one (being an analogue of constant force CM-AFM) employs the feedback electronics to maintain the constant amplitude as the probe scans the surface. As in CM-AFM, the feedback gain is a measure how quickly the probe reacts to changes in topography. The topography map of the surface is acquired.

The constant height AC-AFM mode maintains z = const (as in constant height CM-AFM), with the feedback electronics being disabled. Changes in the probe oscillation amplitude are recorded. The amplitude changes may be caused either by topography changes or by specific interactions.

The cantilever is forced to the oscillatory movement by an external trigger, at a frequency close to its resonant frequency f_0. The oscillations may be invoked by three ways:

- Acoustic driving (AAC-AFM)
- Magnetic driving (MAC-AFM), with a magnetic coil positioned under the sample holder
- Top-magnetic driving (TOP-MAC-AFM), with a solenoid positioned directly above the cantilever (i.e. within the cantilever assembly)

The first mode employs an AC current driven to the z-piezo actuator, oscillating thus the entire cantilever assembly. The latter two methods employ an external magnetic field, allowing thus the magnetically coated cantilever to be oscillated separately. Their benefit is a reduced noise level, allowing the measurement to be carried out under a liquid. The TOP-MAC-AFM mode is somewhat more benefitial than the MAC-AFM one, as a sample and a sample holder may dissipate some energy of the magnetic field, which may lead to a limited range of cantilever oscillation amplitude values.

The AC-AFM is largely used when analysing the surfaces with weakly interacting particles, as the risk of tip-induced particle movement is significantly reduced (over CM-AFM).

With the aid of the lock-in amplifier, one can also observe the phase shift between the driving oscillation (AC z-piezo voltage / magnetic field) and the resulting mechanical probe oscillation. The phase shift is usually set to zero, when the probe is retracted from the sample

surface. It may help to distinguish various materials on the sample surface as it reflects the ability of the surface to retard the probe movement due to the probe/surface adhesion. The phase-sensitive AC-AFM measurements may therefore help to qualitatively distinguish particles of interest from impurities. Figure 14 shows a working principle of both constant amplitude and constant height AC-AFM, respectively

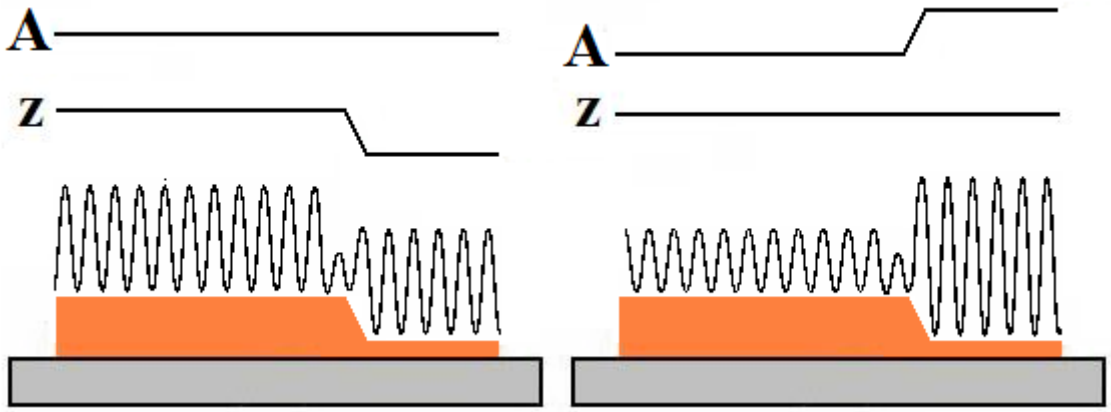

Figure 14: Schematic representation of constant amplitude (left pannel) and constant height (right pannel) AC-AFM. Sine waves represent the probe trajectory.

2.2.2.1.4 Combination of contact mode and alternating mode AFM

Some applications need both CM-AFM and AC-AFM to be used. If some structures are detected only when using AC-AFM and not in CM-AFM, they are highly probably weakly interacting with the surface and are swept away in CM-AFM scanning. The analysis has to be, however, reproduced at several locations on the surface in order to rule out the possibility, that the sample surface is occupied by the adsorbate irregularly with both covered and vacant domains.

The CM-AFM / AC-AFM combination may also provide quantitative information about the surface containing weakly interacting structures. First, the surface with structures of interest (with a reasonably flat underlaying substrate) is pre-imaged by the AC-AFM method. Afterwards, the scan-size is reduced and the sample surface is imaged by the CM-AFM technique employing a suitable force, high enough to sweep the particles but not high enough to damage the underlying substrate. The scan-size is then set back to the original value and the surface is re-imaged using the AC-AFM technique. If the particles interact weakly with the substrate, the CM-AFM scan will sweep them through the imaged domain, revealing a bare substrate observable by subsequent the AC-AFM re-imaging. For reasonably flat surfaces and

sufficiently thin adlayers of particles, this procedure leads to the determination of the layer thickness. This method is, in principle, an interesting alternative to ellipsometry and may serve in the cases where the refractive index of the adsorbed layer needed for layer thickness calculation in ellipsometry is unknown.

This technique, however, suffers from some drawbacks:

- It is applicable only for weakly interacting particles
- Swept particles often adsorb on the probe, which may lead to a significant reduction of the horizontal resolution and imaging artefacts
- The possibility of damaging the underlying substrate has to be excluded by analyzing a pure underlying substrate at the very same conditions (exerted force, scan-speed, feedback gain, the same cantilever and laser configuration)
- The method is suitable only for very smooth surfaces, such as HOPG and Au(111)
- The procedure may lead to a damage of costly probes

Figure 15 shows a general procedure followed in the „surface scratching analysis".

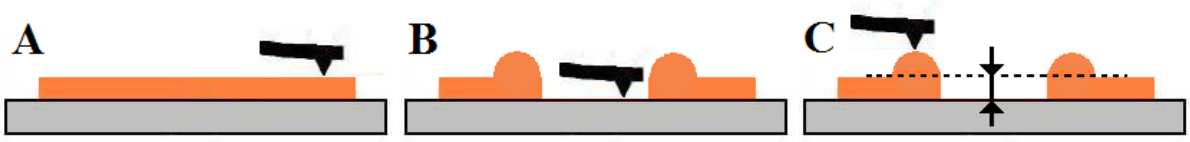

Figure 15: Schematic representation of the „surface scratching analysis" based on CM-AFM / AC-AFM combination. (A) AC-AFM pre-imaging, (B) CM-AFM imaging, (C) AC-AFM re-imaging. The arrows indicate the way how the layer thickness is determined.

2.2.2.1.5 Current sensing atomic force microscopy

Current sensing AFM, CS-AFM (also called conductive probe AFM, CP-AFM) allows the simultaneous detection of the sample conductivity along with the above mentioned quantities [147]. A conductive probe has to be employed, usually a triangular one, coated by Au or Pt/Ir alloy. The CS-AFM is usually run as the constant force CM-AFM. Though sharing some common principles with the STM method, the principal difference lies in the quantity serving as the input into the feedback loop. While the STM uses the electric current as an input variable, the CS-AFM employs, as usual in AFM methods, the interaction force, making thus the current measurement independent. CS-AFM can, therefore, reveal domain of different surface conductivity. Slow scan speeds and loading forces are usually preferred in order to prevent the coated probe from being damaged. Figure 16 shows the general scheme of CS-AFM.

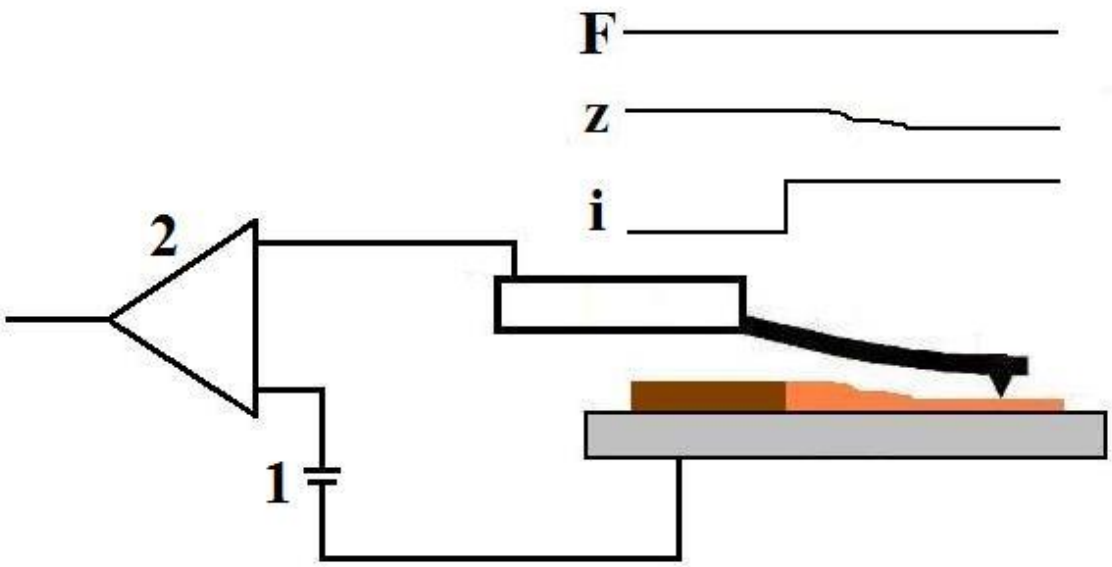

Figure 16: Schematic representation of CS-AFM. A suitable source (1) provides the bias voltage between the conductive probe and the sample. The amplifier (2) converts the electric current into voltage. The surface domains of high (orange) and low (brown) conductivity are discerned by changes in the measured electric current.

2.2.2.1.6 Local probe measurements with atomic force microscopy

Besides being used as a scanning probe technique, the AFM setup may also be employed to investigate local sample properties. Local probe measurements (also called the "spectroscopy") use a stationary probe rather than the scanning one. The vertical position of the probe may either be varied (force-distance and amplitude-distance spectroscopy) or kept constant (current-voltage spectroscopy).

2.2.2.1.6.1 Force – distance spectroscopy in CM-AFM

As mentioned above, no cantilever deflection is observed when a probe retraced from the sample surface. As the probe is approached, at some point, the attractive forces become sufficient to draw the probe tip to the surface and therefore, bend the cantilever, creating a sudden step in a force-distance (or, actually a laser deflection-distance) curve. As the probe assembly is further approached to the surface, the repulsive forces become significant and gradually predominate over the attractive ones. The cantilever bends to the opposite direction, forming a repulsive part of the laser deflection-distance curve. The repulsive part is linear as long as the Hooke's law is satisfied, being curved for higher deflections. The linear segment of the repulsive part of the laser deflection-distance is used to find the deflection sensitivity, *S*,

value being important for determination of the forces acting between the probe and the substrate. Figure 17 shows a typical laser deflection-distance curve.

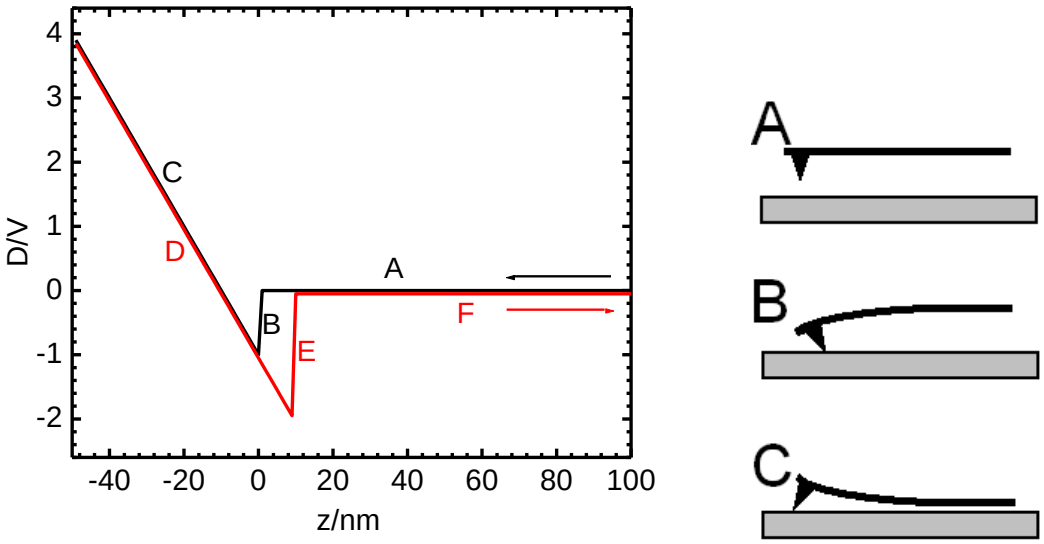

Figure 17: Typical laser deflection-distance curve in CM-AFM. Probe approach (black line) is followed by its retraction (red line). (A) distant probe, (B) the probe attracted by the surface, (C,D) repulsive part of the curve, (E) detachment of the probe from the surface, (F) retracted probe.

The laser deflection-distance curve may show some hysteresis, caused by the capillary forces acting between the probe and water-covered sample surface. The water adsorption may be suppressed by admitting an inert gas into the AFM assembly.

2.2.2.1.6.2 Amplitude – distance spectroscopy in AC-AFM

Local probe measurements may be carried out also in AC-AFM regime. They are frequently performed at the start of an AC-AFM scanning experiment, in order to find a suitable working amplitude A. The A value is usually expressed as a "relative amplitude" $A_r=A/A_0$, with A_0 being the amplitude of the probe retracted from the surface. Usually, $A_r = 90 – 95\ \%$ is taken to investigate smooth surfaces ("soft-touch" AC-AFM), whereas lower A_r values are usually necessary to probe rough surfaces ("hard-touch" AC-AFM).

In a typical local probe AC-AFM experiment, a distant probe is approached to the surface and the reduction of the amplitude due to the interaction forces is observed. The probe is then retracted, leading to the original value of amplitude, A_0. As in CM-AFM, some hysteresis may be noticed due to the capillary forces. Figure 18 shows a typical amplitude – distance curve.

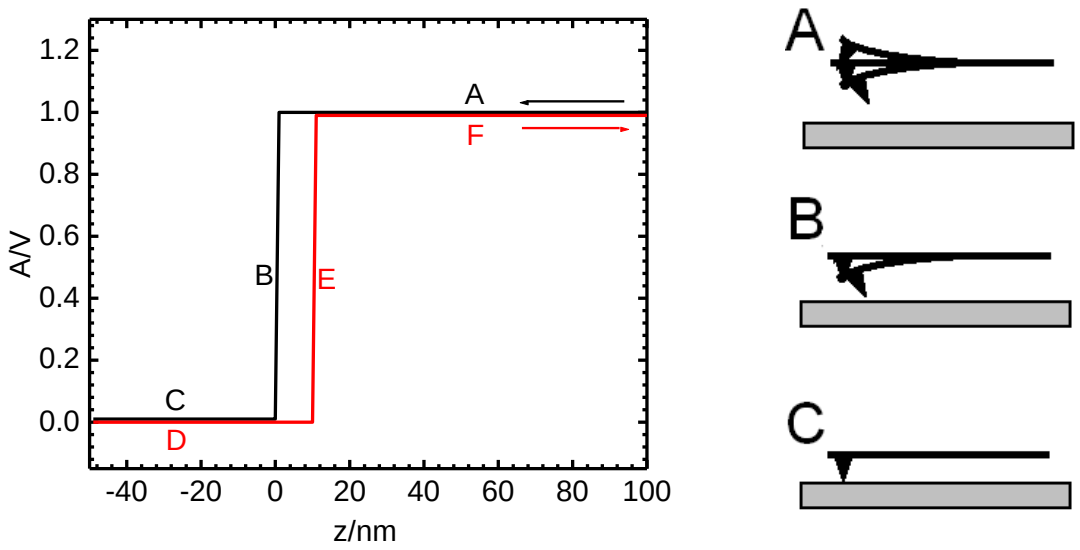

Figure 18: Typical probe amplitude-distance curve in AC-AFM. Probe approach (black line) is followed by its retraction (red line). (A) distant probe, (B) the probe being attracted by the surface, (C,D) strongly reduced amplitude due to the probe/sample strong contact, (E) detachment of the probe from the sample surface, (F) retracted probe.

2.2.2.1.6.3 Current-voltage spectroscopy in CS-AFM

Though usually defined as a CM-AFM technique with additional current profile screening, the CS-AFM technique may also be used to probe local sample properties, being therefore a "spectroscopic technique". This may be useful when investigating fragile surface structures, such as weakly interacting nanoparticles that would be swept through the sample surface if the CM-AFM technique were used.

In the current-voltage spectroscopy (i-V spectroscopy), the probe is very slowly, usually at 50 – 100 nm/s admitted to touch the surface. Afterwards, at a well-defined z-position and loading force, usually on the order of nanonewtons, the sample-probe voltage is swept, with the electric current being recorded. The laser deflection-distance spectroscopy usually follows i-V measurements, in order to record the exact value of the laser deflection. With the help of deflection sensitivity *S* and stiffness constant *k* values of the used probe, one can calculate the exact loading force at which a respective i-V measurement was carried out.

The i-V profile of totally non-conductive surfaces is identical to that obtained with the retracted probe. For conductive surfaces, the i-V measurements may help to distinguish symmetric and rectifying junctions. For a chosen sample-probe voltage *V*, one can define the

rectification ratio as $R(V) = i(V)/|i(-V)|$, the values of R being unity for symmetric junctions and $R >> 1$ for strongly rectifying junctions. Figure 19 (left panel) shows a typical potential profile as well as resulting current-voltage profiles (right panel) for a symmetric (red line) and a rectifying (black line) junction.

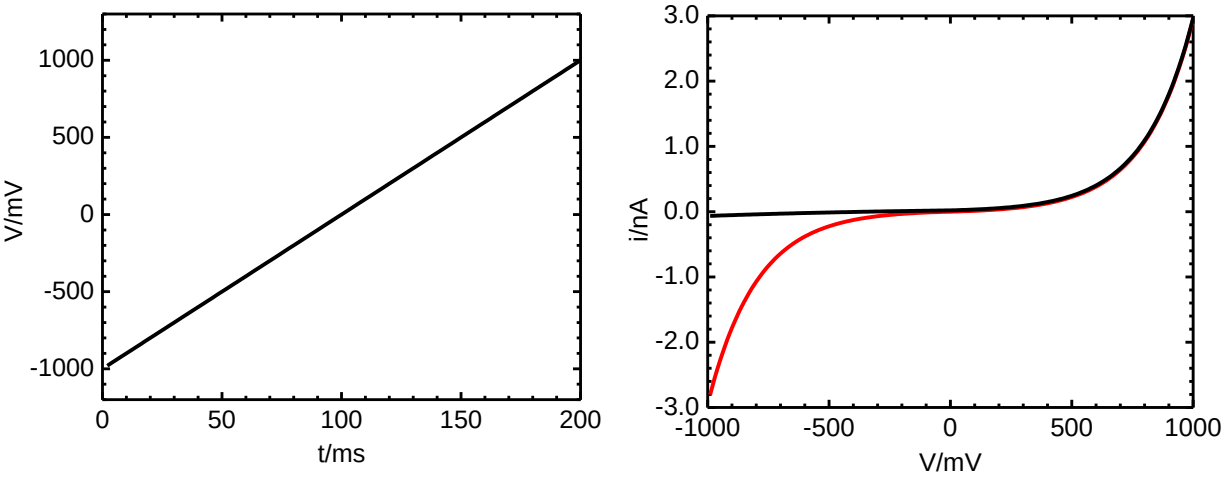

Figure 19: Characteristic potential program for i-V spectroscopy (left panel) and resulting i-V characteristics (right panel) of a symmetric (red line) and a rectifying (black line) junction.

2.2.2.2 Scanning tunneling microscopy

2.2.2.2.1 Principles of scanning tunneling microscopy

Scanning tunneling microscopy (STM) is a branch of SPM that allows a sample surface to be investigated at a molecular or even at an atomic level. The STM was developed in 1981 by physicists Gerd Binnig and Heinrich Rohrer [148,149], earning them the Nobel Prize in Physics in 1986. The basic concept of the STM is the quantum tunneling. The quantum tunneling is an event in which an electron or another particle with a sufficiently low mass may pass through an energy barrier U higher than its own energy E, i.e. $U - E > 0$. This condition is satisfied between the STM tip and the sample substrate, when the voltage is applied. The behavior of electrons is given by the Schrödinger equation [150]

$$-\frac{h^2}{8\pi^2 m}\frac{\partial^2\Psi}{\partial z^2} + U\Psi = E\Psi \qquad (21)$$

the solution of which for an electron between the STM tip and the surface is given as follows

$$\Psi_n(z) = \Psi_n(0)e^{-\kappa z} \qquad (22)$$

where κ is a decay constant that depends on the difference between the barrier height and electron energy

$$\kappa = \frac{1}{h}\sqrt{2m(U-E)} \tag{23}$$

h and *m* being the Planck constant and the electron rest mass, respectively.

On the other hand, the energy barrier within the tip and the sample is lower than the electron energy, $E - U > 0$, leading to a qualitatively different solution of the Schrödinger equation – standing waves in the sample and in the probe

$$\Psi_n(z) = \Psi_n(0)e^{\pm i\kappa z} \tag{24}$$

with

$$\kappa = \frac{1}{h}\sqrt{2m(E-U)} \tag{25}$$

With a suitable bias voltage applied between the sample and the probe their wave-functions may overlap and, therefore, the electrons may be found in the vacuum between the sample and the probe. The probability density *P* for an electron to be found in the barrier is proportional to the wave-function squared

$$P \propto \left|\Psi_n(0)\right|^2 e^{-2\kappa W} \tag{26}$$

with *W* being the width of the energy barrier, i.e. the sample – probe distance. One can get the total tunneling current *I* by summing the *P* contributions for all possible Ψ_n states (local density of states, LDOS, between the Fermi levels of the probe $E_{F,P}$ and the sample $E_{F,S}$) [150]

$$I \propto \sum_{E_{F,S}}^{E_{F,P}} \left|\Psi_n(0)\right|^2 e^{-2\kappa W} \tag{27}$$

The STM probe is therefore sensitive to the LDOS structures rather than to the sample topography itself. Non-conductive surfaces cannot be, therefore, investigated by the STM technique.

The important characteristic of the tunneling current is its exponential dependence on the sample – probe separation *W*, with the decay constant κ being dependent on the barrier height. The κ values are usually very high and, therefore, the *i*–*z* profiles are very steep. This allows only one (or few) atoms at the very end of the STM probe to interact with atoms in the sample. This leads to an impressive lateral resolution of the STM method, on the orders of 100 pm. The vertical resolution is largely determined by the precision of the *z*- actuator and may attain the values as low as on the orders of 10 pm. Figure 20 shows the basic working principle of the STM technique.

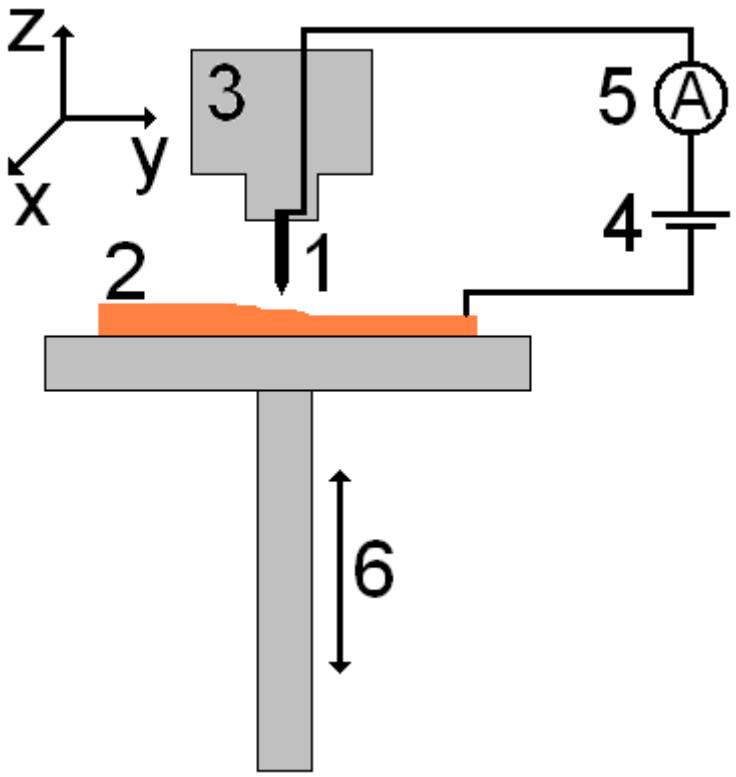

Figure 20: Schematic arrangement of an STM experiment. A sharp metallic probe (1) is scanned over the sample surface (2) with the help of piezoelectric actuators (3). A voltage source (4) is employed to provide a bias voltage between the probe and the sample. The resulting tunneling current is recorded (5). Rough approach of the sample to the probe is accomplished by a step motor (6).

Similarly to AFM techniques, the probe (being usually a Pt/Ir or Au wire) is scanned over the surface, creating thus its topography map. Piezoelectric actuators are employed to control the exact position of the probe with respect to the sample surface. A step motor is employed for a rough approach of the sample to the probe.

2.2.2.2.2 Modes of scanning tunneling microscopy

An STM experiment may be carried in the two modes:

- Constant current STM (an analogue to constant force CM-AFM)
- Constant height STM (an analogue to constant height CM-AFM)

The common denominator of STM and AFM methods is the feedback loop serving as a mechanism to attain a desired quantity constant. In the case of STM, the tunneling current is controlled. The value wished to be kept constant by the feedback electronics is called the set-point current. As in AFM methods, high feedback gain values are necessary to investigate

rough sample surfaces, whereas lower values are sufficient to probe the smoother ones. Extremely flat surfaces may be analyzed with the feedback loop completely disabled i.e. in constant height mode STM. In the constant height mode, the topography image is not obtained, but the surface structures may be deduced from the tunneling current map. As in AFM techniques, the signal-to-noise ratio decreases with higher feedback gain values used, causing thus considerable difficulties when investigating very rough surfaces.

Most of the STM experiments carried out were done in the constant current mode STM, with moderate feedback values being used. Typical bias voltage values spanned the range 0.01 – 1 V, with the set-point tunneling current in the range 0.8 – 2000 pA.

Figure 21 shows the principal differences between the constant current and the constant height mode STM.

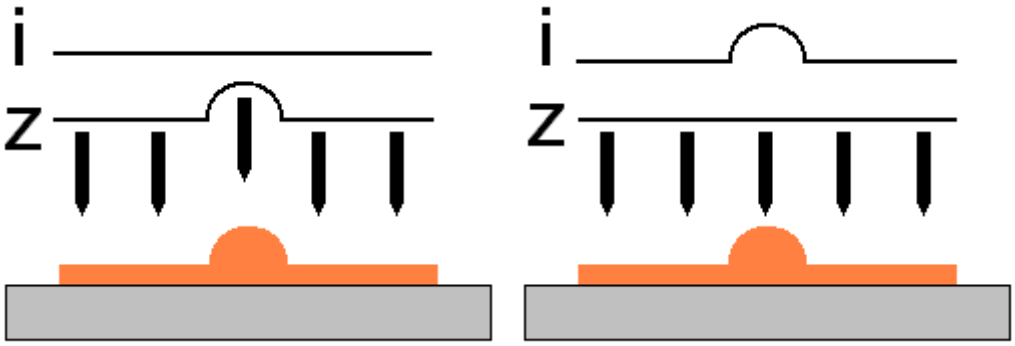

Figure 21: Modes of scanning tunneling microscopy: constant current mode (left panel) and constant height mode (right panel).

2.2.2.2.3 Local probe measurements with STM

Besides being used as a SPM technique, the STM setup may also be employed in "spectroscopic techniques". Two regimes are possible:

- current-distance spectroscopy (i-z spectroscopy)
- current-voltage spectroscopy (i-V spectroscopy), an analogue to local probe CS-AFM

In the former case, the probe is approached to the sample surface to attain a certain desired set-point current value. The feedback electronics is then disabled and the probe is slowly retracted from the sample surface, with the tunneling current being measured. The shape of the *i-z* curve may reveal various features such as pure vacuum tunneling and/or breaking the atomic/molecular junctions between the sample and the probe. The current-distance spectroscopy may be used for determination of the single-molecule conductivity.

The current-voltage spectroscopy in STM is similar to that used in the CP-AFM technique. The probe is approached to the sample surface and, at a defined set-point current, the feedback loop is disabled and the sample-probe voltage is swept, measuring the tunneling current. Figure 22 shows schematic current-distance profiles for a junction containing no (left panel) and one (right panel) molecule attached to the STM probe [35–40].

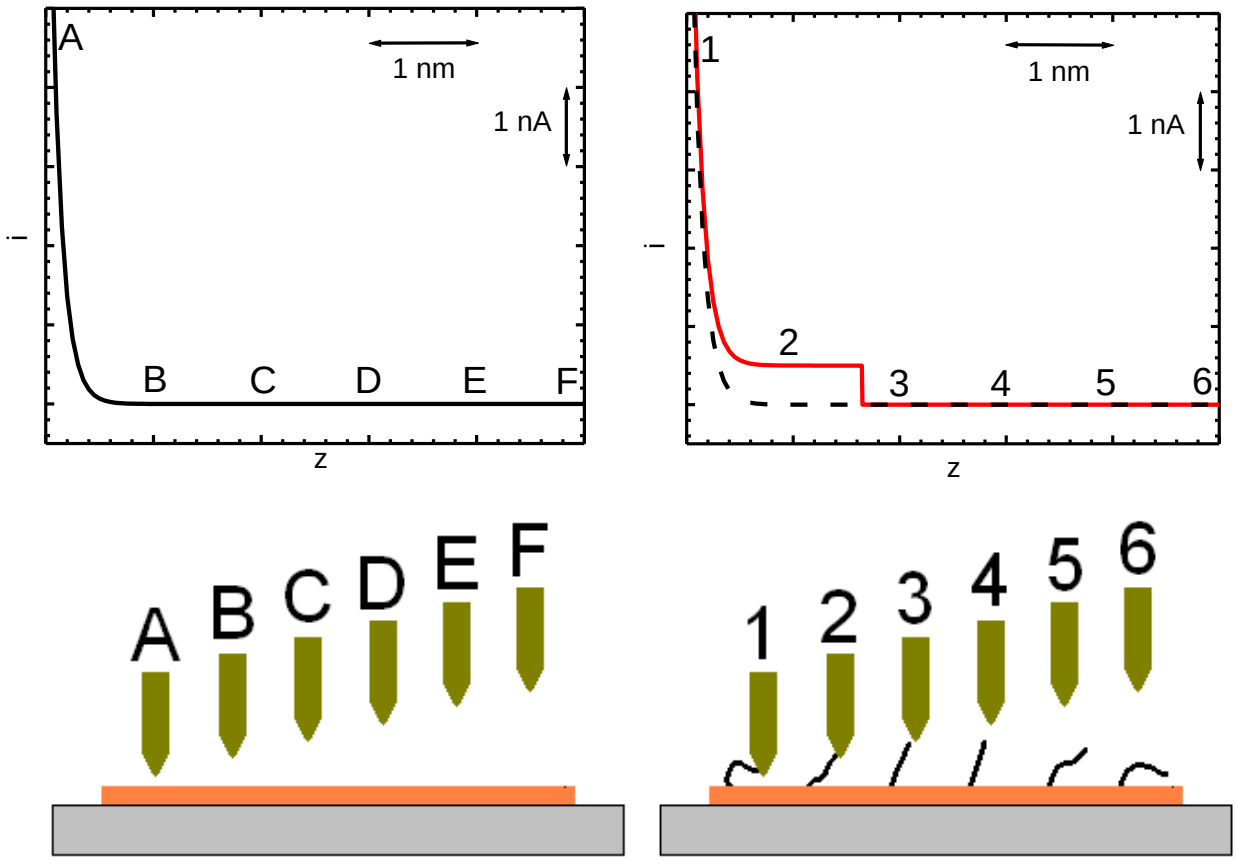

Figure 22: Characteristic i-z profile in the STM configuration without (left panel) and with (right panel, red line) a molecule attached to the STM probe.

2.2.3 Surface spectroscopic techniques

Surface spectroscopy may be used to prove the presence and/or confirm the chemical composition of layers adsorbed on solid surfaces. The two spectroscopic techniques are employed: Attenuated Total Reflection Fourier Transform Infrared Spectroscopy (ATR FTIR) and Polarization Modulation Infrared Reflection Adsorption Spectroscopy (PM IRRAS).

2.2.3.1 Attenuated Total Reflection Fourier Transform Infrared Spectroscopy

ATR FTIR is a reflective surface analysis technique [151]. It is suitable for the characterization of materials that are either too thick or too strongly IR absorbing to be analyzed by transmission IR techniques. Other applications include studies of interfacial phenomena (adsorption, desorption, phase transitions and self-assembly [152,153]).

The main part of the ATR FTIR assembly is an IR transmitting, high refractive index crystal usually made of a diamond, ZnSe or Ge. An IR beam enters the crystal at one of its ends. The high refractive index along with a sufficiently high angle of incidence ("grazing incidence") allows the IR beam to be reflected within the crystal, without being attenuated by the refraction at the crystal/air interface. At its other side, the IR beam exits the crystal and reaches the FTIR detector. Figure 23 shows the principle of ATR FTIR technique. If a sample is pressed into intimate optical contact with a surface of the crystal, the crystal/air surface is replaced by a sample/crystal interface. The IR beam, now being reflected from the sample surface, is allowed to penetrate partly into the sample via what is called the evanescent wave. The IR absorption will occur if the sample contains molecules with IR-absorbing groups. The absorption is enhanced as the IR beam hits the sample surface several times.

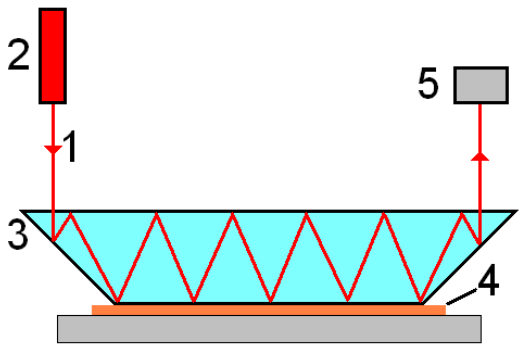

Figure 23: Configuration of an ATR FTIR experiment. The IR beam (1) generated by a suitable source (2) enters the crystal (3) and reflects internally from the interface between the crystal and the sample (4). The beam departing the crystal enters the FTIR detector (5).

2.2.3.2 Polarization Modulation Infrared Reflection Absorption Spectroscopy

The PM IRRAS is used for characterization of thin films, monolayers and sub-monolayes, corrosion processes and biomolecules on solid surfaces [154]. The advantage of the technique is its high surface sensitivity. The selection rules differ from what is commonly known from transmission IR spectroscopy techniques. The mode of the vibration is active only when its associated dipole moment change is normal to the substrate surface. In other words, only vertical molecular vibrations are detected. The important input parameters for the method are:

- optical constants of a film and a substrate
- the angle of incidence
- polarization state of the incident IR radiation
- incident IR radiation intensity

The alternating linear states of polarized light are generated by a photo-elastic modulator (PEM). The electric vectors of both incident and reflected beam may be resolved into the *p* and *s* components (*p* being the parallel and *s* the perpendicular vector component of a polarized radiation, both measured with respect to the plane of incidence). At sufficiently high angles of incidence ("grazing incidence", ca above 80°), only *p* component of incident radiation, E_p, is attenuated by the absorption at the sample surface, while the *s* component, E_s, is not. On the other hand, both E_p and E_s vector components are affected by an isotropic absorption by H_2O and CO_2 in the atmosphere, which allows the air interference to be largely eliminated. This offers a considerable advantage over other surface spectroscopy techniques, namely ATR FTIR.

PM-IRRAS studies the high-frequency modulation between *s* and *p* polarization states, allowing the simultaneous measurement of two signals:

- the difference spectrum between *s* and *p* polarized light, $E_s' - E_p'$
- the corresponding sum, $E_s' + E_p'$
- the results of the measurement are usually expressed as a ratio of the two spectra, $(E_s' - E_p')/(E_s' + E_p')$, being positive for wavelengths, at which the surface structures absorb the E_p component of the incident radiation

For sufficiently thick layers (with the thickness above 10 nm), the absorption of the *p* component is proportional to the film thickness. This allows the quantitative surface analysis to be carried out.

Figure 24 shows the basic working principle of PM IRRAS.

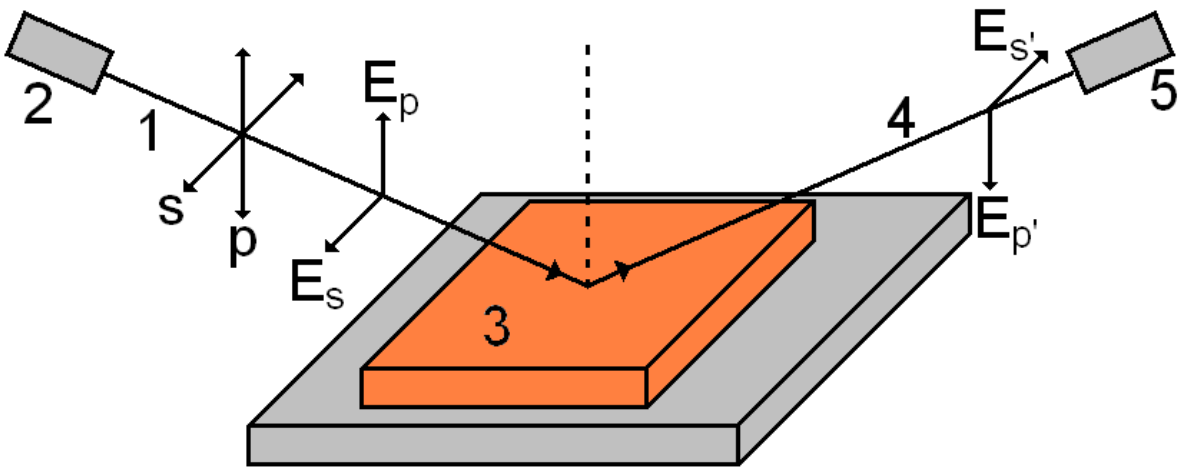

Figure 24: Incident beam (1) generated by the PEM (2) is totally reflected from the sample surface (3), possibly attenuated by the absorption by IR active groups in the molecules adsorbed on the sample surface. The reflected beam (4) reaches the FTIR detector (5).

2.2.3.3 Comparison of the two techniques

Generally speaking, the PM IRRAS technique is of better use than the ATR FTIR method:

- The PM IRRAS method has a higher surface sensitivity.
- The PM IRRAS method offers the possibility to eliminate the IR absorption of water and carbon dioxide in the air.
- The ATR FTIR may possibly damage or contaminate the sample surface due to the direct mechanical contact between the crystal and the sample. On the other hand, no direct contact is necessary in the PM IRRAS technique.
- The ATR FTIR may suffer from lower reproducibility due to the fluctuating pressure applied between the probe crystal and the sample surfaces.

The samples employing HOPG as the substrate cannot be examined by the PM IRRAS technique due to a very high imaginary part of HOPG complex refractive index. The absorption of E_p component of incident light is so high, that the reflected component E_p' is immeasurably small. Instead, the ATR FTIR technique may be employed. On the other hand, the gold supported samples may be analyzed by the PM IRRAS technique without the mentioned inconvenience.

3 EXPERIMENTAL PART

3.1 Chemicals

The extended viologen compounds **1** to **6** were synthesized by Valášek *et al.* according to [155]. The chemical structures of the compounds are shown in Scheme 1.

Compound *α*-[4-(Methylsulfanyl)phenyl]-*ω*-methylsulfanyl-mono[(2,6-diphenylpyridinium-4,1-diyl)-1,4-phenylene-(2,6-diphenylpyridinium-1,4-diyl)-1,4-phenylene]-bis(Trifluoromethanesulfonate) is labeled in the text as **1**.

Compound *α*-[4-(Methylsulfanyl)phenyl]-*ω*-methylsulfanyl-di[(2,6-diphenylpyridinium-4,1-diyl)-1,4-phenylene-(2,6-diphenylpyridinium-1,4-diyl)-1,4-phenylene]-tetrakis(Trifluoromethane-sulfonate)) is labeled in the text as **2**.

Compound *α*-[4-(Methylsulfanyl)phenyl]-*ω*-methylsulfanyl-tri[(2,6-diphenyl-pyridinium-4,1-diyl)-1,4-phenylene-(2,6-diphenylpyridinium-1,4-diyl)-1,4-phenylene]-hexakis(Trifluoromethanesulfonate) is labeled in the text as **3**.

Compound *α*-[4-(Methylsulfanyl)phenyl]-*ω*-methyl-sulfanyl-tetra[(2,6-diphenyl-pyridinium-4,1-diyl)-1,4-phenylene-(2,6-diphenylpyridinium-1,4-diyl)-1,4-phenylene]-oktakis(Trifluoromethanesulfonate) is labeled in the text as **4.**

Compound *α*-[4-(Methylsulfanyl) phenyl]-*ω*-methylsulfanyl-penta[(2,6-diphenylpyridinium-4,1-diyl)-1,4-phenylene-(2,6-diphenylpyridinium-1,4-diyl)-1,4-phenylene]-dekakis(Trifluoromethanesulfonate) is labeled in the text as **5**.

Compound *α*-[4-(Methylsulfanyl)phenyl]-*ω*-methylsulfanyl-hexa[(2,6-diphenylpyridinium-4,1-diyl)-1,4-phenylene-(2,6-di-phenylpyridinium-1,4-diyl)-1,4-phenylene]-dodekakis(Tri-fluoromethanesulfonate) is labeled in the text as **6**.

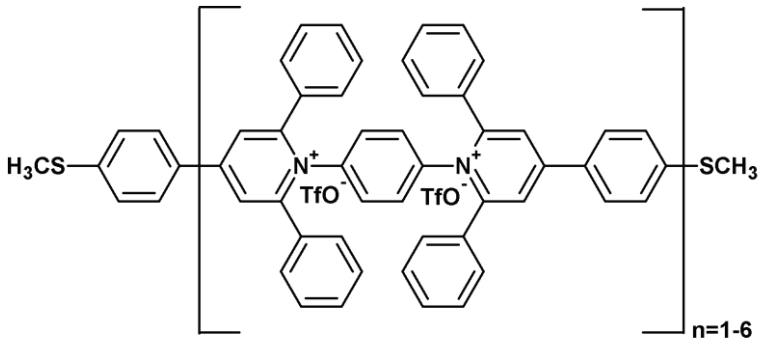

Scheme 1: Chemical structures of extended viologens 1 to 6.

The molecules of the compounds **1** to **6** shown in the Scheme 1 have methylsulfanyl as the terminal groups. Other two employed terminal groups are ethylsulfanyl and tert-butylsulfanyl.

The extended viologen compounds **1'** to **5'** were synthesized by Valášek *et al.* according to [62]. The chemical structures of the compounds are shown in Scheme 2.

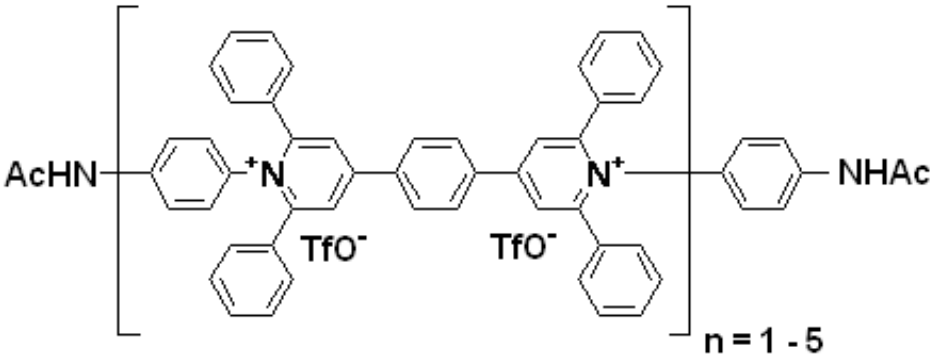

Scheme 2: Chemical structures of extended viologens 1' to 5'.

N-heteroaromatic compounds (quinolinium triflate, **QnTfO** and benzothiazolium triflate, **BzTfO**) were synthesized by F. Teplý. The structures of compounds are shown in Scheme 3.

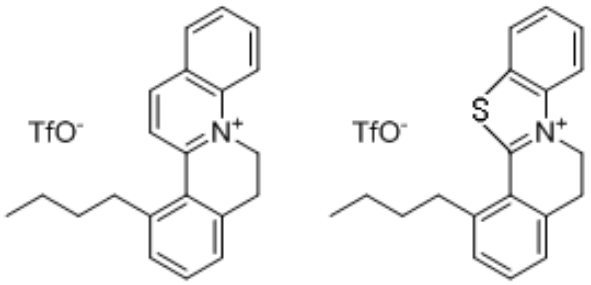

Scheme 3: Structure of quinolinium triflate (left) and benzothiazolium triflate (right).

Hydrated forms of native cyclodextrins (αCD, βCD and γCD) were purchased from Sigma-Aldrich. The chemical structures of the compounds are shown in Scheme 4.

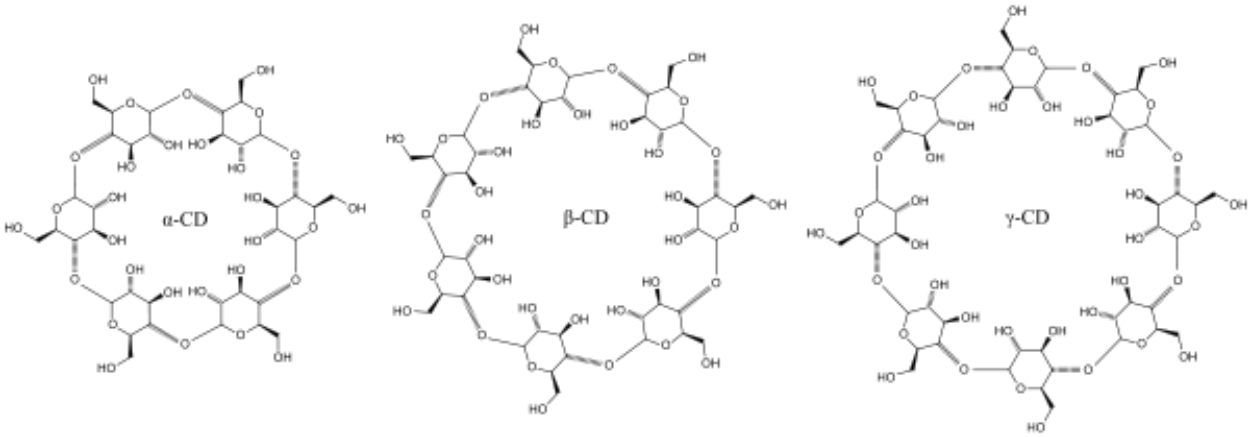

Scheme 4: Structure of αCD (left image), βCD (middle image) and γCD (right image).

Heptakis(2,6-di-*O*-methyl)-β-cyclodextrin (**Me_2βCD**) and Heptakis(2,3,6-tri-O-methyl)-β-cyclodextrin (**Me_3βCD**) were purchased from Cyclolab, Hungary. **Me_3βCD-Cys-SH** was kindly provided by Jean-Maurice Mallet, Centre National de la Recherche Scientifique, Paris, France. The chemical structures of the three compounds are shown in Scheme 5.

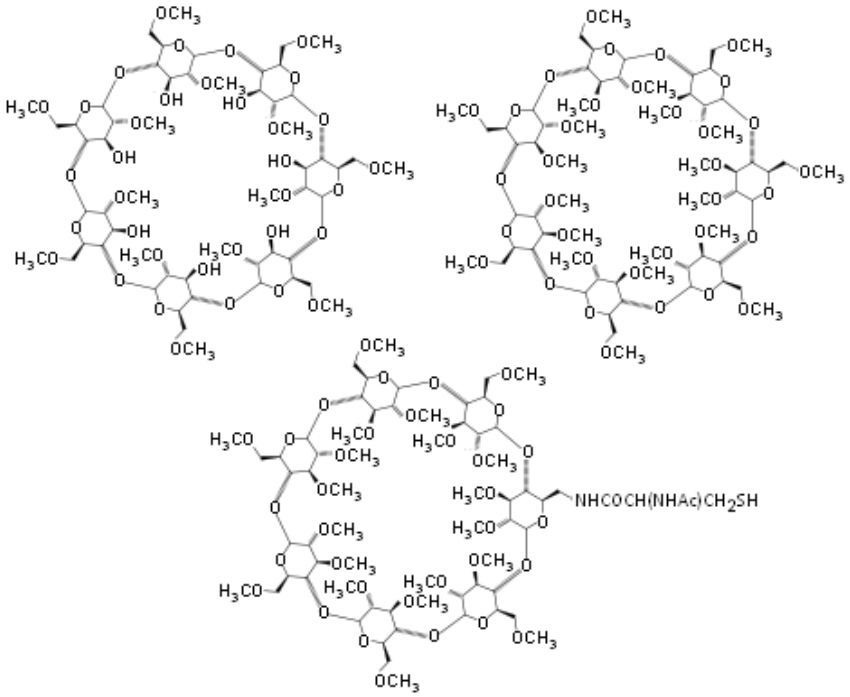

Scheme 5: Me_2βCD (upper left), Me_3βCD (upper right) and Me_3βCD-Cys-SH (lower figure).

Both native and derivatized CDs were dried prior to the use in order to obtain anhydrous compounds. The compound **Me_3βCD-Cys-SH** was stored under the atmosphere of nitrogen.
Ferrocene (Fc) was purchased from Sigma-Aldrich, with the purity >98%. Cobaltocene (in the form of cobaltocenium hexafluorophosphate) was kindly provided by Wolfgang Keim, University of Stuttgart, Germany. The structures of the compounds are shown in Scheme 6.

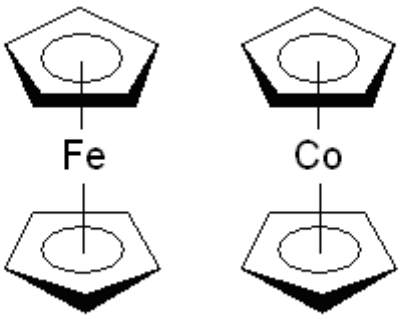

Scheme 6: Chemical structures of ferrocene (left figure) and cobaltocene (right figure).

The three tetrathiafulvalene-oligo(*p*-phenylene-ethynylene) conjugates (abbreviated as OPE-TTF_n, n = 2, 4, 6) were synthesized by Ivo Starý. The structures are shown in Scheme 7.

Compound 4,4'-[Benzene-1,4-diylbis(oxyethane-2,1-diylsulfanediyl)]bis[4',5,5'-tris(butylsulfanyl) -2,2'-bi-1,3-dithiole] is labeled in the text as **OPE-TTF_2.**

Compound 4,4',4",4"'-{Ethyne-1,2-diylbis[benzene-2,1,4-triylbis(oxyethane-2,1-diylsulfanediyl)]}tetrakis[4',5,5'-tris(butylsulfanyl)-2,2'-bi-1,3-dithiole] is labeled as **OPE-TTF_4.**

Compound 4-({2-[2,5-Bis{[2,5-bis(2-{[4',5,5'-tris(butylsulfanyl)-2,2'-bi-1,3-dithiol-4-yl]sulfanyl}ethoxy)phenyl]ethynyl}-4-(2-{[4',5,5'-tris(butylsulfanyl)-2,2'-bi-1,3-dithiol-4-yl]sulfanyl}ethoxy)phenoxy]ethyl}sulfanyl)-4',5,5'-tris(butylsulfanyl)-2,2'-bi-1,3-dithiol is **OPE-TTF_6.**

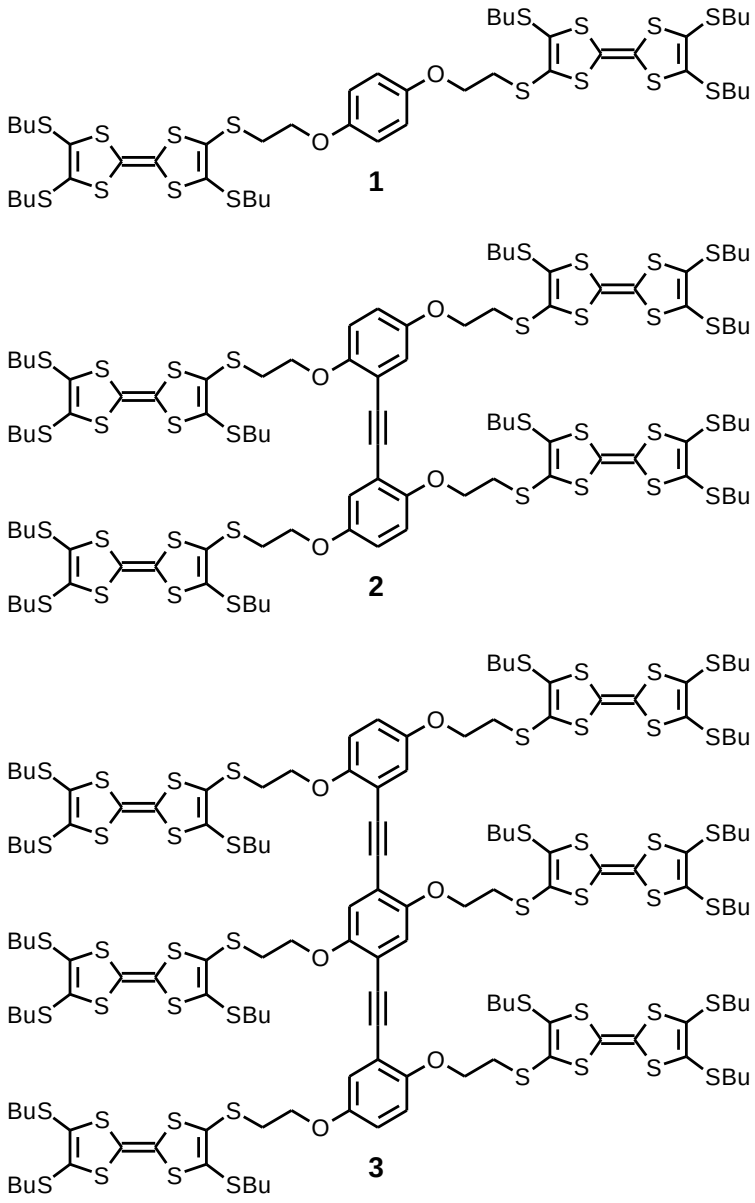

*Scheme 7: Chemical structures of tetrathiafulvalene-oligo(p-phenylene-ethynylene) conjugates **OPE-TTF_2** (1), **OPE-TTF_4** (2) and **OPE-TTF_6** (3).*

Methyl viologen dichloride polyhydrate ($MV^{2+}Cl_2.xH_2O$) was purchased from Sigma-Aldrich. Prior to the use, the compound was dried at 140 °C for 24 hours to get the anhydrous form. The chemical structure of the hydrated form is shown in Scheme 8.

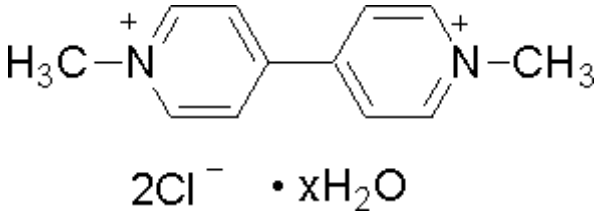

Scheme 8: Chemical structure of methyl viologen dichloride polyhydrate.

Buckminsterfullerene C_{60} was purchased from Sigma-Aldrich (>99.9%) and was used without any purification. Its chemical structure is shown in Scheme 9.

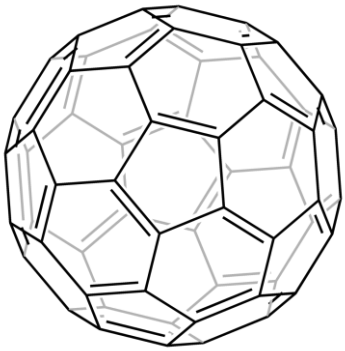

Scheme 9: Chemical structure of buckminsterfullerene.

Solvents for electrochemical experiments were all of analytical or a better grade. Acetonitrile (AN) was purchased from Merck (min. 99.8 %, max. 0.001 % H_2O). 1,2-dichloroethane (DCE) was obtained from Sigma-Aldrich (min. 99.8%, max. 0.003 % H_2O). Dimethyl sulfoxide (DMSO) was purchased from Sigma-Aldrich (min. 99.9 %, max. 0.005 % H_2O). Tetrahydrofuran (THF) was obtained from Sigma-Aldrich (ACS, min. 99.0 %, max. 0.05 % H_2O). Dimethylformamide (p.a.) was purchased from Lachner, Czech Republic. DMF and THF were distilled prior to the use. All solvents were stored in the presence of freshly activated molecular sieve in the dark.

Solid electrolytes for electrochemical experiments were of analytical or a better grade. Potassium chloride was purchased from Lachner (p.a., min. 99.0 %). Lithium chloride was obtained from Fluka (p.a., min. 98.0 %). Tetrabutylammonium hexafluorophosphate ($TBAPF_6$) was purchased form Fluka (electrochemical grade, min 99.0 %). The electrolytes were dried prior to the use.

Piranha solution was prepared by mixing the concentrated solutions of sulfuric acid (95 %, p.a., Lachner) and hydrogen peroxide (30 %, p.a., Lachner).

Methanol (p.a., 99 %), ethanol (p.a., 96 %), isopropanol (p.a., 99.7 %), acetone (p.a., 99.5 %) and acetic acid (p.a., 99 %) were all purchased from Lachner. Trifluoroacetic acid (ReagentPlus, 99 %) was obtained from Sigma-Aldrich.

Benzene (ACS reagent, min. 99.9 %, max. 0.05 % H_2O), toluene (ChromasolvPlus for HPLC, min. 99.9 %, max. 0.02 % H_2O) and methylbenzoate (p.a., min. 99.0 %, max. 0.2 % H_2O) were all purchased from Sigma-Aldrich.

Deionized water with a maximum resistivity of 18 MΩ.cm was obtained by means of a Milli–Q RG purification system (Millipore Co., USA) and was used throughout the studies.

3.2 Experimental techniques

3.2.1 Electrochemical and spectroelectrochemical measurements

Electrochemical measurements were made using a laboratory–built electrochemical system consisting of a fast rise–time potentiostat and a lock–in amplifier (Stanford Research, model SR830). The instruments were interfaced to a personal computer via an IEEE–interface card (PC–Lab, AdvanTech Model PCL–848) and a data acquisition card (PCL–818) using 12–bit precision. A three–electrode electrochemical cell was used. The reference electrode (Ag|AgCl|1M LiCl) was separated from the test solution by a salt bridge with a double fritted junction. A valve–operated static mercury drop electrode SMDE2 (Laboratorní Přístroje, Prague) of area 0.0155 cm^2 was used as a working electrode. Platinum net was used as the auxiliary electrode. Oxygen was removed from the solution by a stream of argon. A protecting argon layer blanketed the solution surface during the entire experiment. Some experiments also employed a polycrystalline platinum electrode as the working electrode.

The optically transparent thin layer cell (OTTLE) employed in spectroelectrochemical measurements was developed by Krejčík et al. [156] and is commercially available at Van‘t Hoff Institute for Molecular Sciences, Amsterdam, The Netherlands. The thickness of its inner space is 0.19 mm. The exact volume of the electrolyzed sample may vary after the cell re-assembly. For this reason the whole set of data presented here was obtained without disassembling the cell. Coulometric and voltammetric measurements were performed using potentiostat/galvanostat Autolab PGSTAT30 (Eco Chemie, The Netherlands).

3.2.2 UV/VIS/IR absorption and fluorescence spectroscopy

UV/VIS/NIR spectra were obtained either using Perkin–Elmer UV/VIS/IR spectrometer Lambda 1050 (Perkin–Elmer, USA) or a diode-array UV/VIS/NIR spectrometer Agilent 8453. The fluorescence emission spectra were recorded using a Perkin–Elmer luminescence spectrometer model LS 50B (Perkin–Elmer, USA).

3.2.3 Scanning probe techniques

The STM and AFM measurements (CM-AFM, AAC-AFM, MAC-AFM, TOP-MAC-AFM and CP-AFM modes) were predominantly performed on 5500 SPM station (Agilent). Some AFM measurements (AAC-AFM mode) employed Nanoscope V (Veeco). AC-AFM modes were largely favored over CM-AFM mode in order to reduce the risk of the sample damage. The "surface scratching analysis" employed the combination of CM-AFM and TOP-MAC-AFM mode, with the same AC-AFM probe being used. All AFM scanning probes were purchased from Agilent. Ex-situ AC-AFM measurements were carried at resonant frequency of the probes (usually 55 – 65 kHz). However, problems were often encountered when trying to oscillate the probes at resonant frequency in liquid environments i.e. in in-situ AC-AFM measurements. The probes were, therefore, oscillated at harmonic frequency values (ca 145 – 160 kHz). CM-AFM measurements employed commercially available conductive probes coated by the Pt/Ir alloy. Metallic wires, either Pt/Ir or Au, were used as STM probes.
The gold substrates on borosilicate glass (250 nm thick gold layer deposited on 1.5 nm thick chromium interlayer) were purchased from Arandee, Germany. They were annealed by a butane flame on a ceramic hob for 2 minutes and then left to cool down to the room temperature. Afterwards, they were immersed into freshly prepared Piranha solution for 30 s to eliminate possible organic impurities from the butane flame. The substrates were then rinsed with water and immersed into ethanol for 1 minute. They were then dried in the air and directly used. The gold substrates on mica with the gold layer thickness of 200 nm pre-annealed by the hydrogen flame were used as received form Agilent, Germany.

3.2.4 Surface spectroscopy techniques

ATR FTIR and PM IRRAS measurements employed usually the same samples as those examined by SPM techniques. ATR FTIR spectra were obtained using a FTS 7000 FTIR

spectrophotometer (Digilab, USA). The spectra were accumulated with the diamond anvil ATR accessory. The presented data were derived from 64 scans at a resolution of 2 cm^{-1}. PM IRRAS measurements employed ZnSe grid polarizer and photoelastic modulator with a nitrogen-cooled MCT detector. The data were derived from 64 scans at a resolution of 4 cm^{-1}.

3.2.5 Preparation of dispersions of C_{60} in water

The water dispersions of C_{60} were prepared as follows. C_{60} was dissolved in benzene, toluene or methylbenzoate at various concentrations ranging from 0.1 to 2.9 mg/mL. The resulting solution was then mixed with the equal volume of doubly de-ionized water to form a two-phase mixture. The mixture was then exposed to the action of the ultrasound at room temperature. The ultrasonic bath (model PK 31H, Bandelin Sonorex, Germany) operated at 35 kHz and 30/240W. The sonication was stopped when the organic phase was evaporated (usually after less than 24 hours). A solid undispersed residue was found at the bottom of the water phase and it was removed by a repeated filtration using 200 nm microfilters (Acrodisc LC, Sigma Aldrich). Freshly filtered dispersions were directly used further.

3.2.6 Deprotection of extended viologen molecules

Samples for the single-molecule conductivity measurements of the compounds **1** to **6** were prepared as follows. Typically, 1.0 μmol of the respective compound with the terminal *tert*-butylthio groups was dissolved in 10.0 mL of CH_3COOH/CF_3COOH mixture (1:1 v/v). The resulting solution was refluxed at its boiling point (ca. 90 – 100 °C) for at least 6 hours. The solution was then left to cool down and the acidic solvent mixture was evaporated under a reduced pressure by a rotary evaporator. The residue was re-dissolved in 10 mL methanol or ethanol and re-evaporated. This procedure was repeated until no acidity traces were detected (based on a litmus test). The residue was then dissolved in 5.0 mL methanol. The gold substrate was immersed in the solution of a respective compound and 20 – 40 μL of concentrated ammonium hydroxide was added. Higher amounts led to a solute precipitation. The procedure was carried out in the argon atmosphere to avoid the oxidation of deprotected SH- groups. The gold substrate was left immersed in this solution overnight and rinsed with methanol. The surfaces were either immediately examined or stored under the nitrogen atmosphere. Single-molecule measurements were carried out in the atmosphere of nitrogen.

3.2.7 Preparation of adsorbed layer of cyclodextrin host molecules

A mono-crystalline gold substrate, with mica as the underlying material, was immersed as a working electrode into the electrochemical cell, containing Me_3βCD-Cys-SH dissolved in water with 0.1 M KF as the supporting electrolyte. The oxygen was removed by a stream of argon prior to the addition of Me_3βCD-Cys-SH, in order to protect –SH groups from the atmospheric oxidation. The potential -0.20 V was then applied for eight hours, with the potentiostat being switched off afterwards. The gold substrate was then rinsed with water and immediately scrutinized by SPM techniques.

4 RESULTS AND DISCUSSION

4.1 Adsorption properties of molecular wires

The extended viologens (compounds **1** to **6**) were found to be insoluble in pure water and, therefore, we employed 20 % (v/v) ethanol/water mixture containing 0.1 M KF as the supporting electrolyte as an environment, in which the adsorption properties of the compounds were investigated. Actually, the compounds were dissolved at high concentrations in a pure ethanol to gain their stock solutions, which were then mixed with 20% water/ethanol mixture, gaining thus solutions of a desired concentration.

The two phase-sensitive AC techniques were employed in adsorption studies:

- AC voltammetry (with the electrode potential being varied)
- differential capacity-time measurements (at a constant electrode potential)

Both methods employed HMDE as the working electrode. Figure 25 shows the AC voltammogram in the absence (black line) and presence (red line) of **1**. A freshly extruded mercury drop was left to interact with the solution of **1** for 3 minutes at the potential -0.70 V vs. the reference electrode, in order to allow the adsorption to reach the equilibrium. Afterwards, the electrode potential was swept with the scan-rate 5 mV/s in either positive or negative direction. The resulting differential capacity values were found to be independent of the electrode potential within a broad range of potentials (between -0.05 V and -0.80 V for **1**), forming thus an adsorption pit being indicative for a two-dimensional condensed film formation. The AC voltammograms for compounds **2** to **6** are similar to that of **1**.

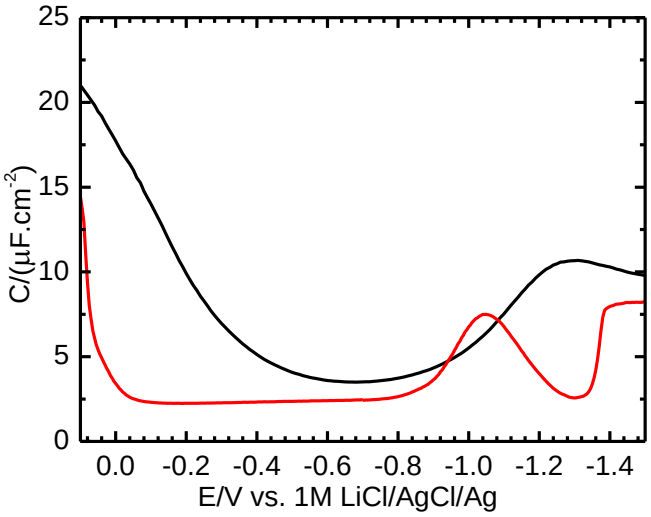

Figure 25: The differential capacity of 0.1 M KF in 20% ethanol/water mixture in the absence (black line) and presence (red line) of 6.0 μM ***1****. Perturbation frequency 160 Hz, ac amplitude 5 mV. Measured at 298 K.*

At the anodic side of the ac voltammogram, the edge of the adsorption pit coincides with the end of the potential window of the mercury/electrolyte interface. On the cathodic side, the adsorption pit is limited by the onset of the electrochemical reduction.

The electrochemical reduction of the compound **1** is discernible from the faradaic peak with the peak potential at -1.04 V, observable both in the in-phase (*Y'*) and out-of-phase (*Y''*) components of the cell admittance (Figure 26). Considerably higher faradaic peak in the out-of-phase component of the cell admittance, Y_F'' , suggests that the electron transfer takes place largely in the adsorbed state. Moreover, the out-of-phase faradaic peak height was found to be independent of the concentration of **1** in the bulk, confirming the surface-confined electron transfer. As both in-phase and out-of-phase peaks have the same peak potential, the electron transfer is believed to be reversible, even in the environment with a high water content. To confirm this, the cyclic voltammetry was employed to study the electron transfer in **1** for water-containing environments (such as DMSO/water mixtures), confirming no impact of water content on the reversibility of electron transfer.

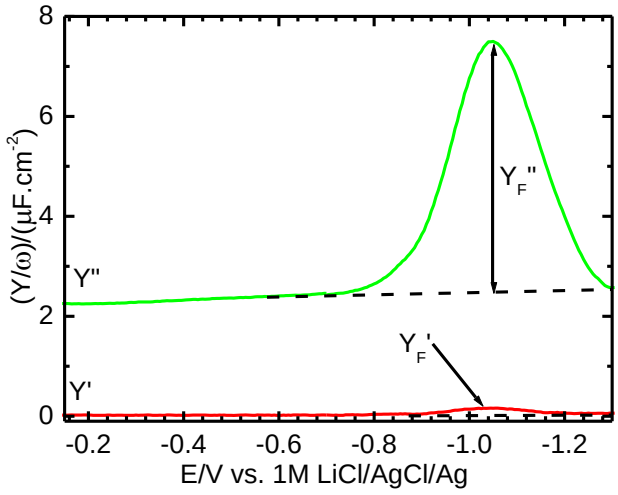

Figure 26: The values of Y/ω (ω=2πf) for 6.0 μM ***1*** *in 0.1 M KF in 20% water/ethanol mixture. Both in-phase (red line) and out-of-phase (green line) cell admittance components are shown. Perturbation frequency 160 Hz, ac amplitude 5 mV. Measured at 298 K.*

The differential capacity measurements were carried out at various perturbation frequencies (Figure 27). The *C* value within the adsorption pit as well as the Y_F'' peak height was found to be independent of the frequency used.

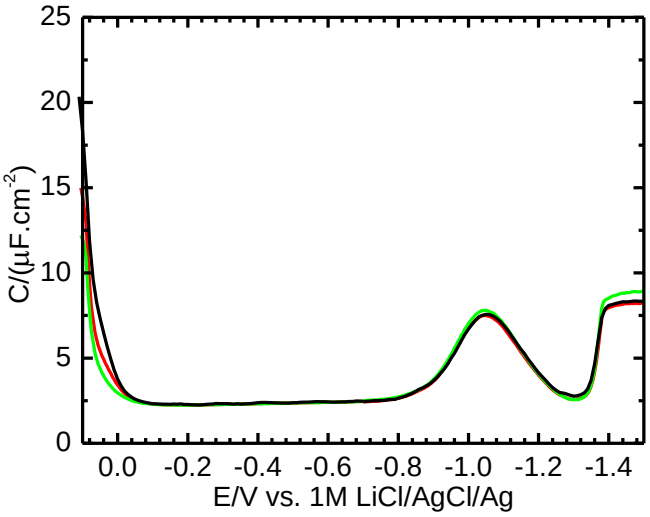

*Figure 27: The differential capacity of 6.0 µM **1** in 0.1 M KF in 20% ethanol/water mixture with the perturbation frequency 16 Hz (black line), 160 Hz (red line) and 1600 Hz (green line) and ac amplitude 5 mV. Measured at 298 K.*

Temperature-resolved differential capacity measurements were also performed (Figure 28). The adsorption pit becomes narrower at elevated temperatures, with both its edges being affected. The temperature dependence of the pit width was not determined as it is limited by the end of the potential window of the electrode at the anodic side. At the cathodic side, the pit is followed by the faradaic peak originating from the surface-confined charge-transfer process. At elevated temperatures, the faradaic peak is shifted towards less negative potential values and its height decreases.

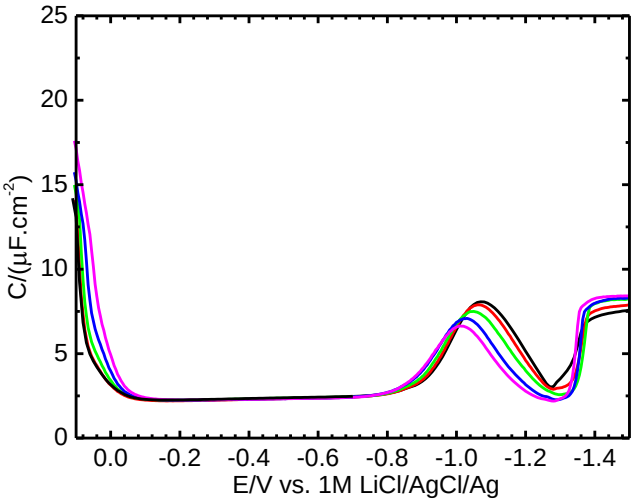

*Figure 28: The differential capacity of 6.0 µM **1** in 0.1 M KF in 20% ethanol/water mixture measured at 283 K (black line), 289 K (red line), 298 K (green line), 309 K (blue line) and 320 K (purple line). Perturbation frequency 160 Hz, ac amplitude 5 mV.*

The faradaic process facilitated at elevated temperatures has the peak potential displacement proportional to the inverse of temperature (Figure 29). Temperature has no impact on the monolayer differential capacity value.

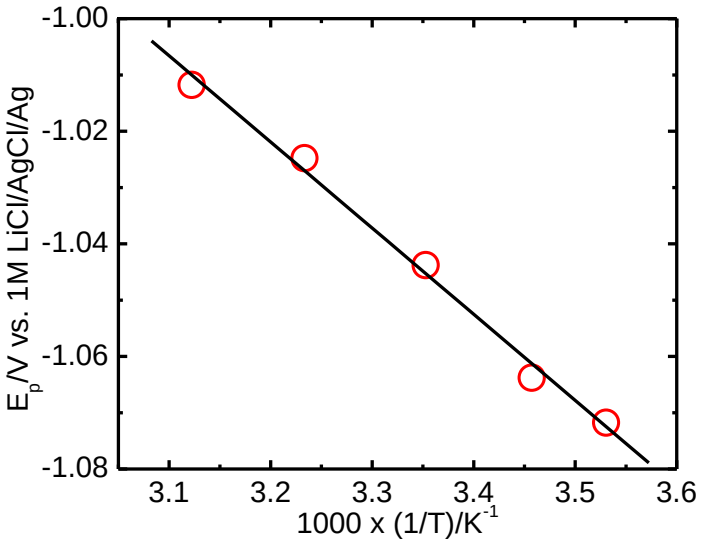

*Figure 29: Peak potential of the faradaic process, E_p, vs. inverse of T. Perturbation frequency 160 Hz, ac amplitude 5 mV. Measured for 6.0 μM **1** in 20% ethanol/water mixture containing 0.1 M KF as the supporting electrolyte. The values were determined from the imaginary part of the cell admittance.*

The faradaic process is most probably accompanied by the reorientation of the molecules (see further). At potentials more negative than -1.35 V, the value of differential capacity increases slowly approaching the value obtained for a pure electrolyte suggesting the desorption of molecules.

The independence of the differential capacity on the electrode potential within the adsorption pit was further confirmed by the differential capacity-time (*C-t*) measurements. Figure 30 shows the examples of potential-controlled differential capacity transients for the compounds **1** and **3**, both at the concentration 6.0 μM. For all potential values within the adsorption pit of a respective compound, the value of the differential capacity as well as the time necessary to form a complete film, ζ, were found to be constant. The characteristic time, however, differs for the two compounds. This is fully in agreement with Koryta [157], suggesting that the adsorption is a diffusion-limited process.

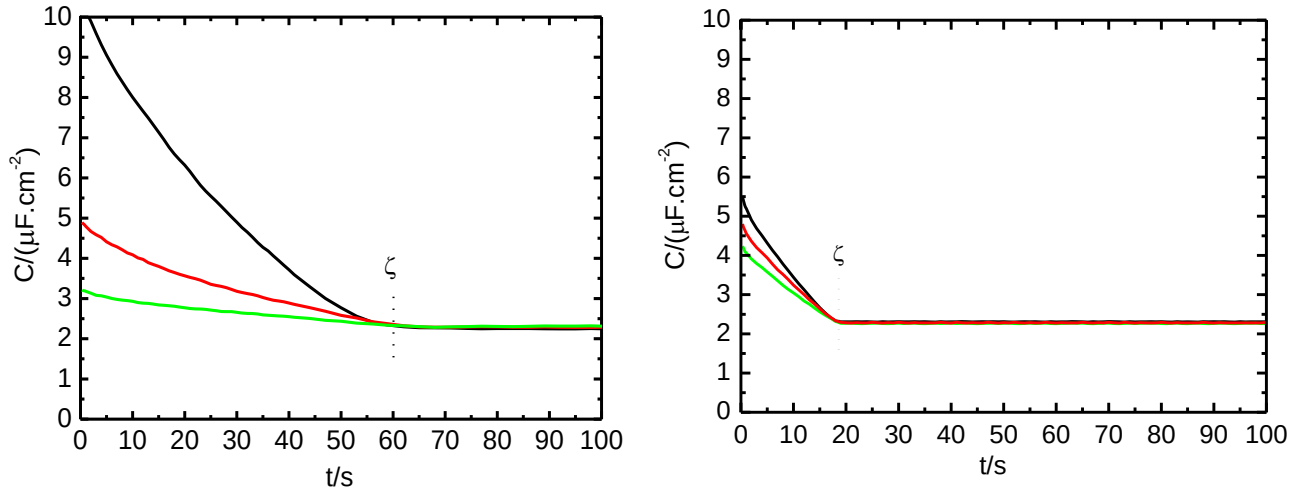

*Figure 30: Differential capacity transients for the compound **1** (left panel) at electrode potentials -100 mV (black line), -300 mV (red line) and -500 mV (green line) and for the compound **3** (right panel) at electrode potentials -150 mV (black line), -175 mV (red line) and -200 mV (green line). Concentration of both compounds is 6.0 μM, perturbation frequency 160 Hz and ac amplitude 5 mV. Measured at 298 K. Vertical dotted lines show the characteristic time of the film formation, ζ.*

The diferential capacity-time measurements were further carried out at various concentrations of respective compounds in the bulk of the solution. The ζ values were found to depend on the concentration of the compounds. However, the differential capacity value of a fully covered electrode surface was found to be independent of the concentration of the compound in the bulk, suggesting thus that a monolayer is formed at the electrode interface.

Figure 31 shows two examples of differential capacity-time curves, namely for the compounds **1** and **3**, measured at various bulk concentrations with the electrode potential being fixed to a value within the adsorption pit. For any given compound, the value of the differential capacity of the fully covered electrode was found to be independent of the bulk concentration.

The differential capacity-time curves were analyzed employing the parallel-plate capacitor equivalent circuit. During the film formation, the electrode is partially covered by adsorbed molecules forming an interface with the differential capacity C_∞, with the rest of the electrode being bare with the differential capacity C_0. The C_0 value is supposed to be identical to that measured in the absence of the compounds (i.e. in a pure electrolyte) at the same electrode potential.

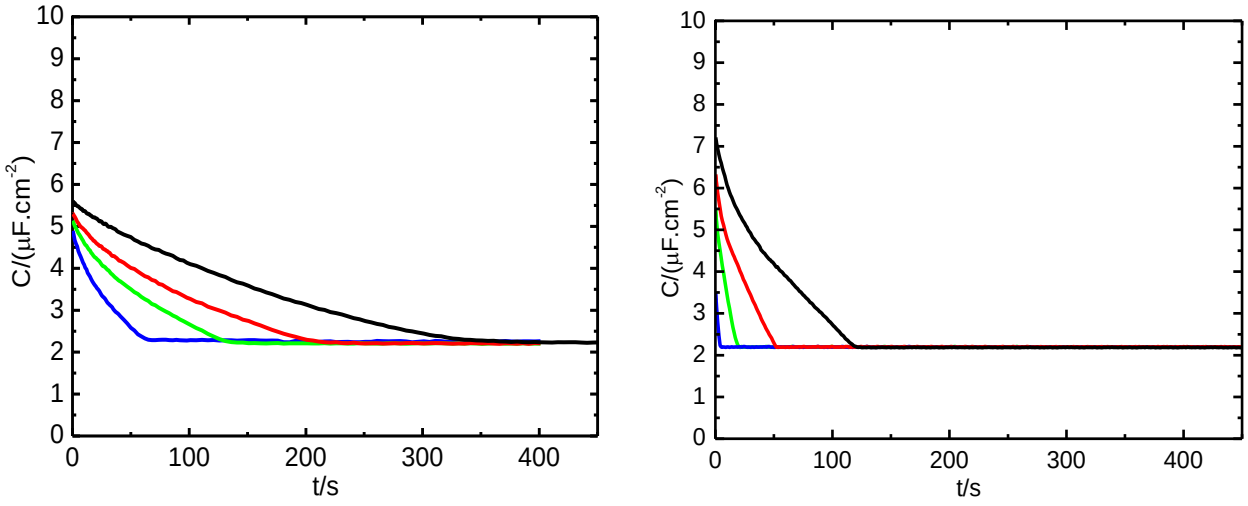

*Figure 31: Differential capacity-time curves for the compound **1** (left panel) at concentrations 2.5 μM (black line), 3.3 μM (red line), 4.3 μM (green line) and 6.0 μM (blue line) and for compound **3** (right panel) at concentrations 1.5 μM (black line), 3.2 μM (red line), 6.0 μM (green line) and 9.5 μM (blue line). The electrode potential was set to values inside the adsorption pit, namely -300 mV for **1** and -150 mV for **3**. Perturbation frequency 160 Hz and ac amplitude 5 mV. Measured at 298 K.*

The solvent, composed of polar molecules of water and ethanol, has a high value of the relative permittivity, ε_r. During the adsorption, the solvent molecules located in the vicinity of the electrode are replaced by the molecules of non-polar compounds **1** to **6** having therefore correspondingly smaller ε_r value.

The electric capacity of a plate capacitor is given by

$$C = \varepsilon_0 \varepsilon_r \frac{A}{d} \tag{28}$$

where A and d is the effective area and distance of the plates, respectively, with ε_0 being the permittivity of a free space. As the electric capacity is proportional to the ε_r value, the inequality $C_\infty < C_0$ can easily be obtained.

If the surface coverage of the adsorbed molecules is denoted as θ, then the bare fraction will have the surface coverage equal to $1 - \theta$. The total capacity of the capacitors in a parallel configuration is given by the sum of individual capacities (see Figure 32) and, therefore, the total electrode capacity, C, is given by [134]

$$C(t) = C_\infty \theta(t) + C_0 (1 - \theta(t)) \tag{29}$$

The inequality $C_\infty < C(t) < C_0$ is satisfied at any time during the film formation $(0 < t < \zeta)$. The above equation will reduce to $C(t) = C_\infty$ for a fully covered surface ($\theta = 1$ and $t \geq \zeta$). The surface coverage is given by

$$\theta(t) = \frac{C(t) - C_0}{C_\infty - C_0} \tag{30}$$

Therefore, if the values of C_∞ and C_0 are known, one can easily calculate the surface coverage at any time during the film formation.

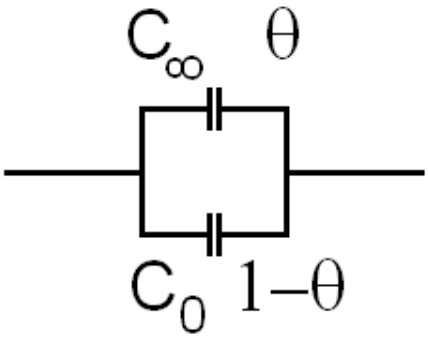

Figure 32: The equivalent circuit of the cell during the adsorption. The effective areas of equivalent capacitors are proportional to θ and 1 – θ for a covered and a bare electrode region, respectively. No faradaic reaction is supposed to take place.

For the diffusion-limited adsorption, the electrode coverage is proportional to the square root of time for which the electrode was immersed in a solution of adsorbable species provided that the electrode potential is set to a value within the adsorption pit [134]

$$\theta = \frac{2cD^{1/2}}{\pi^{1/2}\Gamma_{MAX}} t^{1/2} \tag{31}$$

Here $\Gamma = n/A$ is the surface concentration of adsorbable species (expressed in $mol.m^{-2}$) and $\Gamma = \Gamma_{MAX}$ for $\theta = 1$. Figure 33 shows a typical θ - $t^{1/2}$ plot, being linear during the film formation, except for a very short time interval at the very start of the measurement. This may be possibly attributed to the convective mass-transfer in the solution, induced by an extrusion of the mercury drop.

For a fully covered electrode surface ($t = \zeta$, $\theta=1$), equation (31) reduces to the shape

$$\varsigma = \frac{\pi\Gamma_{MAX}^2}{4Dc^2} \tag{32}$$

which directly relates macroscopic quantities c and ζ to the microscopic quantity Γ_{MAX} [134].

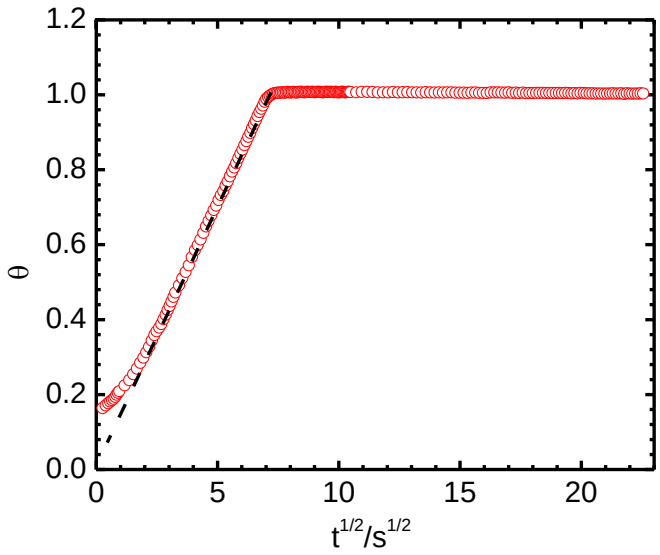

Figure 33: Plot of the electrode surface coverage as a function of square root of time for 6.0 μM ***1*** *at -100 mV. Perturbation frequency 160 Hz, ac amplitude 5 mV. Measured at 298 K.*

The dependence ζ vs. $1/c^2$ allows the maximum surface concentration, Γ_{MAX}, of the molecules to be determined, provided that the diffusion coefficient, D, is known. Figure 34 shows three typical dependences namely for the compounds **1**, **2** and **4**. The linearity in the both mentioned dependences (θ vs. $t^{1/2}$and ζ vs. $1/c^2$) confirms that the compounds **1** to **6** adsorb at the mercury/electrolyte interface with the diffusion as the rate-determining step [134].

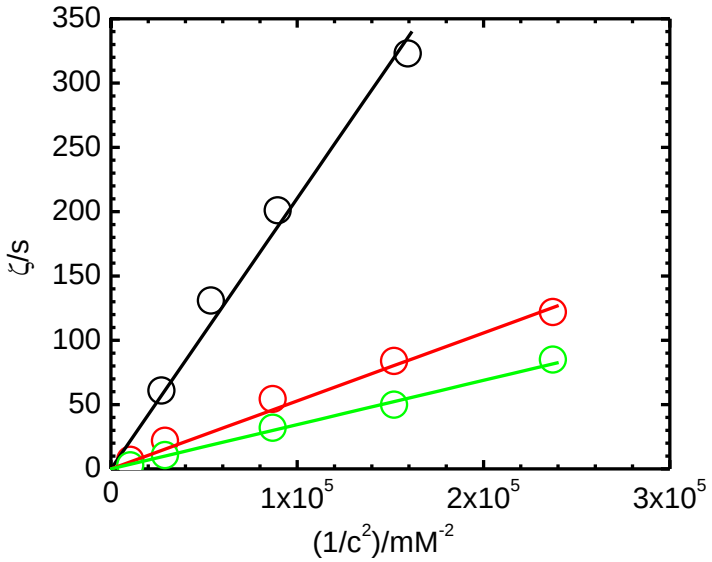

Figure 34: Dependence of ζ vs. $1/c^2$ for three compounds: ***1*** *(black line),* ***2*** *(red line) and* ***4*** *(green line).*

For all compounds, the concentration values employed in experiments fell into the range 0.5 μM – 50 μM. Higher concentrations led to immeasurably small characteristic times of the film formation and, therefore, were of no use. On the other hand, sub-micromolar concentrations led to irreproducible shapes of *C-t* curves, possibly caused by co-adsorption of impurities from the bulk of the solution.

As mentioned above, slope in the Koryta equation, $S = \pi\Gamma_{MAX}^2 / 4D$, may be used to evaluate the surface concentration, Γ_{MAX}, of the molecules when the diffusion coefficients are known. The compounds **1** to **6** belong to the group of extended viologens, with the molecules being structurally very similar to methyl viologen (MV) molecule. Therefore, we decided to calculate the values of diffusion coefficients from the value known for methyl viologen dichloride. According to the Stokes-Einstein relation, the diffusion coefficient of a species composed of roughly spherical molecules (with the effective radius *r*) is [158]

$$D = \frac{kT}{6\pi\eta r} \tag{33}$$

where η is the dynamic viscosity of the environment, in which the molecules diffuse. For a given molecule at a constant temperature, the diffusion coefficients in two environments (D_1 and D_2) of different dynamic viscosity values (η_1 and η_2) are related by

$$D_1\eta_1 = D_2\eta_2 \tag{34}$$

This relation was first found empirically by German physical chemist Paul Walden, in 1905, and is therefore referred to as the Walden's rule [158]. Walden's rule was used to calculate the diffusion coefficient of MV in water/ethanol mixture (D_{MV} = 1.68 × 10^{-10} $m^2.s^{-1}$), from that determined in pure water $D_{MV}(H_2O)$ = 4.40 × 10^{-10} $m^2.s^{-1}$. If the dissolved species of molar mass *M* form roughly spherical particles, their radius is given by

$$r = \left(\frac{3M}{4\pi\rho N_A} \right)^{1/3} \tag{35}$$

with ρ being the effective density of the particle. Though being a purely theoretical quantity for molecules, one can assume it to be constant for similar species such as the compounds **1** to **6** and MV. When combined with the Stokes-Einstein relation, one can easily calculate the diffusion coefficient of the compounds as

$$D = D_{MV}(M_{MV} / M)^{1/3} \tag{36}$$

with M_{MV} = *0.257 kg.mol*$^{-1}$ and D_{MV} = *1.68* × *10*$^{-10}$ *m*^{2}*.s*$^{-1}$, being the molar mass and the diffusion coefficient of MV, respectively. Now that the *D* values are known, one can easily

calculate Γ_{MAX} values for all compounds. The surface concentration can easily be turned into the (experimentally obtained) area occupied by a single molecule

$$A_{exp} = \frac{1}{N_A \Gamma_{MAX}} \tag{37}$$

Table 1 summarizes the adsorption properties of the compounds **1** to **6**. For each compound, the value of differential capacity C_∞ plotted in the second column was determined at various bulk concentrations of the compounds. No dependence of C_∞ on the bulk concentration was observed, which indicates that a monolayer is formed at the interface.

If a film is assumed to behave as an ideal plate capacitor, then its C value is inversely proportional to the film thickness. No C_∞ dependence on the length of the molecule (third column) was, however, observed ($C_\infty = 2.5 \pm 0.2\ \mu F.cm^{-2}$), indicating that the film thickness is constant. Therefore, the molecules lay parallel to the electrode surface.

For all compounds, the linearity in the plot ζ vs. $1/c^2$ was found and the corresponding slope values, S, are listed in the fourth column. With the aid of calculated diffusion coefficients (the fifth column in Table 1), the corresponding maximum surface coverage values listed in the sixth column and experimental single—molecule areas (the eighth column) were obtained.

n	C_∞ ($\mu F.cm^{-2}$)	***l*** (nm)	***S*** ($s.mol^2.m^{-6}$)	***D*** ($m^2.s^{-1}$)	Γ_{MAX} ($mol.cm^{-2}$)	A_{teor} (nm^2)	A_{exp} (nm^2)
1	2.3	2.35	21.0×10^{-4}	1.04×10^{-10}	5.3×10^{-11}	2.8	3.1
2	2.5	4.07	5.29×10^{-4}	0.85×10^{-10}	2.4×10^{-11}	4.9	6.9
3	2.3	5.80	2.87×10^{-4}	0.75×10^{-10}	1.7×10^{-11}	7.0	10.0
4	2.5	7.52	3.44×10^{-4}	0.69×10^{-10}	1.7×10^{-11}	9.0	9.6
5	2.6	9.26	2.39×10^{-4}	0.64×10^{-10}	1.4×10^{-11}	11.1	12.0
6	2.5	11.0	3.23×10^{-4}	0.60×10^{-10}	1.6×10^{-11}	13.2	10.6

*Table 1: Characteristic adsorption parameters for the compounds **1** to **6**: n – number of repeating units in the molecule, C_∞ – differential capacity of the fully covered electrode, l – length of the molecule, S – slope in the Koryta equation, D – diffusion coefficient, Γ_{MAX} - surface concentration, A_{teor} and A_{exp} – theoretically calculated and experimentally obtained (employing parallel-lying model) area occupied by one molecule.*

As mentioned above, no dependence of differential capacity on the length of the molecule suggests that the film thickness is constant with the molecules being positioned parallel to the electrode surface. To support this assumption, the experimentally obtained single-molecule area values, A_{exp}, were compared to those calculated by theoretical models, A_{teor}. In principle, there are two limiting possibilities for the molecules to assemble on the surface:

- Parallel-lying orientation (with the molecular major axis being parallel to the surface)
- Perpendicularly-lying orientation (with the major axis being orthogonal to the surface)

The two possibilities are depicted in Figure 35. In the theoretical calculations the molecules are approximated by cylinders with the constant radius r = 0.60 nm and a varying length listed in the third column of Table 1.

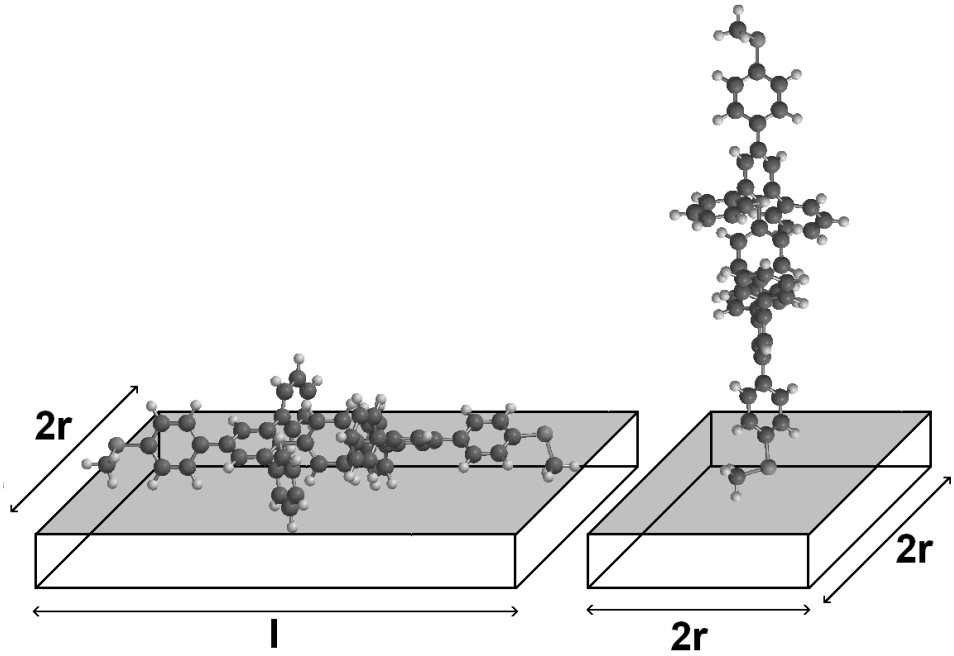

*Figure 35: Schematic representation of parallel-lying (left panel) and perpendicularly-lying (right panel) orientation of adsorbed molecules, used in calculations (shown for the compound **1**). The symbols refer to the molecular dimensions: r – molecular radius, l – length of the molecule.*

If the molecules are assumed to lay parallel to the electrode surface, then the area occupied by the single molecule is proportional to the length of the molecule, $A_{teor} = 2rl$ (the values are listed in the seventh column of Table 1).

On the other hand, if the molecules are supposed to lay perpendicularly to the electrode surface, then the single-molecule area is constant regardless of the length of the molecule. The area may be estimated taking several geometric objects such as a square, circle or a regular hexagon (Figure 36).

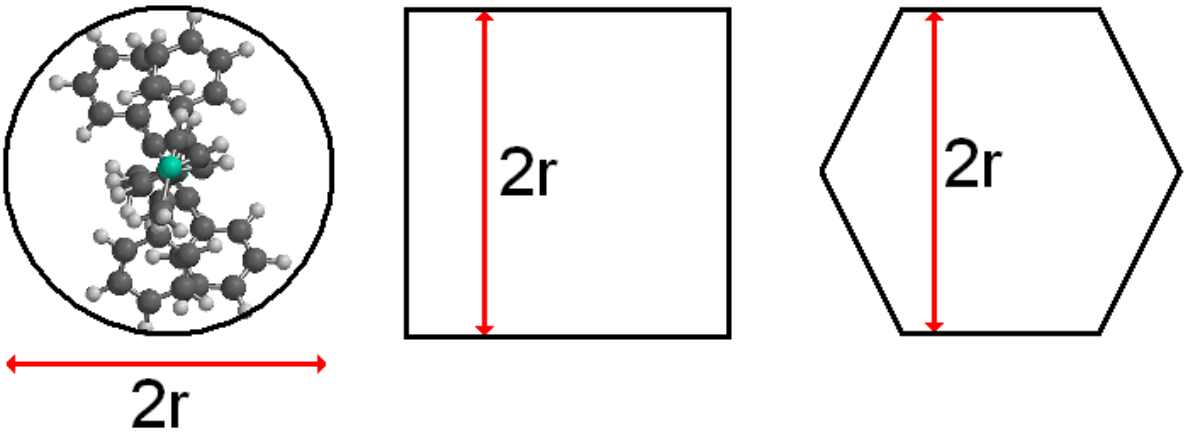

Figure 36: Geometric shapes used for calculation of the single-molecule area when the perpendicularly-lying model is considered.

Figure 37 shows the comparison of theoretically calculated and experimentally obtained single-molecule area values. The A_{teor} values based on the parallel-lying model are well comparable to their experimental counterparts. On the other hand, the model based on perpendicularly-lying molecules using any geometric shape (Figure 36) for the projection fails to explain the experimental data.

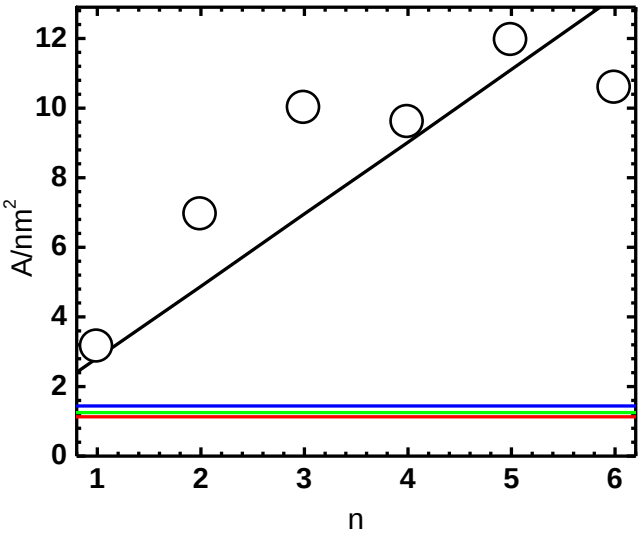

*Figure 37: Experimentally obtained and theoretically calculated single-molecule area values of the compounds **1** to **6**. Open circles are the experimentally obtained values. Theoretically calculated values are denoted by lines: parallel-lying model (black line) and perpendicularly-lying model based on circle (red line), regular hexagon (green line) and square (blue line).*

All above mentioned results can be summarized as follows:

- Upon addition of the compounds **1** to **6** into the solution, the differential capacity of the electric double layer decreases in a certain range of potential values due to the adsorption of compounds at the electrode/electrolyte interface.
- The value of the film differential capacity C_∞ is independent of the concentration in the bulk of the solution, applied AC frequency, amplitude and temperature, strongly supporting the formation of a monolayer.
- During the film formation, the electrode coverage is proportional to the square-root of time, proving that the adsorption is diffusion-limited. This was also confirmed by concentration-resolved measurements, in which the characteristic time of the film formation was found to be inversely proportional to the bulk concentration squared.
- For each of the compounds, the single-molecule area values were obtained from the experimental data and also calculated by two theoretical models (for parallel-lying and for perpendicularly-lying molecules).
- The value of the differential capacity was found not to depend on the length of the molecule suggesting the constant film thickness.
- Experimentally obtained single-molecule area was found to scale with the length of the molecule.
- The parallel-lying model was accepted, while the perpendicularly-lying was rejected.

These conclusions hold only at potential values within the adsorption pit of the respective compound i.e. where no electron-transfer takes place. In the faradaic region, the behavior becomes more complicated.

As mentioned above, if the potential is stepped to a region, where no faradaic process occurs, the differential capacity value after a time ζ reaches the value C_∞, which will then remain constant. However, if the potential is stepped to a faradaic region, a qualitatively different behavior is observed (Figure 38):

- The differential capacity value *increases* during the film formation.
- The maximum of C value is reached at time ζ identical to that measured at potential values within the adsorption pit.
- For $t > \zeta$, the differential capacity value decreases exponentially.
- For $t >> \zeta$, a constant value of C is reached, being an order of magnitude lower than the monolayer value C_∞ obtained at potentials within the adsorption pit.

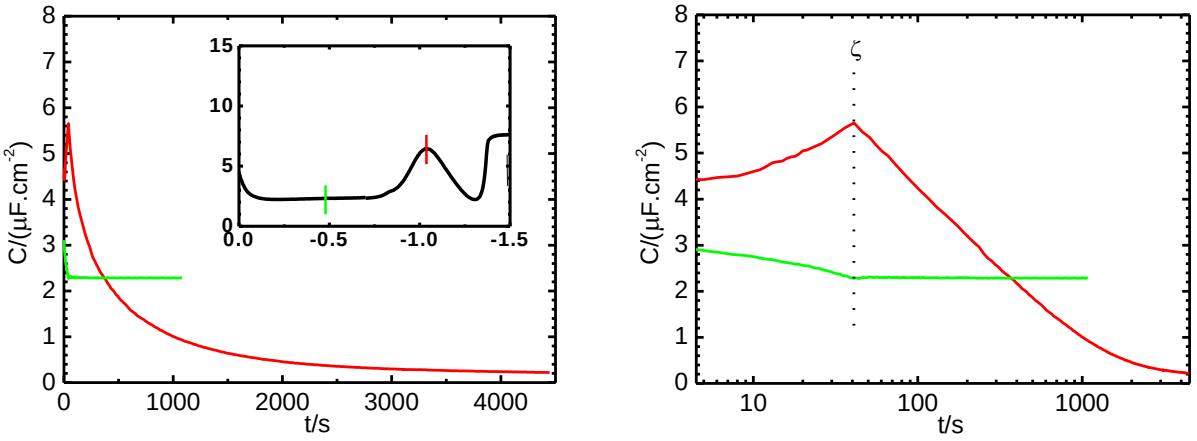

Figure 38: Differential capacity transients obtained for 6.0 μM ***1*** *measured within the adsorption pit (at -0.50 V, green line) and in the faradaic region (at -1.05 V, red line). The both panels show the results of the same measurements: with a linear time scale (left panel) and a logarithmic time scale (right panel). The right panel shows the characteristic time of the film formation, ζ. The inset shows the corresponding ac voltammogram. Perturbation frequency 160 Hz, ac amplitude 5 mV. Measured at 298 K.*

Considerable decrease in the differential capacity value (for $t \rightarrow \infty$) may be explained by changes in the equivalent circuit of the system. For time $t > \zeta$ the electrode is fully covered and, therefore, a single plate capacitor may be taken to model its properties. The capacity decrease may be assigned to a decrease in the effective electrode area, to an increase in the distance between the plates or to a decrease in the relative permittivity of a medium between the plates.

Decrease in the effective area is highly improbable as the electrode is of constant area. Therefore, only the latter two possibilities could account for the changes in the differential capacity value. The separation distance may be changed by the phase transitions within the monolayer. The lying-parallel monolayer is gradually disassembled and a perpendicularly-lying monolayer comes into existence. The latter one has a higher film thickness, leading to lowering of the differential capacity value, which is in the agreement with the experimental observations. The phase transition is very slow as new molecules from the bulk of the solution have to incorporate into a newly formed phase. A very similar behavior was also observed in other systems [159].

For the compound **1**, the time necessary for reorientation of the molecules is roughly 4.0 x 10^3 s, i.e. considerably higher than the characteristic time of the film formation. The capacity value of the reoriented film was found to be approximately ten-times lower than C_∞. The change in the differential capacity value cannot be explained purely by the molecular

reorientation, as the length of the molecule **1** is only two-times higher than its diameter. This cannot fully explain the ten-fold decrease in the differential capacity value.

In the surface-confined faradaic reaction, the molecules of the compound **1** are reduced. It is known from the electrochemical studies that the compound **1** may accept four electrons, each one in one-electron reversible process, with the reduction potentials being close to each other. It was further confirmed that the presence of water has no impact on the chemical and electrochemical reversibility of the electron transfer in **1**. The four peaks are, however, not resolved in a broad faradaic peak. The peak, therefore, highly probably accounts for all four electron transfers. When the electrode potential is set to the peak potential, the molecule is believed to accept two electrons on average. The compound **1** being initially a dication loses its electric charge, which may lead to a considerable decrease in the local relative permittivity value.

The two mentioned phenomena i.e. the molecular reorientation and the decrease in the local permittivity value explain the decrease in the electrode differential capacity value at potential values where the faradaic reaction takes place (Figure 39).

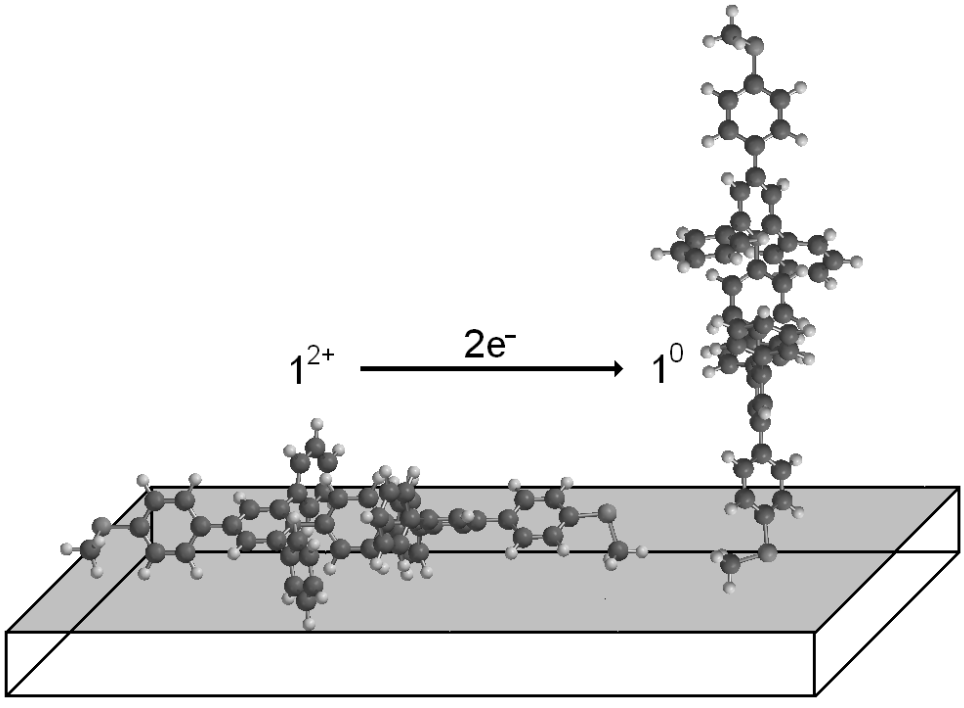

*Figure 39: Possible explanation for decrease in the differential capacity value of the electric double layer containing adsorbed molecules of **1** in the faradaic region.*

4.2 Inclusion complexes of molecular wires with cyclodextrin hosts

As in the adsorption studies of molecular wires (compounds **1** to **6**), 20% ethanol/water (v/v) mixture was employed as an environment, in which the complexation studies were carried out. The studies focused only on the compound **1** being used as a model of molecular wires. The AC voltammetry and differential capacity-time measurements (both with HMDE) as well as UV-VIS absorption and fluorescence spectroscopy were employed. In AC voltammetry and differential capacity-time measurements, potassium fluoride in 0.1 M concentration was added to the solution to serve as the supporting electrolyte.

The cyclodextrin molecules of different cavity sizes, namely alfa-cyclodextrin (αCD), beta-cyclodextrin (βCD) and gamma-cyclodextrin (γCD) were employed as host molecules for the compound **1**.

Absorption spectroscopy is one of the major techniques employed to study the complex formation in the bulk of the solution [160]. The absorption spectrum of the guest molecules changes upon complexation, allowing thus the complex formation to be studied.

For the solution of compound **1** without the host molecules being added, the $\pi - \pi^*$ transition band was found at λ_{max} = 392 nm with the corresponding extinction coefficient 67800±1500 $M^{-1}cm^{-1}$. This band was chosen to trace the absorbance changes induced by the complex formation. Figure 40 shows absorption spectra upon the addition of αCD and βCD.

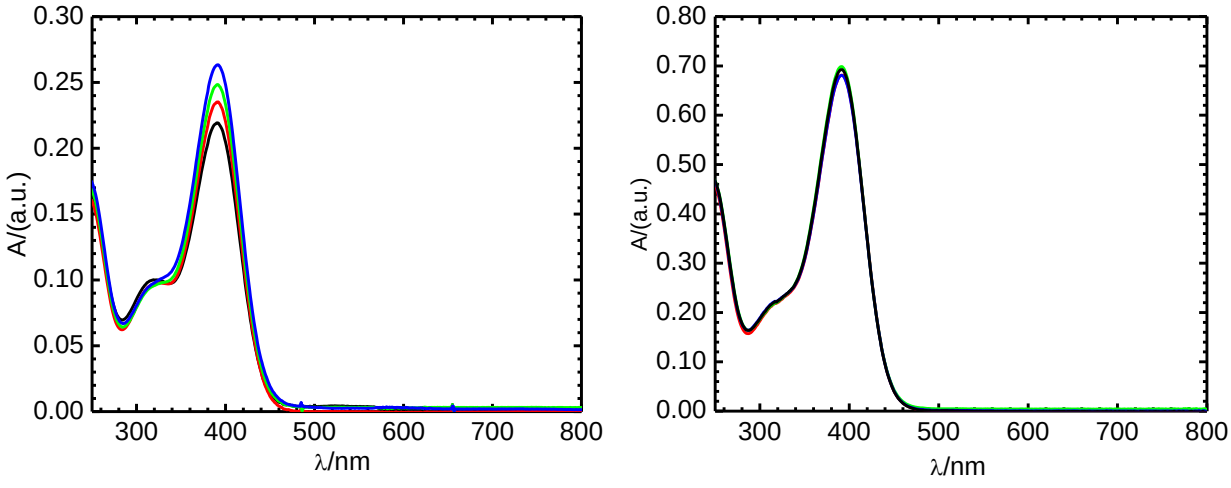

Figure 40: Left panel: UV-VIS absorption spectra of 5.0 μM ***1*** *and 0 mM (black line), 0.2 mM (red line), 1.2 mM (green line) and 2.0 mM (blue line) αCD. Right panel: UV-VIS absorption spectra of 10.0 μM* ***1*** *and 0 mM (black line), 1.2 mM (red line), 3.3 mM (green line) and 5.5 mM (blue line) βCD.*

Upon the addition of the former guest, the height of the peak was found to increase, with the λ_{max} position being unchanged, confirming the complex formation. On the other hand, no change in the spectrum was observed upon the addition of βCD. Data for γCD are not shown as they are identical to those for βCD. Therefore, αCD is the only suitable host for **1**.

Benesi-Hildebrand analysis [161] is frequently used to determine the complex formation constant, K_a, and elucidate the complex stoichiometry. If the guest forms 1:1 complex with the host, the equilibrium constant takes the form K_a = [GH] / [G][H], where [G], [H] and [GH] is the actual concentration of the free guest, free host and the inclusion complex, respectively. Benesi-Hildebrand analysis is based on measuring the absorbance values in the presence (A) and in the absence (A_0) of the host molecules in the solution. The total concentration of the host molecules, c_H, is varied while that of the guest molecules, c_G, is kept constant. The respective absorbance values are given by

$$A = \varepsilon_0[G] + \varepsilon[GH] \qquad A_0 = \varepsilon_0 c_G \tag{38}$$

where ε and ε_0 is the molar extinction coefficient of the complexed and free guest, respectively. The host molecules are not assumed to absorb radiation at chosen wavelength and thus, $\varepsilon_H = 0$. The total (analytical) concentrations of the guest and the host molecules are

$$c_G = [G] + [GH] \qquad c_H = [H] + [GH] \tag{39}$$

For $c_H >> c_G$ one can assume [H] >> [HG] and therefore c_H = [H]. The actual concentrations may be then expressed as

$$[GH] = \frac{A - A_0}{\varepsilon - \varepsilon_0} \qquad [G] = c_G - \frac{A - A_0}{\varepsilon - \varepsilon_0} \qquad [H] = c_H \tag{40}$$

These expressions may substitute the actual concentrations in the equation defining the equilibrium constant

$$\frac{A - A_0}{\varepsilon - \varepsilon_0} = K_a c_H \left(c_G - \frac{A - A_0}{\varepsilon - \varepsilon_0} \right) \tag{41}$$

from which the Benesi-Hildebrand equation for the formation of 1:1 inclusion complex is obtained

$$\frac{1}{A - A_0} = \frac{1}{c_G(\varepsilon - \varepsilon_0)} + \frac{1}{c_G c_H (\varepsilon - \varepsilon_0) K_a} \tag{42}$$

If one plots $1/(A-A_0)$ vs. $1/c_H$, the intercept and slope of the dependence are equal to $1/c_G(\varepsilon-\varepsilon_0)$ and $1/c_G(\varepsilon-\varepsilon_0)K_a$ and the complex formation constant may be obtained as the intercept/slope ratio.

If the guest molecule binds two host molecules, then a 1:2 inclusion complex comes into existence and the Benesi-Hildebrand equation takes the shape

$$\frac{1}{A - A_0} = \frac{1}{c_G(\varepsilon - \varepsilon_0)} + \frac{1}{c_G c_H^2(\varepsilon - \varepsilon_0)K_a} \quad (43)$$

with the complex formation constant defined as $K_a = [GH_2] / [G][H]^2$. If one plots $1/(A-A_0)$ vs. $1/c_H^2$ then the intercept and the slope are equal to those derived in the case of 1:1 complex, with the complex formation constant being the intercept/slope ratio.

In both cases, the equations hold only for [H] >> [HG] and only if the host molecules do not absorb the radiation at the wavelength used for the evaluation of *A* and A_0. These two conditions, to some extent, limit the usefulness of Benesi-Hildebrand analysis.

The values of ε and ε_0 may be determined at a constant c_G value for $c_H \rightarrow \infty$ and $c_H = 0$ though they are not directly necessary for the determination of the K_a value.

Figure 41 shows the results of Benesi-Hildebrand analysis for both 1:1 and 1:2 stoichiometries of the inclusion complexes proposed. The linearity was not obtained in neither of the cases. Therefore, the solutions most likely contain *GH* and GH_2 i.e. **1**:αCD and **1**:αCD_2 complexes being in the equilibrium with the free guest form, *G* (the compound **1**).

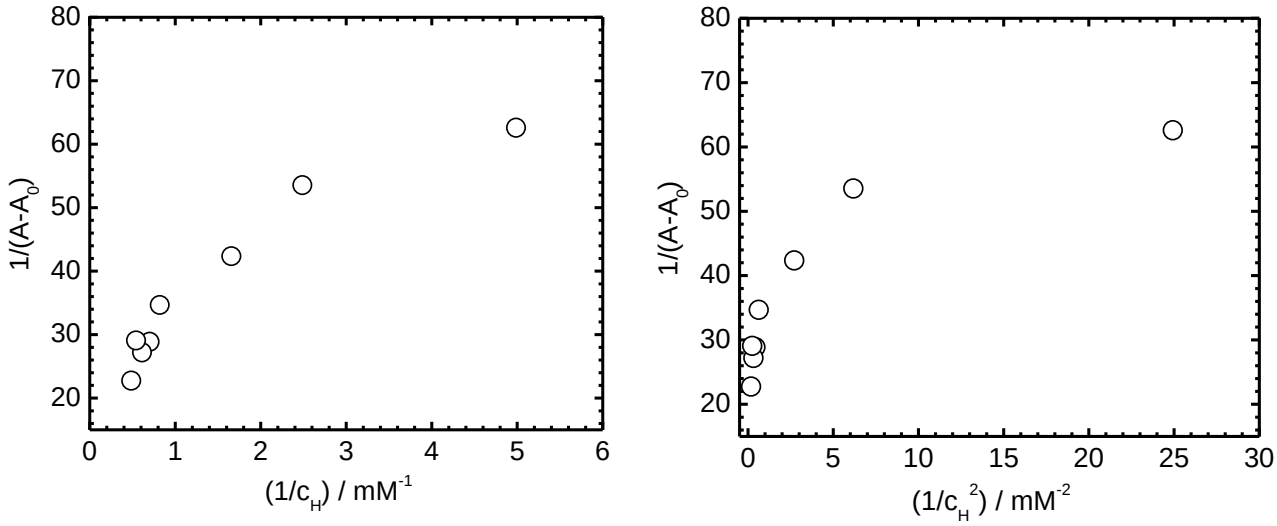

*Figure 41: Benesi-Hildebrand plots for the complex formation between **1** and αCD assuming 1:1 (left panel) and 1:2 (right panel) complex stoichiometry. The absorbance values were obtained at λ = 392 nm, with c_G = 5.0 μM and varying c_H values.*

The molecule of the compound **1** contains six benzene rings as either phenyl or 1,4-phenylene moieties that could possibly interact with the hydrophobic cavity of αCD. The two of them are the 1,4-phenylene linkers between the methylsulfanyl- terminating groups and the rest of the molecule. The other four are phenyl side groups attached to the molecular backbone,

imparting the chemical stability and molecular rigidity. They are highly likely not suitable moieties for the complex formation as they are close to each other, creating thus a considerable sterical hindrance preventing the reaction with the cyclodextrin molecule. Therefore, there are only two suitable moieties that can interact with the cyclodextrin molecules (Figure 42). This is in agreement with the results of UV/VIS absorption spectroscopy measurements, from which the presence of both *GH* and GH_2 complex types may be deduced.

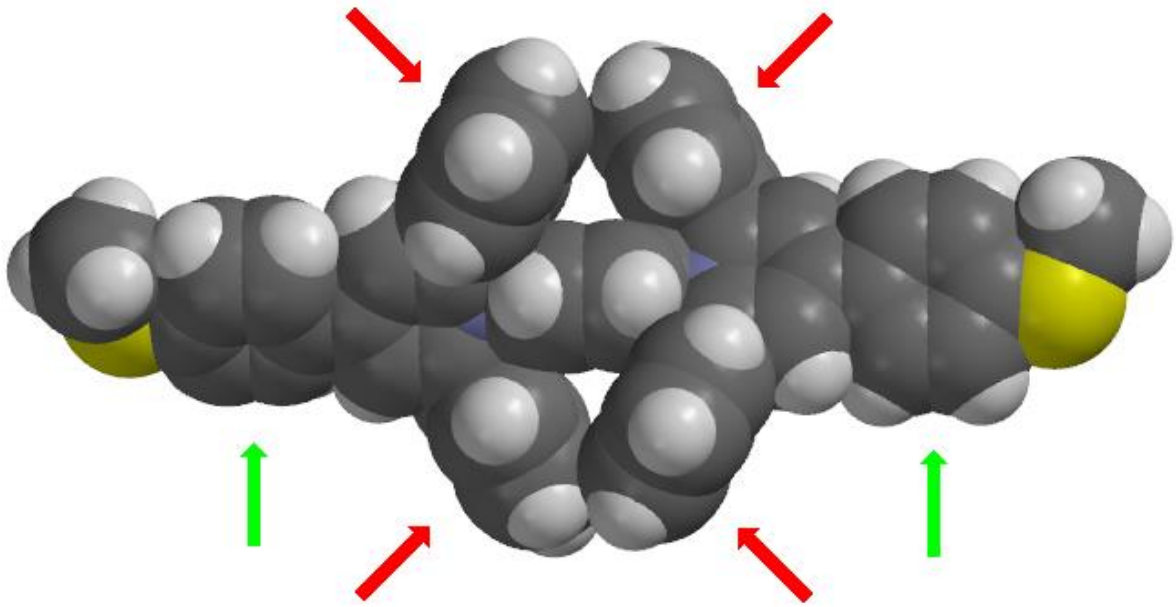

*Figure 42: The molecule of compound **1**. Red arrows indicate sterically hindered phenyl groups. Green arrows indicate the methylsulfanylphenylene moieties, suitable for the inclusion into the cavity of αCD molecule.*

The behavior of the system containing both 1:1 and 1:2 complexes was further studied by the aid of fluorescence spectroscopy. Benesi-Hildebrand analysis was also applied to the data obtained from the fluorescence measurements [162]. First, the excitation spectra were obtained and the excitation maximum was found at 379 nm. Therefore, all emission spectra were recorded employing the excitation wavelength 379 nm. An increase in the fluorescence intensity (FI) upon αCD addition was observed (Figure 43). The FI values were integrated within the fluorescence band, gaining the integrated FI values.

The plot of integrated FI vs. αCD concentration reaches a plateau between 0.4 and 1.4 mM of αCD, indicating the presence of 1:1 complex. At αCD concentrations above 1.5 mM the integrated FI further increases due to the presence of 1:2 complex.

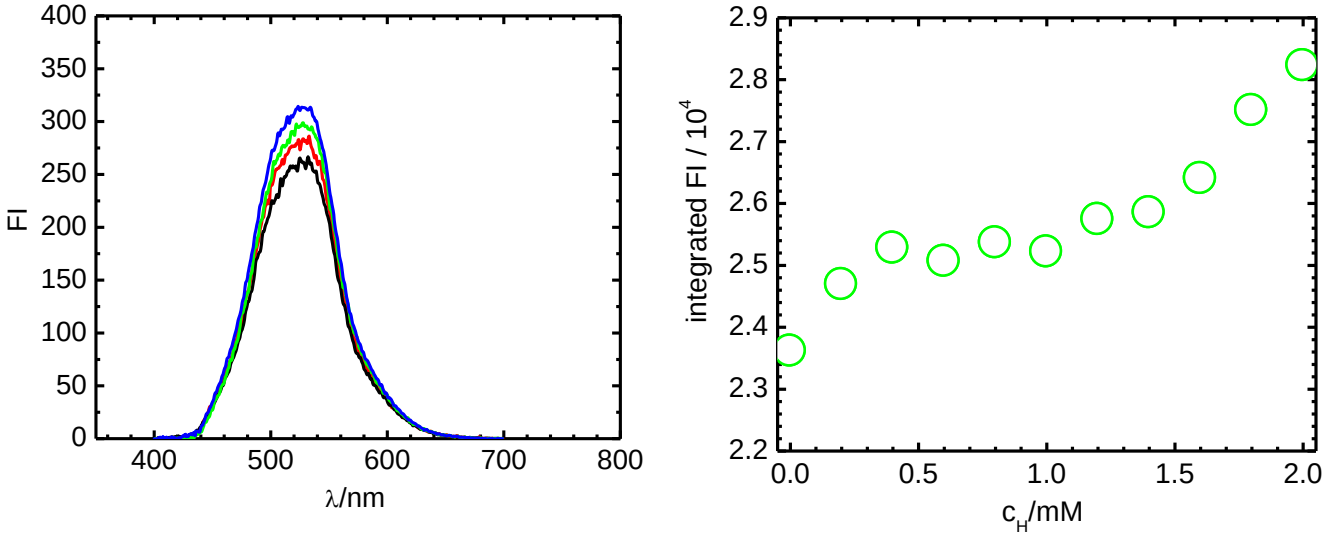

Figure 43: Left panel: fluorescence emission spectra of 5.0 μM ***1*** *in the absence (black line) and presence of 0.8 mM (red line), 1.6 mM (green line) and 2.0 mM (blue line) αCD in 20% ethanol/water solution. Excitation wavelength: 379 nm. Right panel: integrated fluorescence intensity for all additions of αCD.*

The results of the fluorescence spectroscopy measurements were analyzed by means of Benesi-Hildebrand equation. If the formation of 1:1 complex is assumed, the equation takes the form [162]

$$\frac{1}{F - F_0} = \frac{1}{F_\infty - F_0} + \frac{1}{c_H (F_\infty - F_0) K_a} \qquad (44)$$

where F_0 and F_∞ are the fluorescence intensities obtained for a free guest, G, and fully complexed guest, GH, respectively. The both values are easily obtained experimentally, F_0 with $c_H = 0$ and F_∞ with $c_H \rightarrow \infty$. Value F is found in the solution containing both free and complexed guest molecules. Similarly as in the absorption spectroscopy, the dependence $1/(F-F_0)$ vs. $1/c_H$ is plotted and the complex formation constant, K_a, is obtained as the intercept/slope ratio.

For a 1:2 complex the Benesi-Hildebrand equation takes the shape

$$\frac{1}{F - F_0} = \frac{1}{F_\infty - F_0} + \frac{1}{c_H^2 (F_\infty - F_0) K_a} \qquad (45)$$

The equilibrium constant is obtained as the intercept/slope ratio in the plot $1/(F-F_0)$ vs. $1/c_H^2$. Figure 44 shows the Benesi-Hildebrand plots constructed for both 1:1 (left panel) and 1:2 (right panel) types of complexes.

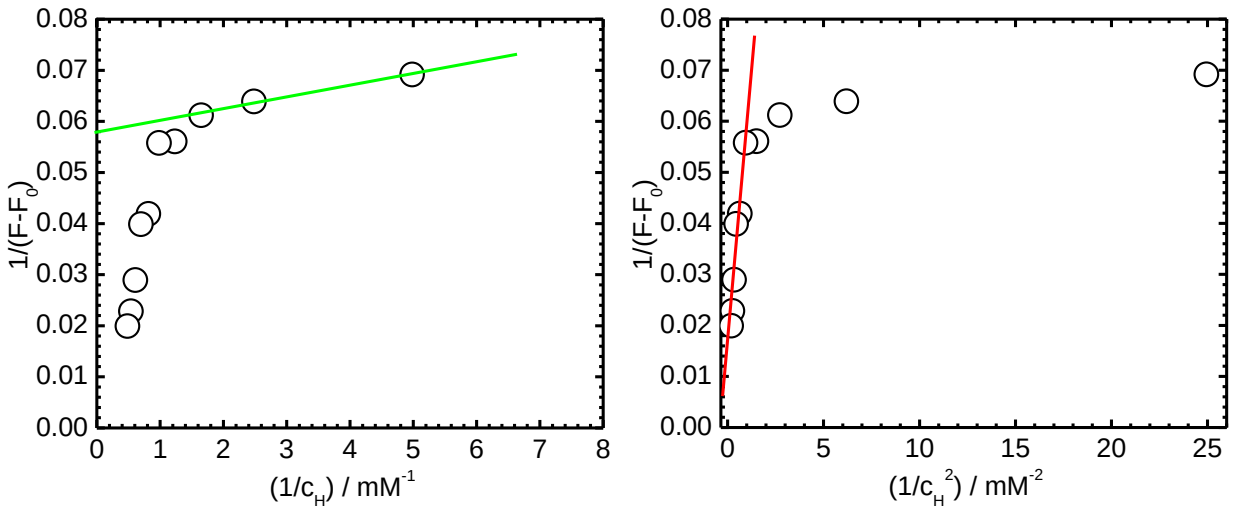

Figure 44: Benesi-Hildebrand plot of $1/(F–F_0)$ vs. $1/c_H$ (left panel) and $1/(F–F_0)$ vs. $1/c_H^2$ (right panel) constructed at λ_{exc} = 379 nm and λ_{em} = 525 nm. The linear regressions used in complex formation determination are shown for 1:1 complex (green) and 1:2 complex (red).

At low αCD concentrations only the 1:1 complex comes into the existence. Therefore, the dependence $1/(F–F_0)$ vs. $1/c_H$ is employed to determine the $K_{a,1}$ value. As $1/c_H$ attains large values for low host concentrations, only the right part of the plot was taken to the analysis.

On the other hand, at higher concentrations of αCD, the 1:2 complex is formed and the dependence $1/(F–F_0)$ vs. $1/c_H^2$ is employed to determine the $K_{a,2}$ value. In this case, low values of $1/c_H^2$, corresponding to the highest αCD concentrations, were employed for the analysis. The following complex formation constants were found

$$K_{a,1} = \frac{[GH]}{[G][H]} = (2.5 \pm 0.3) \times 10^4 \, M^{-1} \qquad K_{a,2} = \frac{[GH_2]}{[G][H]^2} = (2.1 \pm 0.7) \times 10^5 \, M^{-2} \tag{46}$$

One can easily show, that the molar fractions of the complexed guest form $x_{GH} = [GH]/c_G$ and the free guest form, $x_G = [G]/c_G$ are given by

$$\frac{[GH]}{c_G} = \frac{K_{a,1} c_H}{1 + K_{a,1} c_H} \qquad \frac{[G]}{c_G} = \frac{1}{1 + K_{a,1} c_H} \tag{47}$$

with the right-hand sides of the equations summing up to unity. The presence of the second equilibrium was neglected, which may be safely done for αCD concentrations within the first "wave" in the *FI* vs. c_H plot (Figure 43, right panel). If one takes the value c_H = 0.5 mM at the start of the plateau in the plot, then $[GH]/c_G$ = 93 %, which means that nearly all guest molecules are complexed. As the two "waves" are well separated from one another, the αCD concentration value may precisely control the distribution of the guest forms (*G*, *GH* and GH_2) in the solution.

The compound **1** is a model of the organic molecular wires, which may be used in the future electronic devices as molecular conductors. The electric conductors will need to be placed between other circuit elements, forming thus an interface. However, the interfacial properties may significantly differ from those found in the bulk of the solution. Therefore, we decided to employ also the electrochemical techniques to study the complex formation between **1** and αCD. In particular, AC voltammetry and differential capacity-time measurements were used. To avoid complications, we focused only on the αCD concentration range, in which the 1:1 complex is formed i.e. for c_H < 1.4 mM. First, the adsorption behavior of the pure host, αCD, was investigated. Figure 45 shows the ac voltammograms of 20% water/ethanol mixture containing 0.1 M KF as the supporting electrolyte upon an addition of various amounts of αCD. The voltammograms were obtained by scanning the electrode potential from the value -0.20 V with the scan-rate 10 mV/s in the negative direction employing HMDE.

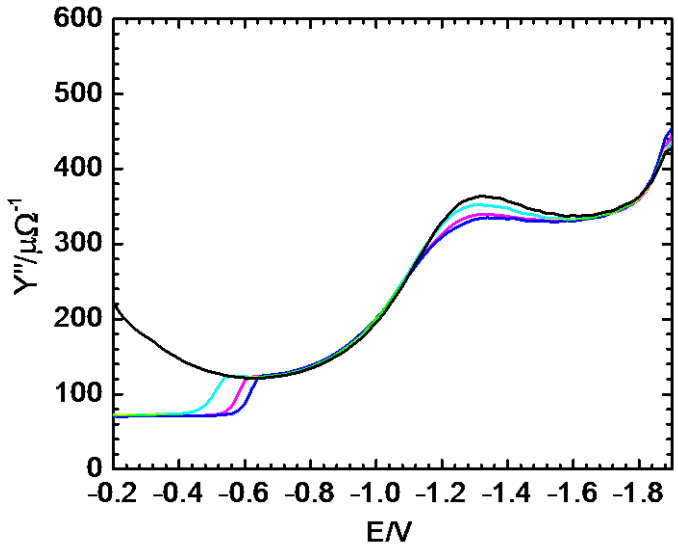

Figure 45: AC voltammogram of 0.1 M KF in 20% ethanol/water mixture containing 0 mM (black line), 0.6 mM (red line), 1.2 mM (green line) and 1.6 mM (blue line) αCD. Perturbation frequency 160 Hz and amplitude 5mV, obtained with HMDE.

The αCD molecules were found to adsorb at the interface in a certain range of electrode potentials, being slightly dependent on the concentration of αCD in the bulk of the solution. For the highest investigated bulk concentration of αCD (1.6 mM), the molecules desorbed at the potential close to -0.60 V. For potentials more negative than -0.60 V the admittance values were nearly identical to those measured in the absence of αCD (Figure 45, black curve) indicating that no αCD is adsorbed in this potential region. The differential capacity within

the pit was found to be independent of the concentration of αCD in the bulk of the solution. Therefore, the αCD molecules form a monolayer at the electrode/electrolyte interface.

As shown in the section dealing with the adsorption properties of the compound **1**, the monolayer is formed in the certain potential region being followed by the onset of faradaic reduction at the cathodic side. Figure 46 shows the AC voltammograms of αCD (red line) and of the compound **1** (green line) measured under the very same experimental conditions. The AC voltammograms reveal the region between ca -0.60 and -0.70 V, in which the molecules of compound **1** are adsorbed, while those of αCD are not. This region, in which the adsorption of **1** is not complicated by that of αCD, was further employed for the differential capacity-time measurements. When any given amount of αCD was added to the solution of compound **1**, no change in the AC voltammogram was observed. The differential capacity of the monolayer was found to be identical to that measured for **1** in the absence of αCD (green line) indicating that the molecules of compound **1** are adsorbed at the interface even when complexed. This is in agreement with the above mentioned model considering the terminal methylthiophenylene groups as being responsible for the complex formation. According to the model, the side phenyl groups are unaffected by the complex formation. Therefore, the adsorption of the molecules may proceed with the parallel-lying orientation being retained.

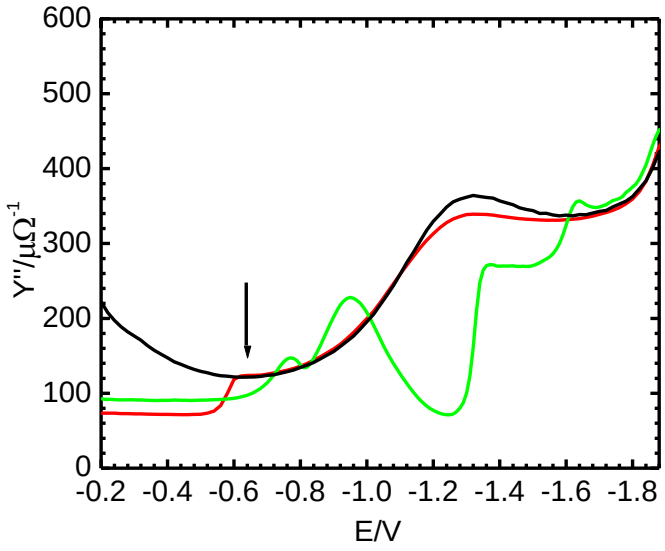

Figure 46: AC voltammogram of 0.1 M KF in 20% ethanol/water mixture in the absence (black line) and the presence of 5.0 μM ***1*** *(green line). Red line denotes the AC voltammogram of 1.2 mM αCD. Frequency 160 Hz, amplitude 5mV, HMDE. The arrow indicates the potential -0.60 V suitable for differential capacity-time measurements.*

At potentials less negative than -0.60 V, the admittance values obtained for the solution containing **1** or a mixture of **1** and αCD differ from those obtained for the solution of pure αCD (Figure 46).

The kinetics of the complex formation was further investigated by the differential capacity-time measurements. The measurements were performed at -0.60 V, where the adsorption of **1** is not complicated by that of αCD. The complexation event affects the diffusion coefficient value, D, and the maximum surface concentration of the adsorbed molecules, Γ_{MAX}. These two quantities are related by Eq. 32. Figure 47 shows the dependence θ vs. $t^{1/2}$ obtained from the differential capacity-time measurements carried out at -0.60 V for the compound **1** in the absence (black line) and presence (red line) of αCD molecules in the bulk of the solution.

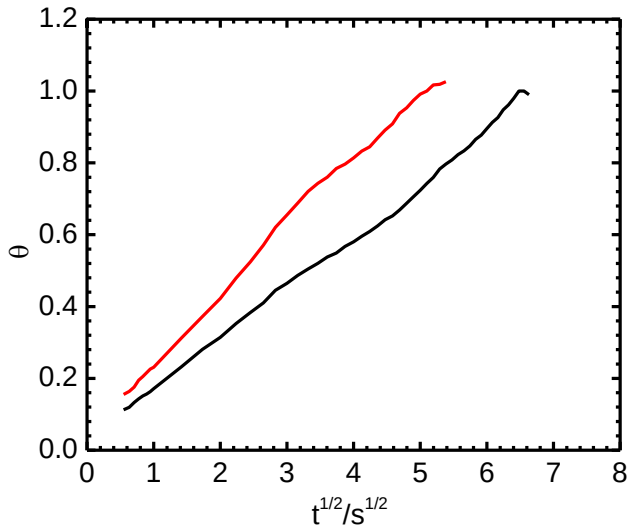

Figure 47: Time dependence of the electrode surface coverage θ for 5.0 μM ***1*** *in the absence (black line) and presence (red line) of 1.34 mM αCD in the 20% ethanol/water solution obtained at the potential –0.60 V. Perturbation frequency 160 Hz and amplitude 5 mV.*

Even upon the addition of αCD molecules, the adsorption remains diffusion-limited as the dependence θ vs. $t^{1/2}$ is nearly linear. Therefore, the complex formation imposes no activation barrier for the molecules to be overcome during adsorption. The characteristic time of the film formation shifts to lower values. The ζ vs. c_H dependence reaches plateau at sufficiently high c_H values (Figure 48), suggesting the complete complexation of **1** with αCD, forming the 1:1 complex.

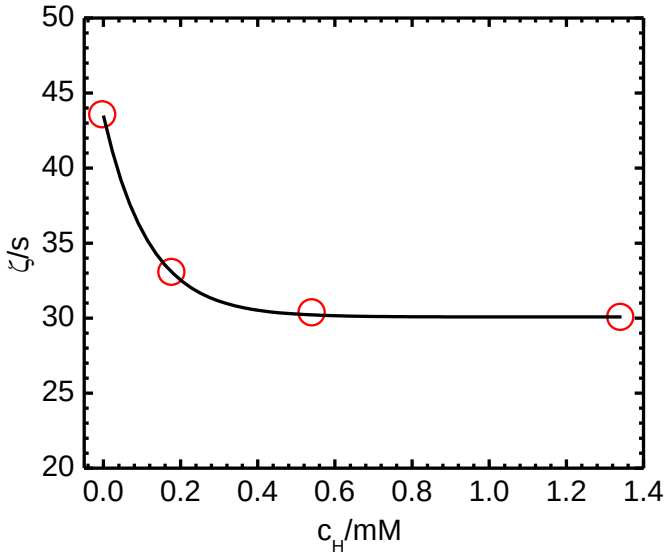

*Figure 48: Characteristic time of the film formation ζ as a function of αCD concentration in the bulk of the solution. The total concentration of **1** is 5.0 μM, measured at electrode potential –0.60 V, perturbation frequency 160Hz and amplitude 5mV.*

When αCD molecules are present in the bulk of the solution, both **1** and **1**:αCD complex diffuse to the electrode and adsorb at the interface (see Figures 25 and 46). Both species have their characteristic time of the film formation. The value ζ_0 = 43.5 s was found for 5.0 μM of **1** in the bulk of the solution in the absence of αCD. As mentioned above, ζ was found to decrease upon the addition of αCD, with ζ_∞ = 30.1 s *(*for $c_H \rightarrow \infty$). The ζ_∞ is the characteristic formation time of the film composed of fully complexed molecules of **1**. The film formation is diffusion-limited process for both **1** and **1**:αCD species with a negligible adsorption activation barrier. Therefore, no preferential adsorption is anticipated between **1** and **1**:αCD molecules. The characteristic time of the film formation obtained for a given solution, ζ, is believed to reflect the solution composition

$$\zeta = \zeta_\infty x_{GH} + \zeta_0 x_G \tag{48}$$

The fractions of the free x_G and complexed x_{GH} guest molecules depend only on the complex formation constant and the concentration of αCD molecules in the bulk of the solution. One can according to Eq. 47 write

$$\zeta = \zeta_\infty \frac{K_{a,1} c_H}{1 + K_{a,1} c_H} + \zeta_0 \frac{1}{K_{a,1} c_H} \tag{49}$$

This equation may be easily rearranged to the shape

$$\frac{\zeta - \zeta_0}{\zeta_\infty - \zeta} = K_{a,1} c_H \tag{50}$$

If one plots the fraction $(\zeta - \zeta_0) / (\zeta_\infty - \zeta)$ vs. c_H, the complex formation constant may be obtained as the slope of the dependence (see Figure 49).

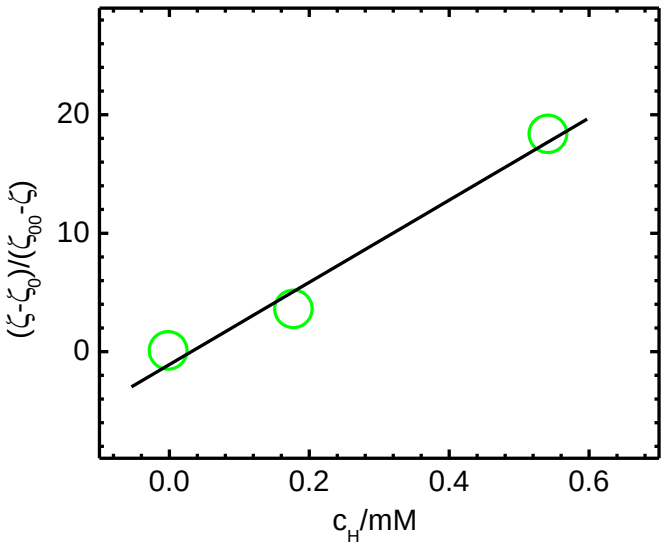

*Figure 49: The plot $(\zeta - \zeta_0) / (\zeta_\infty - \zeta)$ vs. c_H for the formation of the complex 1:αCD. The complex formation constant was evaluated from the slope of the dependence. The analytical concentration of **1** is 5.0 μM, measured at electrode potential –0.60 V, perturbation frequency 160Hz and amplitude 5mV.*

The equilibrium constant determined by this method amounts to $K_{a,1} = (3.4 \pm 0.5) \times 10^4$ M^{-1}, which is in reasonable agreement with the value found by the fluorescence measurements $K_{a,1} = (2.5 \pm 0.3) \times 10^4$ M^{-1}.

One may define the effective diffusion coefficient, D_{eff}, as the property reflecting the solution composition

$$D_{eff} = D_{GH} x_{GH} + D_G x_G \qquad (51)$$

where D_G and D_{GH} are the diffusion coefficients for free and complexed guest molecule, respectively. The former one, treated theoretically in the Chapter 4.1, has the value $D_G = 1.04 \times 10^{-10}$ $m^2 s^{-1}$. The latter one may be calculated from the following expression

$$D_{GH} = D_G \left(\frac{M_G}{M_{GH}} \right)^{1/3} = 0.84 \times 10^{-10} m^2 s^{-1} \qquad (52)$$

where M_G and $M_{GH} = M_G + M_{\alpha CD}$ is the molar mass of the free and the complexed guest, respectively. Employing equations 47 and 51 one can derive [163,164]

$$D_{eff} = \frac{D_G + K_{a,1} c_H D_{GH}}{1 + K_{a,1} c_H} \qquad (53)$$

For c_H = 0.30 mM, one gets D_{eff} = 0.87 $\times 10^{-10}$ $m^2 s^{-1}$, being close to the D_G value.

Exact value of the characteristic time of the film formation reflects not only the solution composition, but also the composition of the adsorbed monolayer. If no host molecules are present in the bulk of the solution, the monolayer is formed by the free guest molecules with the characteristic time ζ_0. For sufficiently high concentration of the host molecules, the monolayer is formed by the complexed guest molecules with the characteristic time ζ_∞. The solutions containing both free and complexed guest molecules form mixed monolayers, the characteristic time of which, ζ, is between the values ζ_0 and ζ_∞ (see equation 48). As shown in the Chapter 4.1, the molecules of **1** form the parallel-lying monolayer, with the maximum surface coverage $\Gamma_{MAX,G}$ = 5.3 $\times 10^{-7}$ $mol.m^{-2}$ and the single molecule area of 3.1 nm^2. According to the equation 32, the characteristic time of the film formation is proportional to the fraction Γ^2_{MAX}/D. One can calculate the maximum surface concentration of complexed guest molecules $\Gamma_{MAX,GH}$ from the following expression

$$\Gamma_{MAX,GH} = \Gamma_{MAX,G} \sqrt{\frac{\zeta_\infty D_{GH}}{\zeta_0 D_G}} = 4.0 \times 10^{-7}\, mol.m^{-2} \qquad (54)$$

Using the equation 37 and the $\Gamma_{MAX,GH}$ value, the single-molecule area of 4.2 nm^2 was calculated for the complexed guest molecules. This value is 35 % higher than that determined for free guest molecules (3.1 nm^2). This is reasonable as the αCD molecules cover some extra electrode region, increasing thus the single-molecule area (Figure 50).

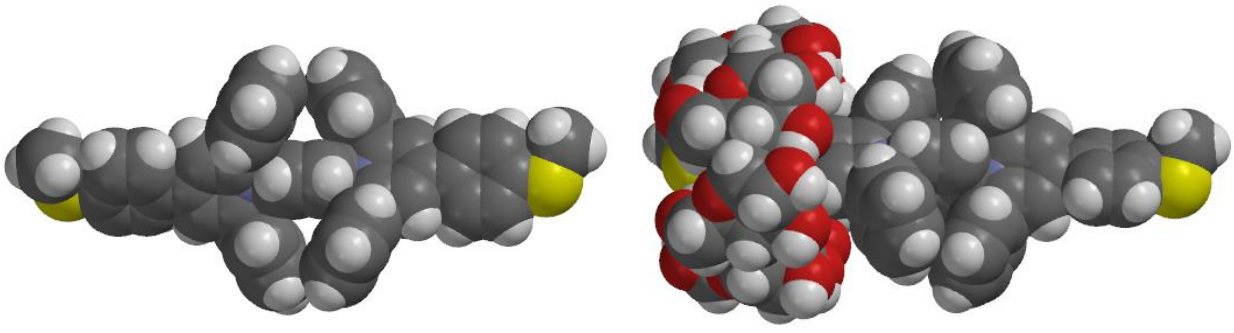

*Figure 50: The free (left figure) and the complexed (right figure) form of **1**.*

4.3 Electrochemical and spectroelectrochemical properties of molecular wires

Electrochemical properties of the compounds **1** to **6** were studied in dimethyl sulfoxide (DMSO), acetonitrile (AN) and in some cases also in 1,2-dichoroethane (DCE), tetrahydrofuran (THF) and dimethylformamide (DMF), containing 0.1 M tetrabutylammonium hexafluorophosphate ($TBAPF_6$) as the supporting electrolyte. All values of potentials in this chapter are related to the Fc/Fc^+ redox couple.

Fugure 51 shows cyclic voltammograms of the compound **1** in AN (left figure) and DMSO (right figure). The cyclic voltammogram obtained in AN shows a pair of tensammetric peaks (centered at -0.81 V) as well as the adsorption peaks (at -1.36 V) superimposed on the peaks originating from the reduction of molecules from the bulk of the solution. The area of the adsorption peaks was found to be nearly independent of the bulk concentration of **1**, suggesting that the compound **1** forms a monolayer on the electrode with $\Gamma_{MAX} = 4.2 \times 10^{-7}$ mol.m^{-2}, obtained by the integration of the adsorption peak. On the other hand, the adsorption peaks were not observed in DMSO (in the concentration range 0.1 – 2 mM and scan-rate range 0.05 – 1 V/s). The electrochemical behavior of the compound **1** in DMSO is therefore not strongly influenced by the adsorption. In order to suppress complications originating from the adsorption effects, the electrochemical studies of the compounds **1** to **6** were mostly performed in DMSO unless stated otherwise.

The shortest molecular wire, the compound **1**, was found to consume four electrons in one-electron processes. This behavior was found in both DMSO and AN. Table 2 shows the comparison of the respective standard reduction potential values, referenced to the Fc/Fc^+ redox couple. No other reduction waves were observed within available potential windows of the solvent/electrolyte systems used. The behavior of the compound **1** is rather general as it

reduction wave/solvent	E^0(DMSO) vs. $E^0_{Fc/Fc+}$	E^0(AN) vs. $E^0_{Fc/Fc+}$
1st	-1.28 V	-1.25 V
2nd	-1.37 V	-1.39 V
3rd	-1.48 V	-1.50 V
4th	-1.62 V	-1.71 V

*Table 2: Standard redox potential values of the compound **1** in DMSO and AN, containing 0.1 M $TBAPF_6$ as the supporting electrolyte. The values are referenced to the Fc/Fc^+ pair.*

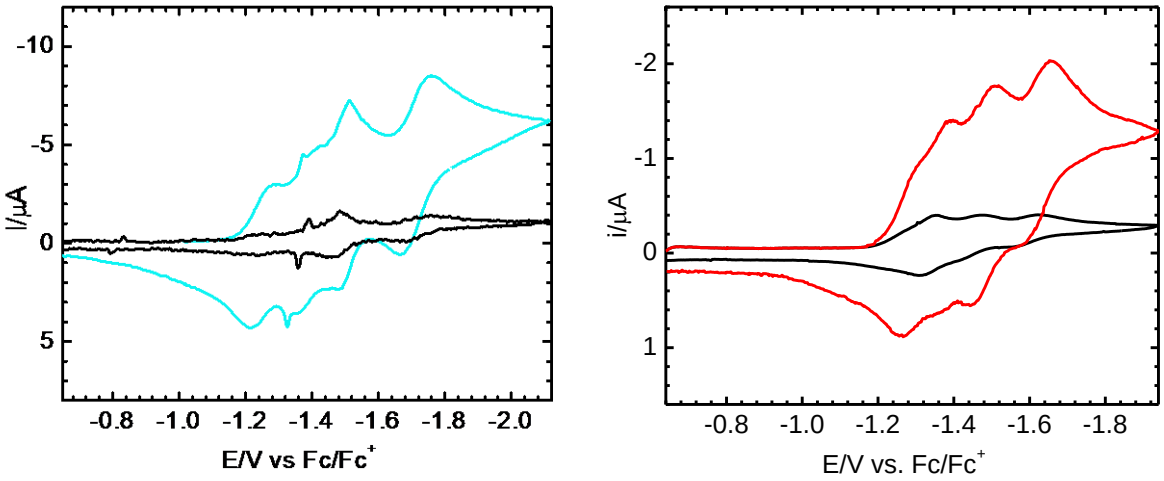

*Figure 51: Cyclic voltammograms of the compound **1** at concentrations 0.10 mM (black line) and 0.50 mM (red line) measured in AN (left panel) and DMSO (right panel). Scan-rate 0.25 V/s, 0.1 M $TBAPF_6$ was used as the supporting electrolyte. Working electrode HMDE.*

was observed also in other solvents (DMF, THF, DCE) and various electrode materials (gold, platinum, HMDE). The four-electron reduction of the compound **1** was also confirmed by several other electrochemical techniques. The sampled DC polarogram in DMSO with SMDE as the working electrode is shown in Figure 52. The limiting current of **1**, obtained at potential values more negative than the standard redox potential of the last fourth reduction wave (-1.62 V vs. Fc/Fc^+), was found to be twice as high as that found for the second reduction step of methyl viologen (MV) at the same conditions. MV is known to accept reversibly two electrons in the aprotic solvents suggesting the consumption of four electrons per one molecule of **1**.

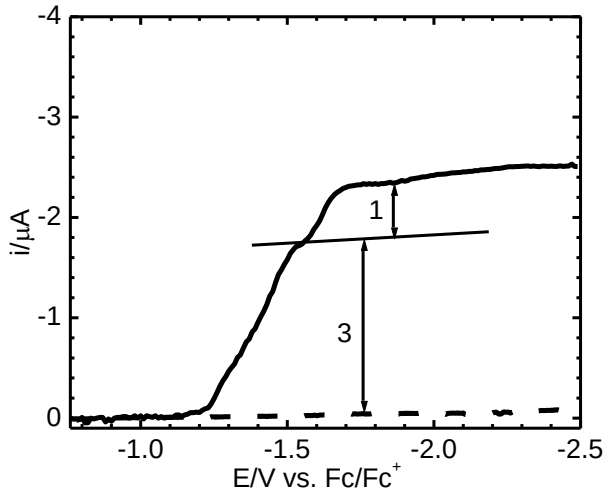

*Figure 52: Sampled DC polarogram of 1.0 mM **1** in DMSO containing 0.1 M $TBAPF_6$ as the supporting electrolyte. Drop-time was set to 3s. Dashed line is measured in the absence of **1**.*

The first three reduction waves that are resolved in cyclic voltammogram (Figure 51) are merged together into one wave in the sampled DC polarogram. The fourth wave is only slightly separated from them. The merged wave is three times higher than the fourth wave. As the fourth wave is separated, it could be subjected to the log-plot analysis [133,134]. Figure 53 shows the „log-plot" for the last reduction wave of the compound **1**.

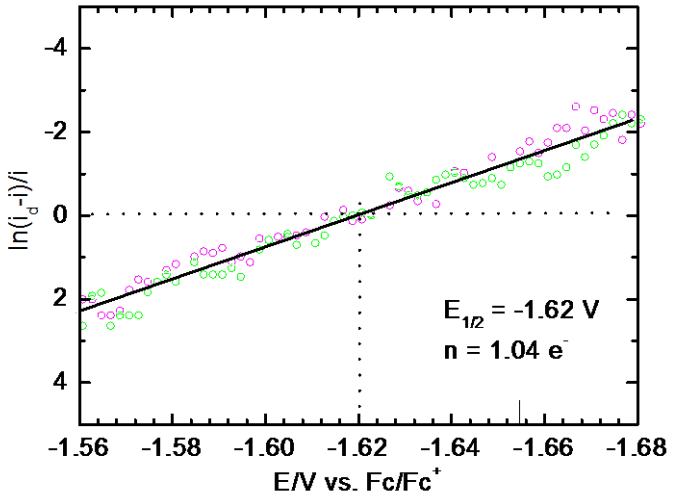

*Figure 53: Log-plot analysis at potential values pertaining to the fourth reduction wave of the compound **1**. Measured in DMSO with 0.1 M $TBAPF_6$ as the supporting electrolyte.*

The log-plot analysis clearly confirmed the consumption of one electron in the fourth wave. Though such analysis could not be applied to the merged wave, its slope is very similar to that of the fourth wave. The consumption of one electron is, therefore, assumed in each of the three reduction steps in the merged wave, which corresponds to results of the cyclic voltammetry and sampled DC polarography with MV used as the standard.

AC polarography employing SMDE as the working electrode was also used to investigate the electrochemical behavior of the compound **1**.

Figure 54 shows the AC polarogram, in which four peaks may be easily discerned, with slightly larger imaginary part of the faradaic cell admittance. Therefore, the electron transfer partly takes place in the adsorbed state of the compound **1**. In the case of all four faradaic peaks, the real and the imaginary admittance components attain a maximum at the same electrode potential value, suggesting the electrochemical reversibility. The maxima match the standard redox potential values found by cyclic voltammetry. The shape of the AC polarogram was found to be independent of the applied AC frequency. Frequency range 1.6 – 3200 Hz was investigated.

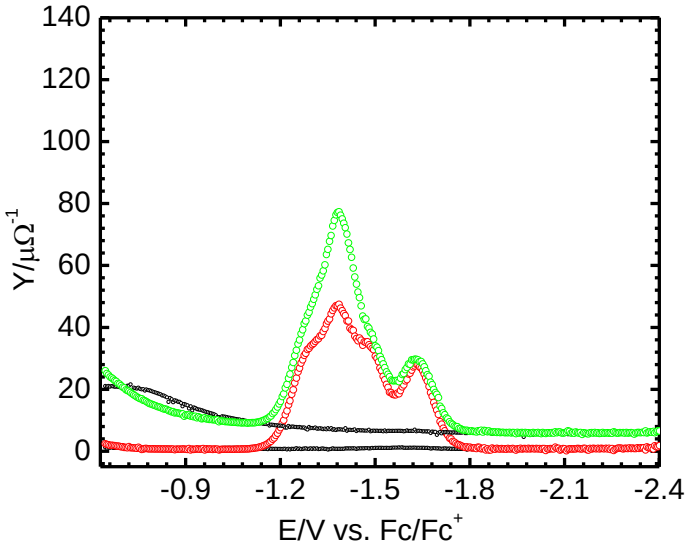

*Figure 54: AC polarogram of **1**. Real part (red line) and imaginary part (green line) of the cell admittance for 0.5 mM **1** in DMSO containing 0.1 M $TBAPF_6$ as the supporting electrolyte. AC frequency 16 Hz, AC amplitude 5mV, drop-time 2 s. Lower and higher black line represent the real and the imaginary part of the cell admittance obtained in the absence of 1, respectively.*

The exhaustive electrolysis at -2.00 V vs. Fc/Fc^+ confirmed the consumption of the electric charge corresponding to four electrons per one molecule of **1**. The current transient obtained during the bulk electrolysis followed a single exponential decay. The electric charge was obtained by the integration of the current transient recorded during electrolysis. The long-term chemical stability of the compound **1** was investigated by the aid of an in-situ UV/VIS/NIR spectroelectrochemistry with the OTTLE cell being employed. An increased supporting electrolyte concentration 0.43 M was employed to suppress the IR drop. In some experiments, DMSO was replaced by AN due to its considerably lower dynamic viscosity and thus shortened times of the electrolysis. Moreover, dried AN contains less water than dried DMSO. The spectroelectrochemical experiments may either be carried out in a sweep-like (cyclic voltammetry) or in a step-like (chronoamperometry) way. The sweep-like experiments are always prerequisite to step-like potentiostatic ones, as one has to find a suitable electrode potential, at which the process of interest is diffusion limited. This potential value is then applied in the potentiostatic electrolysis. As in the CV experiments employing HMDE, gold, and platinum electrodes, four voltammetric waves were found for the compound **1** (data not shown) in the OTTLE cell. The charge consumed in the exhaustive electrolysis at various potentials was determined by the integration of respective current transients. At potentials more negative than the reduction potential of the fourth reduction wave of **1**, the consumed

charge was found to be four times higher than that obtained for MV at a potential, at which its first reduction step is diffusion-limited. This confirms the results of sampled DC polarography, AC polarography, cyclic voltammetry and bulk electrolysis - the consumption of four electrons per one molecule. As the molecule of **1** is initially a dication, its reduced forms will be denoted as 1^{1+}, 1^{0}, 1^{1-} and 1^{2-}.

The reduced forms generated during the electrolysis may be traced by the spectroscopy. After the electrolysis has been completed, the potential is stepped back to the capacitive region, which triggers the re-oxidation of a reduced form. Figure 55 shows the in-situ absorption spectra during electrolysis of the compound **1** in DMSO with 0.43 M $TBAPF_6$.

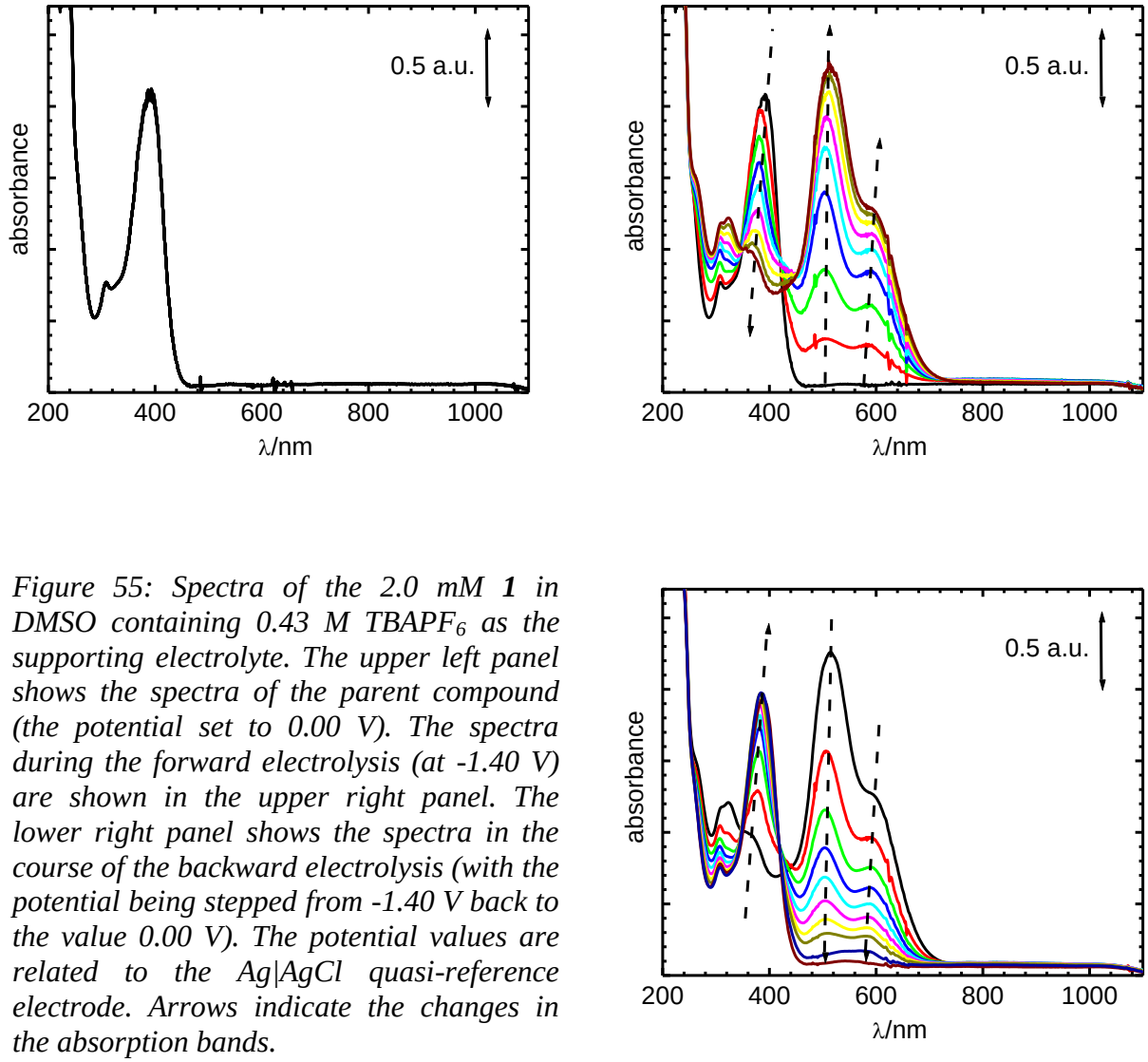

*Figure 55: Spectra of the 2.0 mM **1** in DMSO containing 0.43 M $TBAPF_6$ as the supporting electrolyte. The upper left panel shows the spectra of the parent compound (the potential set to 0.00 V). The spectra during the forward electrolysis (at -1.40 V) are shown in the upper right panel. The lower right panel shows the spectra in the course of the backward electrolysis (with the potential being stepped from -1.40 V back to the value 0.00 V). The potential values are related to the Ag|AgCl quasi-reference electrode. Arrows indicate the changes in the absorption bands.*

The upper left panel of Figure 55 shows the spectra of the parent form of **1**, with the potential being set to the capacitive region (0.00 V against Ag|AgCl quasi-reference electrode). The upper right panel shows the spectra during the forward electrolysis at the potential -1.40 V against Ag|AgCl quasi-reference electrode, where the fourth reduction step is diffusion-limited. The peak at 391 nm, characteristic for the parent compound, quickly decreases with a slight shift in the position of its maximum, while a new peak centered at 512 nm appears. This peak is characteristic for the fully reduced form, 1^{2-}. In the course of the backward electrolysis at 0.00 V vs. Ag|AgCl quasi-reference electrode, the peak at 512 nm decreases and, finally, completely disappears. The peak characteristic for the parent compound reappears at 391 nm, with its final height being nearly identical to that measured before the forward electrolysis. Therefore, the spectroscopic observations suggest the reversibility of the electron transfer.

The electrolysis may also be performed at potential values where the compound **1** accepts less than four electrons per one molecule. The charge consumption obtained at a given electrode potential allows the calculation of the number of accepted electrons. For instance, if the consumed charge equals to one quarter of the value obtained for the fully reduced species, then on the average one electron per one molecule is accepted. The consumed charge may also be related to that obtained for one-electron standards like ferrocene (Fc), cobaltocenium (Cc^{+}) or the first electron transfer of MV. The two approaches are equivalent.

If the solution of **1** has accepted one electron per molecule, the electron is transferred to the molecule by the reaction

$$1^{2+} + 1e^{-} \rightarrow 1^{1+} \tag{55}$$

The simply reduced form 1^{1+} may, in principle, participate in the homogenous reactions such as disproportionation

$$1^{1+} + 1^{1+} \varsigma 1^{2+} + 1^{0} \tag{56}$$

with the disproportionation constant defined as

$$K_{disp} = \frac{[1^{2+}][1^{0}]}{[1^{1+}]^{2}} \tag{57}$$

The disproportionation reaction regenerates the parent form 1^{2+} and also creates the doubly reduced species 1^{0}. According to the Nernst equation (Eq. 2), one can write

$$E = E_1^0 + \frac{RT}{n_1 F} \ln \frac{[1^{2+}]}{[1^{1+}]} \qquad E = E_2^0 + \frac{RT}{n_2 F} \ln \frac{[1^{1+}]}{[1^{0}]} \tag{58}$$

Analogous equations may also be written for the third and the fourth electron transfer. As shown above, $n_1 = n_2 = n_3 = n_4 = 1$. The homogenous reactions take place in the bulk of the

solution with the equilibrium constant being independent of the electrode potential. The right-hand sides of the Equation 58 are equal, provided that the homogenous reaction is in the state of chemical equilibrium and one can easily show that

$$K_{disp} = e^{F(E_2^0 - E_1^0)/RT} \tag{59}$$

Analogous relations may also be written for other disproportionation reactions. Table 3 shows the calculated equilibrium constants for all disproportionation reactions possibly encountered in the solution containing reduced forms of the compound **1**.

disproportionation	K_{disp} expression	K_{disp} value
$1^{1+} + 1^{1+} \varsigma 1^{2+} + 1^{0}$	$K_{(1,1,2,0)} = e^{F(E_2^0 - E_1^0)/RT}$	3.0×10^{-2}
$1^{0} + 1^{0} \varsigma 1^{1+} + 1^{1-}$	$K_{(0,0,1,-1)} = e^{F(E_3^0 - E_2^0)/RT}$	1.4×10^{-2}
$1^{0} + 1^{0} \varsigma 1^{2+} + 1^{2-}$	$K_{(0,0,2,-2)} = e^{F(E_3^0 + E_4^0 - E_1^0 - E_2^0)/RT}$	2.5×10^{-8}
$1^{1-} + 1^{1-} \varsigma 1^{0} + 1^{2-}$	$K_{(-1,-1,0,-2)} = e^{F(E_4^0 - E_3^0)/RT}$	4.3×10^{-3}

*Table 3: Possible disproportionation reactions between the forms of **1** (left column) and their equilibrium constants expressions (middle column) and values (right column).*

As the values of all equilibrium constants are significantly less than unity, the disproportionation reactions do not seem to affect the composition of the reaction mixture. Therefore, if the compound **1** is reduced by *n* electrons, the solution will mostly contain the 1^{2-n} form with negligible distribution of the other reduced forms.

This allows one to directly observe the spectra of the pure forms (1^{2+}, 1^{1+}, 1^{0}, 1^{1-} and 1^{2-}), depending on the electrode potential.

Figure 56 shows spectra during the electrolysis at -0.90 V, where the consumption of 1.3 electrons per molecule was found and the solution contains the forms 1^{1+} and 1^{0}. One may ask whether the two forms may react together by the homogenous reaction

$$1^{1+} + 1^{0} \varsigma 1^{2+} + 1^{1-} \tag{60}$$

The corresponding equilibrium constant is

$$K_{(2,-1,1,0)} = \frac{[1^{2+}][1^{1-}]}{[1^{1+}][1^{0}]} = \frac{[1^{2+}][1^{1-}][1^{0}][1^{1+}]}{[1^{1+}][1^{0}][1^{0}][1^{1+}]} = K_{(1,1,2,0)} \times K_{(1,-1,0,0)} = 4.2 \times 10^{-4} \tag{61}$$

Due to its very small value, the composition of the mixture $1^{1+}/1^{0}$ is not supposed to be influenced by the homogenous reaction. One can come to the same conclusion also for all other mixtures of the reduced forms.

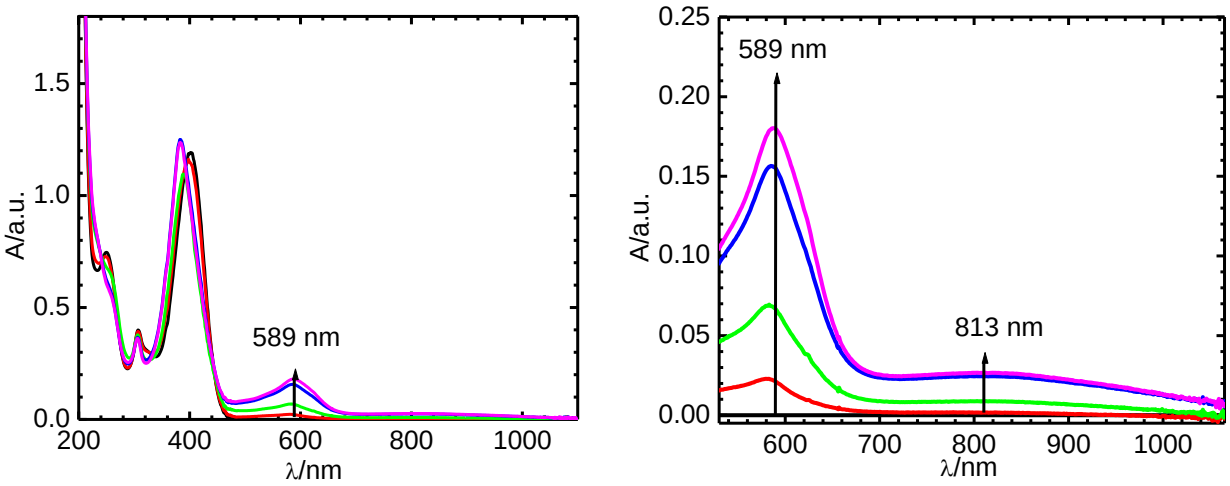

*Figure 56: Spectra of the 0.94 mM **1** in AN containing 0.43 M $TBAPF_6$ as the supporting electrolyte measured during electrolysis. Left panel shows the UV/VIS/NIR spectra during the reduction at -0.90 V vs. Ag|AgCl quasi-reference electrode. The electron consumption of 1.3 e^- per molecule of **1** was determined by the integration of the measured current transient. The right panel is the inset of the left panel, enlarging the NIR portion of the spectra. Black line denotes the spectrum of the parent compound.*

As shown in Figures 55 and 56, no absorption band was observed above 500 nm for the parent form 1^{2+}. On the other hand, all four reduced forms of **1** absorb light in the wavelength range 500 – 800 nm.

Figure 57 (left panel) shows the absorbance transients obtained at 900 nm during the potentiostatic electrolysis of **1** at various electrode potentials. The potential initially set to 0.00V vs. Ag|AgCl quasi-reference electrode was stepped to a respective potential, generating thus various reduced forms of **1**. Afterwards, the potential was stepped back to 0.00 V with reduced forms being re-oxidized.

The NIR band was detected for the forms 1^{1+}, 1^{0} and 1^{1-} (red, green and blue line). No NIR absorbance was observed for the fully reduced species 1^{2-} (purple line), Right panel of Figure 57 shows the absorbance at 900 nm as a function of the electron consumption.

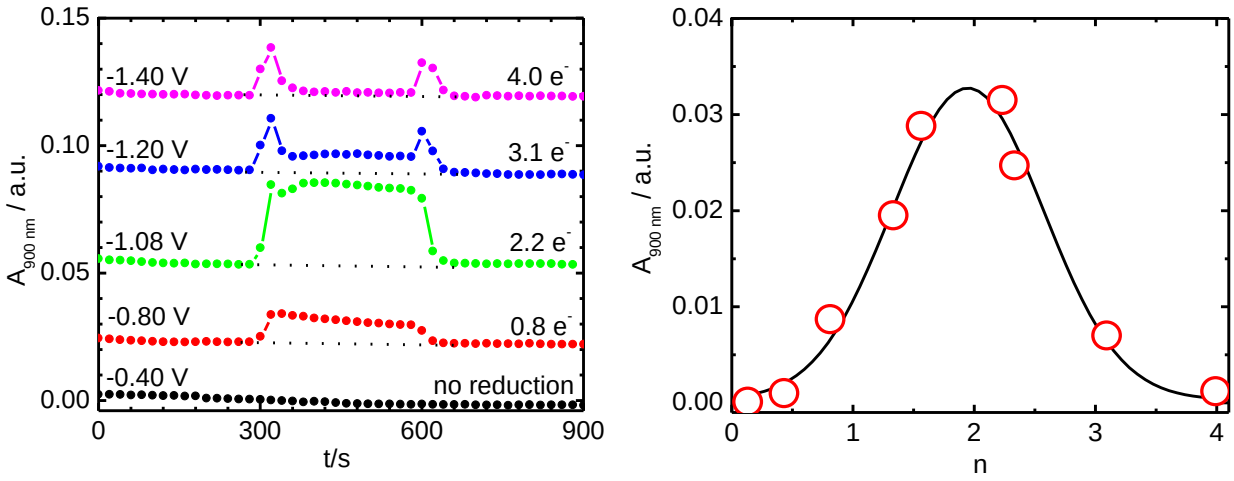

*Figure 57: Electrolysis with spectroscopic detection of 0.94 mM **1** in AN containing 0.43 M $TBAPF_6$ as the supporting electrolyte. Left panel: NIR absorbance transients (at 900nm) recorded during potentiostatic electrolysis at potential values: -0.40 V (black line), -0.80 V (red line), -1.08 V (green line), -1.20 V (blue line) and -1.40 V (purple line). The absorbance transients are vertically displaced for better visualization. The respective potential values were held at a time 300 s < t < 600 s, otherwise set to 0.00 V. The potential values are related to Ag|AgCl quasi-reference electrode. Right panel shows the steady-state NIR absorbance at 900 nm, measured at 550 s as a function of the electron consumption.*

One can ask why the NIR absorbance band emerges temporarily when the 1^{2-} form is generated (Figure 57, purple trace in the left panel). As mentioned above, the reaction

$$1^0 + 1^0 \varsigma 1^{2+} + 1^{2-} \qquad (62)$$

is not energetically favorable as its equilibrium constant, $K_{(0,0,2,-2)}$, has the value 2.5×10^{-8} (see Table 3). This suggests that the corresponding backward reaction

$$1^{2+} + 1^{2-} \varsigma 1^0 + 1^0 \qquad (63)$$

may proceed when both 1^{2+} and 1^{2-} forms are present. This situation is encountered at the onset of the electrochemical reduction of **1** at -1.40 V, where the form 1^{2-} is generated. The 1^{2-} form reacts with the parent compound, 1^{2+}, generating two NIR absorbing species 1^0. The NIR absorbance value quickly decreases in the course of electrolysis as the parent compound is being consumed and, moreover, the 1^0 form is further reduced, generating the non-absorbing form 1^{2-}. Similarly, the NIR absorbance band emerges also at the onset of electrochemical re-oxidation, where the reduced form 1^{2-} reacts with the regenerated parent form 1^{2+} temporarily creating the NIR absorbing form 1^0.

A similar effect was also observed during the electrolysis at -1.20 V with 3.1 electrons being consumed by one molecule. The form 1^{1-} comes into existence. The strongly NIR absorbing 1^0 form is temporarily generated by the reaction

$$1^{2+} + 1^{1-} \varsigma 1^{1+} + 1^0 \qquad (64)$$

and may explain an increased NIR absorbance at the onset of the forward electrolysis. The steady-state NIR absorbance value, however, does not completely fall to zero value as the 1^{1-} form absorbs NIR radiation itself. The same reaction takes place in the course of the backward electrolysis. The regenerated parent form reacts with the 1^{1-} form, forming the highly absorbing 1^{0} form, responsible for the second peak in the absorbance transient observable at the onset of the re-oxidation process.

The electron-transfer kinetics of the compound **1** was also studied by the aid of the electrochemical impedance spectroscopy. We focused on the kinetics of the electron transfer in the first reduction step. Figure 58 (left panel) shows the complex plane plot constructed from the frequency response of the electrochemical cell containing the compound **1** dissolved in AN with 0.1 M $TBAPF_6$ measured at various electrode potential values.

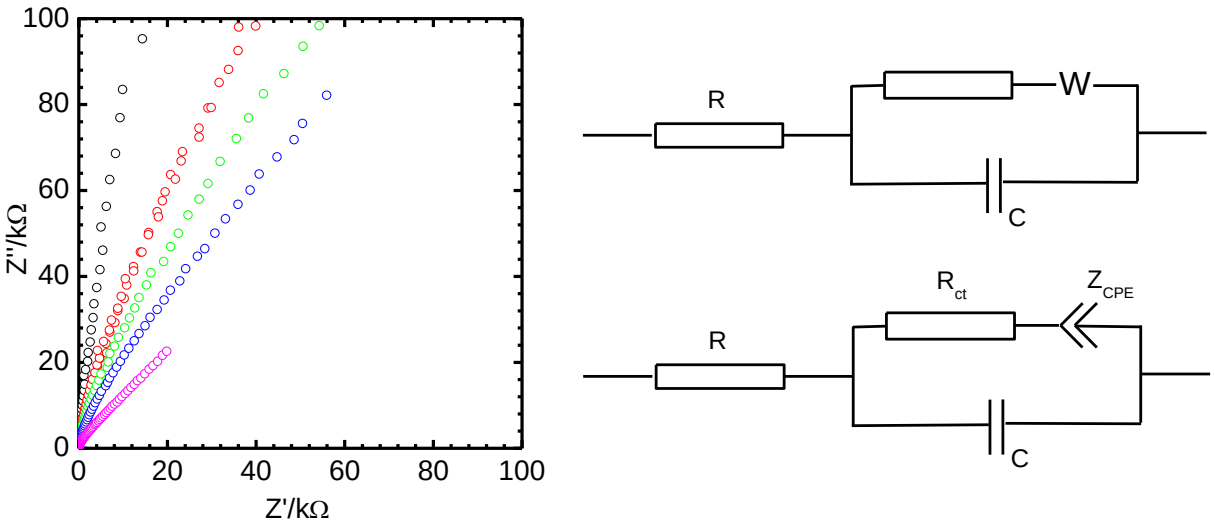

*Figure 58: Electrochemical impedance spectroscopy of 0.50 mM **1** in AN containing 0.1 M $TBAPF_6$ as the supporting electrolyte. Left panel: complex plane plot obtained at electrode potential values: -1.01 V (black line), -1.11 V (red line), -1.13 V (green line), -1.14 V (blue line) and -1.18 V (purple line). The potential values are referenced to the Fc/Fc^{+} couple. Right panel: original (upper scheme) and modified (lower scheme) Randles equivalent circuit.*

The black line shows the frequency response of the electrochemical cell with a potential value set to the capacitive region (-1.01 V vs. Fc/Fc^{+}). The line is slightly deflected from an ideal vertical direction. As the potential is stepped to more negative values, the lines become more slanted. The line making an angle 45° with both axes is obtained for potentials approaching the standard redox potential (-1.25 V).

The data were subjected to numerical fitting employing the Randles equivalent circuit. It is usually composed of four circuit elements – solution resistance, *R*, double-layer capacity, *C*, charge-transfer resistance, R_{ct}, and Warburg impedance, Z_w [165]. More generally, one may take the constant-phase element (CPE) instead of Warburg impedance, defined as

$$Z_{CPE} = |Z_{CPE}| \frac{1}{\omega^n} e^{-j\frac{\pi}{2}n} \tag{65}$$

with $\omega = 2\pi f$ and $0 \leq n \leq 1$. If one takes $n = ½$, then $e^{-j\pi/4}$ is according to the Euler's formula equal to $(1-j)/2^{1/2}$, and the constant-phase element reduces to Warburg element, $Z_{CPE} = Z_W$. The constant-phase element may be used when some non-idealities are observed in the frequency range, where the electrochemical reaction is diffusion-limited. In all numerical fittings performed within this thesis, the Warburg impedance has been replaced by the constant-phase element. The value of *n* was left to be varied by the fitting procedure, with typical values $0.49 < n < 0.51$. It should be mentioned that the constant-phase element may also replace a resistor taking the value n = 0 or a capacitor with n = 1 in the equivalent circuit. Figure 58 (right panel) shows the original (upper scheme) and modified (lower scheme) Randles equivalent circuit, the latter one being employed in the numerical fitting procedure. The R_{ct} values were extracted for all potential values investigated.

The forward heterogenous rate constant k_f is given by [123]

$$k_f = k_0 e^{-\alpha F(E-E_1^0)/RT} = \frac{RT}{F^2 R_{ct}(E) A c} \tag{66}$$

where k_0 is the standard heterogenous rate constant, $k_0 = k_f$ for $E = E_1^0$ and $R_{ct}(E)$ is R_{ct} at a selected *E* value. Charge-transfer coefficient α depends on the shape of the energy barrier of the redox process. *A* and *c* stand for the electrode area and bulk concentration of the electroactive species, respectively. All other variables have the standard meaning. From Eq. 66 one can easily show that

$$\ln \frac{1}{R_{ct}} = \ln \frac{1}{R_{ct}(E_1^0)} - \alpha F(E - E_1^0)/RT \tag{67}$$

where $R_{ct}(E_1^0)$ is R_{ct} at E_1^0. Figure 59 shows the values $\ln(1/R_{ct})$ as a function of the electrode potential. The plot shows the data for electrode potential less negative than the standard electrode potential E_1^0. The potential values more negative than E_1^0 could not be scrutinized as the second elecron transfer (with E_2^0 = -1.37 V) becomes significant and would complicate the analysis of data. The dependence $\ln(1/R_{ct})$ vs. *E* is linear and allowed the evaluation of the $R_{ct}(E_1^0)$ value. The right-hand side of the Equation 66 was employed to turn the $R_{ct}(E_1^0)$ value to k_0. The obtained value k_0 = 10 cm.s^{-1} suggests the very facile electron transfer process.

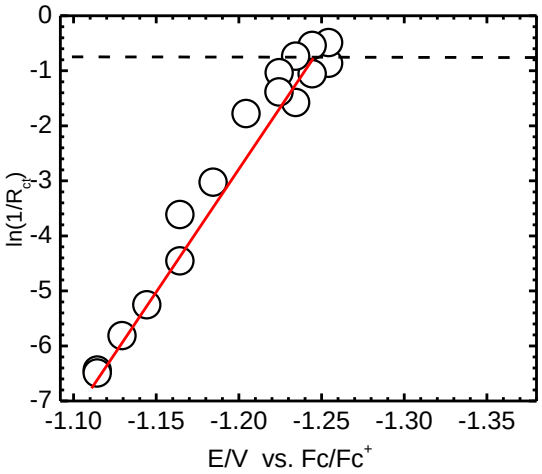

*Figure 59: The dependence of ln(1/R_{ct}) on the electrode potential for 0.50 mM **1** in AN, containing 0.1 M $TBAPF_6$ as the supporting electrolyte.*

The compounds **1** to **6** are intended to serve as passive circuit elements in the devices of molecular electronics. Circuit elements will need to be adsorbed at an interface in a well defined manner. When non-polar surfaces such as HOPG or metallic electrodes are used as the substrate, the adsorption of non-polar molecules is more pronounced in polar solvents or solvent mixtures. Therefore, we investigated the electrochemical behavior of the compound **1** not only in a pure DMSO, but also in water:DMSO mixtures with varying content of water. Figure 60 shows cyclic voltammograms of the compound **1** in various water:DMSO mixtures containing 0.1 M $TBAPF_6$ as the supporting electrolyte.

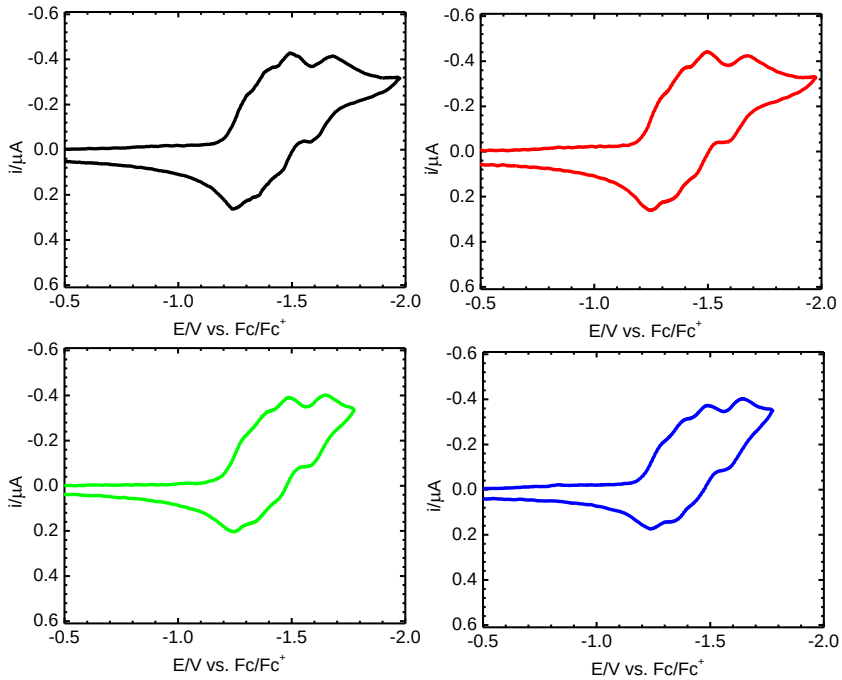

*Figure 60: Cyclic voltammograms of 0.1 M $TBAPF_6$ and 1.0 mM **1** in pure DMSO (black line) and a water:DMSO mixture containing 2% (red line), 9% (green line) and 12% (blue line) of water (v/v). Scan-rate 0.125 V/s. Pt was used as the working electrode.*

Apparently, the presence of water has no impact on the electrochemical behavior of the compound **1**. All four reduction waves remain reversible. The accessible potential window slightly narrows in the presence of water. This is caused by the reduction of H^+ ions. The electrochemical behavior in the mixture with high water content (green and blue lines) was investigated only in the potential range in which hydrogen was not evolved. Slight decrease in the observed faradaic current with respect to that measured in pure DMSO may be assigned to an increase in the solvent dynamic viscosity value upon the addition of water.

The electrochemical properties of the compound **2** were also studied both in AN and DMSO. The compound **2** is prone to strong adsorption in AN and as in the case of **1**, most of the electrochemical experiments were performed in DMSO. Figure 61 shows the cyclic voltammogram and sampled DC polarogram of the compound **2**.

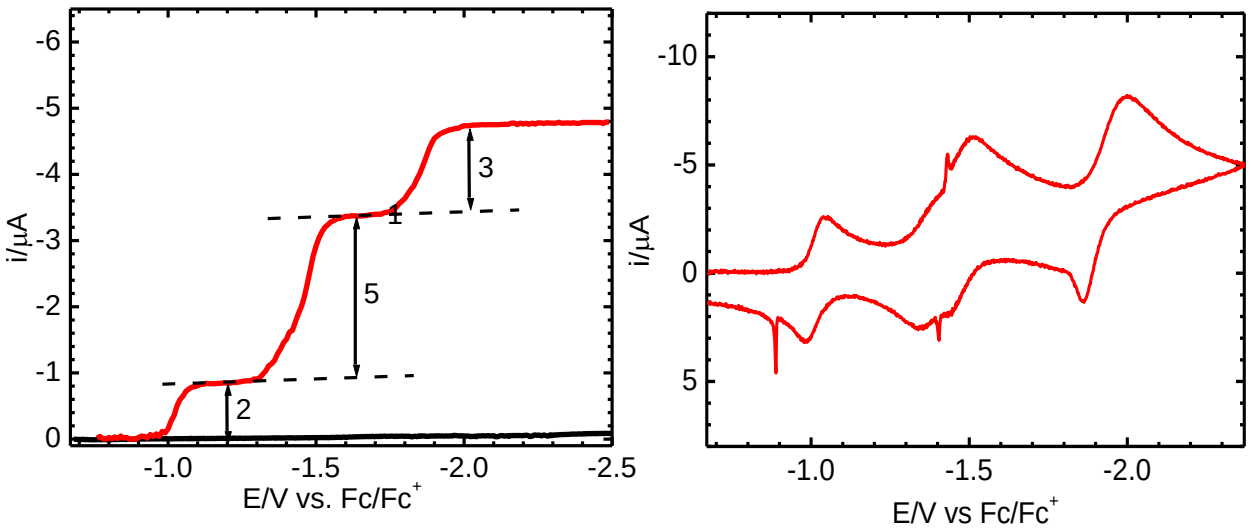

*Figure 61: Sampled DC polarogram (left panel) and cyclic voltammogram (right panel) of 1.0 mM **2** in DMSO containing 0.1 M $TBAPF_6$ as the supporting electrolyte. Left panel: drop-time 3 s, measured on SMDE, right panel: scan-rate 0.25 V/s, measured on HMDE. Black line (left panel) is measured in the absence of **2**.*

Three reduction steps (at -1.02 V, -1.43 V and -1.86 V) may be discerned in both cyclic voltammogram and sampled DC polarogram. The sampled DC polarography allowed the electron consumption to be determined. Two, five and three electrons are transferred in the three successive reduction steps. As the compound **2** is initially a tetracation (i.e. 2^{4+}), the forms 2^{2+}, 2^{3-} and 2^{6-} come in the existence in the respective reduction steps. The electron consumption was determined by comparing the wave heights to that measured for MV at the same concentration. The consumption was confirmed by exhaustive bulk electrolysis at

potential values, at which the respective reduction steps are diffusion-limited. The electron consumption of the compound **2** was also scrutinized by electrolysis employing OTTLE as the working electrode. For all three reduction waves, the determined electron consumption was identical to that found by sampled DC polarography and bulk electrolysis.

AC polarography with SMDE as the working electrode was also employed to study the electrochemical behavior of the compound **2**. Figure 62 shows the AC polarogram of **2** obtained in DMSO containing 0.1 M $TBAPF_6$ as the supporting electrolyte. Though the shape of the waves is somewhat different from an ideal profile, all three overall processes are clearly discerned. The non-ideal shape with peak splittings indicates the adsorption of the molecules on the electrode surface.

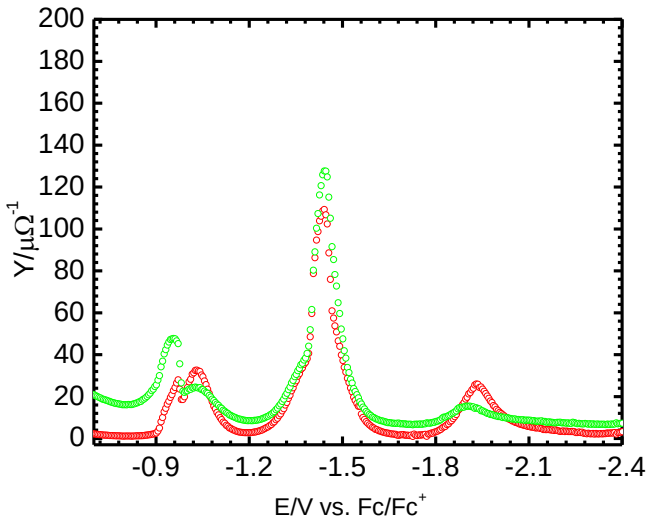

*Figure 62: AC polarogram of **2**. Real part (red line) and imaginary part (green line) of the cell admittance obtained for 0.4 mM **2** in DMSO containing 0.1 M $TBAPF_6$ as the supporting electrolyte. AC frequency 16 Hz, AC amplitude 5mV, drop-time 2 s.*

The electrochemical reversibility of the first reduction wave was scrutinized by cyclic voltammetry, showing a linear dependence of both cathodic and anodic peak currents vs. $v^{1/2}$ (Figure 63, left panel). At all scan-rates, the ratio of anodic and cathodic current peaks approaches unity, which confirms the reversibility of the electron transfer. As the compound **2** accepts two electrons in the first reduction step, one can anticipate that the separation of the anodic and cathodic peak currents in CV will be 59/2 = 29.5 mV. Instead, the value 51 ± 3 mV was found. This value was further found to be independent of the solvent used (DMSO and AN were employed), electrode material (HMDE, platinum), bulk concentration of the compound **2**, concentration of the supporting electrolyte and scan-rate (Figure 63, right panel).

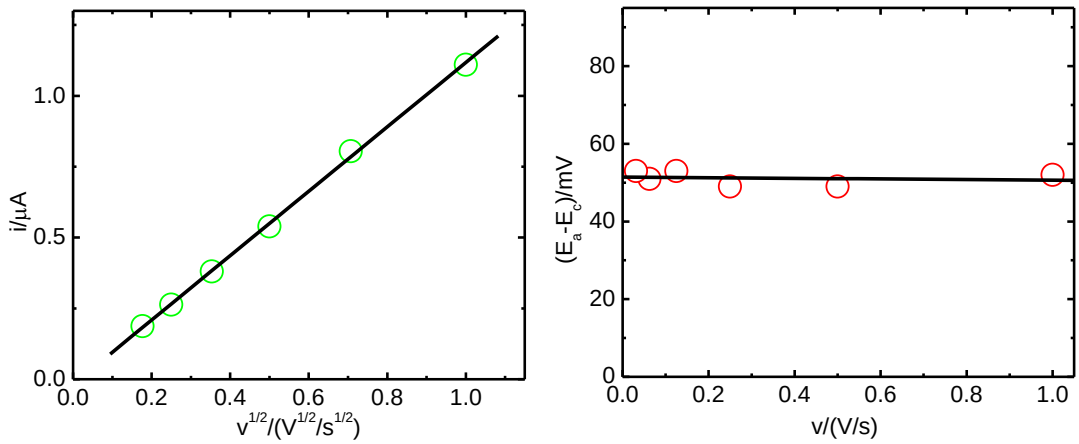

*Figure 63: Cyclic voltammetry of 1.0 mM **2** in DMSO containing 0.43 M TBAPF$_6$ as the supporting electrolyte. The dependence of cathodic peak current (left panel) and cathodic/anodic peak separation (right panel) in the first reduction wave on the scan-rate is shown. Measured on Pt electrode, the both panels show the results for the first (two-electron) reduction process.*

As the peak separation is independent of the scan-rate and bulk concentration of **2**, its increased value cannot be explained by a quasi-reversible nature of the electron transfer or an uncompensated solution resistance. The peak separation remained within the range 51 ± 3 mV even for the slow scan-rate value 30 mV/s and considerably increased supporting electrolyte concentration (0.43 M TBAPF$_6$). This suggests that the acceptance of the two electrons takes place independently. The two electron wave in CV behaves as the sum of two individual waves, each one originating from the electron transfer of one electron to a different part of the molecule of **2**. The log-plot analysis of the sampled DC polarogram at potential values pertaining to the first reduction step also confirmed this observation. Though the slope (52.3 mV) indicates the consumption of 1.13 electrons, the wave height clearly suggests a two-electron process. This confirms that the electrons are transferred independently.

The reversibility of the electron transfer in the compound **2** was confirmed by spectroelectrochemical measurements. Figure 64 shows the in-situ UV/VIS/NIR spectra obtained during the electrolysis of the compound **2** at the potential value where the first i.e. two-electron reduction process is diffusion-limited (red line). The charge consumed in the electrolysis was found to be two times higher than that obtained in the electrolysis of MV at a potential, at which its first reduction process is diffusion-limited. This further confirms the consumption of two electrons in the first reduction wave. The spectrum obtained after the backward electrolysis (re-oxidation, green line) is nearly identical to that obtained for the parent compound (prior to electrolysis, black line). This confirms the chemical reversibility of the electron transfer in the first reduction wave of the compound **2**.

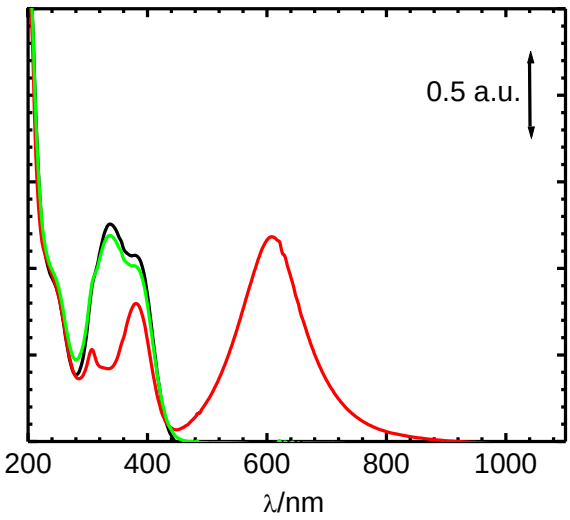

*Figure 64: In-situ spectra of the 1.0 mM **2** in AN containing 0.43 M $TBAPF_6$ as the supporting electrolyte measured prior to the electrolysis (at 0.00 V, black line), at -0.62 V (after forward electrolysis, red line) and at 0.00 V (after backward electrolysis, green line). The potential values are related to Ag|AgCl quasi-reference electrode.*

The electrochemical properties of molecular wires composed of three to six repetitive units (i.e. the compounds **3**, **4**, **5** and **6**) were investigated in DMSO. They share a common electrochemical behavior being considerably different from that of the compounds **1** and **2**. Figure 65 shows the first reduction potential of the compounds **1** to **6** as a function of the number of repetitive units in the molecule. The compounds **1** and **2** have the first reduction potential value at -1.28 V and -1.02 V, respectively, while the value -1.00 V was found for the compounds **3** to **6**.

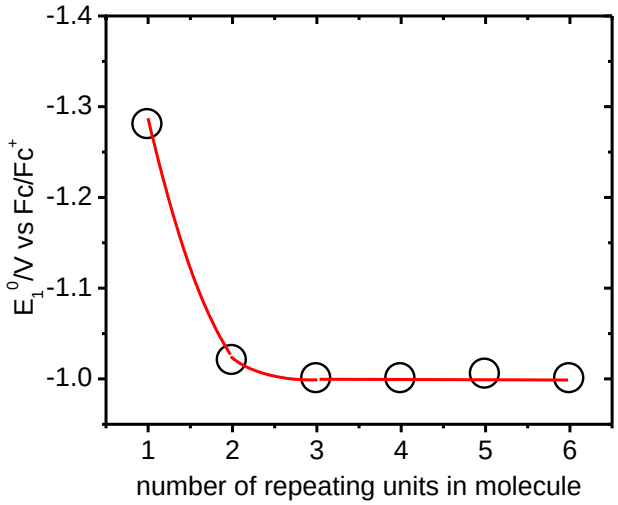

*Figure 65: The first reduction potential of the compounds **1** to **6** as a function of the number of extended viologen subunits in the molecule. The potential values are referenced to the redox potential of Fc/Fc^+ couple. Measured in DMSO containing 0.1 M $TBAPF_6$ as the supporting electrolyte.*

Figure 66 shows the sampled DC polarograms of all the compounds **1** to **6**.

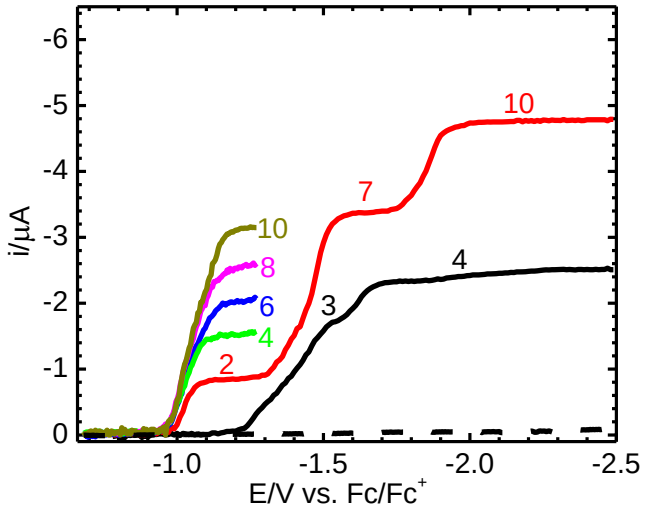

*Figure 66: Sampled DC polarogram of 1.0 mM **1** (black line), **2** (red line), **3** (green line), **4** (blue line), **5** (purple line) and **6** (gold line) in DMSO containing 0.1 M $TBAPF_6$ as the supporting electrolyte. Drop-time was set to 3s. Dashed line is measured in the absence of compounds. The numbers denote the total electron consumption.*

The numbers next to the polarographic waves denote the electron consumption in the respective reduction steps as found by sampled DC polarography and bulk electrolysis. In some cases, these numbers were also confirmed by electrolysis employing OTTLE as the working electrode. One may ask why the two ten-electron waves (for the compound **2** - red line and for the compound **6** - gold line) are not of equal height. The relative height measurements may only be applied for compounds having similar diffusion coefficient values. As the molecules of the compounds **2** and **6** have significantly different molar masses (1992 g/mol and 5638 g/mol), their diffusion coefficient values are different. In sampled DC polarography, the height of the wave depends not only on the electron consumption, but also on the diffusion coefficient value. The wave heights of compounds with strongly differing molar masses cannot be, therefore, compared directly.

For the compounds **3** to **6**, common features in the electrochemical behavior may be noticed. The electron consumption in the first reduction step scales nicely with the number of repeating units in the molecule. The molecule containing *n* repeating units accepts *2(n-1)* electrons (with $3 \leq n \leq 6$). The first reduction wave actually comprises two steps, discerned by cyclic voltammetry. The cyclic voltammograms of the compounds **3** to **6** are shown in Figure 67. For all compounds, two voltammetric peaks appear. The first reduction potential, E_1^0, plotted in the Figure 65, refers to the standard redox potential value of the first reduction process being merged with the second one in the sampled DC polarogram.

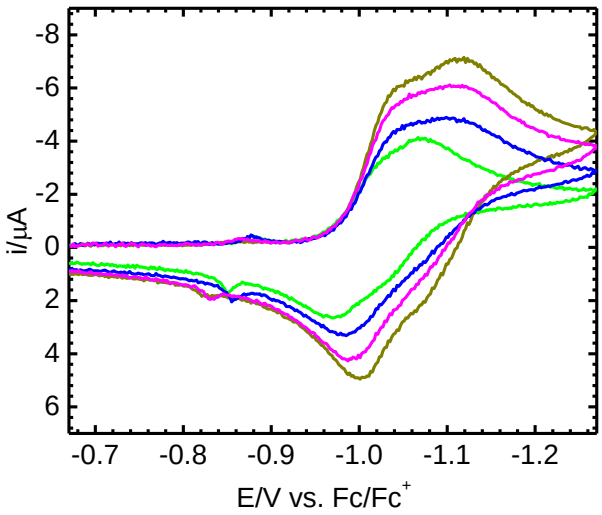

*Figure 67: Cyclic voltammogram of 1.0 mM **3** (green line), **4** (blue line), **5** (purple line) and **6** (gold line) in DMSO containing 0.1 M $TBAPF_6$ as the supporting electrolyte. Scan-rate 0.25 V/s. HMDE was used as the working electrode.*

The separation of two processes was also confirmed by the log-plot analysis. Figure 68 shows the results for compounds **4** and **6** performed at potentials pertaining to the merged wave.

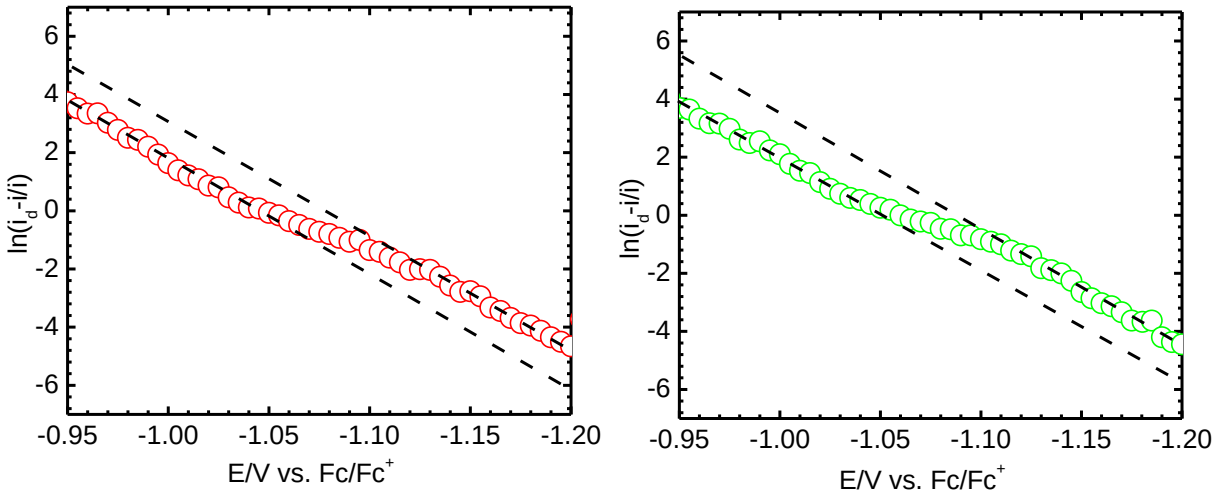

*Figure 68: Log-plot analysis of the merged reduction process of the compounds **4** (left panel) and **6** (right panel). Measured in DMSO containing 0.1 M $TBAPF_6$ as the supporting electrolyte. Bulk concentration of the compounds is 1.0 mM.*

As mentioned above, sampled DC polarography and bulk electrolysis confirmed the consumption of 4, 6, 8 and 10 electrons in the merged reduction wave of the compounds **3**, **4**, **5** and **6**, respectively. For all compounds, the merged wave consists of two reduction processes, being separated in cyclic voltammograms as well as in the log-plots. For all four compounds, the slopes in the log-plot analysis, however, clearly indicate the apparent consumption of one electron (in each of the two processes). For instance, the compound **6** (its log-plot is plotted in the right panel of Figure 68), shows two slopes with the corresponding

apparent electron consumption 0.98 and 1.02 in the two reduction processes. As the polarographic wave height and bulk electrolysis results suggest the overall consumption of ten electrons, the electrons are transferred separately, five in each step. The same conclusions may be drawn for the compounds **3**, **4** and **5**.

In the voltammograms of the compounds **3** to **6** (Figure 67), one may find sharp peaks roughly at -0.85 V, being of a tensammetric nature. The compounds are all cations and adsorb at the mercury electrode at potentials more negative than -0.85 V against Fc/Fc^{+}. The tensammetric peaks were also observed for the compounds **1** and **2** (see Figures 51 and 61).

Figure 69 shows the cyclic voltammograms of all studied extended viologens - compounds **1** to **6**, in the entire accessible potential window of 0.1 M $TBAPF_6$ in DMSO employing HMDE electrode.

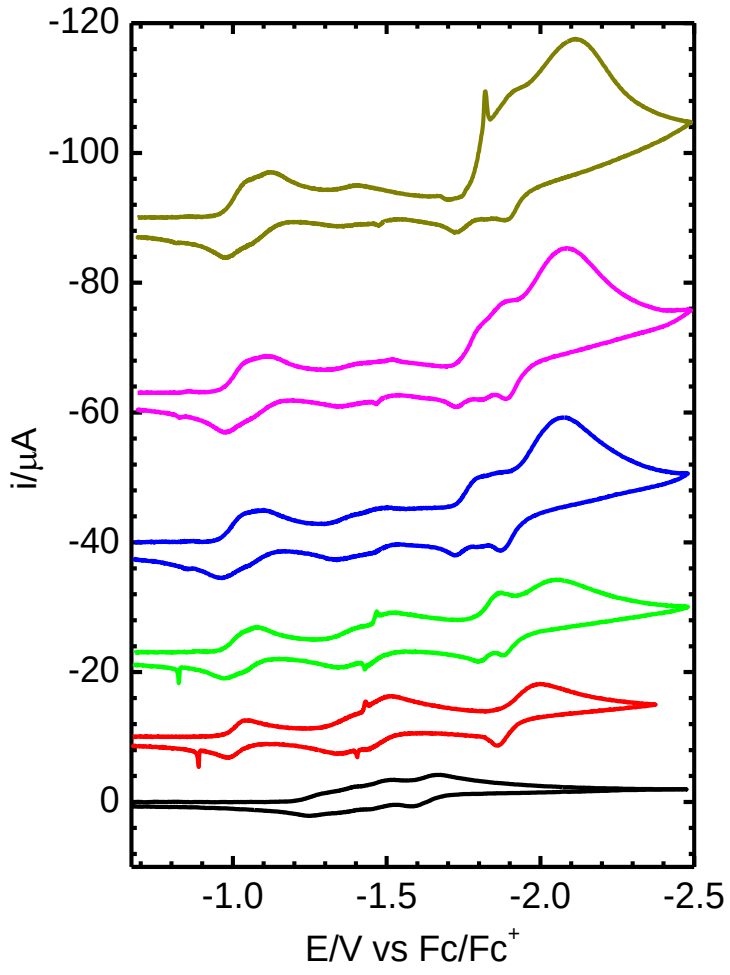

*Figure 69: Cyclic voltammogram of 1.0 mM **1** (black line), **2** (red line), **3** (green line), **4** (blue line), **5** (purple line) and **6** (gold line) in DMSO containing 0.1 M $TBAPF_6$ as the supporting electrolyte. Scan-rate 0.25 V/s. HMDE was used as the working electrode. The voltammograms are vertically shifted for better visualization.*

4.4 Spectroelectrochemical determination of the electron consumption

The number of electrons, *n*, exchanged in an electrochemical process is one of the most important properties of species being potentially used as a redox mediator, in medicine, catalysis and industry. Various electrochemical methods can determine the electron consumption - classical and sampled DC polarography [123,126,127,129,130,133,134], cyclic voltammetry [123,135,136,166], methods employing rotating disc electrodes [123,167] and ultramicroelectrodes [123,168]. Malachesky's method is based on the combination of cyclic voltammetry and chronoamperometry [169,206]. These methods are, however, applicable only to reversible electrochemical systems [123]. Moreover, CV needs the electrode area and the diffusion coefficient of the species to be known [123,135,136]. Most reliable method is coulometry combined with the constant potential bulk electrolysis [123,170]. This method does not require the diffusion coefficient and electrode area to be known. However, the method is rather time consuming and needs considerable amount of substance to be spent in experiments. Moreover, large time scales increase the risk of homogenous reactions with atmospheric oxygen and water possibly penetrating into the electrochemical cell. Time scales along with the consumption of the investigated species may be significantly reduced by using an optically transparent thin layer electrode (OTTLE) cell [137,138,171]. Unlike the stirred bulk electrolysis, the mass transport to the electrode is driven exclusively by the diffusion. The transparent slides confine the space (of a volume *V*) around the working electrode and allow the reaction extend to be investigated by the spectroscopic techniques. If the parent species with the extinction coefficient ε_0 is initially present in the solution at concentration *c*, the initial cell absorbance is $A_0 = l\ c\ \varepsilon_0$, provided that the solvent and the electrolyte do not absorb radiation at the wavelength of interest. The optical path length of the cell, *l*, may be determined by the calibration, employing a standard of known extinction coefficient. In our case, ferrocene was used as the standard yielding the value $l = 0.19$ mm. The value A_0 may be obtained at a potential value at which no faradaic process occurs.

As the working electrode is of considerable area, high concentrations of a supporting electrolyte should be employed to suppress the IR drop. In all experiments employing OTTLE cell for the electrolysis DMSO containing 0.43 M $TBAPF_6$ was used.

In the course of the electrochemical process triggered by stepping the potential to a value where it takes place, a product with the extinction coefficient ε is generated at the electrode. If the conversion of the reaction is denoted as α, then the overall absorbance is given by

$$A = c(1-\alpha)l\varepsilon_0 + c\alpha l\varepsilon \tag{68}$$

The value of ε may be easily obtained at $t \rightarrow \infty$, at which the entire amount of the parent form is converted to the product, with $\alpha = 1$ and $A = A_\infty = c\ l\ \varepsilon$. The reaction conversion is then given by

$$\alpha = \frac{A - A_0}{A_\infty - A_0} \tag{69}$$

The electric charge, Q, consumed in the electrochemical process is at any time obtained by the integration of current transients. This charge is, according to the Faraday's law, proportional to the number of moles of electrochemically altered species. Therefore, Q increases with the conversion of the reaction, $Q = \alpha cVnF$. The conversion value is related to the measured charge by $\alpha = Q/Q_\infty$ with $Q_\infty = cVnF$ being the charge consumption for $\alpha = 1$. One may easily show that

$$Q = Q_\infty\left(1 - \frac{A_\infty - A}{A_\infty - A_0}\right) \tag{70}$$

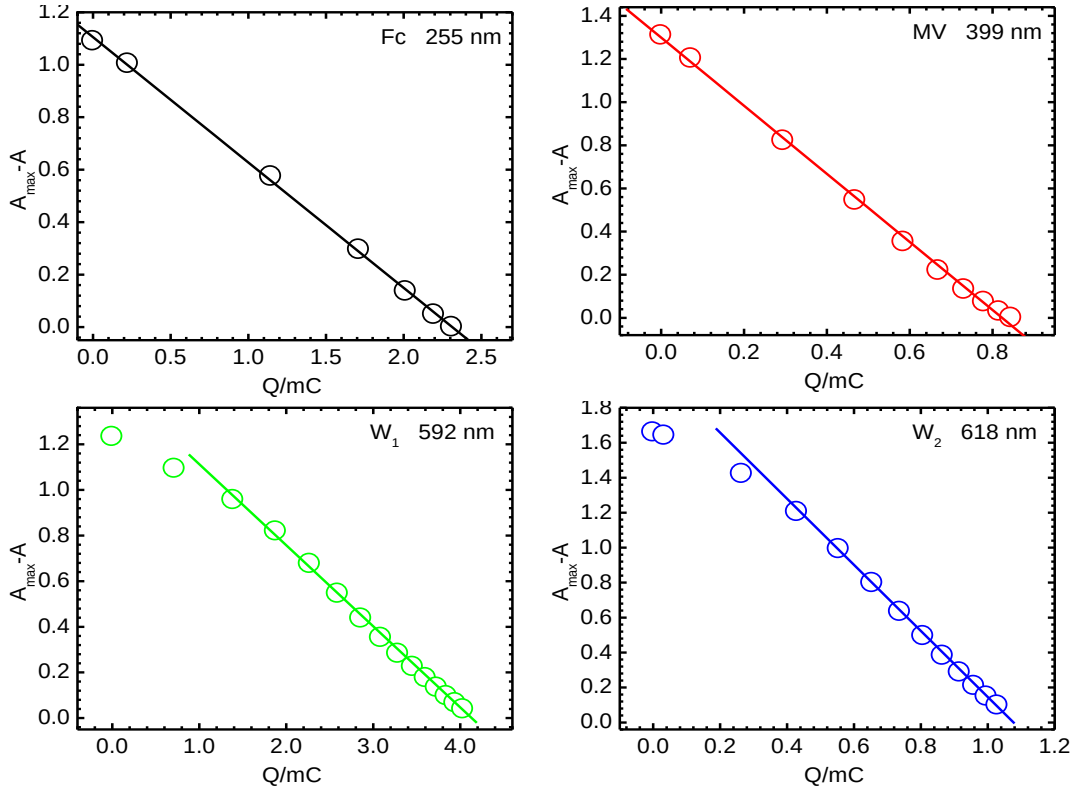

*Figure 70: The A_∞-A vs. Q plots for 4.51 mM ferrocene (black line, measured at 255 nm), 1.83 mM methyl viologen (red line, 399 nm, first reduction wave), 2.04 mM **1** (green line, 592 nm, fourth reduction wave) and 1.03 mM **2** (blue line, 618 nm, first reduction wave). Measured in DMSO containing 0.43 M $TBAPF_6$.*

If one plots Q vs. A_∞ - A, the value of Q_∞ can easily be obtained as the intercept (with $\alpha = 1$ and $A = A_\infty$). The consumed charge is proportional to the number of accepted electrons, bulk concentration of the species and the reaction volume. The latter quantity is unknown and, therefore, a standard has to be employed to determine it.

Figure 70 shows the plots of A_∞ - A, vs. Q. The Q_∞ value was determined as the intercept on the x-axis. The measurements were carried out for both standards - ferrocene (Fc) and methyl viologen (MV) and investigated species - the compounds **1** and **2**.

Slight deviations at the start of the measurements may either be caused by the adsorption processes, double-layer charging or hindrance offects. The deviations have probably not a significant effect on the results of the analysis as the overall time of electrolysis is much higher than that during which they are observed.

Table 4 brings the results of the all four measurements shown in the Figure 70.

Compound	Q_∞/mC	c/mM	$(Q_\infty/c)/(C/M)$	n
ferrocene	2.25	4.51	0.492	1
methyl viologen	0.88	1.83	0.481	1
1 (4^{th} reduction)	4.04	2.04	1.98	4.07
2 (1^{st} reduction)	1.05	1.03	1.02	2.09

Table 4: The determination of electron consumption from the intercept Q_∞ in A_∞-A vs. Q plot. The electron consumption of methyl viologen (first reduction wave) and ferrocene standards is set to n_{st}=1.

The fraction Q_∞/c is proportional to the electron consumption, $Q_\infty/c = nVF$, with the proportionality constant involving the effective cell volume, V. Its value may be determined by using a standard or more conveniently, the electron consumption may be calculated as the ratio of the fractions Q_∞/c determined for investigated species and the standard, $n = n_{st} (Q_\infty/c) / (Q_{\infty,st}/c_{st})$. The two procedures are mathematically equivalent and the latter one has been employed in this thesis.

The fraction Q_∞/c has almost the same value for Fc and MV (fourth column of Table 4). The compound **1** was found to consume four electrons in its fourth reduction step, whereas the compound **2** accepts two electrons in the first reduction step. The results are in full agreement with those obtained by conventional electrochemical techniques (sampled DC polarography, cyclic voltammetry and bulk electrolysis). The experiments with OTTLE were repeated

several times for both standards and investigated compounds, at various bulk concentrations. The values of the fractions Q_∞/c were found to be independent of the c value as long as c > 0.5 mM. For lower concentrations, Q_∞/c values deviated from those obtained at higher concentrations. This may be attributed to a large contribution of a capacitive charge, being significant for small bulk concentrations of electroactive species. Figure 71 shows the results of measurements of capacitive charges i.e. the charge consumed in the absence of electroactive species in the bulk of the solution at various potential values. For most investigated values of the electrode potential the charge did not exceed the value ± 0.20 mC. Therefore, the experiments should employ the bulk concentrations of electroactive species leading to the integrated charges at least on the orders of millicoulombs. Under these conditions, the contribution stemming from the double-layer charging may be neglected or properly corrected.

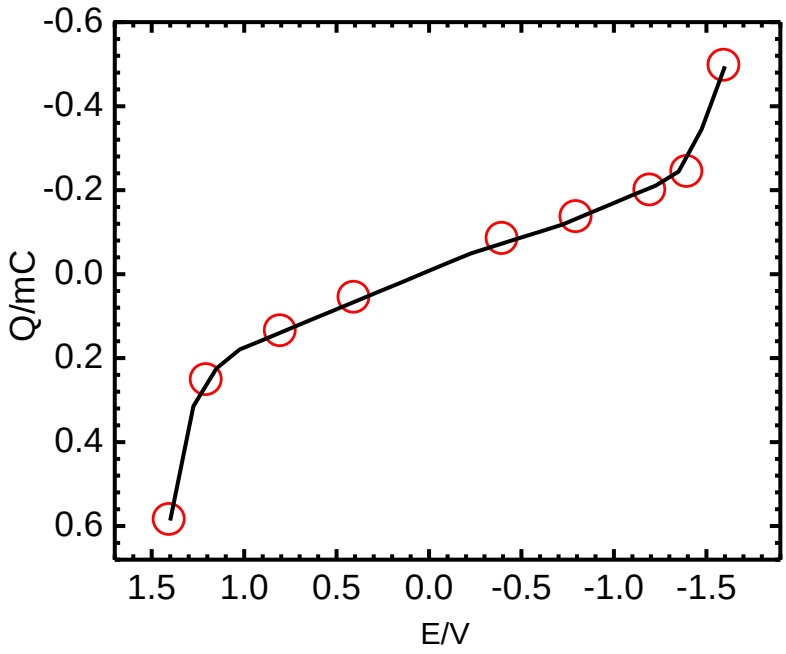

Figure 71: Capacitive charge in DMSO containing 0.43 M $TBAPF_6$ as a function of the electrode potential. The potential was stepped to a desired value from 0.00 V. Measured at the very same conditions as in the presence of electroactive species. Black curve is shown just to guide the eye. The values are obtained by integrating the current transients.

Table 5 summarizes the results of all measurements for both standards and investigated species. All measurements were repeatedly pursued at various bulk concentrations.

Compound	$(Q_\infty/c) / (C/M)$	*n*
Methyl viologen (1st reduction)	0.484 ± 0.010	1.00
Ferrocene	0.486 ±0.020	1.00
1 (1st reduction)	0.52 ± 0.04	1.07 ± 0.09
1 (2nd reduction)	0.99 ± 0.06	2.04 ± 0.13
1 (3rd reduction)	1.41 ± 0.10	2.94 ± 0.22
1 (4th reduction)	1.93 ± 0.11	3.99 ± 0.24
2 (1st reduction)	1.00 ± 0.07	2.06 ± 0.15
2 (2nd reduction)	3.24 ± 0.16	6.75 ± 0.36
2 (3rd reduction)	4.93 ± 0.22	10.19 ± 0.50

Table 5: The determination of the electron consumption from the intercept Q_∞ in A_∞-A vs. Q plot. The values shown here are the average results from all experiments performed.

As shown in Table 5, the electron consumption may be determined for various reduction steps of the compounds. The compound **1** has four slightly separated one-electron reduction steps. Its electrochemical behavior was investigated by cyclic voltammetry, sampled DC polarography, AC polarography and bulk electrolysis as described in previous chapters. The consumption of four electrons was also confirmed by the electrolysis employing OTTLE. The compound **2** shows three well-separated reduction waves consuming two, five and three electrons, respectively. The numbers were determined by sampled DC polarography and bulk electrolysis. The electrolysis employing OTTLE confirmed the consumption of two, seven (two + five) and ten (two + five + three) electrons in the three reduction steps, respectively.

The electrolysis with OTTLE offers one great advantage over the other electrochemical techniques. The simultaneous spectroscopic detection allows possible homogenous follow-up reactions to be discerned. After the complete electrolysis, the potential may be stepped back into the capacitive region in order to investigate the behavior of electrogenerated products. If the backward integrated charge matches its forward counterpart and the spectrum of a back-electrolyzed solution is identical to that obtained for the parent species, no irreversible homogenous reactions take place. On the other hand, if the final spectrum after the backward electrolysis is different from that obtained for the parent compound, the homogenous reactions irreversibly change the chemical composition of the system. This may help to reveal possible decomposition reactions as well as to detect the presence of impurities in the solvent/electrolyte used. This may lead to misleading electron consumption. The method

based on the spectroscopic observations, however, suffers from a considerable drawback. It is applicable only for species having both ε_0 and ε values sufficiently high. The optical path length of the spectroelectrochemical cell is only on the orders of 100 μm. This may be insufficient for weakly-absorbing species. Therefore, we also developed a technique which does not require the spectroscopic detection. This procedure has only a limited possibility to detect follow-up and side reactions. It is based on the determination of integrated electric charges at various bulk concentrations of electroactive species. The double-layer capacity is assumed to be independent of the bulk concentration of the species of interest. This is satisfied for non-adsorbing species and for the species forming a monolayer on the electrode. The overall electric charge is given by the sum of capacitive and faradaic components, the latter one being proportional to the bulk concentration. The electron consumption is determined from the slope dQ_∞/dc rather than from the fraction Q_∞/c itself. The slope reflects the faradaic process, while the capacitive contribution is responsible for the presence of an intercept in the Q_∞ vs. c plot. As the spectroscopic detection is not performed, the state of the complete electrolysis has to be discerned from the current transients. The current value, however, never completely falls to zero value as some amount of the parent species may diffuse to the space of the working electrode from the surroundings. This causes an additional faradaic current, which cannot be considered in the data analysis. To avoid inconveniences, the electrolysis is usually stopped at a time, for which the electric current value falls to $1 - \alpha = 5$ % of its initial value (i.e. having $Q/Q_\infty = 0.95$). If this procedure is accomplished for both investigated species and standards, the error stemming from an incomplete electrolysis may largely be eliminated. The method still retains a possibility to detect erroneous experiments – the forward and backward integrated charges may be compared. Their equality suggests the absence of irreversible follow-up reactions.

Figure 72 shows typical current transients measured in the double potential step experiment. The transients are recorded for 2.04 mM **1** at the potentials corresponding to the first (black line), second (red line), third (green line) and fourth (blue line) reduction step, respectively.

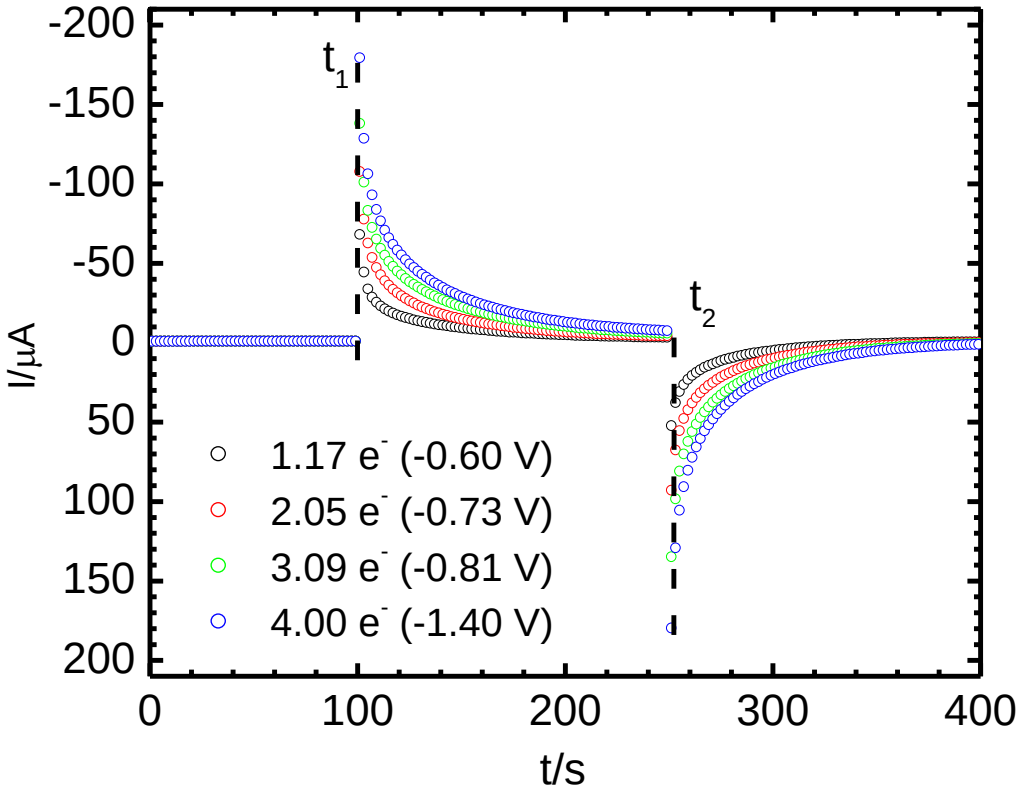

*Figure 72: Current transients obtained for 2.04 mM **1** at -0.60 V (black line), -0.73 V (red line), -0.81 V (green line) and -1.40 V (blue line). Measured in DMSO containing 0.43 M $TBAPF_6$ as the supporting electrolyte. The potentials are related to Ag|AgCl quasi-reference electrode.*

For $t < t_1$ (t_1 = 100 s), the electrode potential was set to the value 0.00 V vs. Ag|AgCl quasi-reference electrode. For $t_1 < t < t_2$ (t_2 = 250 s), the potential was stepped to a value, at which the respective step of the electron transfer takes place. For $t > t_2$, the potential was set back to the value 0.00V, allowing the oxidation of the generated product to occur. The value of the electric current for $t < t_1$ is nearly zero. The absolute values of the electric current measured at times t_1 and t_2 are almost equal, suggesting the reversibility of the electron transfer. The two values scale nicely with the number of electrons accepted by one molecule. In the case of the compound **1**, the time t_2 - t_1 = 150 s corresponds to 95 % completion of the electrolysis. For the standards which have higher diffusion coefficients, lower time intervals t_2 - t_1 were found to be sufficient for 95 % electrolysis completion.

Figure 73 shows the plots of the integrated charge (with $Q = 0.95\ Q_\infty$) against the bulk concentration, c, obtained for Fc, MV and the compounds **1** and **2**.

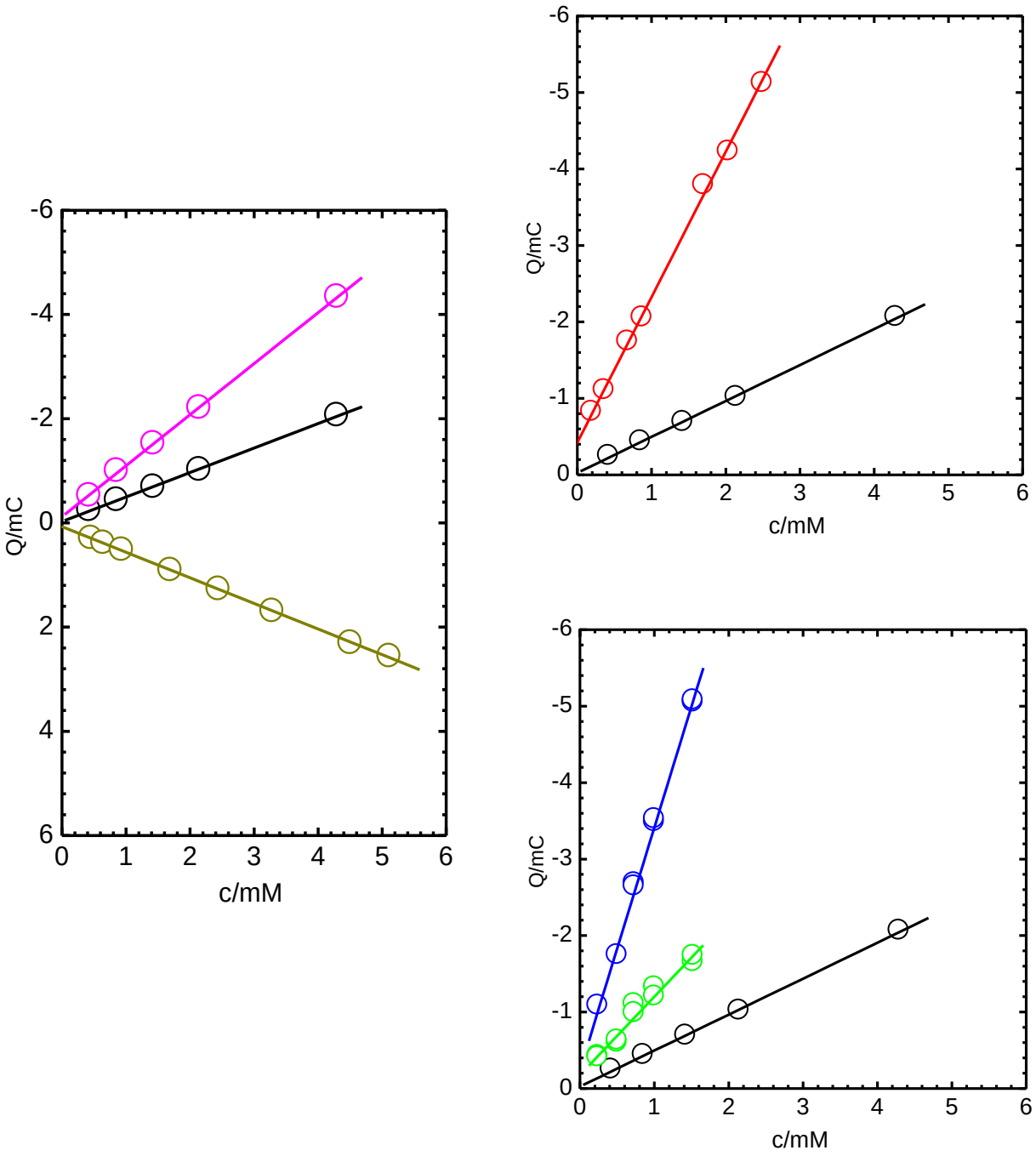

*Figure 73: The dependence of the charge consumption on bulk concentration of species: first reduction step of methyl viologen (black line), second reduction step of methyl viologen (purple line), fourth reduction step of **1** (red line), first reduction step of **2** (green line), second reduction step of **2** (blue line) and oxidation of Fc (golden line). The electrolysis was completed to α = 95 % for all cases. Measured in DMSO containing 0.43 M $TBAPF_6$ as the supporting electrolyte.*

Table 6 summarizes the results extracted from the *Q* vs. *c* plots shown in Figure 73.

Compound	dQ_∞/dc / (C/M)	*n*
Methyl viologen (1st reduction)	0.470 ± 0.006	1
Methyl viologen (2nd reduction)	0.979 ± 0.008	2.08 ± 0.02
Ferrocene	0.491 ± 0.003	1
1 (4th reduction)	1.900 ± 0.034	4.04 ± 0.09
2 (1st reduction)	1.020 ± 0.066	2.17 ± 0.14
2 (2nd reduction)	3.170 ± 0.068	6.74 ± 0.17

Table 6: The determination of the electron consumption from the slope dQ_∞/dc extracted from the Q vs. c plots with $Q = 0.95\ Q_\infty$. The slopes dQ_∞/dc for methyl viologen and ferrocene correspond to the consumption of one electron.

The technique based on the measurement of the dQ_∞/dc slopes shows the results that match those obtained by the method using the spectroscopic detection (Table 5). For both methods, the results are reliable only for c > 0.5 mM. Lower bulk concentration values lead to a significant contribution of the charging current. On the other hand, high concentration values (above 10 mM) cause considerable faradaic currents, inducing thus a high IR drop.

If the working electrode is set to a potential value *E*, with *I* being the current flowing through it, then the actual electrode potential will be $E' = E - IR$. For large IR values, the E' may significantly differ from *E*, being usually set to a value beyond the E^0 of an investigated process. Therefore, the E' value may fall into the range where the process of interest is not diffusion-limited, which leads to erroneous electron consumption. The *R* value is low at high concentrations of the supporting electrolyte. Therefore, we employed high concentration of the supporting electrolyte (0.43 M) in all experiments. The value of *I* increases with the bulk concentration of the studied species. In our experiments, the concentration fell into the range 0.5 mM – 6.0 mM. For all investigated compounds, the integrated charges were found to be well proportional to the bulk concentration, with no significant intercepts being found. For all compounds, the electron consumption found by both methods (the spectroscopic and the slope-finding technique) was identical to that found by the other electrochemical techniques, namely sampled DC polarography, cyclic voltammetry and bulk electrolysis.

4.5 Single-molecule conductivity measurement of molecular wires

The electric conductivity of junctions containing molecular wires (compounds **1** to **6**) was investigated by Tao's method [172]. The STM probe is first vertically approached to the sample surface with the molecules of interest adsorbed. In a given trial, the probe is not displaced in *x*- and *y*- direction and therefore, the local properties of the sample surface are traced. The set-point current value (usually 0.10 nA) dictates the separation distance between the probe and the sample surface. In the case of a proper contact, the feedback electronics maintain the electric current value equal to that of the set-point current, with no change in the probe *z*-position. The feedback electronics are then disabled and the probe is intentionally crashed into the surface. The distance which the probe travels, is called the penetration depth. The probe atoms make chemical bonds with those from the underlying substrate, creating thus a metallic junction. The probe is then retracted at given velocity, with the junction being broken. If a molecule is attached with both its ends to the substrate and to the probe, its presence may be discerned in the current-distance curve recorded during the withdrawal.

The Tao's method was first applied to the pure gold substrate (5000 measurements, Figure 74). Withdraw curves with no observable current plateaus or irregular structures were found only when the probe penetration depth was set to 10 nm or more. In this case, roughly 99 % of the current-distance curves followed a smooth exponential decay.

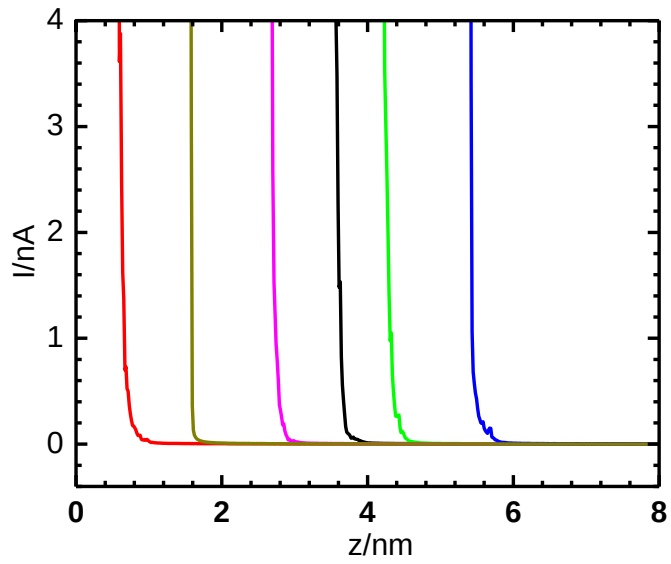

Figure 74: Typical current-distance curves obtained on the pure gold substrate at withdraw velocity 50 nm/s. Penetration depth 12 nm, set-point current 100 pA, bias voltage 100 mV. The curves are horizontally shifted for better visualization. The blue line (right) was selected intentionally to show a slight current irregularity (observed in 1% of experiments).

Only in 1 % of the experiments, the current irregularities were observed. This may be attributed to improper contact between the probe and the surface. If the penetration depth was set to less than 10 nm, the current irregularities became more frequent.

To suppress false positive errors, the single-molecule measurements of the junctions containing the compounds **1** to **6** were performed with the penetration depth of at least 10 nm. This ensures that the current plateaus originate from the detachment events of the adsorbed molecules rather than from the improper contact between the probe and the surface.

For all studied compounds, 7 - 12 % of trials led to the interpretable current-distance curves, being one order of magnitude more frequent than those for the pure gold substrate (less than 1 %). The rest of the curves either followed an exponential decay (i.e. with no molecules attached) or showed irregularities. The irregular curves probably resulted from multiple attachment-detachment events and were not taken into consideration.

Figure 75 shows six interpretable withdraw curves obtained for the gold substrate with adsorbed molecules of the compound **6**.

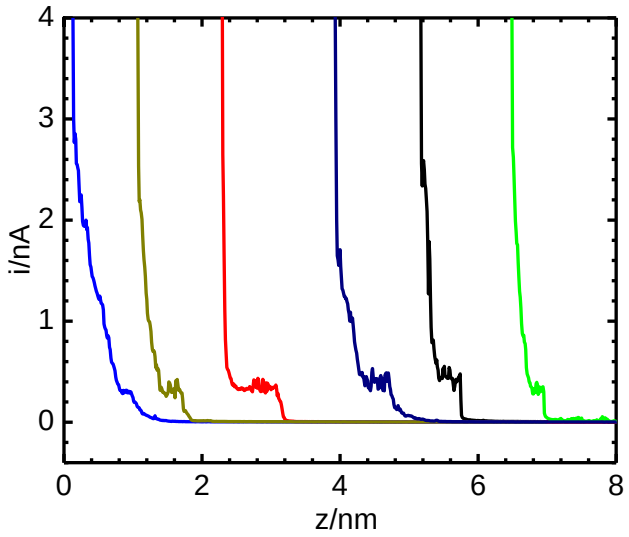

*Figure 75: Examples of interpretable current-distance curves obtained on the gold substrate containing adsorbed molecules of compound **6**. Withdraw velocity 50 nm/s, penetration depth 12 nm, set-point current 100 pA, bias voltage 100 mV. The curves are horizontally shifted for better visualization.*

For each extended viologen compound, 5000 current-distance curves were obtained, out of which 350 – 600 were interpretable. For each interpretable curve, the height of the current plateau was determined. In some cases, more than one current plateau was observed, forming thus the current steps. This corresponds to the subsequent detachment of more molecules. In such cases, the current step height values were determined as height differences between the

two subsequent current plateaus. In all cases, the electric conductivity was calculated by dividing the current value by the applied bias voltage (0.10 V in all experiments).

Figure 76 shows the current-distance curve with four current steps discerned, obtained for the gold substrate with adsorbed molecules of the compound **1**.

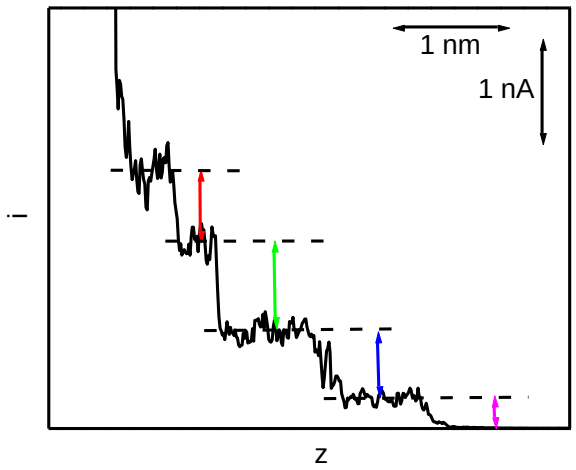

*Figure 76: An example of current-distance curve with four subsequent detachment events. Obtained for the gold substrate containing adsorbed molecules of compound **1**. Withdraw velocity 50 nm/s, penetration depth 12 nm, set-point current 100 pA, bias voltage 100 mV. The current values are indicated by the colored arrows.*

The conductance histograms for the compounds **1** to **6** were constructed. Figure 77 shows two typical conductance histograms, namely for the compounds **3** and **6**.

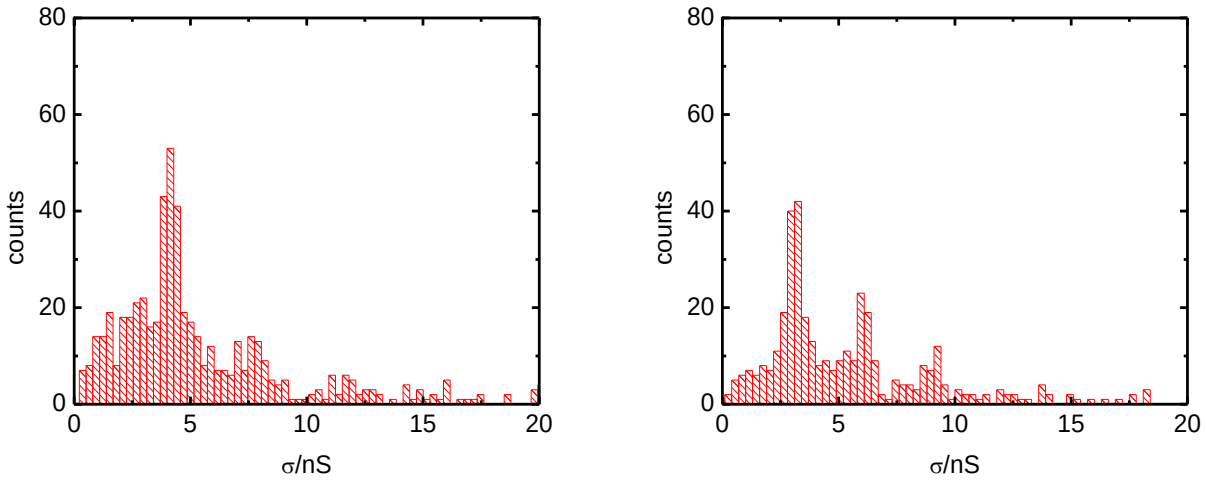

*Figure 77: Conductance histograms constructed for the compound **3** (left panel) and **6** (right panel). The histograms are constructed from 574 (compound **3**) and 383 (compound **6**) values. In the case of both compounds, 5000 current-distance curves were acquired.*

The first maximum, the one with the highest number of counts, is believed to represent the single-molecule conductance. The second and the third maximum, being correspondingly

lower than the first one but still discernible, may be explained by the simultaneous detachment of two and three molecules, respectively. For all investigated compounds, the single-molecule conductance values along with those pertaining to two- and three-molecule detachments are listed in Table 7.

compound	σ_1/nS	σ_2/nS	σ_3/nS
1	5.1	9.5	15.0
2	4.6	8.7	13.3
3	4.1	7.8	11.8
4	3.7	7.4	11.0
5	3.4	6.8	10.6
6	3.1	6.1	9.3

Table 7: Single-molecule conductance values (σ_1) and conductance values pertaining to simultaneous detachments of two (σ_2) and three (σ_3) molecules.

For all compounds, the values of σ_2 and σ_3 are two and three times higher than the single-molecule conductance, σ_1. The natural logarithm of σ_1 value was found to linearly decrease with the molecular length (Figure 78). This feature was encountered also in other series of compounds, formed of both aliphatic [172] and aromatic [173] molecules.

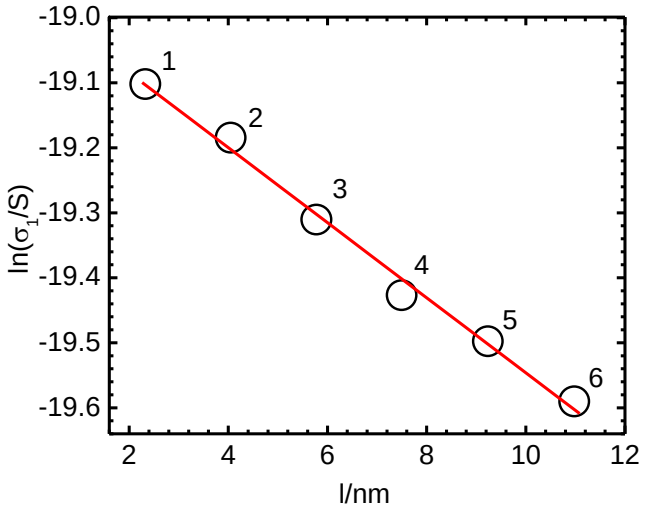

*Figure 78: The natural logarithm of the single-molecule conductance as a function of the length of the molecule, for the compounds **1** to **6**.*

The presence of molecules of the compounds **1** to **6** on the gold substrate was confirmed by the scanning tunneling microscopy (STM) and polarization modulation infrared reflection absorption spectroscopy (PM IRRAS). Figure 79 shows the PM IRRAS spectrum of the pure gold substrate and gold substrate with adsorbed molecules of the compound **1**.

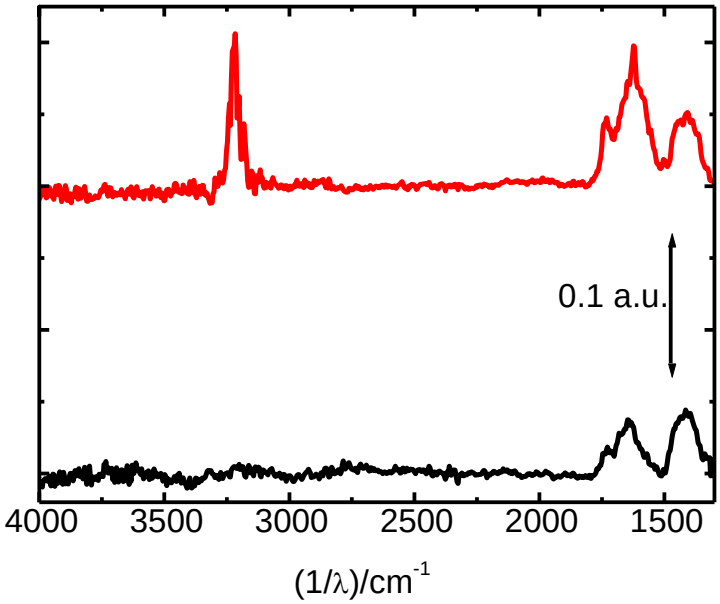

*Figure 79: PM IRRAS spectrum of the pure gold substrate (black line) and the gold substrate with adsorbed molecules of the compound **1** (red line). In both cases, the shown profile is the sum of 64 collected spectra. Spectral resolution 4 cm^{-1}.*

The PM IRRAS spectrum of the compound **1** (red line) shows a band centered at 3200 cm^{-1}. The benzene, phenyl group or 1,4-phenylene linkers show vibrations bands at roughly 3100 - 3150 cm^{-1}. Therefore, this band may be assigned to the vibration in phenyl groups and phenylene linkers, present in the molecule.

The absorption at 1630 cm^{-1} is increased when compared to the absorption spectrum of the pure gold substrate. The C=N bond stretching is known to absorb at 1615 – 1700 cm^{-1}. Therefore, this band may be attributed to C=N stretching in the pyridinium rings of the molecule. Note that the structure around 1400 cm^{-1} is unchanged. No other absorption bands were observed.

Figure 80 shows the scanning tunneling micrograph of the gold substrate with the molecules of the compound **2** being adsorbed. One can easily see steps in the underlying gold substrate. The presence of holes all over the micrograph is also discernible, indicating the presence of adsorbed molecules. The depth of the hole should theoretically be equal to the size of one gold atom (0.25 nm) for a well prepared Au(111) surface.

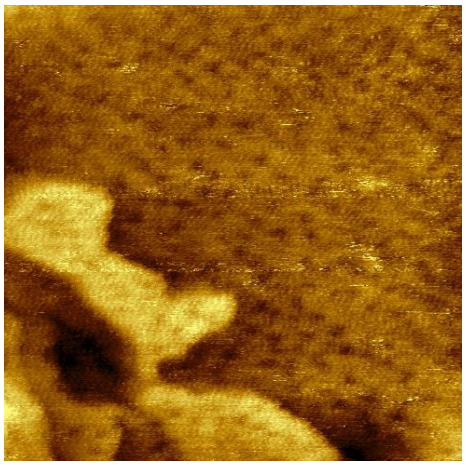

Figure 80: Scanning tunneling micrograph (topography map) of the gold substrate with adsorbed molecules of the compound 2. Scan-size 120 nm, set-point current 100 pA, bias voltage 100 mV, scan-speed 0.4 lines/s, z bar 0.7 nm. Mechanically cut Pt/Ir wire was used as the probe. Measured in the nitrogen atmosphere.

Figure 81 (left panel) shows a histogram of the step heights, measured as the topographic difference between the upper and the lower planes in the micrograph shown in Figure 80. The average value of the step height is 0.26 ± 0.04 nm, being very close to the theoretical thickness of the single gold layer (0.25 nm). The right panel of Figure 81 shows the histogram constructed from the hole depth values. The average value is 0.20 ± 0.04 nm, which is slightly lower than the theoretical value, possibly due to the insufficient penetration of the probe.

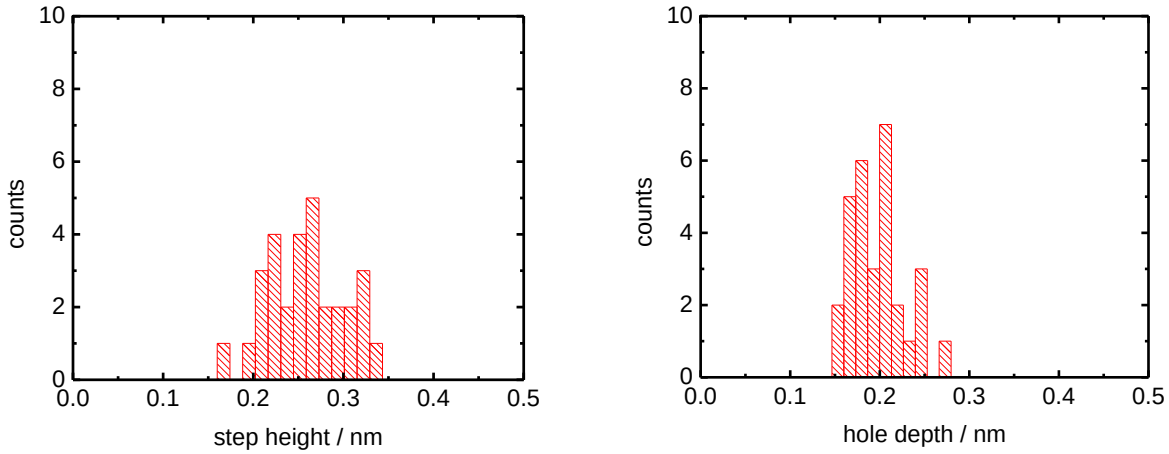

Figure 81: Histogram of step height values (left panel) and hole depth values (right panel). Both histograms are constructed from 30 individual measurements.

4.6 Homogenous reactions in solutions of molecular wires, electrochemical oscillations

Compounds **1'** and **4'** were found to show a remarkable behavior, rather different from that observed in the molecules of the compounds **1** to **6**. The electrochemical behavior of **1'** was already investigated [63,64]. Recently, it was found that the electrochemical behavior of both compounds is strongly influenced by the presence of homogenous kinetics. As in the case of the compounds **1** to **6**, the behavior of the compounds **1'** and **4'** was scrutinized by various electrochemical techniques. Determination of the electron consumption in the electrochemical reduction of the compound **1'** was carried out by three methods:

- Potentiostatic bulk electrolysis
- Sampled DC polarography
- Potentiostatic electrolysis using OTTLE as the working electrode

The bulk electrolysis clearly confirmed the consumption of a charge corresponding to one electron per molecule. The experiment was repeated several times.

Sampled DC polarography was carried out in two solvents: acetonitrile (AN) and dimethyl sulfoxide (DMSO). The reduction wave height of the compound **1'** was related to that of cobaltocenium (Cc^+), measured at the very same conditions. Figure 82 shows the results of the measurements in both solvents.

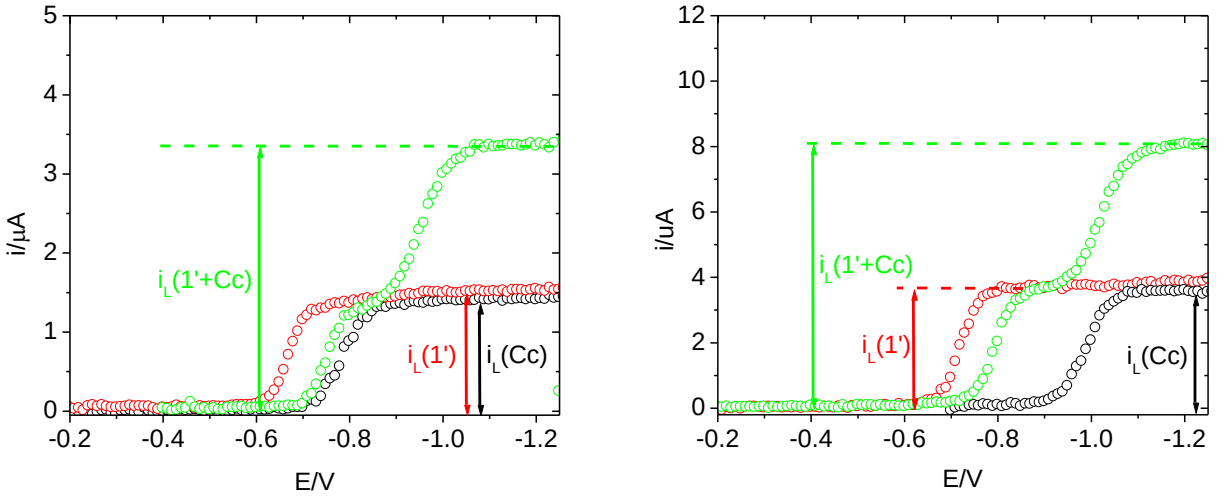

*Figure 82: Sampled DC polarograms obtained in DMSO (left panel) and AN (right panel). The polarogram for **1'** (red circles), Cc^+ (black circles) and the **1'** + Cc^+ mixture (green circles) are shown, for 1.0 mM concentration of the compounds. Obtained on SMDE with drop-time 3 s, employing 0.2 M $TBAPF_6$ as the supporting electrolyte.*

For both solvents, the height of the reduction wave of **1'** is nearly identical to that measured for Cc^+, which is known to transfer one electron per molecule in the electrochemical reduction. Therefore, the sampled DC polarography confirms the results of the bulk electrolysis experiments with one electron being consumed per one molecule of **1'**.

The mixture of **1'** and Cc^+ yielded the polarogram with the limiting current higher than the sum of the limiting currents in the polarograms obtained for the individual solutions of **1'** and Cc^+ at the same concentration

$$i_L(1'+Cc^+) > i_L(1') + i_L(Cc^+) \tag{71}$$

This effect was observed in both AN and DMSO. The unexpected current increase strongly supports the presence of a homogenous chemical reaction between forms of species Cc^+ and **1'**. If there were no homogenous reactions, only the heterogeneous one-electron transfer would occur to both Cc^+ and **1'** molecules, consuming $2e^-$ altogether

$$Cc^+ + 1e^- \rightarrow Cc^0 \tag{72}$$

$$(1')^{2+} + 1e^- \rightarrow (1')^{1+} \tag{73}$$

If there is a homogenous process, its mechanism could possibly look as follows

$$Cc^+ + 1e^- \rightarrow Cc^0 \tag{74}$$

$$(1')^{2+} + 1e^- \rightarrow (1')^{1+} \tag{75}$$

$$Cc^0 + (1')^{1+} \varsigma Cc^+ + (1')^0 \tag{76}$$

$$Cc^+ + 1e^- \rightarrow Cc^0 \tag{77}$$

The Cc^+/Cc^0 redox pair serves as a mediator rather then a catalyst as it is changed itself in the reaction pathway. The equations 75, 76 and 77 may be summed up to yield

$$(1')^{2+} + 2e^- \rightarrow (1')^0 \tag{78}$$

This reaction is not thermodynamically possible (as the heterogeneous electron transfer) at the electrode potential values considered, but may take place in the bulk of the solution being mediated by the Cc^+/Cc^0 couple. If all four equations were quantitative, three electrons would be consumed for one pair of molecules **1'** and Cc^+ at the same concentration in the experiments. However, the latter two reactions need not be quantitative as the equilibrium constant of the homogenous reaction need not be high and not all regenerated Cc^+ diffuses back to the electrode to be re-reduced. Therefore, the total electron consumption n_T (counted for both **1'** and Cc^+) is $2 < n_T < 3$. This is in full agreement with the results of the experiment, from which n_T(DMSO) = 2.34 and n_T(AN) = 2.21, n_T evaluated as the fraction

$2\times i_L(1'+Cc^+)/\left[i_L(1')+i_L(Cc^+)\right]$. The proposed mechanism therefore explains an unexpected increase in the electron consumption in the mixed solution of **1'** and Cc^+.

A closely related type of the homogenous process taking place during the electrochemical reduction in the solution of pure **1'** is the disproportionation of $(1')^{1+}$ radical cation

$$(1')^{1+} + (1')^{1+} \quad \varsigma \quad (1')^{0} + (1')^{2+} \tag{79}$$

with the corresponding homogenous equilibrium constant

$$K_{disp} = \frac{k_f}{k_b} = \frac{\left[(1')^0\right]\left[(1')^{2+}\right]}{\left[(1')^{1+}\right]^2} \tag{80}$$

with k_f and k_b being the forward and backward homogenous rate constant, respectively. When taking the presence of homogenous kinetics into account, the following mechanism of the electrochemical reduction of $(1')^{2+}$ may be proposed

$$(1'_A)^{2+} + 1e^- \rightarrow (1'_A)^{1+} \tag{81}$$

$$(1'_B)^{2+} + 1e^- \rightarrow (1'_B)^{1+} \tag{82}$$

$$(1_A')^{1+} + (1_B')^{1+} \varsigma (1_A')^{0} + (1_B')^{2+} \tag{83}$$

$$(1'_B)^{2+} + 1e^- \rightarrow (1'_B)^{1+} \tag{84}$$

$$(1'_C)^{2+} + 1e^- \rightarrow (1'_C)^{1+} \tag{85}$$

$$(1_B')^{1+} + (1_C')^{1+} \varsigma (1_B')^{0} + (1_C')^{2+} \text{ etc.} \tag{86}$$

The molecules were named by X = A, B, C, … to make them tractable. The two molecules $(1_X')^{1+}$ and $(1_Y')^{1+}$, (X,Y) = (A,B), (B,C), (C,D),… react together by the homogenous reaction. The reaction product $(1_Y')^{2+}$ (identical to the parent form) is further electroactive, but may be electrochemically detected only when sufficient time is provided for $(1_Y')^{2+}$ to diffuse back to the electrode. If it is swept away from the electrode such as in the convection-controlled bulk electrolysis or sampled DC polarography, it cannot be re-reduced. Therefore, only one electron per one **1'** molecule is detected. This is in agreement with the results of bulk electrolysis and sampled DC polarography. If the solution is left in the contact with the electrode for longer time, then the products of the homogenous reaction have sufficient time to get back to the electrode and accept another electron leading to the consumption of two electrons per one **1'** molecule. Such condition is met in the OTTLE cell. In it, the reaction volume around the working electrode is confined by the transparent slides allowing the reaction extend to be traced by UV/VIS/IR spectroscopy. Figure 83 shows a typical cyclic voltammogram of **1'** in AN containing 0.2 M $TBAPF_6$ as the supporting electrolyte.

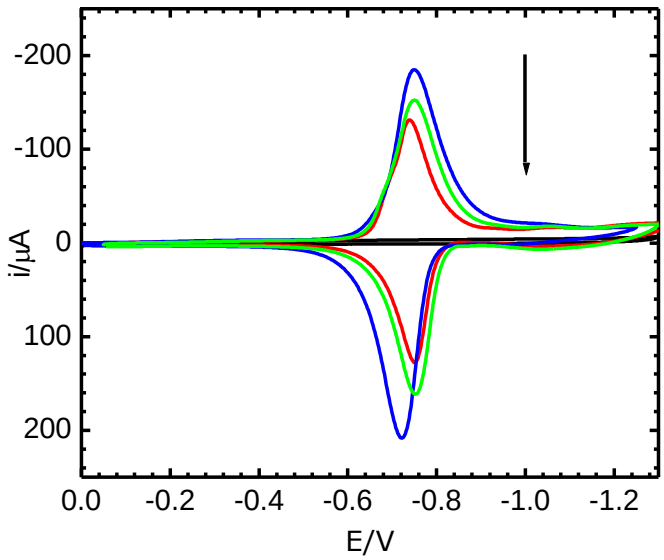

*Figure 83: Cyclic voltammogram of 0.2 M $TBAPF_6$ in AN containing 0 mM (black line), 2.94 mM (red line), 3.94 mM (green line) and 5.20 mM (blue line) **1'**. OTTLE was employed as the working electrode. Arrow indicates a suitable potential for the subsequent potentiostatic electrolysis.*

The cyclic voltammogram is somewhat distorted, with slightly irreproducible peak separation. This is largely caused by the fact that the equations governing the electrochemical behavior in cyclic voltammetry are derived with specific boundary conditions including the one for the composition of a distant solution. The solution composition is supposed to be unperturbed at $x \rightarrow \infty$, with x being the distance from the electrode, which is not satisfied in the OTTLE cell. Other complications are caused by a considerable electrode area, causing large *IR* drop and charging currents. Irreproducible peak position may be caused also by the quasi-reference electrode, used in the OTTLE cell due to a limited space.

Once the voltammetric behavior is known, one can carry out the potentiostatic electrolysis. The measurements are accomplished by stepping the electrode potential from the value in the capacitive region, E_0, to a potential, E, at which the process of interest takes place. For electrochemical reductions, the E value is set more negative than the $E^{1/2}$ value of a respective process, usually with $E^{1/2} - E \approx 200$ mV, to avoid inconveniences caused by the *IR* drop and reference electrode irreproducibility. If the complete electrolysis is assumed, the electric charge obtained by the integration of the current transient is given by

$$Q = FncV + \int_{E_0}^{E} C(E)dE \qquad (87)$$

with the two terms on the right-hand side of the equation being the faradaic and capacitive contributions, respectively. An electroactive species is dissolved in an electrolyte to produce a

solution with the bulk concentration *c*, which is then scrutinized in an electrochemical cell with a confined space in the vicinity of the working electrode (of the volume *V)*. If the differential capacity *C* is assumed to be independent of the bulk concentration of the electroactive species, then the right-hand term vanishes upon differentiation with respect to *c* and the Eq. 87 leads to

$$dQ / dc = FnV \tag{88}$$

This allows the effective cell volume to be calculated. The cell volume is most conveniently determined by measuring a standard, such as ferrocene (Fc), cobaltocenium (Cc^+) or methyl viologen (MV). In practice, the *dQ/dc* values are obtained for investigated species by integrating the current transients at various bulk concentrations and relating them to the *dQ/dc* value of a standard. Figure 84 shows the concentration dependence of integrated electric charge for Fc (green line), Cc^+ (red line) and **1'** (black curve). Note that no mixed solutions of Cc^+ and **1'** were used here. Cc^+ serves only as the standard to which the electron consumption of **1'** is referenced.

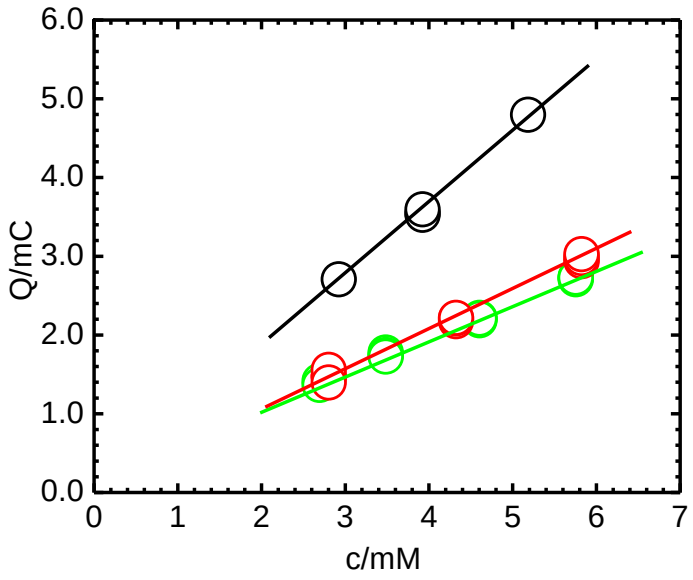

*Figure 84: The dependence of electric charge Q on bulk concentration of Fc (green line), Cc^+ (red line) and **1'** (black line). Measured in AN containing 0.2 M $TBAPF_6$ as the supporting electrlyte. Obtained at potential values of the diffusion limited electron transfer.*

The *Q*. against *c* dependences for all three species were subjected to the linear regression analysis. Slopes of dependences for Fc and Cc^+ are $(dQ/dc)_{Fc}$ = 0.44 mC/mM and $(dQ/dc)_{Cc+}$ = 0.48 mC/mM, respectively. The two values are very similar and correspond to one-electron reduction (Cc^+) and oxidation (Fc). The slope determined for the compound **1'** is $(dQ/dc)_{1'}$ = 0.93 mC/mM, being roughly two times higher than those found for Fc and Cc^+. This confirms that **1'** accepts two electrons in the OTTLE cell.

A clear discrepancy between the results of open-space methods i.e. sampled DC polarography and bulk electrolysis (the consumption of $1e^-$) and the confined-space method i.e. electrolysis in OTTLE cell (the consumption of $2e^-$) deserves further discussion.

When the OTTLE cell is employed, the molecules of the parent form $(1')^{2+}$ regenerated by the homogenous disproportionation may diffuse back to the electrode and accept a further electron. The bulk disproportionation is considerable only when K_{disp} attains sufficiently high values. Figure 85 shows the simulated sampled DC polarograms for the electrochemical reduction of **1'** followed by the homogenous disproportionation regenerating the parent form $(1')^{2+}$. For large values of K_{disp} the faradaic current is twice as high (dark yellow line) as that calculated for K_{disp} = 0 i.e. in the absence of the homogenous reaction (black line). As follows from the results of the measurements, the K_{disp} value is sufficiently high for the reactant regeneration to occur in a confined space of the OTTLE cell at long reaction times. However, the disproportionation is insufficient in open-space experiments i.e. sampled DC polarography and bulk electrolysis.

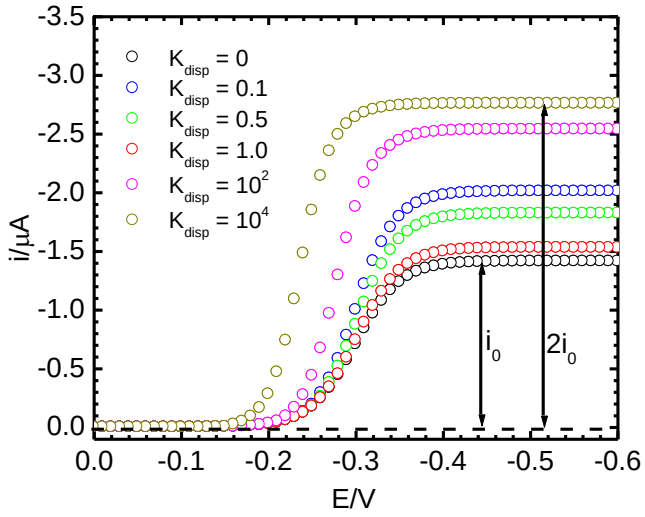

*Figure 85: Simulated DC polarograms of electrochemical reduction of **1'** followed by the homogenous disproportionation, with the equilibrium constant K_{disp}. The curves are simulated for various values of K_{disp} stated in the left part of the figure. Drop-time 1 s.*

The presence of homogenous reactions may also bring other interesting properties to electrochemical systems. When the octacationic compound **4'** (the tetramer of **1'**) is electrochemically reduced, various its forms may come into existence. The molecule of the compound **4'** is composed of four repeating units, each one having two redox-active centers. Overall, the molecule possesses eight reducible centers. This is in accordance with the results of the measurements carried out for the compound **1'** in the OTTLE cell, which confirmed the transfer of two electrons.

If the **4'** molecule is reduced, for example, by three electrons, $(4')^{8+} + 3e^- \rightarrow (4')^{5+}$, some of the possible triply reduced species are

$$(\mathbf{10\text{-}10\text{-}10\text{-}00})^{5+} \qquad (\mathbf{10\text{-}10\text{-}00\text{-}01})^{5+} \qquad (\mathbf{10\text{-}01\text{-}10\text{-}00})^{5+}$$

where "1" and "0" stand for the reduced and oxidized state of a given center, respectively. The parent species are, therefore, denoted as $(4')^{8+} = (\mathbf{00\text{-}00\text{-}00\text{-}00})^{8+}$. The first accepted electron has eight possible locations in the molecule, while the second and the third have only seven and six possibilities, respectively. The overall number of possible triply reduced species is $C_3^8/2 = 28$ where $C_k^n = n!/(n-k)!k!$ being the combination number. The symmetry of the molecule was taken into account by counting only ½ of the possible configurations. The various reduced forms may mutually react by homogenous reactions

$$\mathbf{(10\text{-}10\text{-}10\text{-}00)^{5+} + (00\text{-}10\text{-}00\text{-}00)^{7+} \varsigma (00\text{-}10\text{-}10\text{-}00)^{6+} + (00\text{-}11\text{-}00\text{-}00)^{6+}} \quad (89)$$

There is a multitude of possibilities, by which various configurations of differently reduced states of **4'** may react together. This may lead to current oscillations. Electrochemical oscillations may serve as the models for periodic and chaotic processes as the parameters, at which the current oscillations occur, may continuously be varied. The number of electrons accepted by one molecule can be precisely controlled by the electrode potential. The number of molecules in the contact with the electrode is determined by the bulk concentration. Other variable parameters include temperature, solution resistivity, relative permittivity and the electrode material.

Mathematically speaking, chaos is defined as a state of unpredictability, being very sensitive to initial conditions. The metaphor "butterfly effect" is often used to depict a sensitive dependence on the initial conditions. This phrase refers to the idea that the atmospheric changes induced by a flap of butterfly's wings may change the trajectory of a tornado or even induce it, observed in a totally different part of the world.

The history of chaos dates back to 1890, when French mathematician and philosopher Henry Poincaré, an early proponent of the chaos theory, studied the three-body problem, in which the bodies are mutually perturbed by gravitational attractions [174]. He found that under certain initial conditions (masses, initial velocities and positions) the bodies would follow non-periodic trajectories.

In 1961, American meteorologist Edward Lorenz discovered [175] that even very small differences in initial conditions such as rounding the variables may have considerable impact on the long-term outcome of a weather simulation. It suggests that a long-term weather forecast is never correct, as the initial conditions cannot be stated with an infinite precision.

In 1978, Americal mathematical physicist Mitchell Feigenbaum described the logistic maps [176] and discovered the universality in chaos, permitting an application of the chaos theory to many different phenomena. The logistic map is defined by the reccurence relation

$$x_{N+1} = r x_N (1 - x_N) \tag{90}$$

and belongs to a group of quadratic difference equations. A certain member of the sequence x_{N+1} is calculated from the previous one, x_N, depending on an adjustable parameter, $r > 0$. All members of series are normalized, $0 \leq x_i \leq 1$ for $i = 0,1,2,\ldots\ n,n+1,\ldots$. The shape of the equation may be explained as follows:

- x_N represents a population (number of members of a given species) at year N. The initial condition (population at year 0) is therefore denoted as x_0.
- x_{N+1} is the population at a year $N+1$, being dependent on x_N.
- The parameter r depends on the rates of reproduction and mortality.
- For $x_N \rightarrow 0$, the population increases with the rate proportional to the population.
- For $x_N \rightarrow 1$, the population increases with the rate proportional to the free capacity (maximum population minus current population).

The behaviour of the solution of the logistic map [177] strongly depends on the parameter r:

- For $0 \leq r \leq 1$, x_N will converge to 0 for $N \rightarrow \infty$ irrespective of x_0.
- For $1 < r \leq 2$, x_N will eventually approach **one** value $(r-1)/r$ independent of x_0.
- For $2 < r \leq 3$, the same limiting behavior with some initial fluctuations.
- For $3 < r \leq 1+\sqrt{6}$, x_N eventually oscillates between **two** solutions that depend on r.
- For $1+\sqrt{6} < r \leq 3.54$ (approximately) x_N oscillates between **four** solutions.
- For $r > 3.54$, x_N oscillates between **eight, sixteen, thirty-two…** solutions.
- Above 3.57 (so called Feigenbaum point) a **chaotic behavior** occurs.

In the range $0 \leq r < 3.57$, the x_N may (for $N \rightarrow \infty$) attain one, two, four, eight values…, depending on the r value. Therefore, a qualitative change in the system behavior (change in the number of attainable solutions) occurs as the r value increases. This qualitative change is termed the bifurcation. The r value, at which the number of attainable solutions changes, is called the bifurcation point, b_i. Bifurcation intervals I are bounded by the two successive bifurcation points, $I_i = (b_{i-1}, b_i)$ with the number of attainable solutions being constant within them. Their length, $\delta_i = | I_i |$, rapidly decreases with the r value. The Feigenbaum constant δ is defined as the ratio of the lengths of two successive intervals [178]

$$\delta = \delta_{k-1} / \delta_k \tag{91}$$

Its value is $\delta = 4.669\ldots$ being an irrational and universal number.

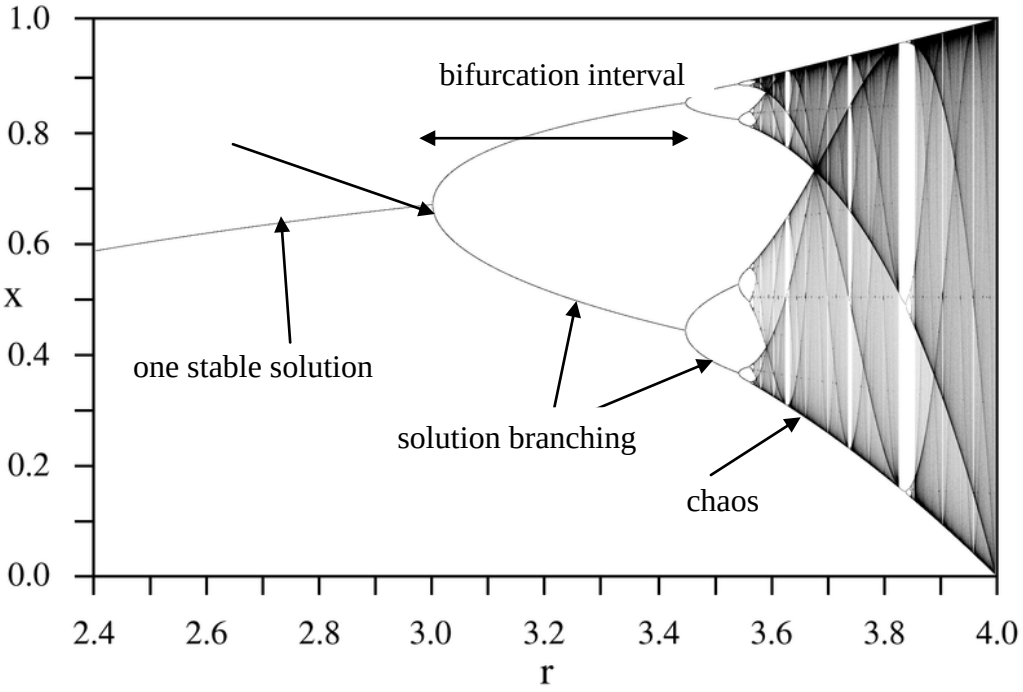

Figure 86: Bifurcation diagram for the logistic map.

The logistic map is a very simple example, which shows that the order and chaos may be derived from the very same mathematical decription – a simple quadratic difference equation. Figure 86 shows all stable solutions of the logistic map as a function of *r*, so-called bifurcation diagram. The order is obtained for $r \leq 3$ (left part of Figure 86). A chaotic behavior (right part of Figure 86) is observed for *r* value greater than the Feigenbaum point (ca 3.57). For $3 \leq r \leq 3.57$, the x_N value oscillates between stable solutions. As the number of solutions increases with increasing *r*, the middle part of the bifurcation diagram is sometimes referred to as the frequency doubling.

As mentioned above, the sampled DC polarogram of the compound **1'** shows one-electron process. The second electron is transferred only in the OTTLE cell. During the electrochemical reduction of **1'**, the radical cation $(1')^{1+}$ is formed and coexists with the parent form, $(1')^{2+}$. The situation is different in the case of **4'**, which may be reduced to a higher extent, with variously reduced forms mutually reacting by the homogenous reactions. Figure 87 shows the sampled DC polarograms for both **1'** (red line) and **4'** (green line).

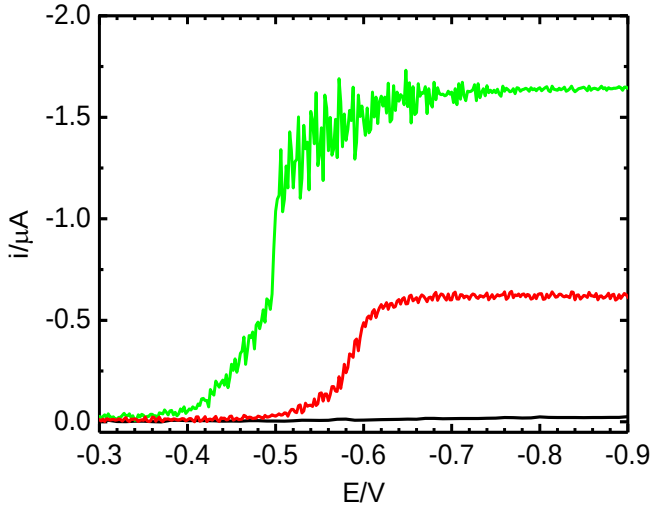

*Figure 87: Sampled DC polarogram of 0.1 M $TBAPF_6$ in AN in the absence (black line) and presence of 0.50 mM **1'** (red line) and **4'** (green line).*

No current irregularities are observed for the compound **1',** while the noise level is increased in the case of **4'**. The increased noise level was observed in the case of HMDE, SMDE and Au electrodes. Therefore, it cannot be attributed to streaming maxima known for the SMDE. The DC polarogram also shows a sudden increase in the measured current at -0.50 V. Figure 88 shows the power spectrum obtained by the fast Fourier transform (FFT) analysis of the voltammograms of both **1'** (red line) and **4'** (green line).

The power densities for the compounds were obtained for the potential range -0.50 and -0.65 V. For potentials more negative than -0.80 V, the power density spectrum of **4'** was very similar to that obtained for **1'**.

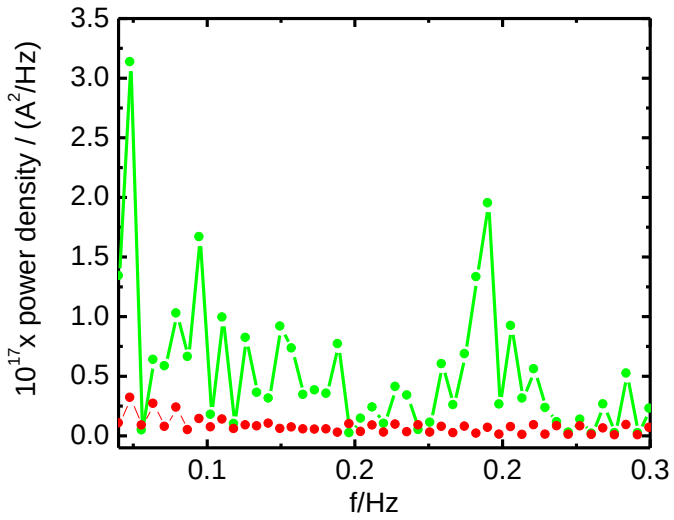

*Figure 88: The power spectra obtained by FFT for **1'** (red line) and **4'** (green line). The potential range between -0.50 and -0.65 V was used.*

The current transients at constant potential values were also measured. Typical profiles obtained at the potentials pertaining to a noisy part of the sampled DC polarogram are shown in Figure 89.

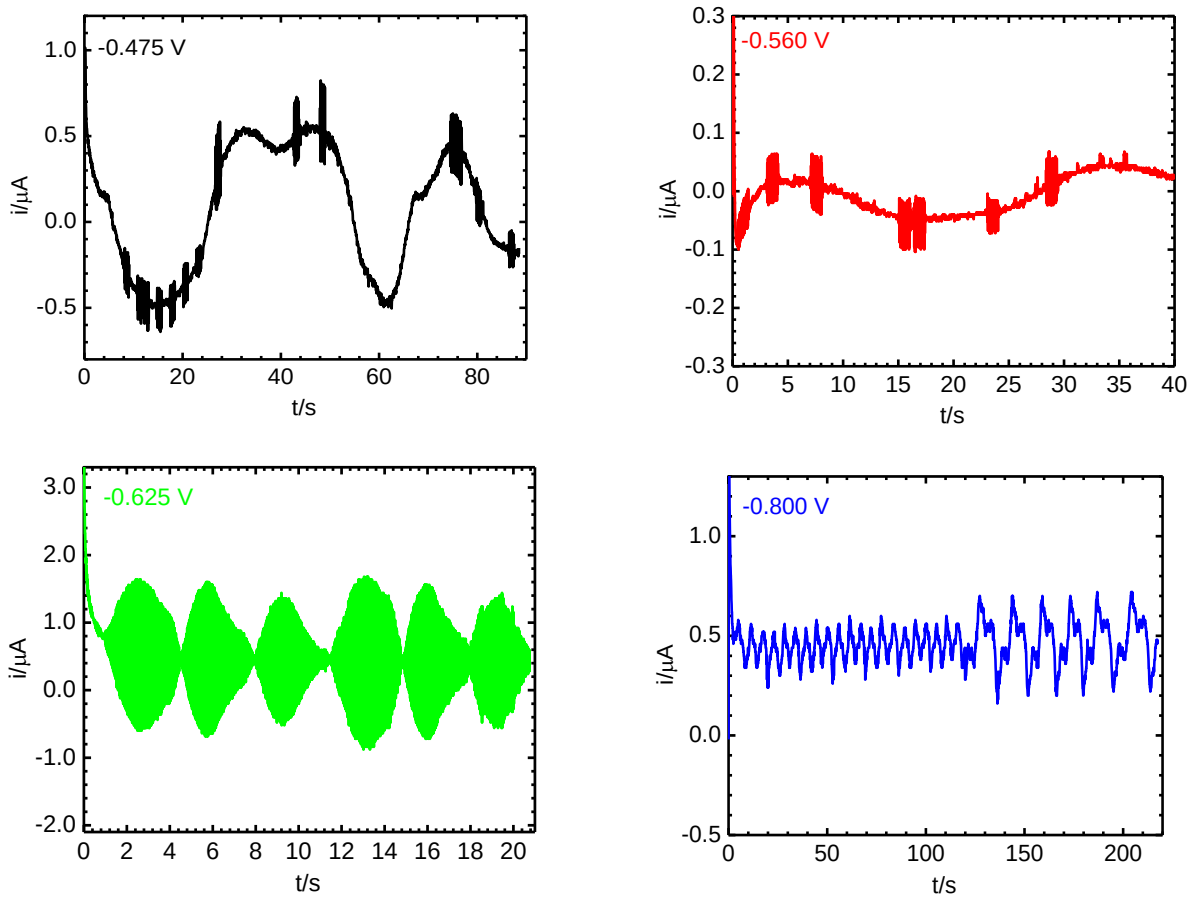

*Figure 89: Current transients measured in AN with 0.1 M $TBAPF_6$ containing 0.50 mM **4'** obtained at -0.475 V (black line), -0.560 V (red line), -0.625 V (green line) and -0.800 V (blue line). Measured on HMDE.*

All current transients show features not usually encountered in the chronoamperometric experiments. The transients obtained at the potentials -0.625 V (green line) and -0.800 V (blue line) show clear periodic behavior. A sudden frequency change may be discerned in the transient measured at -0.800 V. A frequency doubling is a typical feature of the oscillating systems. The current transients at -0.475 V and -0.560 V show low-frequency oscillations, with superimposed chaotic current bursts.

One of the basic properties of chaotic systems is their high sensitivity towards small changes in the initial conditions. Subsequent electrochemical experiments can never be repeated in the very same way as a new mercury drop is extruded for each new trial and the solution composition may slightly change between the experiments. Moreover, the electrode potential is never measured with an absolute accuracy. Even these, usually neglected, fluctuations may

serve as perturbations having significant impact on the time evolution of the system. Therefore, current transients may differ from each other. Figure 90 shows other current transient obtained at -0.475 V considerably differing from that shown in the upper left panel of Figure 89.

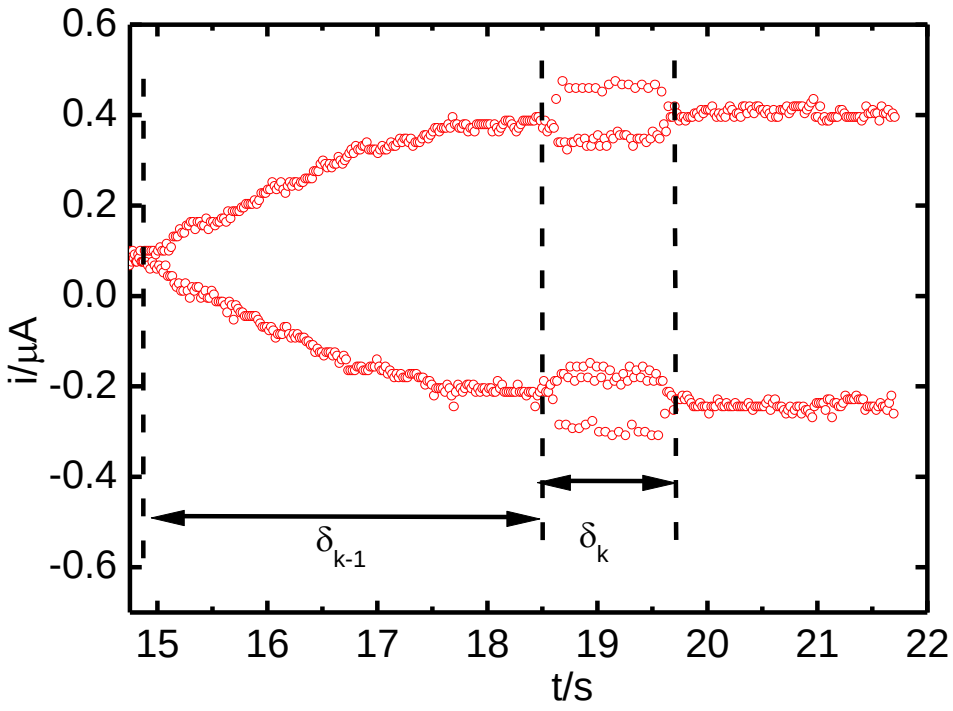

*Figure 90: Current transient measured in AN with 0.1 M TBAPF$_6$ containing 0.50 mM **4'**, at -0.475 V. The values δ_K and δ_{K-1} refer to the bifurcation interval lengths. Their ratio yields the Feigenbaum constant.*

The two subsequent bifurcation intervals with the lengths δ_K and δ_{K-1} may be discerned. Figure 90 is similar to the bifurcation diagram for the logistic map (Figure 86). The current transient shown in the Figure 90 yields the value $\delta = \delta_{K-1}/\delta_K = 4.68$, being very close to the theoretical value of the Feigenbaum constant, $\delta = 4.6692...$.

The current transients were investigated at various electrode potential values in order to exclude the possibility that the current oscillations are caused by a malfunction of electronics. Figure 91 shows a typical current transient obtained at the potential -0.900 V. In this region, no current oscillations were observed in the sampled DC polarogram. The current transient is featureless, following a well-known Cottrell-like shape. For sufficiently negative potential values, the molecules of **4'** are "saturated" by electrons, excluding the possibility of mutual interactions by homogenous reactions.

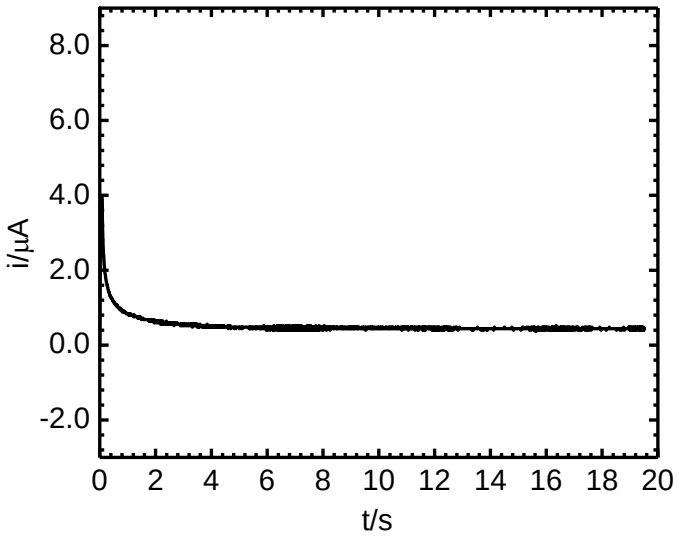

*Figure 91: Current-time profile for AN with 0.1M $TBAPF_6$ containing 0.50 mM **4'**. Measured at potential -0.900 V, where no current oscillations were observed in the sampled DC polarogram.*

The smooth current profile measured at -0.900V proves that the current oscillations are not caused by the malfunction of the instrumentation.

The electrode potential may be to some extent compared to the *r* parameter in the logistic map. The system behavior, depending on the electrode potential, may change from the order to chaos via the frequency doubling. The studied electrochemical system serves not only for the experimental verification of the value of Feigenbaum constant but may also be considered as a model of the oscillator based on a single (or few) molecule(s). This may be employed in the future devices of molecular electronics. We are not aware of any electrochemical system that would lead to the experimental verification of the Feigenbaum constant. This is the first example.

4.7 Host-guest interactions and their potential use for molecular electronics

This chapter focuses on the host-guest interactions between ferrocene (Fc) and cyclodextrins (CDs). For 1:1 inclusion complexes the complex formation constant is defined as K = [Fc-CD] / [CD] [Fc], where [Fc] and [Fc-CD] are the actual concentrations of free and complexed Fc, respectively. The actual concentration of the free cyclodextrin host is [CD]. We employed the direct dissolution of both Fc and host molecules, according to Matsue et al. [97]. We only worked in the environments, where no solubility problems were encountered. The environment was composed of DMSO:water mixture [179,180] with the volume fraction of DMSO, φ_{DMSO}, characterizing its composition. Either LiCl (for $\varphi_{DMSO} < 0.80$) or $TBAPF_6$ (for $\varphi_{DMSO} \geq 0.80$) was added to the mixture to serve as the supporting electrolyte at 0.1 M concentration in both cases. Fc was dissolved at 2.0 mM concentration usually with the aid of the ultrasonic treatment. The cyclodextrin host was added to the Fc solution in successive steps, with the total concentration falling into the range of 2 – 30 mM. Four types of cyclodextrin molecules were employed in this study, namely αCD, βCD, heptakis(2,6-di-*O*-methyl)-β-cyclodextrin (abbreviated as Me_2βCD) and heptakis(2,3,6-tri-O-methyl)-β-cyclodextrin (Me_3βCD). The behavior of inclusion complexes between Fc and all mentioned hosts was investigated by cyclic voltammetry.

If no host molecules are added to the Fc solution, the anodic peak current i_{pa}^{0} is given by Randles-Ševčík equation (Eq. 6). Here, for brevity, it is written as

$$i_{pa}^{0} = kD_{Fc}^{1/2} c_{Fc} \tag{92}$$

with the proportionality constant k comprising the electrode area A, scan-rate v and the number of electrons n transferred in the electrochemical reaction (n = 1 for Fc/Fc^{+}). As all these variables are constant in experiments, they are grouped in the constant k. When host molecules are present in the solution, the measured anodic current is the sum of currents originating from the oxidation of both free and complexed form of Fc

$$i_{pa} = kD_{Fc}^{1/2}[Fc] + kD_{C}^{1/2}[Fc-CD] \tag{93}$$

with the actual concentrations of free [Fc] and complexed [Fc-CD] ferrocene forms summing up to the analytical concentration c_{Fc} = [Fc] + [Fc-CD]. The values D_{Fc} and D_C are the diffusion coefficients of the free and complexed form. Similarly, c_{CD} = [CD] + [Fc-CD] holds for CD molecules. For $c_{CD} >> c_{Fc}$, one may assume [CD] >> [Fc-CD] and c_{CD} = [CD]. One may easily show that the actual concentrations [CD], [Fc-CD] and [Fc] are given by

$$[CD] = c_{CD} \qquad [Fc-CD] = \frac{i_{pa}^0 - i_{pa}}{k(D_{Fc}^{1/2} - D_C^{1/2})} \qquad [Fc] = \frac{i_{pa}^0}{kD_{Fc}^{1/2}} - \frac{i_{pa}^0 - i_{pa}}{k(D_{Fc}^{1/2} - D_C^{1/2})} \tag{94}$$

These expressions may substitute the corresponding terms in the relation defining the complex formation constant. The following relation is obtaied

$$\frac{i_{pa}^0 - i_{pa}}{k(D_{Fc}^{1/2} - D_C^{1/2})} = Kc_{CD}\left(\frac{i_{pa}^0}{kD_{Fc}^{1/2}} - \frac{i_{pa}^0 - i_{pa}}{k(D_{Fc}^{1/2} - D_C^{1/2})}\right) \tag{95}$$

Note that *k* may be dropped in the denominator and, therefore, the *K* value does not depend on the measuring conditions provided that the complex formation reaction is in the state of the chemical equilibrium. The Eq. 95 may be rearranged to [111]

$$\left(\frac{i_{pa}}{i_{pa}^0}\right)^2 + \frac{1}{Kc_{CD}}\left(\frac{i_{pa}^2 - i_{pa}^{0\ 2}}{i_{pa}^{0\ 2}}\right) = \frac{D_C}{D_{Fc}} \tag{96}$$

The right-hand term in the left-hand side vanishes for $c_{CD} \rightarrow \infty$ leaving the relation

$$\lim_{cCD\to\infty} \frac{i_{pa}}{i_{pa}^0} = \sqrt{\frac{D_C}{D_{Fc}}} \tag{97}$$

As $D_C < D_{Fc}$, the peak current height is supposed to decrease upon complexation, gradually approaching the value $(D_C/D_{Fc})^{1/2} i_{pa}^{\ 0}$. This value is the peak current height for fully complexed Fc, with no free form being present in the solution. The rate, at which the anodic peak current decreases with increasing c_{CD} value, reflects the value of the complex formation constant *K*. Figure 92 shows the cyclic voltammograms of Fc/Fc^+ redox pair in the absence and presence of the host molecules: αCD (upper left panel), βCD (upper right panel), Me_2βCD (lower left panel) and Me_3βCD (lower right panel). The black lines show the cyclic voltammograms of Fc/Fc^+ redox couple at 2.0 mM in the absence of the host molecules. The $i_{pa}^{\ 0}$ values fall into the range 0.62 and 0.70 μA, with slight differences being explainable by varying water content in the DMSO:water mixtures, causing slight changes in the solvent viscosity. Red, green and blue lines show cyclic voltammograms in the presence of the host molecules, with ascending c_{CD} values, falling into the range 2 – 11 mM. The addition of αCD has no impact on the anodic peak current height. Therefore, a low value of the complex formation constant may be deduced for this host molecule. The anodic peak current differs from the $i_{pa}^{\ 0}$ value only for αCD concentrations higher than those shown in Figure 92. On the other hand, the addition of βCD, Me_2βCD and Me_3βCD led to a more pronounced current decrease and a higher value of the complex formation constant may be inferred for these three host molecules.

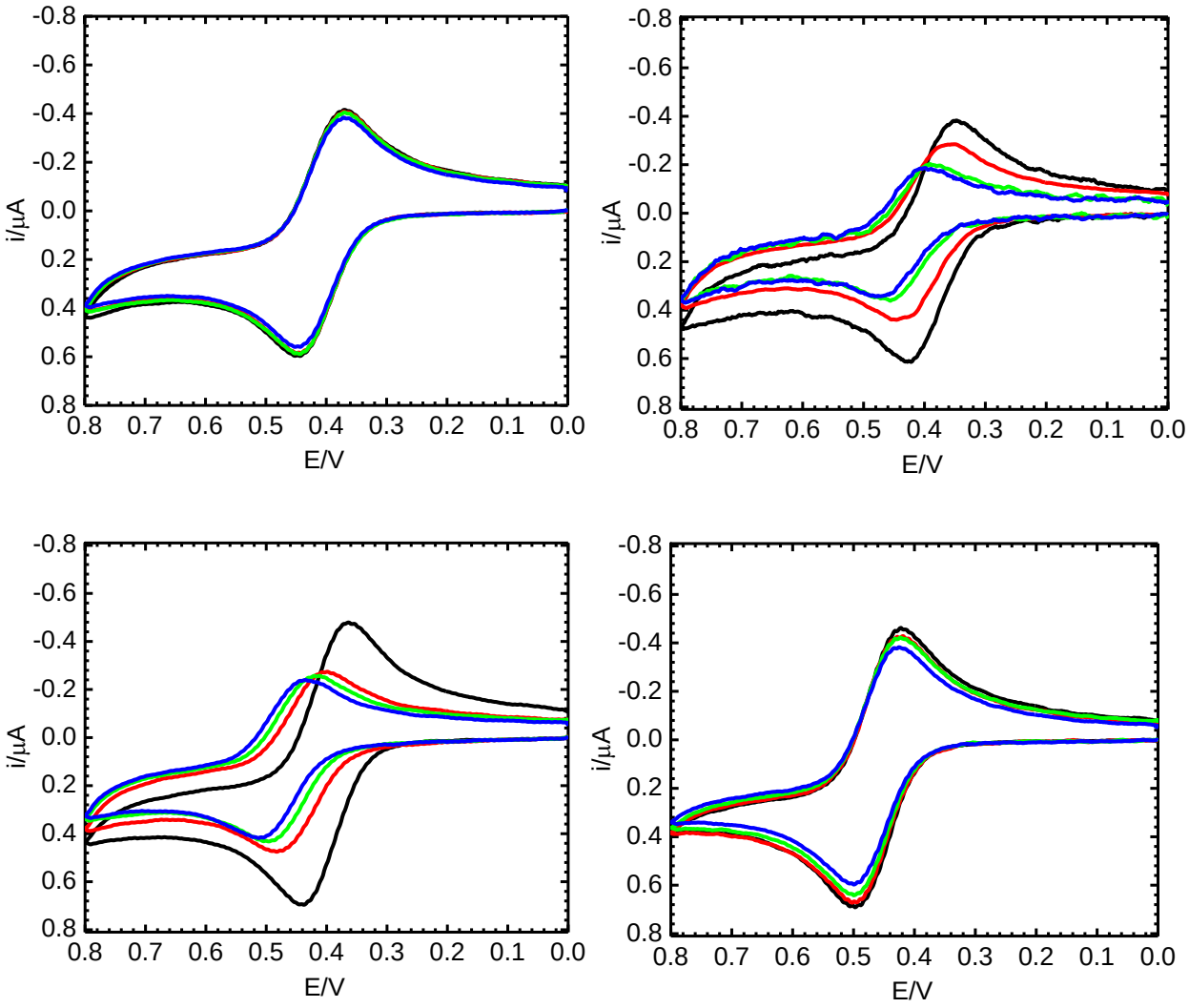

Figure 92: Cyclic voltammograms of 2.0 mM Fc upon the addition of different CDs.
Upper left panel: αCD 0.00 mM (black line), 6.23 mM (red line), 8.34 mM (green line) and 10.63 mM (blue line), measured in the mixture with φ_{DMSO} = 0.70 containing 0.1 M LiCl
Upper right panel: βCD 0.00 mM (black line), 2.12 mM (red line), 6.63 mM (green line) and 10.37 mM (blue line), measured in the mixture with φ_{DMSO} = 0.70 containing 0.1 M LiCl
Lower left panel: Me_2βCD 0.00 mM (black line), 3.92 mM (red line), 6.22 mM (green line) and 9.93 mM (blue line), measured in the mixture with φ_{DMSO} = 0.75 containing 0.1 M LiCl
Lower right panel: Me_3βCD 0.00 mM (black line), 3.14 mM (red line), 5.13 mM (green line) and 7.67 mM (blue line), measured in the mixture with φ_{DMSO} = 0.90 with 0.1 M $TBAPF_6$
Scan-rate: 0.125 V/s.

Figure 93 shows a typical dependence of the i_{pa}/i_{pa}^{0} ratio vs. c_{CD} upon the addition of Me_2βCD in the mixture with φ_{DMSO} = 0.90. The ratio slowly approaches the value $(D_C/D_{Fc})^{1/2} i_{pa}^{0}$, being characteristic for the fully complexed Fc.

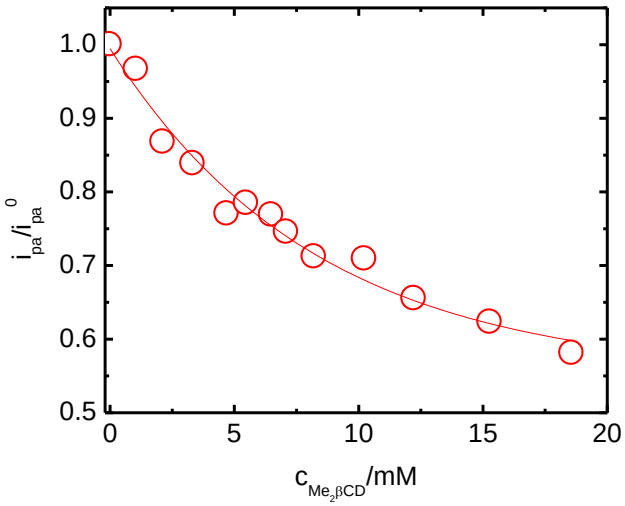

Figure 93: The ratio i_{pa}/i_{pa}^0 for the Fc/Fc^+ couple as a function of the analytical concentration of $Me_2\beta CD$ in 90% DMSO containing 0.1 M $TBAPF_6$ as the supporting electrolyte.

As may be noticed from Figure 92, the standard redox potential slightly shifts upon the addition of βCD and Me_2βCD hosts. For αCD and Me_3βCD hosts, this effect becomes pronounced only at host concentrations higher than those shown in Figure 92. With increasing concentration of the host, a higher fraction of Fc molecules becomes complexed. Complexation makes the Fc molecules hidden in the host cavity. Therefore, Fc molecules are less prone to the oxidation. A more positive potential value is necessary to trigger the oxidation in complexed molecules. If the standard redox potential in the presence of a host molecules is denoted as E^0, its shift with respect to its original value, E_{Fc}^0, is given by [181]

$$\Delta E = E^0 - E_{Fc}^0 = \frac{RT}{F}\ln(1+Kc_{CD}) + \frac{RT}{F}\ln\left(\frac{D_C}{D_{Fc}}\right)^{1/2} \qquad (98)$$

This equation is derived assuming c_{CD} = [CD], i.e. for sufficiently large c_{CD} values. The equation (98) may be easily rearranged to the shape

$$e^{\frac{F}{RT}\Delta E^0 - \frac{1}{2}\ln\frac{D_C}{D_{Fc}}} - 1 = Kc_{CD} \qquad (99)$$

If one plots the left-hand term (abbreviated as e^{ψ}-*1*) vs. c_{CD}, the complex formation constant equals to the slope of the dependence. Right panel of Figure 94 shows the plot e^{ψ}-*1* against c_{CD} for the additions of Me_2βCD to Fc in 90% DMSO. Only the values c_{CD} > 5 mM were taken for the analysis. For lower host concentrations, the dependence was somewhat curved and the corresponding c_{CD} values were, therefore, not considered. Left panel of Figure 94 shows the corresponding ΔE^0 values, from which the right panel was constructed.

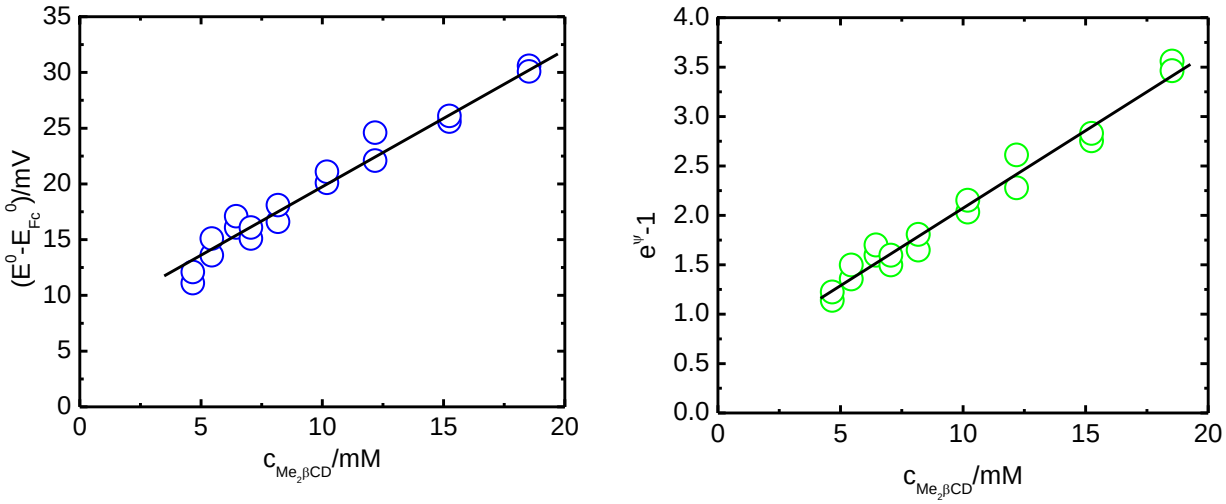

Figure 94: The dependence of E^0-$E_{Fc}{}^0$ (left panel) and e^{ψ}-1 (right panel) against total $Me_2\beta CD$ concentration. Measured in 90% DMSO containing 0.1 M $TBAPF_6$ as the supporting electrolyte.

The separation between the cathodic and anodic peak in the voltammograms was also investigated. Its value for the free Fc was found to fall into the range 60 – 70 mV, not being far from the theoretical value 59.2 mV known for the transfer of one electron. Slightly increased peak separation is highly probably caused by a small uncompensated solution resistance. We could not increase the concentration of the supporting electrolyte as, in some DMSO:water mixtures, it would lead to the precipitation of the host molecules. Even at 0.1 M of either LiCl or $TBAPF_6$ the maximum attainable c_{CD} concentration was roughly 15 mM for $Me_2\beta CD$ and $Me_3\beta CD$. Higher concentrations of the supporting electrolyte would lead to a further decrease in the host solubility. The determination of K value would not be feasible in such a narrow range of attainable c_{CD} values. Therefore, all experiments were carried out in the presence of the supporting electrolyte at 0.1 M concentration. As the concentration was kept constant, the effect of the ionic strength on the K value may be neglected. An important point is that the peak separation remained in the range 60 – 70 mV also upon the the addition of host molecules showing that the reversibility of the electron transfer is retained also in the complexed Fc molecules.

Another way to investigate the electrochemical reversibility is tracing the ratio of the anodic and the cathodic peak current height, i_{pa}/i_{pc}. The ratio attains the values close to unity for the reversible systems [123]. Figure 95 shows the ratio i_{pa}/i_{pc} for the addition of $Me_2\beta CD$ in 90 % DMSO, which attains the values in the range 0.94 ± 0.03 being very close to unity. Moreover, i_{pa}/i_{pc} vs. c_{CD} plot shows no observable trend and the i_{pa}/i_{pc} ratio is independent of the host

concentration. From the peak separation and peak current ratio values one can conclude that the Fc/Fc^+ redox pair has the reversible electrochemical behavior, even with the Fc molecules being complexed by the cyclodextrin host molecules.

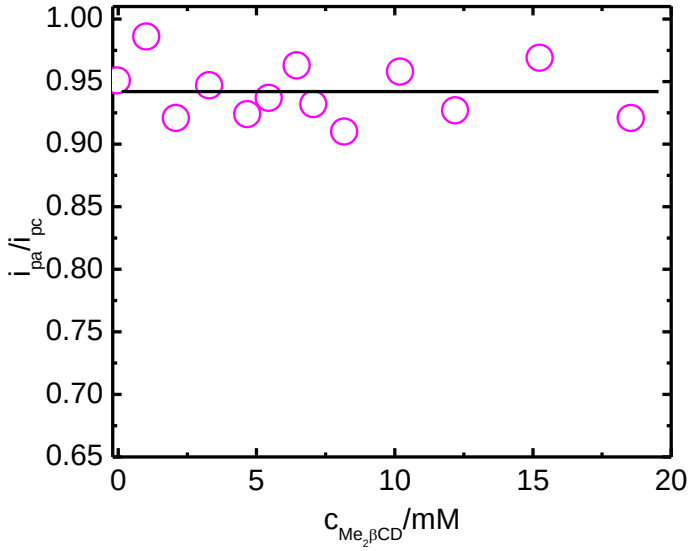

Figure 95: The ratio of the anodic to cathodic peak currents i_{pa}/i_{pc} as a function of the total $Me_2\beta CD$ concentration. Measured in 90% DMSO containing 0.1 M $TBAPF_6$ as the supporting electrolyte.

The e^{ψ}*-1* against c_{CD} plots were constructed for all host molecules in various water:DMSO mixtures. The corresponding complex formation constants were determined as slopes of these dependences. Figure 96 (left panel) shows the *K* values for all host molecules as a function of φ_{DMSO}. The corresponding standard complex formation Gibbs energy, ΔG^0, are plotted in the right panel. The Gibbs reaction isotherm was employed to calculate ΔG^0 values, $\Delta G^0 = -RT \ln K$.

For all four host molecules, the values of the complex formation constant *K* increase with the water content in the mixture. This is plausible as water is not a "good" solvent for non-polar Fc molecules. With increasing content of water, Fc molecules are more likely to form inclusion complexes with CD host molecules possessing the hydrophobic cavities. In pure DMSO and the mixtures with low water content, Fc is well soluble and is not prone to the complexation. Fc was found to be soluble enough only in the water:DMSO mixtures containing more than 50 % of DMSO (to attain 2.0 mM concentration).

Therefore, the both panels contain the values only for $\varphi_{DMSO} \geq 0.50$. As mentioned above, another limitation is given by the solubility of the host molecules. While αCD and βCD were found to be well soluble in all environments, we encountered problems when dissolving Me_2βCD and Me_3βCD in the mixtures with $0.50 \leq \varphi_{DMSO} \leq 0.70$. The corresponding *K* values are therefore missing in Figure 96.

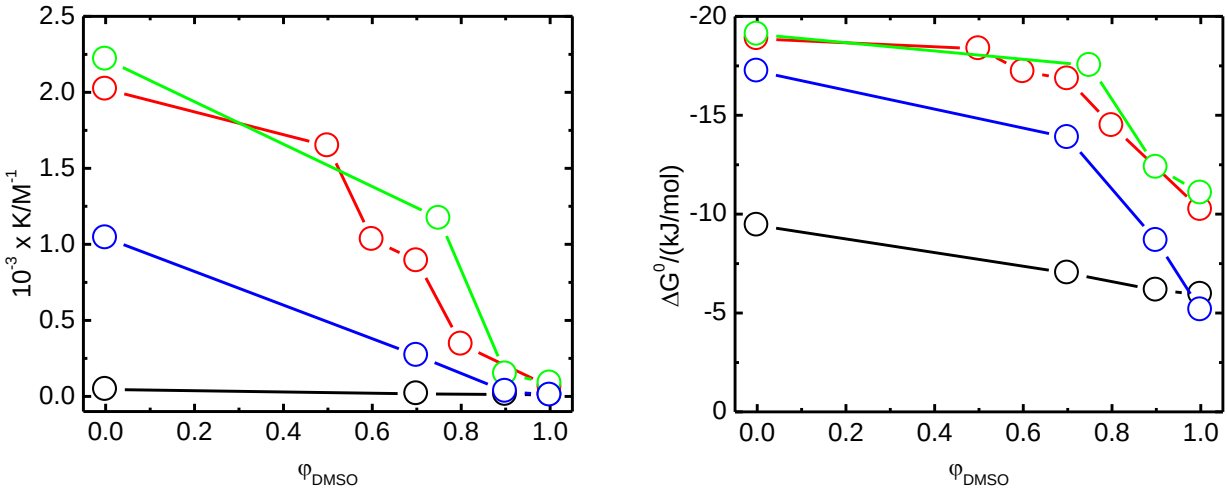

Figure 96: The values of K (left panel) and corresponding ΔG^0 (right panel) as a function of the volume fraction of DMSO in DMSO:H_2O mixture, shown for all CD molecules: αCD (black circles), βCD (red circles), Me_2βCD (green circles) and Me_3βCD (blue circles).

Relative permittivity ε_r of a solvent is a measure of its polarity. Polar solvents such as water have a strong ability to attenuate electric forces acting between the dissolved charged species, making thus their dissolution energetically favorable. On the other hand, polar solvents are not suitable for dissolving molecules containing non-polar groups. Cylodextrins may be considered as a special class of substances, having considerably different local value of relative permittivity on the surface of the molecule and in its cavity. Polar surface groups make the cyclodextrins soluble in polar solvents, while the hydrophobic cavity allows them to serve as the host molecules for non-polar species. The ability of the host molecule to bind species depends also on the relative permittivity of the surrounding solvent. Figure 97 shows the plot of the *K* value against the relative permittivity of the DMSO:water mixture [180,182]. The dependence is roughly linear. The permittivity, being dependent on the solvent composition, may therefore be considered as a tunable parameter controlling the strength of the complex.

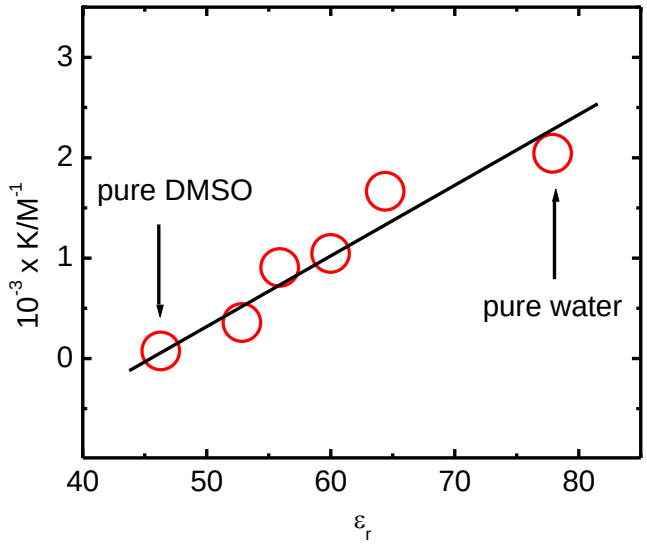

Figure 97: The complex formation constant, K, as a function of relative permittivity, ε_r, of the water:DMSO mixture for βCD.

Other important parameter is the cyclodextrin cavity size and the presence of the side groups. While αCD is not a suitable host for the inclusion of Fc guest, βCD and its derivatives seem to be of use. Among them, βCD and Me_2βCD form complexes with very high *K* values.

The results of measurements will be employed in the construction of molecular switches [118,119]. Figure 98 shows a possible arrangement of the molecular switch exploiting the host-guest interactions [120–122]. Depending on the electrode potential the ferrocene molecules may form inclusion complexes with βCD or its methylated derivatives. The switch may be reproducibly turned "on" and "off" by the electrode potential applied. The working switch needs to be placed in a suitable environment, where an inclusion complex of a suitable strength may be formed. We have shown that DMSO:water mixture represents such an environment. The ability to form the switches may be controlled by a simple solvent property – its relative permittivity.

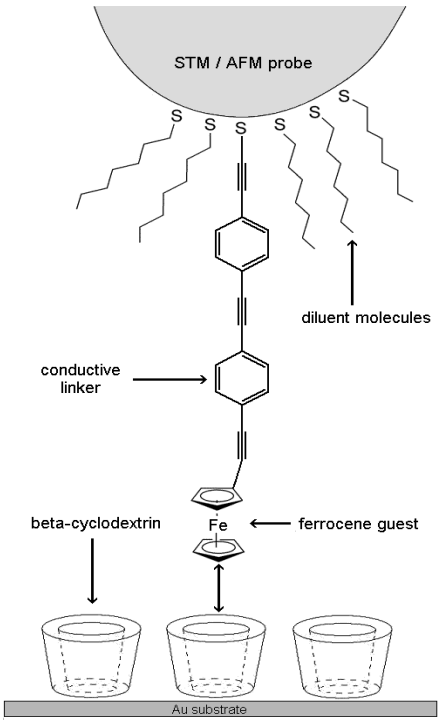

Figure 98: Possible arrangement of a molecular switch based on the host-guest interactions.

The molecule $Me_3\beta CD$, which was proved to form a 1:1 inclusion complex with Fc was also available in the thiolated form, $Me_3\beta CD$-Cys-SH. In this molecule, one $-OCH_3$ moiety in the smaller ring is replaced by the amino acid cysteine, providing the anchoring –SH group. The molecule assembled on a surface may serve as a host molecule for Fc moiety (see Figure 98). One needs to investigate the adsorption properties of the compound $Me_3\beta CD$-Cys-SH. The electrochemical (cyclic voltammetry, AC voltammetry and AC polarography) as well as scanning probe techniques (AFM and STM) were employed for adsorption studies.

Figure 99 shows cyclic voltammogram of 0.1 M KF containing $Me_3\beta CD$-Cys-SH.

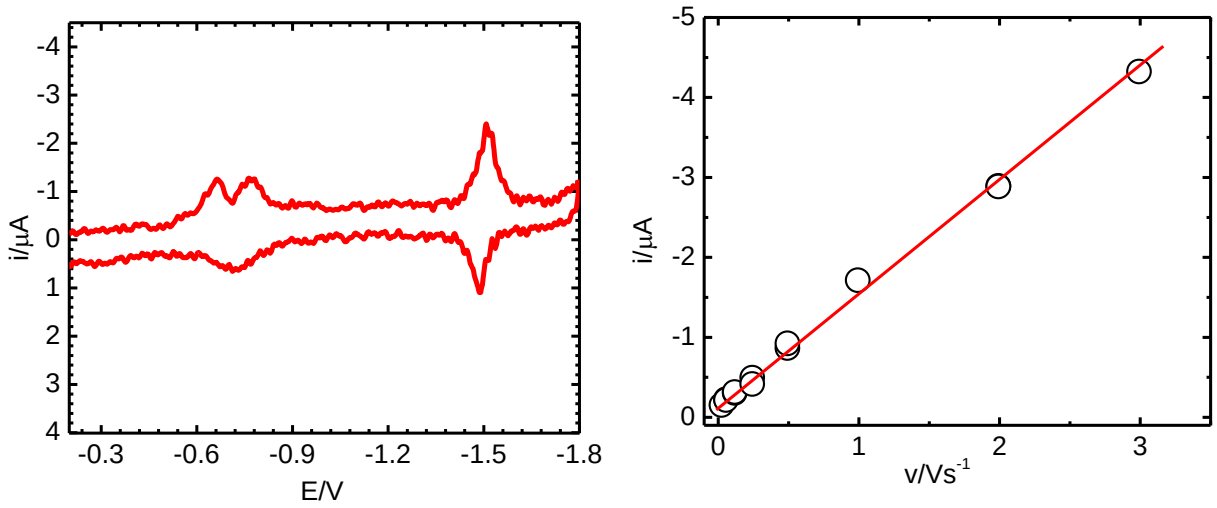

Figure 99: Left panel shows cyclic voltammogram of 0.1 M KF containing 0.39 mM $Me_3\beta CD$-Cys-SH. Scan-rate: 1 V/s, HMDE. Right panel shows the forward peak height (at -1.50 V) as a function of scan-rate.

The peak at -1.50 V pertains to their reductive desorption of adsorbed molecules. For all scan-rate values, the peak separation is less than 15 mV. The corresponding peak current is proportional to the scan-rate value in the range 0.1 – 3 V/s, which suggests the surface-confined electron transfer. Cyclic voltammetry by this simple experiments confirmed the adsorption of $Me_3\beta CD$-Cys-SH on HMDE.

The adsorption on mercury was further scrutinized by AC voltammetry (working electrode HMDE) and AC polarography (working electrode SMDE). Both methods revealed the presence of adsorbed molecules. Figure 100 shows the corresponding AC voltammogram (upper panel) and AC polarogram (lower panel). Both were obtained by scanning the potential from -0.20 V in the negative direction with potential increment 20 mV and drop-time 3 s.

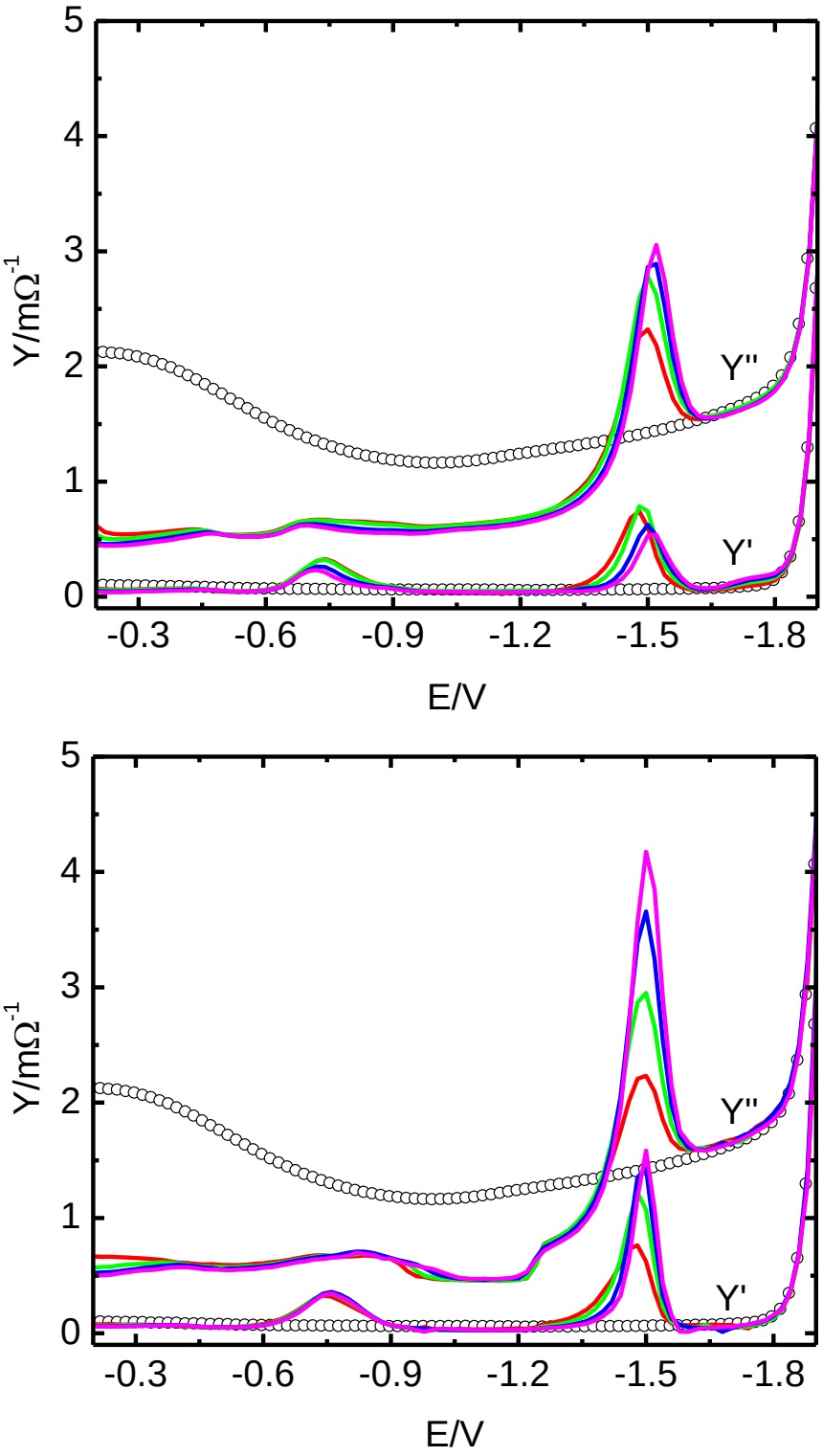

Figure 100: AC voltammogram (HMDE, upper panel) and AC polarogram (SMDE, lower panel) of 0 mM (black circles), 0.09 mM (red line), 0.17 mM (green line), 0.27 mM (blue line) and 0.39 mM (magenta line) Me_3βCD-Cys-SH in water containing 0.1 M KF as the supporting electrolyte. AC frequency 160 Hz and amplitude 5 mV. HMDE scan-rate is 20 mV/s, SMDE drop-time is 3 s.

Both AC voltammogram and AC polarogram show a decrease in the imaginary part of the cell admittance at potential values less negative than -1.30 V. This confirms that molecules of adsorb at the mercury/electrolyte interface. The adsorption pit is limited by the sharp peak centered at -1.50 V, which well corresponds to desorption process observed in the cyclic voltammogram. At potentials more negative than -1.62 V, both real and imaginary components of cell admittance are identical to those obtained in the absence of Me_3βCD-Cys-SH molecules in the bulk of the solution. Therefore, at these potential values, the electrode interface contains no molecules adsorbed. Within the adsorption pit, the value of differential capacity is nearly independent of the bulk concentration of Me_3βCD-Cys-SH, which suggests that a two-dimensional film is formed.

Another process observed at -0.75 V (also noticed in the cyclic voltammetry), is probably a reorientation of adsorbed molecules. A faradaic process is not likely as the molecule of Me_3βCD-Cys-SH does not contain moieties that could be easily reduced at this potential value. AC voltammogram and AC polarogram are very similar, which suggests that the adsorption must be diffusion-limited.

AC techniques confirmed the results of the cyclic voltammetry. Me_3βCD-Cys-SH adsorbs at the mercury/electrolyte interface in a broad range of potential values. The positive edge of the adsorption pit could not be determined as the adsorption pit was limited by the end of the potential window of the electrode/electrolyte interface. At the negative side, the adsorption pit is limited by a sharp desorption peak, centered at -1.50 V.

The experiments employing the mercury electrode are useful to determine the electrode potential, at which a compound may adsorb at interfaces of solid electrodes.

Figure 101 shows the scanning probe micrographs of the adsorbed layer of Me_3βCD-Cys-SH on the Au(111) substrate. Very similar micrographs (not shown) were obtained even after one week, implying that the adsorbed Me_3βCD-Cys-SH layer is not sensitive to the atmospheric oxygen.

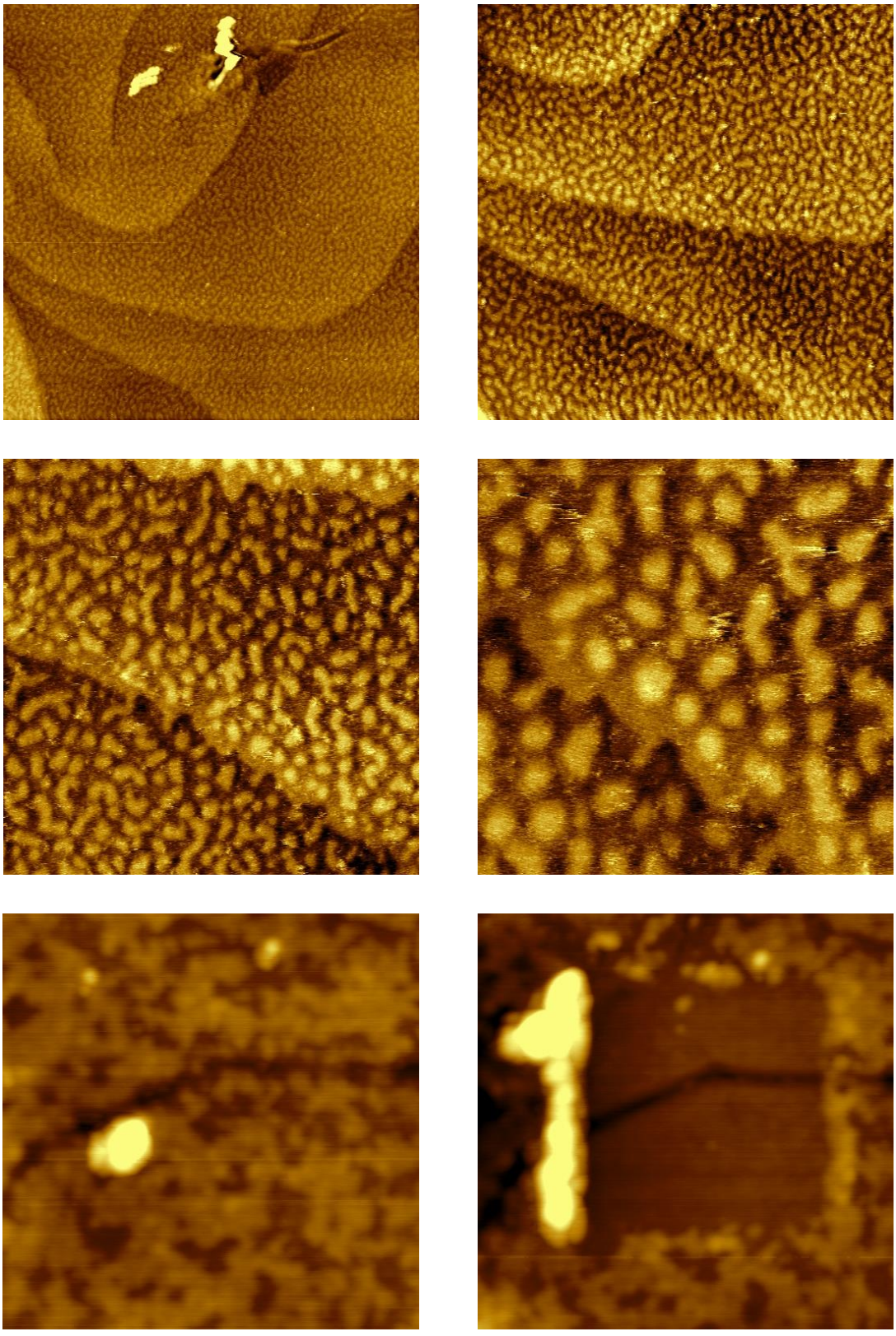

Figure 101: Scanning probe micrographs of adsorbed layer of $Me_3\beta CD$-Cys-SH. Scanning tunneling micrographs: scan-size 500 nm (upper left), 300 nm (upper right), 150 nm (middle left) and 75 nm (middle right). Bias voltage 100 mV, set-point current 20 pA, z bar 2 nm. TOP-MAC atomic force micrographs: scan-size 1000 nm before (lower left) and after (lower right) CM imaging. A/A_0 = 90 %, probe frequency 62 kHz, scan-speed 1 line/s, z bar 20 nm.

Scanning tunneling micrographs are of much better resolution than their atomic force counterparts. For instance, the upper left panel of Figure 101 shows the STM micrograph with 500 nm scan-size, showing discernible the structures on the surface. Lower left panel is the AFM micrograph with the scan-size 1000 nm, showing clusters of structures rather than the structures themselves. The discrepancy between the two SPM techniques may easily be explained by a finite size of the AFM probe. The resulting AFM micrograph is always the convolution of both sample topography and the probe shape. On the other hand, the STM probe is believed to have only one (or few) atoms at its apex, through which the tunneling current flows. Generally speaking, scanning tunneling micrographs are usually of a better resolution.

Both AFM and STM topography maps were further subjected to the quantitative analysis. In the STM technique, the height of the surface structures is correct only when a structure is connected to the surface conductively. The molecule of Me_3βCD-Cys-SH is not an ideal conductor as it not conjugated. The height of the found structures is therefore misleading. On the other hand, lateral dimensions of the structures are reliable. Though STM predominantly revealed the presence of the bead-like structures (see four upper panels in Figure 101), one can also find round separated particles well discerned in the middle two panels. Twenty different individual particles were measured and their average diameter was found to be 4.3 ± 0.7 nm.

As mentioned above, the AFM figures reflect both the sample topography and the probe shape. For structures much smaller than the AFM probe diameter usually in the range 10 – 20 nm, the resulting AFM image may differ from the real topography of the sample surface, with lateral dimensions of the structures being overestimated. The atomic force micrographs (lower two panels of Figure 101) are therefore not as sharp as scanning tunneling micrographs of a comparable scan-size. However, the AFM technique may be very useful in the determination the height of the adsorbed layer. Surface scratching analysis revealed that the difference between the top-sites of the structures and the underlying gold substrate is 4.2 ± 0.7 nm, being in a perfect agreement with the average particle diameter found by the STM technique (4.3 ± 0.7 nm).

The average diameter of the Me_3βCD-Cys-SH molecule is ≈ 2.0 nm. One single spherical particle is therefore composed of a small number of molecules.

4.8 Electrochemical properties of benzothiazolium and quinolinium cations

N-heteroaromatics are organic compounds containing nitrogen atom in an aromatic ring. One necessary condition for a compound to be called "aromatic" is the planarity. The sp^2 hybridized nitrogen atom may serve as a constituent of planar aromatic rings. For instance, the pyridine molecule contains sp^2 hybridized nitrogen atom in the ring, with a lone pair being outside. When protonized, the lone pair forms a σ-bond between the nitrogen and hydrogen atoms, with the aromaticity being retained. Generally, when the hydrogen atom is replaced by an alkyl or an aryl moiety, N-heteroaromatic cations are obtained.

N-heteroaromatics comprise many compounds important in human history. For instance, berberine, a yellow pigment found in the roots of goldenseal, was used in ancient and medieval times to dye wood, leather and wool [183]. In 1664, Irish physicist and chemist Robert Boyle discovered that litmus, a plant extract composed of the fifteen N-heteroaromatic compounds [184], would gradually change color upon additions of acids and bases [185,186]. Litmus thus became the first chemical indicator. A more recent member of the family of N-heteroaromatics is ethidium bromide, a synthetic compound frequently used in the gel electrophoresis to stain DNA [187].

Synthetic N-heteroaromatic compounds [188–190] are generally of considerable interest due to their potential applications as fluorescent dyes, stains and markers. When transported to living cells, they may undergo redox reactions due to the presence of various oxidizing and reducing agents.

The properties of extended viologens, which are pyridinium-based N-heteroaromatic cations, were treated in the previous chapters. In this part of the thesis, the electrochemical properties of two newly synthesized N-heteroaromatic cations, namely a benzothiazolium $\mathbf{Bz}^+$ and a quinolinium $\mathbf{Qn}^+$, are investigated. Both compounds could one day serve as electroactive elements in the molecular switches. The molecules involve positively charged nitrogen atom incorporated within the aromatic skeleton. Additionally, the $\mathbf{Bz}^+$ ion contains a sulfur atom. In both compounds, the positive ion is balanced by the triflate anion. As these compounds are cationic, they are assumed to be susceptible to the electrochemical reduction.

Figure 102 (left panel) shows the cyclic voltammogram of $\mathbf{Bz}^+$ measured in acetonitrile containing 0.1 M $TBAPF_6$ as the supporting electrolyte. The two reduction waves are observed. The first one at -0.95 V is of main interest this study. The ratio of cathodic and anodic peak current heights approaches unity, suggesting that no follow-up reactions occur upon the electron transfer. The separation of the two peak currents is 59 mV at scan-rate

65 mV/s, with slightly increased values for higher scan-rate values. This suggests that the electron transfer is nearly reversible. The right panel of Figure 102 shows the corresponding sampled DC polarogram with no signs of irreversibility.

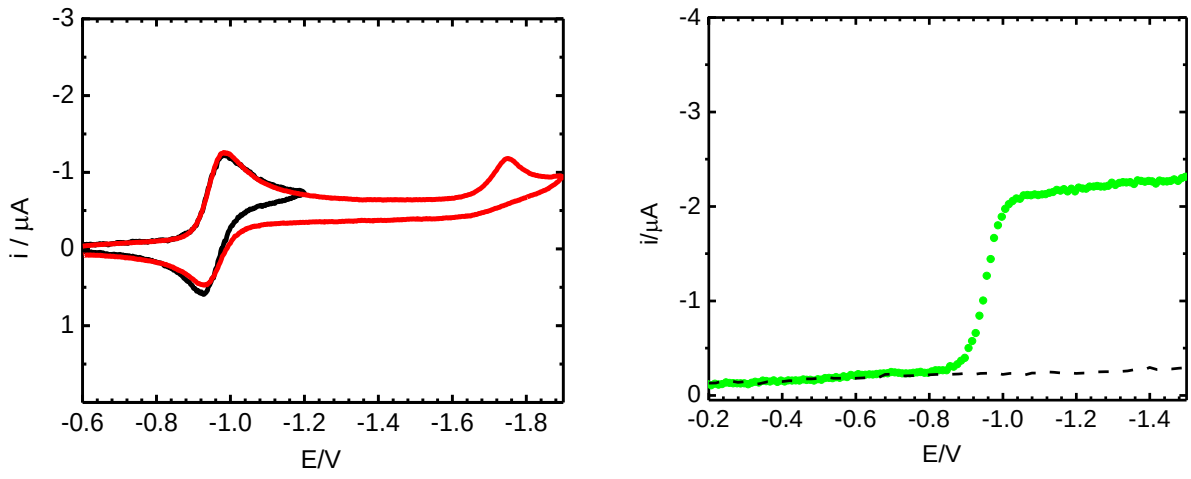

*Figure 102: Cyclic voltammogram (left panel) and sampled DC polarogram (right panel) of 1.0 mM **BzTfO** in AN containing 0.1 M TBAPF$_6$ as the supporting electrolyte.*
Left panel: scan-rate 0.065 V/s, platinum electrode was employed.
*Right panel: sampling time 2s, SMDE. Only the first wave is shown (green curve). Dashed line represents sampled DC polarogram obtained in the absence of **BzTfO**.*

The results of both cyclic voltammetry and sampled DC polarography were subjected to further analysis. The peak current height was well comparable to that measured for Fc at the same concentration and scan-rate, indicating that one electron is transferred in the reduction step at -0.95 V. The height of the reduction wave observed in sampled DC polarogram was comparable to that obtained for the first reduction wave of MV, confirming the consumption of one electron. The second reduction step was, due to its significantly more negative potential value, not investigated. The following very simple mechanism depicts the electrochemical behavior of **Bz**$^+$ cation

$$Bz^+ + 1e^- \longrightarrow Bz^0 \qquad (100)$$

The compound **Bz**$^+$ was further scrutinized by AC polarography. The electrochemical behavior was investigated at various AC frequency values, falling in the range 6.4 Hz – 1600 Hz. Figure 103 shows two typical AC polarograms of **BzTfO** at 16 Hz and 160 Hz**.**

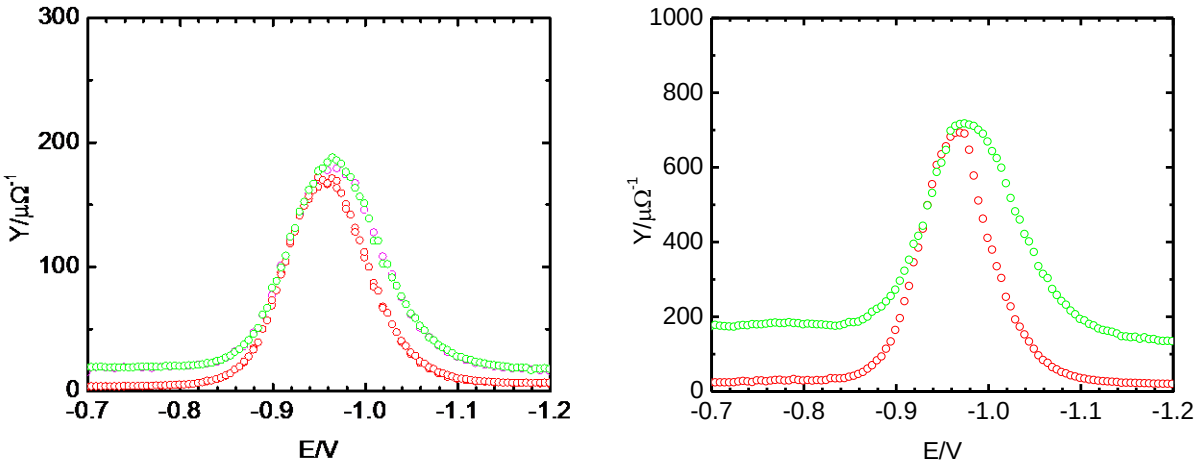

*Figure 103: AC polarograms of 0.1 M $TBAPF_6$ in AN containing 1.0 mM **BzTfO** at 16 Hz (left panel) and 160 Hz (right panel). SMDE was used as the working electrode with drop-time 3s. Red line and green line represent the real and the imaginary part of the cell admittance, respectively.*

AC polarogram at 16 Hz (left panel) shows no signs of the electrochemical quasi-reversibility as the real and the imaginary part of the faradaic admittance are of equal height. The faradaic maxima are only slightly shifted (by less than 15 mV) from the standard redox potential of the first reduction wave (-0.95 V), determined by the cyclic voltammetry and sampled DC polarography. AC polarogram at 160 Hz shows slightly quasi-reversible electrochemical behavior, with the real and imaginary faradaic maxima shifted by 15 and 25 mV from the standard redox potential value. Obviously, the height of the imaginary component of the faradaic admittance is somewhat lower than that of its real counterpart, the feature being characteristic for electrochemically quasi-reversible systems. The measurements at various frequency values allowed the value of the standard heterogeneous rate constant to be determined. Only frequency values greater than 64 Hz were considered, as the measurements at lower frequencies led to AC polarograms, in which the real and imaginary components of faradaic admittance were of equal height. The resulting value k^0 = 0.2 cm/s suggests a very fast electron transfer in the first reduction step of $\mathbf{Bz}^+$.

A qualitatively different behavior was observed for $\mathbf{Qn}^+$ cation. Figure 104 shows the cyclic voltammogram of 1.0 mM **QnTfO** in AN containing 0.1 M $TBAPF_6$ as the electrolyte.

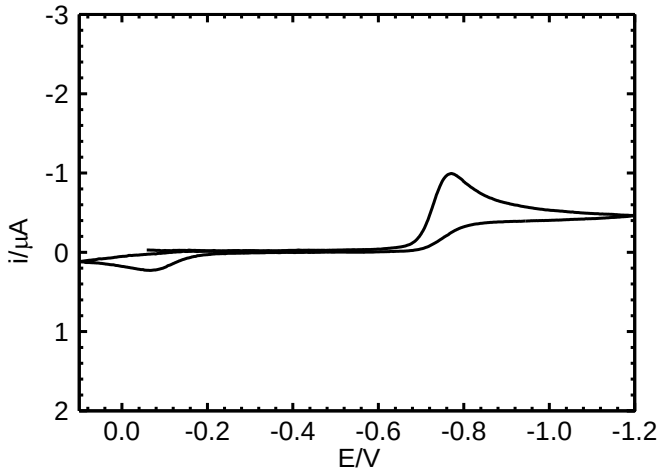

*Figure 104: Cyclic voltammogram of 1.0 mM **QnTfO** in AN containing 0.1 M $TBAPF_6$ as the supporting electrolyte. Platinum electrode, scan-rate 0.065 V/s. Initial potential: -0.10 V, first vertex potential: -1.20 V, second vertex potential: +0.10 V, final potential: -0.40 V.*

When the potential is swept in the negative direction, a reduction (forward) peak appears at ca -0.75 V. The peak has the shape characteristic for a reversible electrochemical process. However, the corresponding backward peak is absent. The back-scan shows an oxidative process at -0.07 V with the peak shape corresponding to a reversible electron transfer, with the complementary (i.e. reduction) peak absent. The separation between the two observed peak currents (0.68 V) is considerably larger than that expected for a reversible transfer of one electron (59.2 mV). The increased peak separation may either be caused by a slow electron transfer (electrochemical irreversibility) or by the presence of homogenous kinetics (chemical irreversibility). Figure 105 shows the sampled DC polarogram of 1.0 mM **QnTfO** in AN containing 0.1 M $TBAPF_6$.

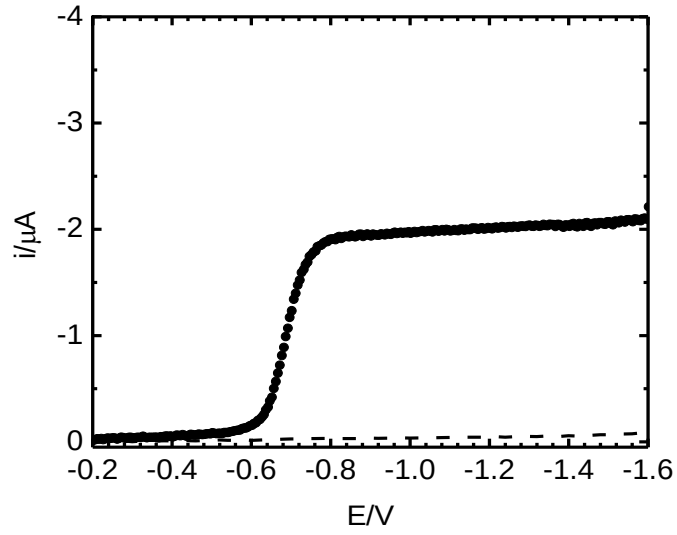

*Figure 105: Sampled DC polarogram of 1.0 mM **QnTfO** in AN containing 0.1 M $TBAPF_6$ as the supporting electrolyte. Sampling time 2s, measured with SMDE. Dashed line obtained in the absence of **QnTfO**.*

No signs of a the wave broadening are observed and, therefore, the irreversibility is probably of a chemical and not of an electrochemical nature. This is consistent with the forward peak shape shown in the cyclic voltammogram. To further confirm this assumption, we decided to calculate the heterogeneous standard rate constant of the electrochemical reduction. The value may either be deduced from AC polarograms (as it was done in the case of **Bz**$^+$) or from the electrochemical impedance spectroscopy measurements. The latter option was chosen for **Qn**$^+$. Figure 106 shows the complex plane plots measured for the electrochemical cell containing 1.0 mM **QnTfO** at electrode potential values pertaining to the reduction process.

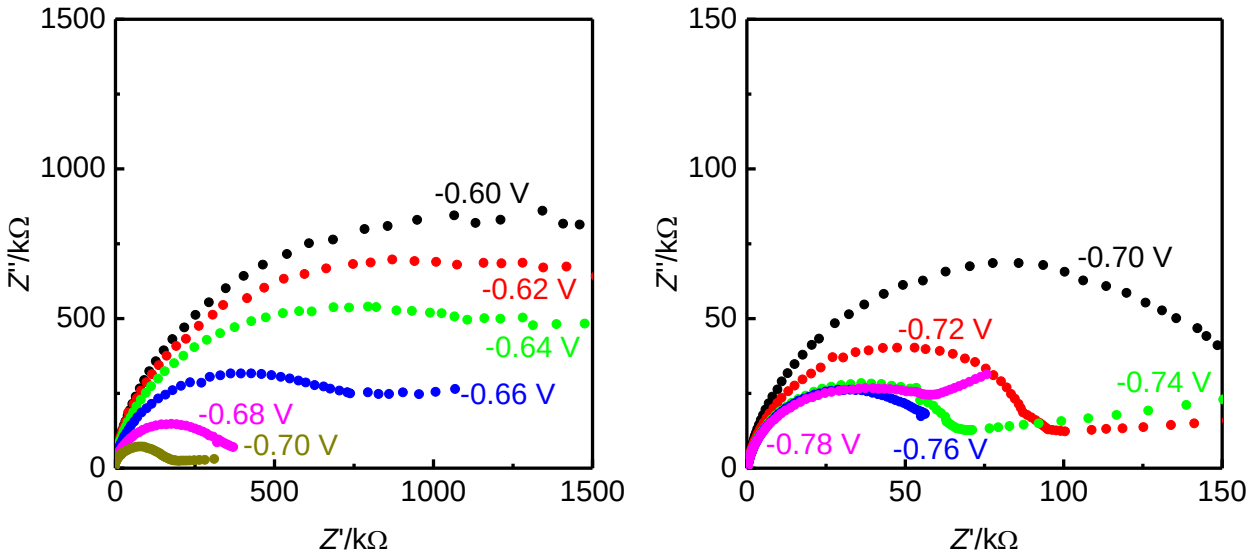

*Figure 106: Complex plane plot obtained at various electrode potential values close to standard redox potential of electrochemical reduction of **QnTfO** (-0.75 V). The respective potential values are denoted by different colors. The left panel shows the frequency response at potentials $E \leq$ -0.70 V, while the data obtained for more negative potential values are plotted in the right panel. Notice the scale difference between the two panels. For better insight, the data for -0.70 V are shown in the both panels.*

The radius of the circles equal to $R_{ct}/2$ decreases as the potential becomes more negative. The linear part of the frequency responses, where the diffusion is the rate-determining step should theoretically make the angle 45° with both axes. This was, however, not observed (see for example the green and red traces in the right panel of Figure 106), possibly due to the presence of homogenous reaction. In the equivalent circuit, the Warburg impedance was therefore replaced by the constant phase element with a variable exponent *n*, with $0 < n < 1$ (n = ½ holds for the Warburg element). Figure 107 shows two characteristic AC polarograms of 1.0 mM **QnTfO** (at 16 Hz a 160 Hz) in AN containing 0.1 M $TBAPF_6$.

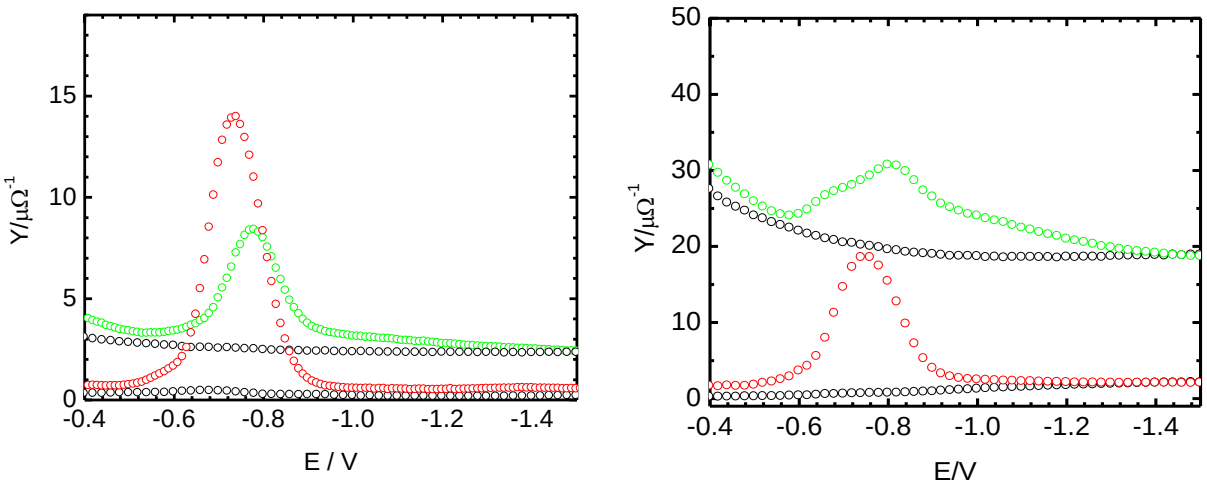

*Figure 107: AC polarograms of 0.1 M $TBAPF_6$ in AN containing 1.0 mM **QnTfO** at 16 Hz (left panel) and 160 Hz (right panel). SMDE was used as the working electrode, with drop-time 3s. Red line and green line represent the real and the imaginary part of the cell admittance. Black lines depict the cell admittance obtained in the absence of **QnTfO**.*

The data shown in Figure 107 may be compared to those obtained for the compound **BzTfO** in Figure 103. While only slight differences in peak the heights were observed for **BzTfO** at 160 Hz, a severe peak broadening is noticed at this frequency for **QnTfO**. This further confirms large differences in the electron transfer of the compounds **BzTfO** and **QnTfO**.

Results of electrochemical impedance spectroscopy measurements were subjected to numerical fitting (employing the program FRA, Autolab, Ecochemie, The Netherlands). Figure 108 shows the found charge transfer resistance as a function of the electrode potential.

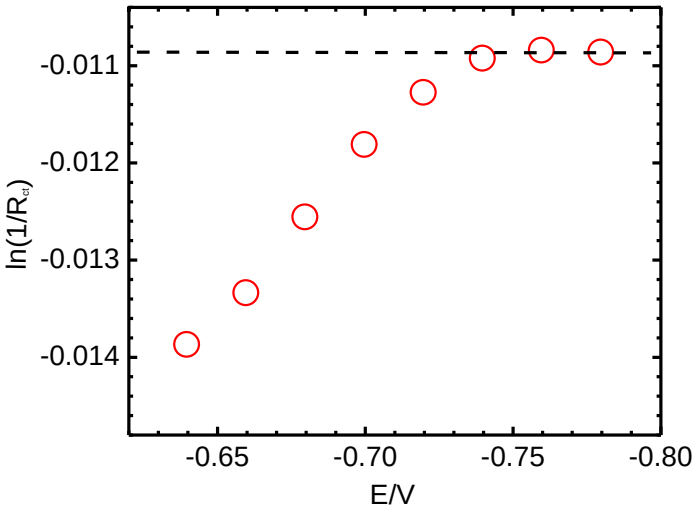

*Figure 108: Charge transfer resistance as a function of the applied electrode potential for the reduction wave of 1.0 mM **QnTfO**. Each point is the ln(1/R_{ct}) value extracted from numerical fitting using the modified Randles equivalent circuit. Measured in AN containing 0.1 M $TBAPF_6$ as the supporting electrolyte.*

For the potential value E = -0.75 V, the value R_{ct} = 56 kΩ was found, which gives the value k^0 = 0.007 cm/s. Based on this value, the electron transfer is rather facile and the observed irreversibility must be of a chemical nature.

The electrochemical reduction process generates neutral species

$$Qn^{+} + 1e^{-} \longrightarrow Qn^{0} \qquad (101)$$

which are not mutually repelled by coulombic interactions and contain an unpaired electron. They seek a reaction partner possessing an unpaired electron to recombine the two electrons. The dimerization may therefore take place

$$Qn^{0} + Qn^{0} \longrightarrow Qn_2^{\ 0} \qquad (102)$$

As the Qn^0 are consumed in the course of homogenous dimerization, the backward oxidation peak is absent. The dimer molecules $Qn_2^{\ 0}$ may transfer two electrons at sufficiently positive potential values

$$Qn_2^{\ 0} \longrightarrow 2Qn^{+} + 2e^{-} \qquad (103)$$

with the parent form being regenerated.

Figure 109 shows the simulated voltammograms (for the presence and absence of the dimerization) along with the experimentally obtained one.

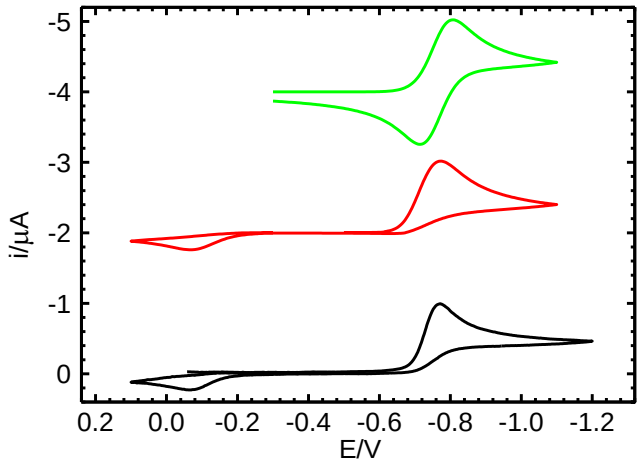

*Figure 109: Experimentally obtained (black line) and simulated voltammograms of **QnTfO** in the presence (red line) and absence (green line) of dimerization. Scan-rate 0.065 V/s.*

Green line shows the simulated voltammogram of a quasi-reversible electron transfer in the absence of the dimerization employing the simulating parameters E^0 = -0.75 V and k^0 = 0.007 cm/s. The voltammogram shows the backward oxidation peak and is therefore different from its experimental counterpart. Therefore, the shape of the experimentally obtained voltammogram cannot be explained by the electrochemical quasi-reversibility.

Red line shows the simulated voltammogram of the quasi-reversible electron transfer with the above mentioned parameters in the presence of homogenous dimerization

$Qn^0 + Qn^0 \longrightarrow Qn_2^{\,0}$, with the electron transfer reaction $Qn_2^{\,0} \longrightarrow 2Qn^+ + 2e^-$ being taken into account at E_2^0 = -0.07 V. The simulated voltammogram fits nicely its experimental data. Therefore, the dimerization explains the electrochemical behavior of **QnTfO**.

One may notice that in both simulated and experimentally obtained voltammogram, the height of the anodic peak at -0.07 V is lower than that of the cathodic peak at -0.75 V. The height inequality may be explained as follows. Dimer species $Qn_2^{\,0}$ are generated by the homogenous process in the solution. The back-scan traces the oxidation of only those molecules that are sufficiently close to the electrode. Some portion of the dimer molecules never diffuses back to the electrode and therefore some dimer molecules cannot be oxidized in the back-scan. Moreover, the diffusion coefficient of the dimer molecules is lower than that of the parent form, which further decreased the observed anodic current value.

The question remains why the two compounds have considerably different electrochemical behavior though their molecules are very similar. To answer it the theoretical calculations employing density functional theory (DFT) were carried out. The two important input parameters besides the structure of the molecule are total electric charge and spin multiplicity. The reduced forms of both species are neutral and possess an unpaired electron, which implies the doublet spin multiplicity and zero overall charge. The DFT calculations were carried out employing B3LYP functional and 6-31G* basis set with exactly the same conditions for both molecules. Figure 110 shows the relative spin density of the reduced forms of the compounds, $Bz^{0\cdot}$ (left image) and $Qn^{0\cdot}$ (right image).

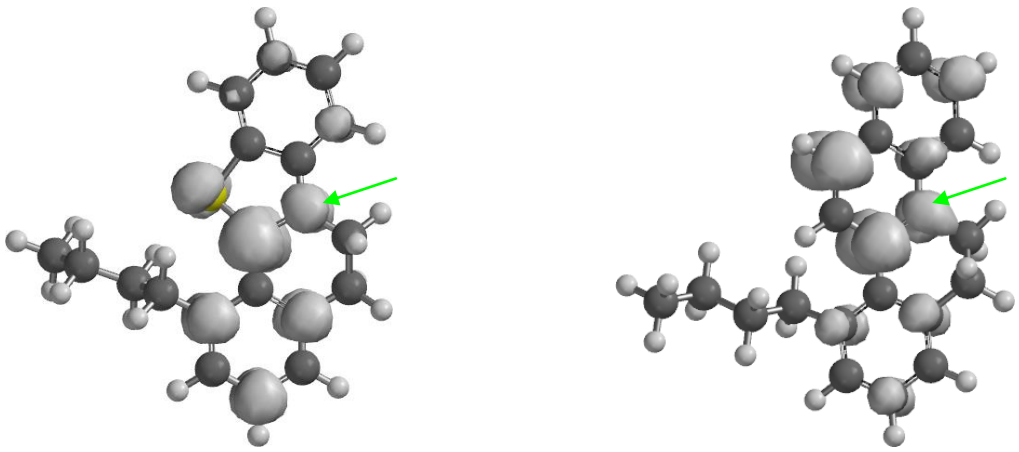

Figure 110: Relative spin density of the reduced forms of $Bz^{0\cdot}$ (left image) and $Qn^{0\cdot}$ (right image). The spin density is proportional to the size of the gray lobes. Sulfur atom is denoted by yellow color, nitrogen atoms are hidden behind the lobes and are indicated by green arrows.

Though the molecules are very similar, some differences in the spin density may easily be discerned. In the molecule of $Bz^{0\cdot}$ (left figure), an unpaired electron is mainly localized on the carbon atom between the nitrogen atom (green arrow) and sulfur atom (yellow ball). A high spin density is also found on an equivalent carbon atom in the molecule of $Qn^{0\cdot}$ (lower carbon atom in the second upper ring, right next to the nitrogen atom). In both molecules, this atom is not assumed to be reactive as it is hidden within the aromatic skeleton of the molecule. Moreover, the dimerization employing this atom as a reactive site would lead to severe disintegration of the aromatic conjugation, which is not energetically favorable. The other atom with high localized spin density may be found on the carbon atom in the second upper ring of the molecule of $Qn^{0\cdot}$ opposite to the nitrogen atom. This atom is a possible active site as it is easily accessible and the dimerization may take place without the loss of aromaticity. This type of the reaction site is not encountered in the $Bz^{0\cdot}$ molecule. Sulfur atom is not assumed to serve as the reaction site for the dimerization. This may explain the resistance of the $Bz^{0\cdot}$ form with respect to the dimerization.

5 CONCLUSION

Anchoring of molecular wires to the metallic electrodes is a crucial issue for possible communication of molecular devices with the outside environment. This can be elucidated from a spontaneous adsorption. To the best of our knowledge, the adsorption studies of the extended viologen molecules have not been carried out. In this work we show that the compounds **1** to **6** all adsorb at the mercury/electrolyte interface. In a certain range of electrode potentials, the compounds form a self-organized compact monolayer, the formation of which is diffusion-limited. The experimentally obtained single-molecule area values were compared to those calculated by the space-filling model. The parallel orientation of the molecules was inferred. At the potentials pertaining to the electron transfer of the compounds, the reorientation of the molecules was observed. The presence of the molecules on metallic interfaces was also confirmed by scanning tunneling microscopy and polarization modulation infrared reflection absorption spectroscopy.

Lateral electronic communication between individual molecules in a monolayer is not desirable. Proper insulation, which does not impede the vectorial electron transfer, was not addressed till now. In this respect, inclusion complexes of the compound **1** with CD hosts were scrutinized. While no inclusion of **1** into the cavity of βCD and γCD was observed, the complexes **1**:αCD and **1**:$(\alpha CD)_2$ were found. Hence cyclodextrin complexes of the extended viologen molecules may serve as the models of insulated molecular wires.

The electrochemical studies of the extended viologen compounds are very rare. The results of our investigations suggest that all compounds **1** to **6** reversibly transfer electrons. The shortest extended viologen (the compound **1**) was found to transfer four electrons. The molecule of **1** behaves as a fully delocalized system. On the other hand, the compound **2** accepts two electrons independently, having thus two non-communicating redox centers. Extended viologens with longer molecules (the compounds **3** to **6**) transfer *2(n-1)* electrons, *n* being the number of repeating units in the molecule.

Electric conductivity of the metal/molecule/metal junctions containing the compounds **1** to **6** was investigated by the scanning tunneling spectroscopy technique. The single-molecule conductivity was found to decrease exponentially with the length of the molecule forming the junction. The found conductivity values are in the range of 3 – 5 nS and are higher than those obtained for aliphatic molecular wires of a comparable length e.g. 1.6 nS for decanedithiol.

Proper isolation methods should suppress the homogenous cross-exchange reactions of multiply reduced forms of the extended viologens. Indeed, homogenous reactions were found

to strongly affect the electrochemical behavior of the compounds **1'** and **4'**. In the case of the compound **1'**, the electron consumption in the first reduction step was found to depend on the time scales of the experiments. Electrochemical systems, containing the molecules of the compound **4',** show transitions from stability to a periodical and a chaotic behavior. In some cases, the obtained current transients resembled the bifurcation diagram constructed for the logistic map. We were the first to experimentally verify the value of the Feigenbaum universality constant employing an electrochemical system. When a well-defined bias potential is applied, the compound **4'** yields sinusoidal current oscillations. It may be considered as a model of the single-molecule oscillator.

Besides the extended viologens, benzothiazolium and quinolinium cations were also investigated in this study. Benzothiazolium cation was found to reversibly accept an electron, while a strong tendency towards the dimerization was observed in the case of quinolinium cation. The results of electrochemical measurements were supported by the DFT calculations. The two compounds may be considered as possible candidates for electroactive components in molecular electronic devices.

Besides the research of the long conducting molecules, the experimental work also tackled a simple isolated redox systems. Inclusion complexes of Fc with αCD, βCD, Me_2βCD and Me_3βCD hosts were investigated in the environments with a varying relative permittivity. The hosts βCD, Me_2βCD and Me_3βCD were found to form reasonably strong complexes with Fc. A good correlation between the complex formation constant and the solvent relative permittivity was found. The layer of anchored Me_3βCD molecules on the monocrystalline gold surface was prepared. The results of the studies will be exploited in the construction of non-covalent Fc:CD-based molecular switches.

6 APPENDIX

Besides the topics discussed in the previous chapters, I also focused on the study of the electron transfer in the oligo(p-phenylene-ethynylene)-based molecular wires and on the interfacial properties of fullerene clusters.

6.1 Electrochemical and spectroelectrochemical properties of molecular wires with oligo(p-phenylene-ethynylene) backbone

Oligo(p-phenylene-ethynylene)s (OPEs) attract considerable attention as they may serve as molecular wires [191–196] and form the shape-persistent molecular scaffolds [197–201]. The OPEs often need to be functionalized in order to increase their solubility [198,202] or alter their physicochemical properties [194].

This part of the thesis focuses on the electrochemical properties of short monodisperse OPEs bearing attached tetrathio- substituted tetrathiafulvalene (TTF) units. The compounds are denoted as **OPE-TTF$_2$**, **OPE-TTF$_4$** and **OPE-TTF$_6$**, according to the number of TTF groups in the molecule. Molecules of all three compounds are neutral. TTF group is known to transfer one electron per one molecule in its first oxidation step [199]. One therefore expects that in the first oxidation step, the molecule of the compounds **OPE-TTF$_2$**, **OPE-TTF$_4$** and **OPE-TTF$_6$** transfers two, four and six electrons, respectively.

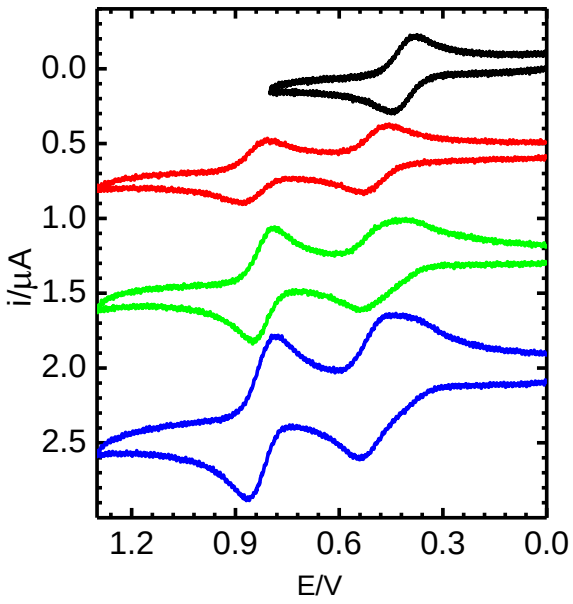

*Figure 111: Cyclic voltammograms of 0.20 mM ferrocene (black line), **OPE-TTF$_2$** (red line), **OPE-TTF$_4$** (green line) and **OPE-TTF$_6$** (blue line). Measured in DCE containing 0.1 M TBAPF$_6$ as the supporting electrolyte. Pt was used as the working electrode. Scan-rate: 0.5 V/s. The voltammograms are vertically displaced for better visualization.*

Figure 111 shows the cyclic voltammograms of the compounds **OPE-TTF$_2$**, **OPE-TTF$_4$** and **OPE-TTF$_6$** along with that obtained for the Fc/Fc^+ redox couple under the same conditions.
For all three compounds, two oxidation processes were observed. Table 8 summarizes the standard redox potential values of both oxidation processes for all three compounds as well as that of Fc/Fc^+ couple. DCE was used as the solvent with 0.1 M $TBAPF_6$ as the supporting electrolyte. The voltammograms shown in Figure 111 were all obtained using the same platinum electrode at scan-rate 0.5 V/s.

Compound	E_1^0 / V	E_2^0 / V	m_1^∞ / ($\mu C/s^{1/2}$)	m_2^∞ / ($\mu C/s^{1/2}$)
Fc	0.41	-	0.119	-
OPE-TTF$_2$	0.49	0.85	0.103	0.096
OPE-TTF$_4$	0.48	0.83	0.173	0.176
OPE-TTF$_6$	0.49	0.84	0.279	0.276

*Table 8: Comparison of the standard redox potential and limitting current values (see further) of the compounds **OPE-TTF$_2$**, **OPE-TTF$_4$** and **OPE-TTF$_6$** and Fc.*

In the case of all three compounds, the both oxidation steps take place nearly at the same potential. For all compounds, the peak current height of the first and the second oxidation processes is roughly equal. This suggests that, for a given compound, the same number of electrons is transferred in the two successive oxidation processes. For any oxidation wave, the ratio of the anodic and cathodic peak current values approaches unity, suggesting thus the reversibility of the electron transfer. In the case of **OPE-TTF$_2$**, the separation of the anodic and cathodic peak current values is 60 mV, which further confirms the electrochemical reversibility. For the compounds **OPE-TTF$_4$** and **OPE-TTF$_6$**, the first wave is, however, slightly split with the main wave being preceded by a shoulder.
At first sight, the peak current height of the first oxidation step of the compound **OPE-TTF$_2$** (red line in Figure 111) is roughly equal to that obtained for the oxidation of Fc at the same concentration (black line). This suggests that only one electron is transferred. As mentioned above, the two-electron process was anticipated in the first oxidation step for the compound **OPE-TTF$_2$** as it contains two TTF moieties.
In the first oxidation step of the compounds **OPE-TTF$_4$** (green line in Figure 111) and **OPE-TTF$_6$** (blue line in Figure 111) the peak current is roughly two and three times higher than that observed for the compound **OPE-TTF$_2$** and Fc. This suggests that two and three electrons

are transferred in the first oxidation step, instead of four and six, deduced from the number of TTF moieties in the molecules.

The voltammetric data were further transformed into the steady-state current profiles. They are more convenient for the exact determination of the electron consumption. The transformation based on the convolution principle is employed [123].

In the cyclic voltammetry, one may consider the electric current to be a function of time, $i = i(t)$, rather than the function of the electrode potential, $i = i(E)$. Time and electrode potential are related by the scan-rate, v, always precisely defined. For an anodic sweep, the potential value may easily be obtained at any time as $E = E_i + vt$, with E_i being the initial potential, $E_1 = E(t=0)$. For a chosen time one may evaluate an integral

$$m(t) = \int_0^t \frac{i(u)}{(t-u)^{1/2}}\,du \qquad (104)$$

The value of integral $m(t)$ depends on the contributions of electric current $i(u)$ at times u smaller than time t at which the integral value is to be determined. For oxidation processes, the anodic current decreases for $E > E^0$, or alternatively, for time values higher than time at which the E_0 value was reached. For sufficiently high times i.e. at sufficiently positive electrode potential the $m(t)$ value reaches a constant value. If one plots the m value against t (or alternatively against E), a shape resembling the sampled DC polarogram is obtained. The height of the "wave" is denoted as m^∞. The electric current value is proportional to the number of electrons transferred. The m^∞ value may therefore be used to determine the electron consumption. From the mathematical point of view, $m(t)$ is called the semi-integral of the electric current

$$m(t) = \frac{d^{-1/2}}{dt^{-1/2}} i(t) \qquad (105)$$

The above-mentioned procedure is therefore frequently called the semi-integration. In practice, the integral is replaced by the sequence of sufficiently small time intervals, through which the contributions of electric current are summed. The semi-integrated curves $m = m(E)$ are treated in the very same way as the common polarographic waves.

Table 8 shows the values of m^∞ of the two successive oxidation steps for all three compounds as well as for the oxidation of Fc. Figure 112 shows the corresponding m against E curves (Fc is not shown here). The m^∞ value for the first oxidation step of **OPE-TTF$_2$** (0.103 μC/s$^{1/2}$) is nearly identical to that measured for the oxidation of Fc (0.119 μC/s$^{1/2}$). Slightly lower value for **OPE-TTF$_2$** is likely caused by an inequality of the diffusion coefficient values, as the molecule of **OPE-TTF$_2$** is much larger than that of Fc. The second oxidation step gives the

value m_2^{∞} = 0.096 μC/s$^{1/2}$, corresponding to the transfer of one electron. Similarly, the compounds **OPE-TTF$_4$** and **OPE-TTF$_6$** were found to consume two and three electrons in both their oxidation steps.

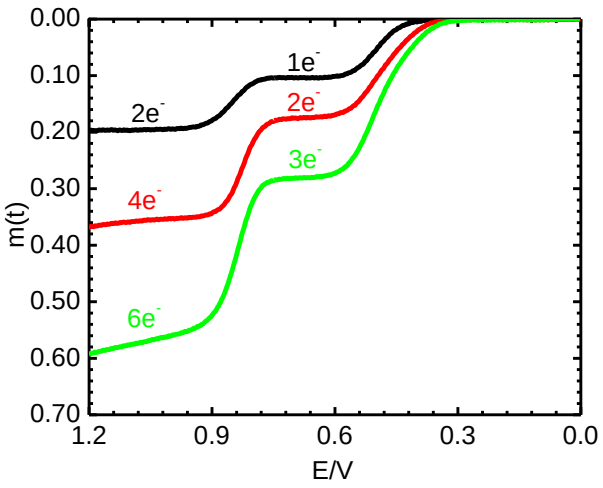

*Figure 112: The semi-integral m as a function of the electrode potential for the compound **OPE-TTF$_2$** (black line), **OPE-TTF$_4$** (red line) and **OPE-TTF$_6$** (green line). Measured in DCE containing 0.1 M TBAPF$_6$ as the supporting electrolyte. Pt was used as the working electrode. Numbers denote the overall electron consumption.*

For all three compounds, the experimentally found electron consumption was exactly one half of that deduced from the number of TTF groups present in the molecules. Therefore, only one half of the TTF moieties transfer an electron, the second half of the groups being electrochemically silent.

To elucidate the nature of electron transfer in the compounds, the first oxidation "waves" of the semi-integrated curves were further subjected to the log-plot analysis. For all compounds, the slope was equal to roughly 60 mV, indicating the transfer of one electron. However, as mentioned above, the wave height clearly confirmed the transfer of two and three electrons for the compound **OPE-TTF$_4$** and **OPE-TTF$_6$**. Therefore, the transfer of electrons takes place independently. An individual TTF group pair, which is composed of one electroactive and one silent TTF group, is not communicating with the other group pair(s) in the molecule. Each individual group pair transfers one electron independent of the other group pair(s). The slope of the first oxidation wave indicates the transfer of an individual electron in each group pair, while the wave height is proportional to the number of group pairs.

The individuality of the TTF group pairs in the molecules was further confirmed by the in-situ UV/VIS/NIR spectroelectrochemical techniques. Figure 113 shows the in-situ UV/VIS/NIR spectra of the compounds **OPE-TTF$_2$** (upper two panels), **OPE-TTF$_4$** (middle two panels)

and **OPE-TTF$_6$** (lower two panels). The spectra are obtained in the course of electrolysis at potential values +0.70 V (left panels) and +1.00 V (right panels), where the first and the second oxidation steps are diffusion limited.

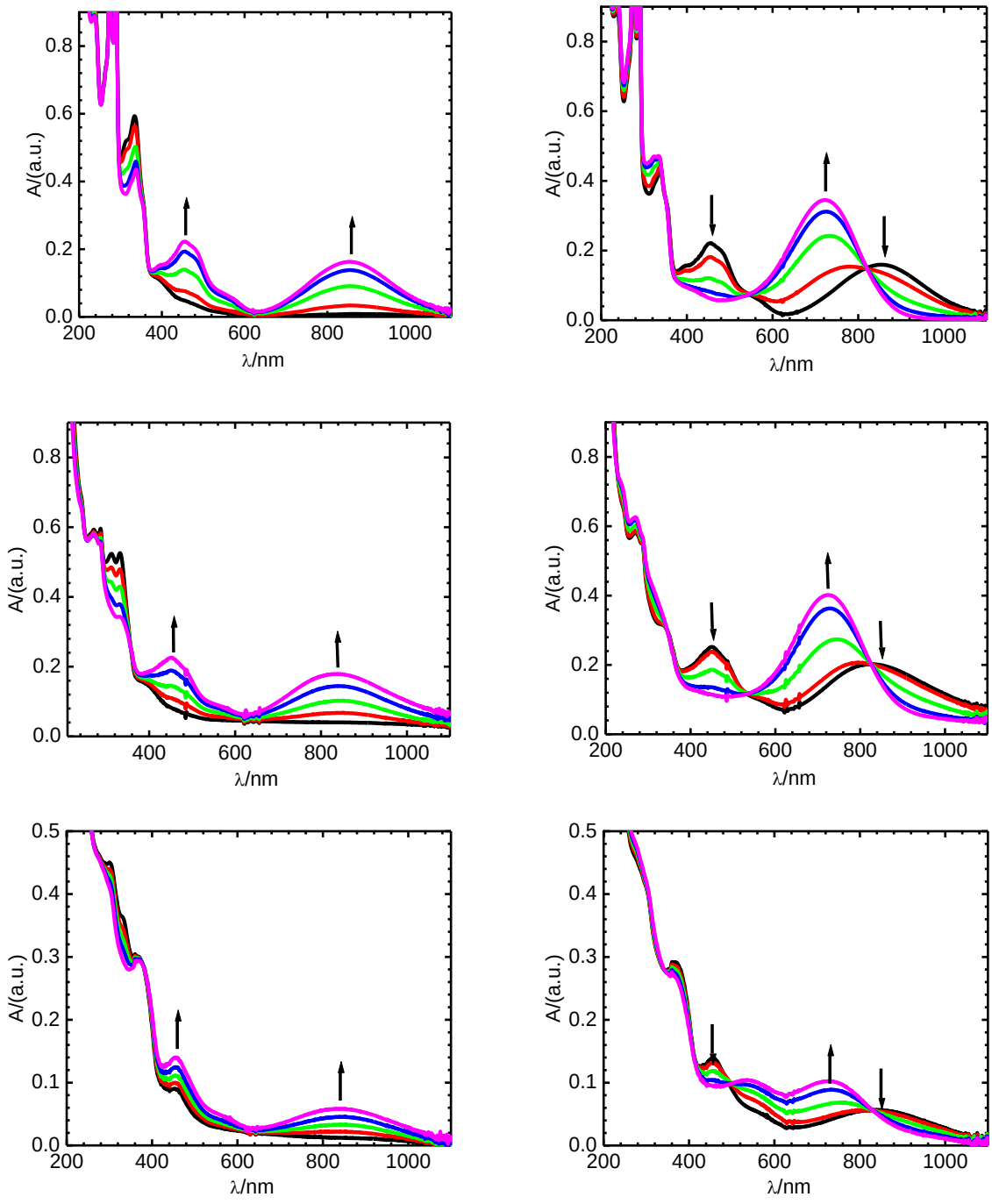

*Figure 113: In-situ UV/VIS/NIR spectra of 0.97 mM **OPE-TTF$_2$** (upper two panels), 0.48 mM **OPE-TTF$_4$** (middle two panels) and 0.34 mM **OPE-TTF$_6$** (lower two panels) during the electrolysis at +0.70 V (left panels) and +1.00 V (right panels). Measured in DCE containing 0.2 M $TBAPF_6$ as the supporting electrolyte. Arrows indicate changes of the absorption bands. Initial and final spectra are denoted by black and purple line, respectively.*

For all three compounds, the spectra measured at the respective potential values are very similar. Table 9 shows the absorption band maxima emerging during the first and the second oxidation step.

Compound	1st oxidation step		2nd oxidation step
OPE-TTF$_2$	457 nm	853 nm	723 nm
OPE-TTF$_4$	451 nm	839 nm	725 nm
OPE-TTF$_6$	453 nm	842 nm	724 nm

*Table 9: Absorption maxima of characteristic bands for the compounds **OPE-TTF$_2$**, **OPE-TTF$_4$** and **OPE-TTF$_6$** during the electrolysis in the first (middle column, at potential +0.70 V) and the second (right column, at potential +1.00 V) oxidation step. Measured in DCE containing 0.2 M TBAPF$_6$ as the supporting electrolyte.*

During the electrolysis at potential, where the first oxidation process is diffusion-limited (+0.70 V), the two bands at roughly 450 nm and 840 nm emerge for all three oligomers. The occurrence of the latter spectral band reflects the formation of $TTF^{+\cdot}$ radical cation [203–205]. The two bands gradually disappear, when the potential is stepped to the value where second oxidation process is diffusion-limited (+1.00 V). A new band emerges at roughly 720 nm. As the band centered at 840 nm disappears upon the second oxidation process, the form $TTF^{+\cdot}$ is not present in the system anymore. A doubly oxidized form, TTF^{2+}, is generated instead. As the absorption maxima for all three compounds are located nearly at the same wavelength values (450 nm and 840 nm for the first and 720 nm for the second oxidation step), the mentioned mechanism highly likely applies to the oxidation of all three oligomers.

The first oxidation process was triggered by stepping the electrode potential from the capacitive region (0.00 V), where no faradaic reaction occurs, to the value, where the first oxidation step is diffusion-limited (+0.70 V). The same procedure may also be followed, when investigating the second oxidation process (at +1.00 V), or, alternatively, the potential +1.00 V may be reached from the value +0.70 V. The latter option was chosen, in order to trace the formation of TTF^{2+} from $TTF^{+\cdot}$ directly.

Table 10 suggests the reaction mechanism of the electrochemical oxidation of all three oligomers.

compound/step	corresponding electrochemical reaction
OPE-TTF$_2$ / 1st	$OPE-(TTF^0)_2+1e^- \xrightarrow{at\ +0.49V} OPE-(TTF^0)(TTF^{+\bullet})$
OPE-TTF$_2$ / 2nd	$OPE-(TTF^0)(TTF^{+\bullet})+1e^- \xrightarrow{at\ +0.85V} OPE-(TTF^0)(TTF^{2+})$
OPE-TTF$_4$ / 1st	$OPE-(TTF^0)_4+2e^- \xrightarrow{at\ +0.48V} OPE-(TTF^0)_2(TTF^{+\bullet})_2$
OPE-TTF$_4$ / 2nd	$OPE-(TTF^0)_2(TTF^{+\bullet})_2+2e^- \xrightarrow{at\ +0.83V} OPE-(TTF^0)_2(TTF^{2+})_2$
OPE-TTF$_6$ / 1st	$OPE-(TTF^0)_6+3e^- \xrightarrow{at\ +0.49V} OPE-(TTF^0)_3(TTF^{+\bullet})_3$
OPE-TTF$_6$ / 2nd	$OPE-(TTF^0)_3(TTF^{+\bullet})_3+3e^- \xrightarrow{at\ +0.84V} OPE-(TTF^0)_3(TTF^{2+})_3$

*Table 10: Suggested reaction mechanism for the oxidation of **OPE-TTF$_2$**, **OPE-TTF$_4$** and **OPE-TTF$_2$** compounds.*

In the second oxidation step, one may ask why a mixed valence species, such as $OPE-(TTF^0)(TTF^{2+})$, is considered rather than a biradical form $OPE-(TTF^{+\bullet})(TTF^{+\bullet})$. This was confirmed by the spectroelectrochemical measurements. In the first oxidation step, when one electron per one TTF group pair is transferred, a NIR band, centered at 840 nm, is observed. The band may be assigned to a radical cation $TTF^{+\cdot}$ formed from one TTF^0 group of the pair, with the other group being silent. The NIR band vanishes upon the transfer of the second electron i.e. in the second oxidation process, which suggests that the $TTF^{+\cdot}$ form ceases to exist. If a biradical came into existence, the NIR band would be retained or even increased. Instead, a mixed valence species $OPE-(TTF^0)(TTF^{2+})$ is formed. The same was also observed for the higher two oligomers. This implies that the forms generated in the second oxidation step are also mixed valence species.

The forms generated in the first oxidation step are mixed valence species as they contain partly oxidized group pairs, such as $OPE-(TTF^0)(TTF^{+\bullet})$.

Two other independent approaches were further employed to confirm the electron consumption determined by the semi-integration method employing wave height measurements. First, the Malachesky's method was applied [206]. The method combines the cyclic voltammetry at various scan-rates and chronoamperometry at potential values where the faradaic process of interest is diffusion limited. In both cases, the observed current profiles depend on the bulk concentration of the electroactive species, electrode area, diffusion coefficient and the electron consumption, see the Cottrell equation (Eq. 9) for chronoamperometry and Randles-Ševčík equation (Eq. 6) for cyclic voltammetry. The

electrode area and bulk concentration may easily be fixed, when the two methods employ the same solution and electrode. Then, the problem reduces to the system of two equations in two variables (*D* and *n*), which may be easily solved, giving the value of *n*.

The second applied method was the bulk electrolysis. The electrode potential was set to the value, where the first oxidation step is diffusion limited (+0.70 V). The resulting electric charge, obtained by the integration of current transients, was converted to the electron consumption by the Faraday's law.

Table 11 shows the electron consumption of all three compounds determined for the first oxidation step by the semi-integration method, Malachesky's method and bulk electrolysis.

Compound	Expected consumption	Semiintegration method	Malachesky's method	Bulk electrolysis	Average value
OPE-TTF$_2$	2	1.2	1.0	1.1	1.1
OPE-TTF$_4$	4	2.1	1.9	2.3	2.1
OPE-TTF$_6$	6	3.4	2.5	2.6	2.8

*Table 11: Comparison of the electron consumption values for the compounds **OPE-TTF$_2$**, **OPE-TTF$_4$** and **OPE-TTF$_6$** obtained by the semi-integration method, Malachesky's method and bulk electrolysis. The right column lists the average electron consumption.*

For the compounds **OPE-TTF$_2$** and **OPE-TTF$_4$**, the Malachesky's method and bulk electrolysis clearly confirmed the results of the wave-height measurements, employing Fc as the standard. For compound **OPE-TTF$_6$** the electron consumption value determined by the semi-integration method (3.4e$^-$) is somewhat higher than those obtained by the Malachesky's (2.5e$^-$) method and bulk electrolysis (2.6e$^-$). The discrepancies may be caused by the adsorption effects, slightly underestimating the real electron consumption due to a partial electrode blockage. On the other hand, the semi-integration method may suffer from some inaccuracy as the measurements are related to a standard (Fc in our case). For compounds with a high molar mass, the diffusion coefficient may significantly differ from that of ferrocene. Therefore, for all three compounds, the difference in the diffusion coefficient values was taken into account. For the compound **OPE-TTF$_6$,** the average electron consumption is 2.8 ± 0.5. Therefore, three electrons are transferred in the first oxidation step.

As mentioned above, for all three compounds the wave-height of the first and the second oxidation step is almost equal. Therefore, one, two and three electrons are transferred in the second oxidation steps of the compounds **OPE-TTF$_2$**, **OPE-TTF$_4$** and **OPE-TTF$_6$**. The

second oxidation step of the compound **OPE-TTF$_4$** was further scrutinized by the bulk electrolysis technique. The compounds **OPE-TTF$_2$** and **OPE-TTF$_6$** could not be investigated due to the limited amounts of provided samples. The electrolysis clearly confirmed the consumption of eight electrons, whereas only four electrons (two + two) were transferred in the cyclic voltammetry in the second oxidation step. In the bulk electrolysis, the time scale of the electrochemical reaction is usually on the order of hours, while the time scales in cyclic voltammetry fall into the range of seconds or even to fractions of seconds. Therefore, the silent TTF groups transfer electron only when sufficiently high time is provided. Figure 114 shows an overview of all oxidation steps in all three investigated compounds.

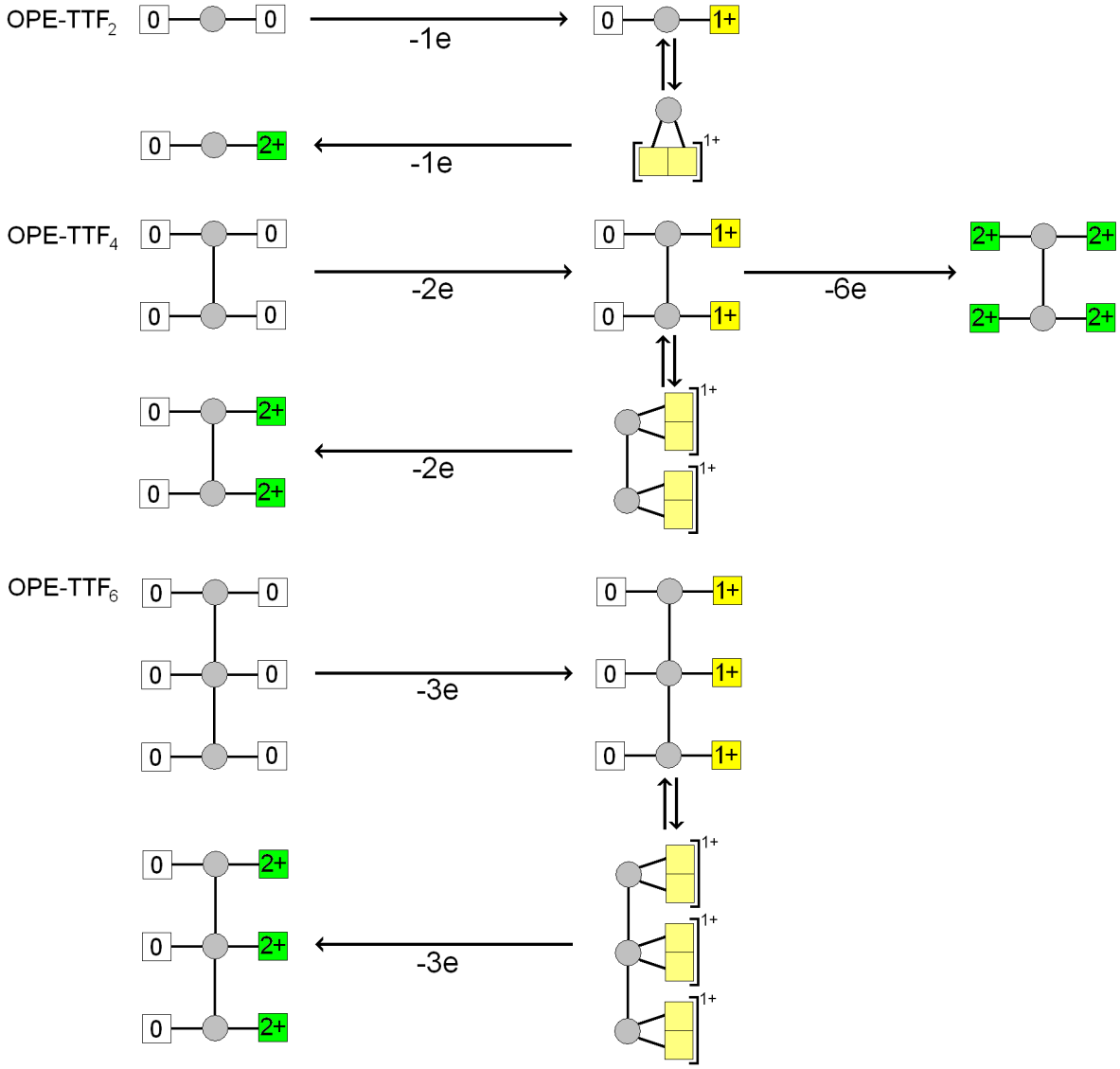

*Figure 114: Oxidation routes of the compounds **OPE-TTF$_2$**, **OPE-TTF$_4$** and **OPE-TTF$_6$**. Squares represent the TTF groups, molecular backbone is denoted by gray circles.*

6.2 Characterization of fullerene clusters on solid surfaces

Fullerenes are molecules composed of carbon atoms forming a hollow sphere, ellipsoid or a tube. They all may be considered as carbon allotropes. The spherical molecules are sometimes called buckyballs while the cylindrical ones are called carbon nanotubes. The oldest member of the family, buckminsterfullerene C_{60}, was first prepared by Richard Smalley, Robert Curl and Harold Croto in 1985 [207]. The three scientists were awarded by the Nobel Prize in Chemistry in 1996.

Fullerenes are of considerable scientific interest due to their potential use in various technical and biological applications [208]. The molecule C_{60} may reversibly accept up to six electrons in aprotic solvents [209,210]. The resulting radical anion and polyanions may serve as redox mediators [211,212]. The attractive applications of C_{60} molecule are hampered in water due to its very limited solubility [213,214]. Several approaches were implemented to overcome this limitation. One can exploit the host-guest interactions to increase the C_{60} solubility [215,216]. Other possibilities comprise the use of electrodes modified by C_{60} layers [217]. C_{60} molecules may be dispersed in water by the aid of ultrasound [218–220]. Ultrasonic treatment is known to generate high local pressures and temperatures, which may help C_{60} molecules to include in the cavities in the water structure [221]. A clathrate-like structure comes into existence, with water molecules surrounding the particles composed of C_{60} molecules. The term "C_{60} dispersion" is more appropriate than the term "solution of C_{60}" as dispersed particles are probably composed of several C_{60} molecules. As the C_{60} molecule has a diameter 0.71 nm, any particle composed of at least of two C_{60} molecules has characteristic dimensions exceeding 1 nm, being therefore a colloidal particle – a cluster of molecules. The dispersion of C_{60} clusters in water is very stable when stored in dark at room temperature. The stability of the dispersion with respect to the aggregation may be explained by electrostatic interactions between the charged clusters. The dispersion becomes unstable upon the addition of an electrolyte. Electrolyte ions adsorb on the cluster surface, decreasing thus its electrokinetic potential, which leads to the aggregation of clusters followed by their precipitation from the dispersion.

The chemical state of the C_{60} molecules in the water dispersion is not properly understood. Labille at al. [222] showed that C_{60} molecules may acquire some degree of hydrophilicity by chemical modification of the molecule surface by hydroxyl groups. On the other hand, Scharff at al. [223] performed the semi-empirical quantum chemistry calculations, in which it was showed that $C_{60}(H_2O)_{60}$ are the smallest stable clathrate-type clusters. It was suggested that

the C_{60} molecules are only hydrated, without any chemical modification. Other studies [218,224] suggest that the C_{60} molecules within the clusters are neither chemically modified nor hydrated.

In principle, there are three mutually contradicting attitudes suggesting that C_{60} molecules are unhydrated and chemically unmodified [218,224], hydrated [223] and chemically modified [222]. Therefore, a more detailed study of C_{60} water dispersions is necessary.

This part of the thesis focuses on physico-chemical properties of C_{60} clusters adsorbed on the mono-crystalline gold surfaces. The clusters were scrutinized by scanning probe microscopy techniques (AFM and STM) and surface spectroscopy techniques (ATR FTIR and PM IRRAS).

Dispersions of C_{60} in water were prepared according to Scharff [223] (see experimental part). Figure 115 shows ex-situ scanning probe micrographs of fullerene clusters freshly adsorbed on monocrystalline gold substrate from the undiluted water dispersion. Toluene was used as the organic phase during sonication. The gold substrate was immersed into the water dispersion for one hour and rinsed with water.

STM micrographs (upper two panels) show atomic terraces confirming a proper surface preparation. However, no C_{60} clusters are observed. On the other hand, the TOP-MAC atomic force micrograph (lower two panels) clearly confirms the presence of clusters on the surface. The discrepancy between the results of STM and TOP-MAC-AFM measurements may easily be explained by the absence of electric contanct between the fullerene clusters and gold substrate. The AFM techniques trace changes in the surface topography, while the STM method is sensitive to changes of LDOS on the sample surface. Nonconductive structures or structures electrically insulated from the underlying substrate remain silent in STM measurements, but are traceable by the AFM methods. This indicates that C_{60} molecules assembled in the clusters are not directly connected to the gold surface. Therefore, the molecules are either chemically modified or coated by an insulating layer.

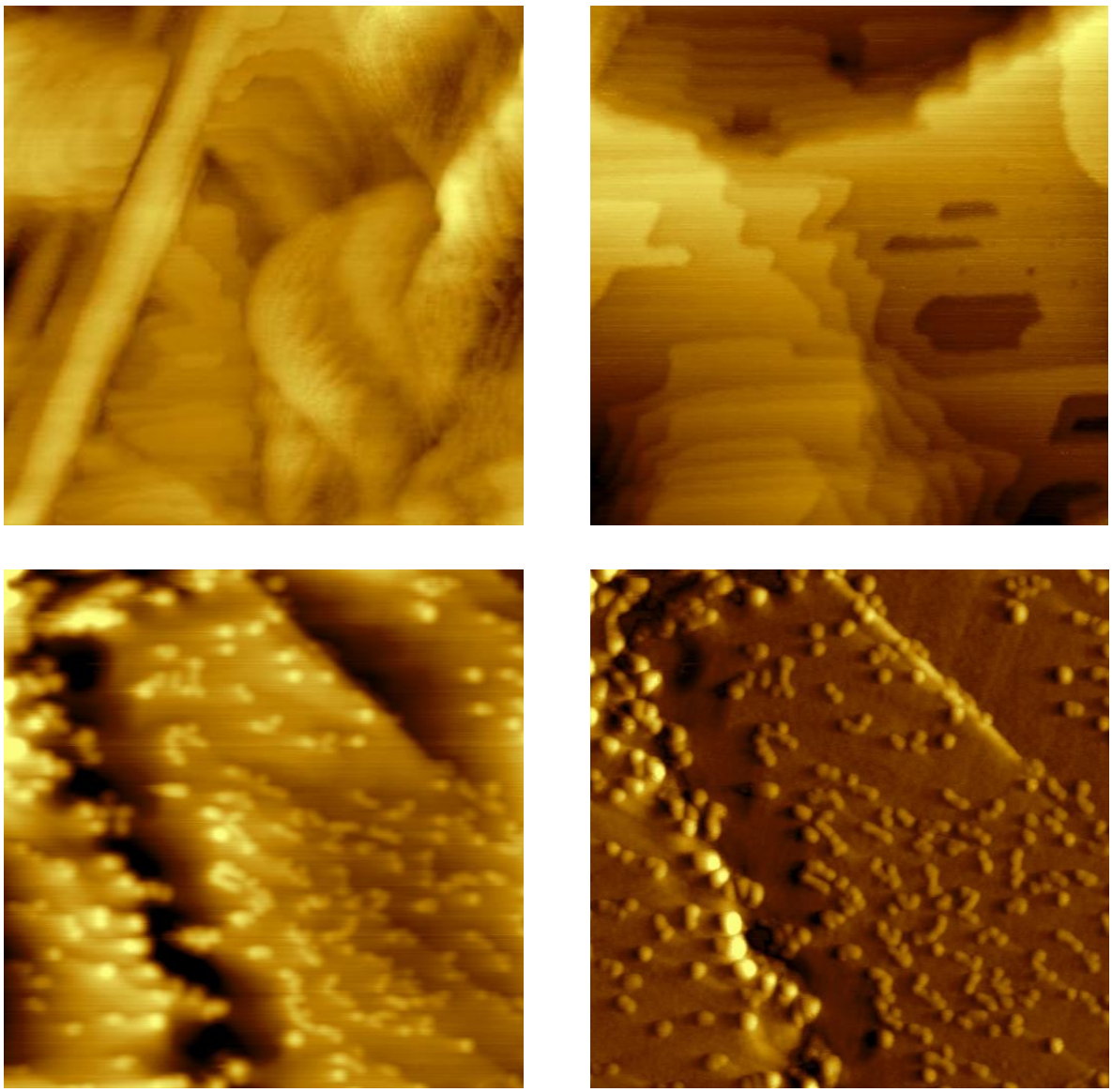

Figure 115: Ex-situ scanning probe micrographs of freshly adsorbed fullerene clusters.
Upper two panels show scanning tunneling micrographs at two different locations on the sample surface, with scan-size 250 nm (upper left panel) and 160 nm (upper right panel). Set-point current 1 nA, bias voltage 100 mV, scan-speed 0.8 lines/second, z bar is 7 nm.
Lower two panels show topography (lower left panel) and amplitude (lower right panel) representations of the TOP-MAC atomic force micrograph. Scan-size 1000 nm, z bar is 14 nm, A/A_0 = 90 %, scan-speed 1 line/second.

The TOP-MAC-AFM topography map shown in the lower left panel of Figure 115 was further subjected to the quantitative analysis. Figure 116 show the histograms of fullerene cluster heights, obtained from both ex-situ (Figure 115) and in-situ (the data not shown) TOP-MAC-AFM measurements.

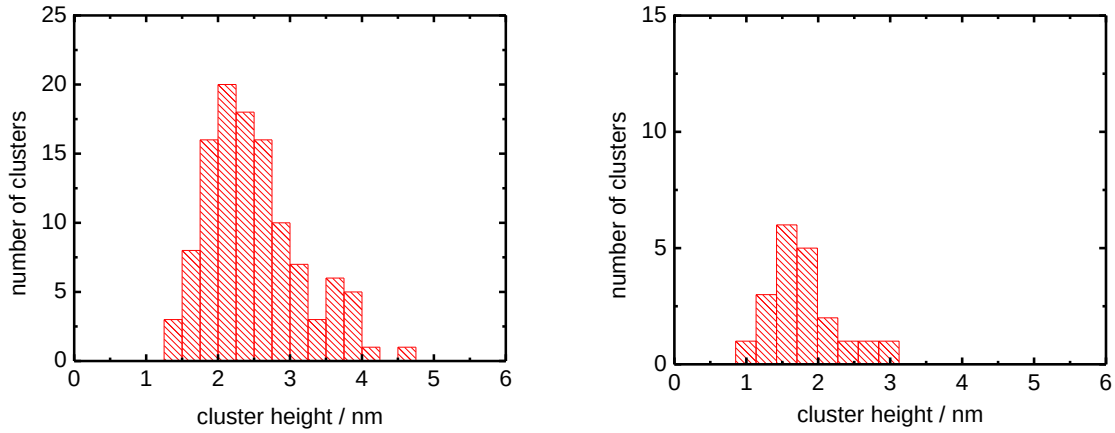

Figure 116: Histogram of fullerene cluster heights extracted from ex-situ (left panel) and in-situ (right panel) TOP-MAC micrographs. Constructed from measurements of 114 (ex-situ) and 20 (in-situ) individual fullerene clusters.

Average values of the cluster heights are 2.2 ± 0.7 nm and 1.8 ± 0.5 nm for ex-situ and in-situ measurements, respectively. The two values are well comparable. The diameter of C_{60} molecule is 0.71 nm and therefore, the cluster could be composed of C_{60} molecules assembled in three layers. Figure 117 shows two possible arrangements in C_{60} molecules in the cluster, the both containing fourteen C_{60} molecules in one cluster.

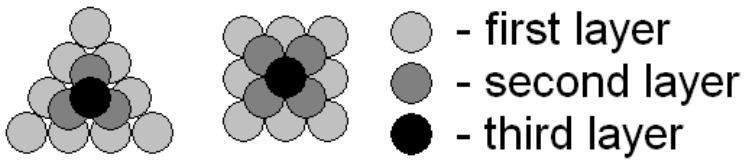

Figure 117: Two possible arrangements of C_{60} molecules in the cluster.

It should be noted that the lateral dimensions of clusters are overestimated due to a finite size of the AFM probe. Therefore, the number of molecules within the cluster cannot be calculated from its lateral dimensions. On the other hand, the vertical dimension i.e. the cluster height should not be affected by the size of the AFM probe as long as the method is not destructive. The "soft touch" TOP-MAC-AFM (with A_r = 90 %) was therefore employed.

As may be noticed in the atomic force micrograph in Figure 115, the surface is only sparsely covered by C_{60} clusters, which indicates that the adsorption of clusters is not energetically

very favorable. The in-situ TOP-MAC atomic force micrograph revealed even lower surface coverage (not shown). Weakly interacting structures are known to be prone to lateral surface diffusion. To confirm this, the very same sample as that shown in Figure 115 was scrutinized again by ex-situ TOP-MAC-AFM after 24 hours from the sample preparation. Figure 118 shows the corresponding TOP-MAC AFM micrograph.

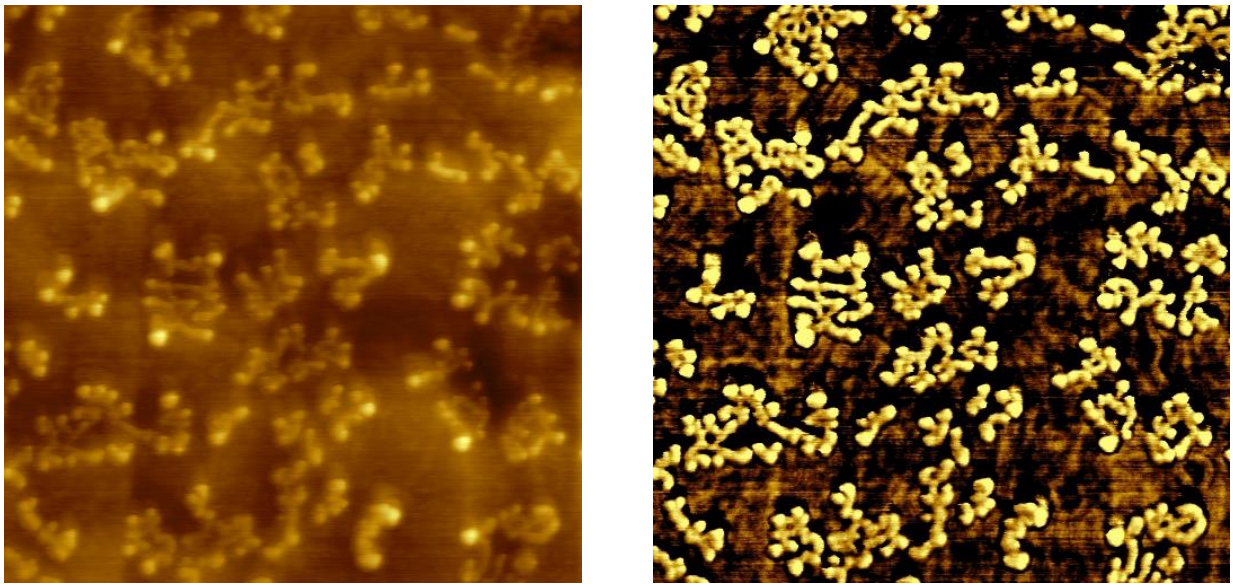

Figure 118: Topography (left panel) and phase (right panel) representation of the ex-situ TOP-MAC atomic force micrograph of fullerene clusters adsorbed on gold substrate obtained after 24 hours from the adsorption. Scan-size 1000 nm, z bar is 10 nm, A/A_0 = 90 %, scan-speed 1 line/second.

Obviously, the micrograph is very different from that obtained immediately after the sample preparation (Figure 115). No isolated clusters are present on the surface. Instead, the structures resembling "Chinese letters" are observed. In each structure, one may discern individual clusters, markedly resembling those observed in Figure 115. The height of the structures is largely retained (≈ 2 nm). This confirms that the fullerene clusters diffuse on the surface.

One may ask why the attraction occurs between the clusters on the surface and not in the liquid phase (in which the clusters repel each other and form a stable colloidal dispersion). One should keep in mind that a surface may have specific influence on the processes that take place on it. Many processes such as those encountered in the heterogeneous catalysis proceed on a surface and not in the bulk of a solution or a gaseous phase. Moreover, if the cluster surface is protected by a physically adsorbed layer, the rinsing after the adsorption may cause the layer to be partially removed. Bare C_{60} molecules within a cluster may be attracted by the

molecules in neighboring clusters. This may explain the presence of “Chinese letters” in the aged sample.

The SPM techniques were also employed to investigate the structures obtained for fullerene adsorbed directly from the toluene phase. Toluene is known to dissolve C_{60} molecules to form an analytical solution and not the dispersion. Figure 119 shows ex-situ scanning probe micrographs of fullerene clusters adsorbed from C_{60} solution in toluene (obtained 24 hours from the sample preparation.

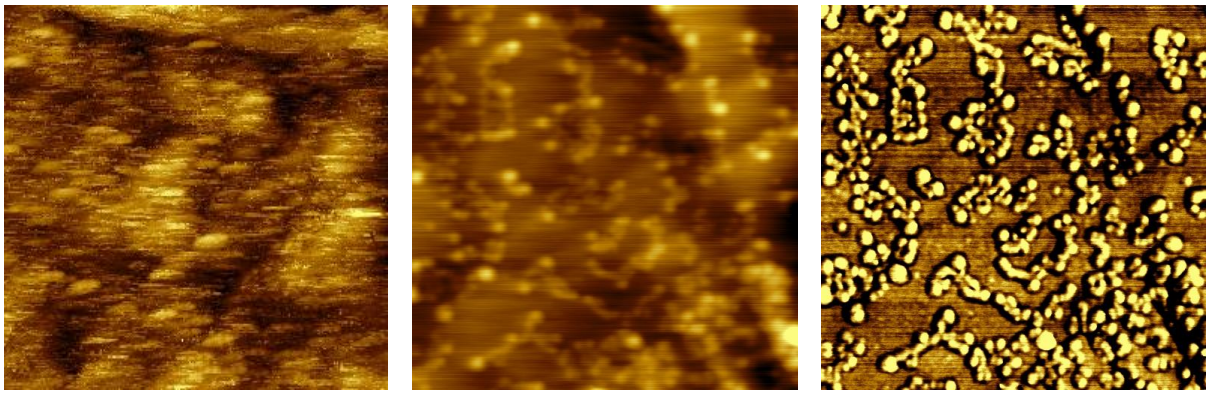

Figure 119: Ex-situ scanning probe micrographs of aged fullerene clusters adsorbed from the solution of C_{60} in toluene.
The left panel shows scanning tunneling micrograph with scan-size 250 nm. Set-point current 1 nA, bias voltage 100 mV, scan-speed 0.5 lines/second, z bar is 3.5 nm.
The middle and the right panel show the topography and phase representations of the ex-situ TOP-MAC atomic force micrograph, respectively. Scan-size 1000 nm, z bar is 10 nm, A/A_0 = 90 %, scan-speed 1 line/second.

The atomic force micrograph shows the structures resembling the “Chinese letters” found in the aged sample obtained by the adsorption from the water dispersion (see Figure 118). Individual C_{60} cluster may be discerned in the structures. However, the clusters may also be noticed in the scanning tunneling micrograph. Therefore, they are communicating with the gold substrate and are not coated or chemically modified. This suggests the differences between the structure of the cluster surface, prepared from the water dispersion and the toluene solution.

The fullerene clusters on the gold surface, adsorbed from the water dispersion and the toluene solution were further scrutinized by surface spectroscopy techniques. Figure 120 shows PM IRRAS spectrum of fullerene clusters adsorbed from the water dispersion (red line) and the toluene solution (blue line). The spectrum of a pure gold surface is shown (black line) as a reference.

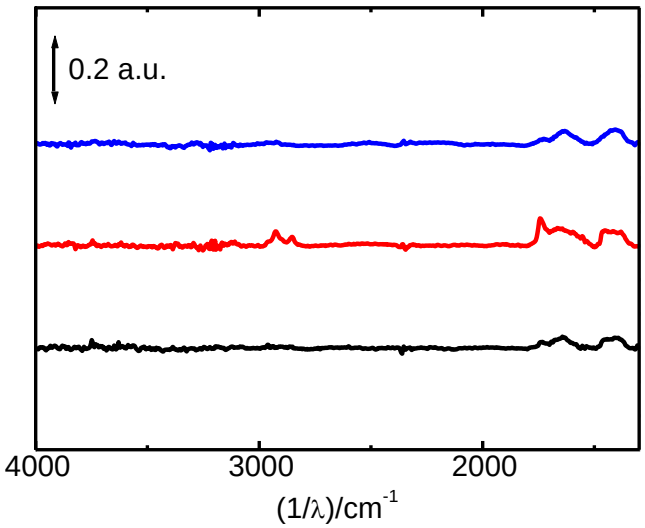

Figure 120: PM IRRAS spectrum of pure gold (black line), fullerene clusters adsorbed from water dispersion (red line) and toluene solution (blue line). Tthe shown profile is the sum of 64 collected spectra obtained at resolution 4 cm^{-1}.

The PM IRRAS spectrum of fullerene clusters obtained by the adsorption from toluene solution (blue line) is indistinguishable from that obtained for a pure gold surface (black line). The PM IRRAS method cannot detect the presence of C_{60} molecules on the surface. This is likely caused by a very low surface coverage (≈ 10%). When fullerene clusters are adsorbed from the water dispersion (red line), new peaks at 1740 cm^{-1}, 2850 cm^{-1} and 2920 cm^{-1} originate. Since the ester group is known to absorb at 1735 cm^{-1}, the fullerene clusters are probably coated by a species containing the ester group. The signals at 2850 cm^{-1} and 2920 cm^{-1} may both be assigned to the vibrations in C-H bonds.

The water dispersion of C_{60} clusters was subjected to TOF SIMS analysis (data not shown). The peaks with the *m/z* values 31, 59, 121 and 720 were found in the negative ion mode. The peak at *m/z* = 720 shows the presence of pristine C_{60} molecules. Therefore, the molecules within the clusters are not chemically modified. The peaks at 31, 59 and 121 may belong to the fragments $–OCH_3$, $-COOCH_3$ and $-C_7H_5O_2$, respectively. This is in accordance with PM IRRAS measurements, which revealed the presence of an ester group and C-H bonds in the molecule. The fragment $-C_7H_5O_2$ may be the C_6H_5COO- moiety. All these findings suggest the presence of methyl benzoate $C_6H_5COOCH_3$. This compound is slightly soluble in water and dissolves well C_{60} molecules. It may be formed by the oxidation of toluene during the sonication as the mixture is not protected from oxygen. Methyl benzoate probably acts as a surfactant, allowing the water dispersion of C_{60} clusters to be formed.

To confirm the ability of methyl benzoate to support C_{60} clusters in water, the following experiment was carried out. The solution of C_{60} molecules in methyl benzoate used instead of toluene was sonicated with an equal amount of water for 24 hours. The procedure followed that used in the preparation of C_{60} water dispersion with toluene.

Figure 121 shows TOP-MAC atomic force micrographs of freshly prepared (upper two panels) and aged (24 hours, lower two panels) fullerene clusters prepared from the water phase.

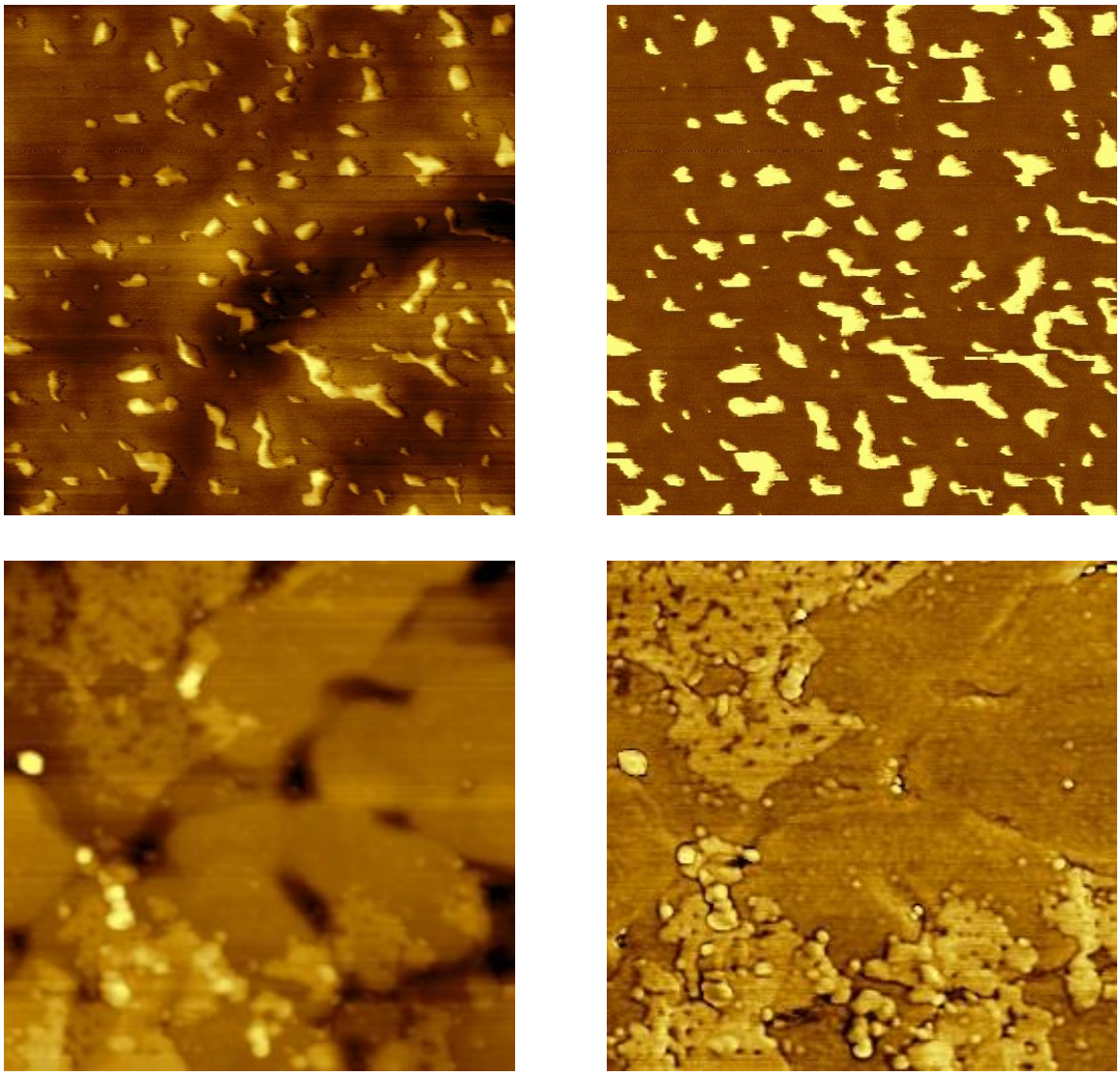

Figure 121: Topography (left panels) and phase (right panels) representations of ex-situ TOP-MAC atomic force micrographs of freshly prepared (upper panels) and aged (lower panels) fullerene clusters. The clusters are adsorbed from water phase, after sonication with the solution of C_{60} in methyl benzoate. Gold on mica was used as the substrate.
Upper two panes: Scan-size 250 nm, z bar is 5 nm
Lower two panes: Scan-size1000 nm, z bar is 20 nm
Probe frequency 65 kHz, A/A_0 = 90 %, scan-speed 1 line/second.

The C_{60} clusters show, to a considerable extent, similar behavior to those prepared with toluene as an organic phase during the sonication. Freshly prepared surfaces largely contain isolated C_{60} clusters, somewhere aligned to the snake-like structures (upper two panels of Figure 121). The height of the clusters is 2.3 ± 0.4 nm (figure 122 shows the corresponding histogram) and is practically identical to that found for the clusters adsorbed from water dispersion sonicated with C_{60} solution in toluene (2.2 ± 0.7 nm). Similarly, the clusters are stable in the liquid phase and aggregate on the surface. The aged samples show incomplete "patches" rather than "Chinese letters", with individual C_{60} clusters being still discernible.

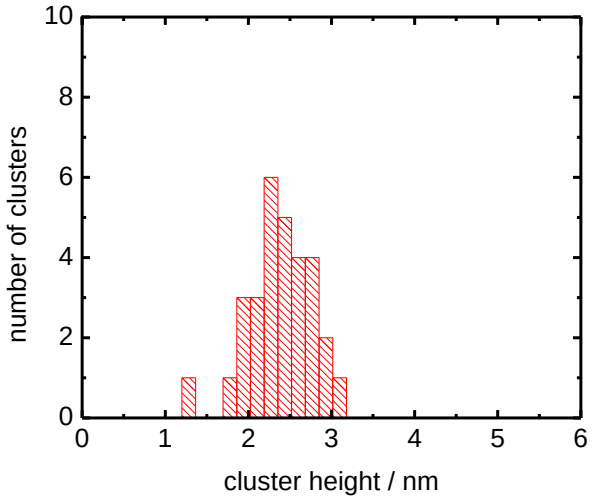

Figure 122: Histogram of the fullerene cluster heights extracted from ex-situ TOP-MAC atomic force micrograph. Constructed from 30 individual measurements. Clusters are adsorbed from water dispersion with methyl benzoate being used as the organic phase.

7 REFERENCES

1 I. Kratochvílová, K. Král, M. Bunček, S. Nešpůrek, T. Todorciuc, M. Weiter, J. Navrátil, B. Schneider, J. Pavluch, *Cent. Eur. J. Phys*., 2008, **6**, 422.
2 R. García, J. Yuqiu, E. Schabtach, C. Bustamante, *Ultramicroscopy*, 1992, **42**, 1250.
3 S. Hong, S. Myung, *Nature Nanotechnology*, 2007, **2**, 207.
4 D. Vrbanić, M. Remškar, A. Jesih, A. Mrzel, P. Umek, M. Ponikvar, B. Jančar, A. Meden, B. Novosel, S. Pejovnik, P. Venturini, J. C. Coleman, D. Mihailović, *Nanotechnology*, 2004, **15**, 635.
5 C. Perrin, M. Sergent, *J. Chem. Res.* 1983, **5**, 38.
6 D. Mihailovic, *Progress in Materials Science*, 2009, **54,** 309.
7 J. M. Tarascon, G.W. Hull, F.J. Di Salvo, *Mater. Res. Bull.*, 1984, **19**, 915.
8 F. A. Cotton, C. A. Murillo, R. A. Walton, "*Multiple Bonds Between Metal Atoms"*, 3rd edition, Springer (2005).
9 S. M. Peng, C. C. Wang, Y. L. Jang, Y. H. Chen, F. Y. Li, C. Y. Mou, M. K. Leung, *J. Magn. Magn. Matter*, 2002, **209**, 80.
10 J. D. Watson, F. H. C. Crick, *Nature*, 1953, **171**, 737.
11 W. Saenger, "*Principles of Nucleic Acid Structure"*. 1984, New York, Springer-Verlag.
12 F. A. Cotton, L. M. Daniels, C. A. Murillo, I. Pascual. *J. Am. Chem. Soc.*, 1997, **119**, 10223.
13 M. C. Petty, M. R. Bryce, D. Bloor, "*Introduction to Molecular Electronics"*, 1995, New York, Oxford University Press.
14 J. Tour, W. A. Reinerth, L. Jones, T. P. Burgin, C. W. Zhou, C. J. Muller, M. R. Deshpande, M. A. Reed, *Annals of the New York Academy of Sciences*, 1998, **852**, 197.
15 G. E. Moore, *Electronics*, 1965, **38**, 8.
16 J. B. Waldner, "*Nanocomputers and Swarm Intelligence*", 2008, London, John Wiley & Sons.
17 A. Aviram, M. A. Ratner, *Chem. Phys. Lett.*, 1974, **29**, 277.
18 J. P. Desvergne, H. Bouas-Laurent, *J. Chem. Soc., Chem. Commun.*, 1978, 403.
19 H. Bouas-Laurent, A. Castellan and J. P. Desvergne, *Pure & Appl. Chem. 5*, 1980, **52**, 2633.
20 R. McNeill, D. E. Weiss and D. Willis, *Australian Journal of Chemistry*, 1965, **18**, 477.
21 B. A. Bolto, D. E. Weiss, D. Willis, *Australian Journal of Chemistry*, 1965, **18**, 487.
22 IUPAC Gold Book, definition of the term „viologen".
23 M. Heyrovský, L. Novotný, *Collect. Czech. Chem. Commun.* 1987, **52**, 1097.
24 M. Heyrovský, *J. Chem. Soc., Chem. Commun.*, 1987, 1856.
25 „Paraquat". *Pesticides News* 1996, **32,** 20.
26 L. A. Summers, *„The Bipyridinium Herbicides",* 1980, Academic Press, New York.
27 B. Rada, T. L. Leto, *Contrib. Microbiol.* 2008, **15**, 164.
28 G. E. Conner, M. Salathe, R. Forteza, *Am. J. Respir. Crit. Care. Med.*, 2002, **166**, 77.
29 J. S. Bus, J. E. Gibson, *Experimental Health Perspectives*, 1984, **55**, 37.
30 S. C. Buzik, H. B. Schiefer, D. G. Irvine, „*Understanding Toxicity: Chemicals, Their Benefits and Risks",* 1997, Boca Raton: CRC Press.
31 K. Ossowska, M.S'Mialowska, K.Kuter, J.Wieron'ska, B.Zieba, J.Wardas, P.Nowak, J. Dabrowska, A. Bortel, I. Biedka, G. Schulze and H. Rommelspacher, *Neuroscience*, 2006, **141**, 2155.
32 Court of the first instance of the european communities, press release No. 45/07.
33 V. Jain, M. Khiterer, R. Montazami, H. M. Yochum, K. J. Shea and J. R. Heflin, *ACS Appl. Mater. Interfaces*, 2009, **1**, 83.
34 P. Monk, R. Mortimer, D. Rosseinsky, „*Electrochromism and electrochromic devices",* 2007, Cambridge University Press.
35 W. Haiss, H. van Zalinge, S. J. Higgins, D. Bethell, H. Höbenreich, D. J. Schiffrin, R. J. Nichols, *J. Am. Chem. Soc.*, 2003, **125**, 15294.
36 E. Leary, S. J. Higgins, H. van Zalinge, W. Haiss, R. J. Nichols, S. Nygaard, J. O. Jeppesen, J. J. Ulstrup, *J. Am. Chem. Soc.*, 2008, **130**, 12204.
37 C. Wang, A. S. Batsanov, M. R. Bryce, S. M., R. J. Nichols, S. J. Higgins, V. M. Garcia-Suarez, C. J. Lambert, *J. Am. Chem. Soc.*, 2009, **131**, 15647.

38 Z. Li, B. Han, G. Meszaros, I. Pobelov, T. Wandlowski, A. Błaszczyk, M. Mayor, *Faraday Discuss.*, 2006, **131**, 121.
39 I. V. Pobelov, Z. Li, T. Wandlowski, *J. Am. Chem. Soc.*, 2008, **130**, 16045.
40 N. S. Lee, H. K. Shin, D. J. Qian, Y. S. Kwon, *Thin Solid Films*, 2007, **515**, 5163.
41 A. Bagrets, A. Arnold, F. Evers, *J. Am. Chem. Soc*., 2008, **130**, 9013.
42 M. Heyrovský, L. Novotný, C*ollect. Czech. Chem. Commun.* 1987, **52**, 54.
43 L. Gómez, J. J. Ruiz, L. Camacho, R. Rodríguez-Amaro, *J. Electroanal. Chem.* 2004, **564**, 179.
44 L. Gómez, J. J. Ruiz, L. Camacho, R. Rodríguez-Amaro, *Langmuir* 2005, **21**, 369.
45 M. Sanchez-Maestre, R. Rodriguez-Amaro, E. Munoz, J. J. Ruiz, L. Camacho, *Journal of Electroanalytical Chemistry*, 1995, **390**, 2.
46 K. Kobayashi, F. Fujisaki, T. Yoshimine, K. Niki, *Bull. Chem. Soc. Jpn.*, 1986, **59**, 3715.
47 L. Pospíšil, J. Kůta, *J. Electroanal. Chem.* 1978, **90**, 231.
48 J. I. Millán, J. J. Ruiz, L. Camacho, R. Rodríguez-Amaro, *Langmuir*, 2003, **19**, 2338.
49 J. I. Millán, R. Rodríguez-Amaro, J. J. Ruiz, L. Camacho, *J. Phys. Chem. B*, 1999, **103**, 3669.
50 J. I. Millán, R. Rodríguez-Amaro, J. J. Ruiz, L. Camacho, *Langmuir*, 1999, **15**, 618.
51 J. I. Millán, J. J. Ruiz, L. Camacho, R. Rodríguez-Amaro, *J. Electrochem. Soc.* 2002, **149**, E440.
52 C. A. Widrig, M. Majda, *Langmuir*, 1989, **5**, 689.
53 K. Shimazu, M. Yanagida, K. Uosaki, *J. Electroanal. Chem.*, 1993, **350**, 321.
54 K. Arihara, T. Ohsaka, F. Kitamura, *Phys. Chem. Chem. Phys.*, 2002, **4**, 1002.
55 H. C. De Long, D. A. Buttry, *Langmuir*, 1992, **8**, 2491.
56 X. Tang, T. W. Schneider, J. W. Walker, D. A. Buttry, *Langmuir* 1996, **12**, 5921.
57 W. Haiss, R. J. Nichols, S. J. Higgins, D. Bethell, H. Höbenreich, D. J. Schiffrin, *Faraday Discuss.* 2004, **125**, 179.
58 W. Haiss, H. van Zalinge, H. Höbenreich, D. Bethell, D. J. Schiffrin, S. J. Higgins, and R. J. Nichols, *Langmuir*, 2004, **20**, 7694.
59 J. Volke, J. Urban, V. Volkeová, *Electrochemica Acta*, 1992, **37**, 2481.
60 J. Volke, L. Dunsch, V. Volkeová, A. Petr, J. Urban, *Electrochimica Acta*, 1997, **42**, 1771.
61 W. W. Porter, T. P. Vaid, A. L. Rheigold, *J. Am. Chem. Soc*., 2005, **127**, 47.
62 M. Valášek, J. Pecka, J. Jindřich, G. Calleja, P. R. Craig, J. Michl, *J. Org. Chem.*, 2005, **70**, 405.
63 A. Funston, J. P. Kirby, J.R. Miller, L. Pospíšil, J. Fiedler, M. Hromadová, M. Gál, J. Pecka, M. Valášek, Z. Zawada, P. Rempala, J. Michl, *J. Phys. Chem. A*, 2005, **109**, 10862.
64 L. Pospíšil, J. Fiedler, M. Hromadová, M. Gál, M. Valášek, J. Pecka, J. Michl: *J. Electrochem. Soc*., 2006, **153**, E179.
65 J. Szejtli, „*Cyclodextrins and their inclusion complexes*“, 1982, Akadémiai Kiadó, Budapest.
66 A. Villiers, *Compt. Rend. Fr. Acad. Sci.*, 1891, 435.
67 L. Pospíšil, M. Hromadová, M. Gál, J. Bulíčková, R. Sokolová, N. Fanelli, *Electrochim. Acta*, 2008, **53**, 7445.
68 L. Pospíšil, R. Sokolová, M. Hromadová, S. Giannarelli, R. Fuoco, M.P. Colombini, *J. Electroanal. Chem*., 2001, **517**, 28.
69 L. Pospíšil, M. Hromadová, M. Gál, J. Bulíčková, R. Sokolová, S. Filippone, J. Yang, Z. Guan, A. Rassat, Y. Zhang, *Carbon*, 2010, **48**, 153.
70 J.A. Imonigie, D.H. Macartney, *Inorg. Chim. Acta*, 1994, **225**, 51.
71 M.V. Rekharsky, Y. Inoue, *Chem. Rev.*, 1998, **98**, 1875.
72 S. Menuel, J.P. Joly, B. Courcot, J. Elysée, N.E.Ghermani, A.Marsua, *Tetrahedron*, 2006, **67**, 1706.
73 A. Motoyama, A. Suzuki, O. Shirota, R. Namba, *Journal of Pharmaceutical and Biomedical Analysis*, 2002, **28**, 97.
74 R. S. Brown, J. H. T. Luong, O. H. J. Szolar, A. Halasz, J. Hawari, *Anal. Chem.*, 1996, **68**, 287.
75 W. Maruszak, M. G. Schmid, G. Gübitz, E. Akiert, M. Trojanowicz, *Methods in Molecular Biology*, 2003, **243**, 275.
76 S. K. Rodal, G. Skretting, Ø. Garred, F. Vilhardt, B. van Deurs, K. Sandvig, *Molecular Biology of the Cell*, 1999, **10**, 961.
77 J.Nishijo, S.Moriyama, S. Shiota, M. Kamigauchi, M. Sugiura, *Chem.Pharm. Bull*., 2004, **52**, 1405.
78 J. D. Artiss, K. Brogan, M. Brucal, M. Moghaddam, K. L. C. Jen, *Metabolism*, 2006, **55**, 195.

79 A. Yasuda, H. Kondo, M. Itabashi, J. Seto, *J. Electroanal. Chem*.,1986, **210**, 265.
80 U. Sivagnanam, M. Palaniandavar, *J. Electroanal. Chem*., 1992, **341**, 197.
81 A. Mirzoian, A. E. Kaifer, *Chem. Eur. J*., 1997, **3**, 1052.
82 F. Kitamura, T. Ohsaka, K. Tokuda, *J. Electroanal. Chem*., 1994, **368**, 281.
83 C. M. Lee, M. S. Moon, J. W. Park, *J. Electroanal. Chem*., 1996, **407**, 161.
84 C. M Lee, Y. W. Sung, J. W. Park, *J. Electroanal. Chem*., 1997**, 431**, 133.
85 A. Yasuda, J. Seto, *J. Appl. Electrochem*., 1988, **18**, 333.
86 M. Taniguchi, T. Kawai, *Chem. Phys. Lett*., 2006, **431**, 127.
87 F. Cacialli, J. S. Wilson, J. J. Michels, C. Daniel, C. Silva, R. H. Friend, N. Severin, P. Samorì, J. P. Rabe, M. J. O'Connell, P. N. Taylor, H. L. Anderson, *Nature Materials*, 2002, **1**, 160.
88 T. Shimomura, T. Akai, M. Fujimori, S. Heike, T. Hashizume, K. Ito, *Synth. Met*., 2005, **153**, 497.
89 T. Shimomura, T. Akai, T. Abe, K. Ito,. *J. Chem. Phys*., 2002, **116**, 1753.
90 K. Yoshida, T. Shimomura, K. Ito, R. Hayakawa, *Langmuir*, 1999, **15**, 910.
91 N. G. Connely, W. E. Geiger, *Chemical Reviews*, 1996, **96**, 877.
92 G. Gritzner, J. Kůta, *Pure Appl. Chem.* 1984, **56,** 461.
93 T. Kuwana, D. E. Biblitz, G. Hoh, J. Am. Chem. Soc., 1960, **82**, 5811.
94 http://www.chemicalbook.com/ProductMSDSDetailCB1414721_EN.htm
95 F. Hapiot, S. Tilloy, E. Monflier, *Chemical Reviews*, 2005, **106**, 767.
96 B. Siegel, R. Breslow, *J. Am. Chem. Soc.,* 1975, **97**, 6869.
97 T. Matsue, D. E. Evans, T. Osa, N. Kobayashi, *J. Am. Chem. Soc*., 1985, **107**, 3411.
98 N. Kobayashi, T. Osa, *Chemistry letters*, 1986, 421.
99 J. S. Wu, K. Toda, A. Tanaka, I. Sanemasa, *Bull. Chem. Soc. Jpn*., 1998, **71**, 1615.
100 A. Harada, S. Takahashi, *Chemistry Letters*, 1984, 2089.
101 T. Matsue, U. Akiba, K. Suzufuji, T. Osa, *Chem. Abstr.*, 1985, **103**, 130044.
102 T. Matsue, U. Akiba, K. Suzufuji, T. Osa, *Denki Kagaku*, 1985, **53**, 108.
103 N. Kobayashi, T. Osa, *Bull. Chem. Soc. Jpn*., 1991, **64**, 1878.
104 T. Komura, T. Yamaguchi, K. Noda, S. Hayashi, *Electrochimica Acta*, 2002, **47**, 3315.
105 E. Coutouli-Argyropoulou, A. Kelaidopoulou, C. Sideris, G. Kokkinidis, *J. Electroanal. Chem.*, 1999, **477**, 130.
106 R. Isnin, C. Salam, A. E. Kaifer, *J. Org. Chem*., 1991, **56**, 35.
107 J. Cassidy, J. O'Gorman, M. Ronane, E. Howard, *Electrochemistry Communications*, 1999, **1**, 69.
108 V. V. Strelets, I. A. Mamedjarova, M. N. Nefedova, N. I. Pysnograeva, V. I. Sokolov, L. Pospíšil, J. Hanzlik, *J. Electroanal. Chem.*, 1991, **310**, 179.
109 C.S. Lu, X.M. Ren, L. Liu, Y. Zhang, C.J. Hu, H.Z.Zhu, Q.J.Meng, *J. Incl. Phenom.*,2002, **43**, 19.
110 D. Osella, A. Carretta, C. Nervi, M. Ravera, R. Gobetto, *Organometallics*, 2000, **19**, 2791.
111 T. Matsue, T. Osa, D. H. Evans, *J. Incl. Phenom. Macro*., 1984, **2**, 547.
112 L. A. Godínez, S. Patel, C. M. Criss, A. E. Kaifer, *J. Phys. Chem*., 1995, **99**, 17449.
113 L. A. Godínez, L. Schwartz, C. M. Criss, A. E. Kaifer, *J. Phys. Chem. B*, 1997, **101**, 3376.
114 R. Bakthiar, A. E. Kaifer, *Rapid Communications in Mass Spectrometry*, 1998, **12**, 111.
115 A. Harada, Y. Hu, S. Yamamoto, S. Takahashi, *J. Chem. Soc., Dalton Trans*. 1988, 729.
116 V. T. Yilmaz, A. Karadag, H. Icbudak, *Thermochimica Acta*, 1995, **261**, 107.
117 A. U. Moozyckine, J. L. Bookham, M. E. Deary, D. M. Davies, *Chem. Soc., Perkin Trans.*, 2001, **2**, 1858.
118 H. Schönherr, M. W. Beulen, F. C. J. M. van Veggel, J. Bügler, J. Huskens, D. N. Reinhoudt, G. J. Vancso, *J. Am. Chem. Soc.*, 2000, **122**, 4963.
119 S. Zapotoczny, T. Auletta, M. R. de Jong, H. Schönherr, J. Huskens, F. C. J. M. Van Veggel, D. N. Reinhoudt, G. J. Vancso, *Langmuir*, 2002, **18**, 6988.
120 C. J. Yu, Y. Chong, J. F. Kayyem, M. Gozin, *J. Org. Chem.*, 1999, **64**, 2070.
121 R. P. Hsung, C. E. D. Chidsey, L. R. Sita, *Organometallics*, 1995, **14**, 4808.
122 S. Creager, C. J. Yu, C. Bambad, S. O'Connor, T. MacLean, E. Lam, Y. Chong, G. T. Olsen, J. Luo, M. Gozin, J. F. Kayyem, *J. Am. Chem. Soc.*, 1999, **121**, 1059.
123 A. J. Bard, L. R. Faulkner, "*Electrochemical Methods, fundamentals and applications, second edition*", New York, 2001, John Wiley & Sons.

124 A. Fick, *Poggendorff's Annel. Physik*, 1855, **94**, 59.
125 A. Fick, *Phil. Mag.*, 1855, **10**, 30.
126 J. Heyrovský, *Chem. Listy*, 1922, **16**, 256.
127 J. Heyrovský, M. Shikata, *Rec. Trav. Chim.*, 1925, **44**, 496.
128 J. Pfitzner, *Anaesthesia* 1976, **31,** 273.
129 D. Ilkovič, *Collection*, 1934, **6**, 498.
130 D. Ilkovič, *J. Chim. Phys.*, 1938, **35**, 129.
131 W. M. Peterson, *Am. Lab.*, 1979, **11**, 69.
132 Z. Kowalski, K. H. Wong, R. A. Osteryoung, J. Osteryoung, *Anal. Chem.*, 1987, **59**, 2216.
133 J. Tomeš, *Collect. Czech. Chem. Commun.* 1937, **9**, 12.
134 J. Heyrovský, J. Kůta, „*Základy polarografie",* Nakladatelství Československé akademie věd, Prague, 1962
135 J. E. B. Randles, *Trans. Faraday Soc.*, 1948, **44**, 327.
136 A. Ševčík, *Coll. Czech. Chem. Commun*., 1948, **13**, 349.
137 N. Winograd, T. Kuwana, *Electroanal. Chem.*, 1974, **7**, 1.
138 R. Cieslinsky, N. R. Armstrong, *Anal. Chem*, 1979, **51**, 565.
139 F. G. Cottrell, *Z. Physik. Chem.*, 1902, **42**, 385.
140 L. Pospíšil, R. de Levie, *J. Electroanal. Chem.*, 1969, **22**, 227.
141 R. Hooke, *Lectiones Cutlerianæ or A collection of lectures: physical, mechanical, geographical, & astronomical*, 1679, London.
142 A.R.Hall,"Horology and criticism:Robert Hooke",*Studia Copernicana,XVI,Ossolineum,*1978, 261.
143 G. Binnig, C. F. Quate, Ch. Gerber, *Physical Review Letters*, 1986, **56**, 930.
144 F. J. Giessibl, *Reviews of Modern Physics* 2003, **75,** 949.
145 www.engineeringtoolbox.com/young-modulus-d_417.html
146 www.capphysics.ca/PhysLab/Phys114115/exp_2%20-%20loaded%20beam/content/BEAM.pdf
147 L. Zhang, T. Sakai, N. Sakuma, T. Ono, K. Nakayama, *Applied Physics Letters*, 1999, **75**, 3527.
148 G. Binnig, H. Rohrer, *IBM Journal of Research and Development* 1986, **30,** 4.
149 G. Binnig, H. Rohrer, Ch. Gerber, E. Weibel, *Applied Physics Letters* 1982, **40**, 178.
150 C. J. Chen, "*Introduction to Scanning Tunneling Microscopy*", 1993, Oxford University Press.
151 http://las.perkinelmer.com/content/TechnicalInfo/TCH_FTIRATR.pdf
152 Reena Banga, J. Yarwood, A. M. Norgan, B. Evans, J. Kells, *Thin Solid Films*, 1996, **284**, 261.
153 X. F. Lin L. He, L. H. Xu, D. S. Lu, Z. C. Chen, *Chinese Chemical Letters*, 2000, **11**, 267.
154 W.Golden, D.Saperstein, *Journal of Electron Spectroscopy and Related Phenomena*, 1983, **30**, 41.
155 M. Valášek, R. Betík, J. Pecka, J. Michl, *J. Org. Chem,*. submitted.
156 M. Krejčík, M. Daněk, F. Hartl, *J. Electroanal. Chem.* 1991, **317**, 179.
157 J. Koryta, *Collect. Czech. Chem. Commun.* 1953, **18**, 206.
158 P. W. Atkins, „Physical Chemistry", Second Edition, 1982, Oxford University Press.
159 A.P.Henderson, L.N.Seetohul, A.K.Dean, P.Russell, S.Pruneanu, Z.Ali, *Langmuir*, 2009, **25**, 931.
160 A. A. Abdel-Shafi, S. S. Al-Shihry, *J. Incl. Phen.*, 2010, **67**, 7.
161 H. Benesi, J. Hildebrand, *J. Am. Chem. Soc.*, 1949, **71**, 2703.
162 A. A. Abdel-Shafi, *Spectrochimica Acta Part A*, 2007, **66**, 732.
163 J. Taraszewska, A. K. Piasecki, *J. Electroanal. Chem*., 1987, **226**, 137.
164 J. Taraszewska, *J. Incl. Phen.*, 1991, **10**, 69.
165 A. Lasia. "Electrochemical impedance spectroscopy and its applications, *Modern Aspects of Electrochemistry*, 1999, **32**, 143.
166 R. S. Nicholson, *Anal. Chem.* 1965, **37**, 1351.
167 V. G. Levich, "*Physicochemical Hydrodynamics"* 1962,Prentice Hall, Englewood Cliffs, USA.
168 M. Fleischmann, J. Ghoroghchian, D. Rolison, S. Pons, *J. Phys. Chem.,*1986, **90**, 6392**.**
169 C.Amatore, M.Azzabi, P.Calas, A.Jutand, C.Lefrou, Y.Rollin, *J.Electroanal.Chem.* 1990, **288**, 45.
170 C. Zoski (editor), „Handbook of Electrochemistry", 2006, Elsevier, USA.
171 C. R. Christensen, F. C. Anson, *Anal. Chem.* 1963, **35**, 205.
172 B. Xu, N. J. Tao, *Science*, 2003, **301**, 1221.

173 J. He, F. Chen, J. Li, O. F. Sankey, Y. Terazono, C. Herrero, D. Gust, T. A. Moore, A. L. Moore, S. M. Lindsay, *J. Am. Chem. Soc*., 2005, **127**, 1384.
174 J. H. Poincaré, *Acta Mathematica*, 1890, **13**, 1.
175 E. N. Lorenz, *Journal of Atmospheric Sciences*, 1963, **20**, 130.
176 M. Feigenbaum, *Journal of Statistical Physics*, 1978, **19**, 25.
177 R. M. May, *Nature*, 1976, **261**, 459.
178 M. Feigenbaum, *Ann. New York. Acad. Sci.*, 1980, **357**, 330.
179 A.K. Soper, A. Luzar, *J. Chem. Phys.*, 1992, **97**, 1320.
180 X. Q. Yang, L. J. Yang, K. M. Huang, W. Y. Tian, H. Shang, *J. Solution Chem,*. 2010, **39**, 849.
181 X. J. Dang, M.Y. Nie, J. Tong, H. L. Li, *J. Electroanal. Chem*., 1997, **437**, 53.
182 Y. Uosaki, S. Kitaura, T. Moriyoshi, *J. Chem. Eng. Data*, 1997, **42**, 580.
183 D. Weiß, "Fluoreszensfarbstoffe in der Natur", 2008, (in German), http://www.chemie.uni-jena.de/institute/oc/weiss/naturstoffe.htm
184 H. Musso, C. Rathjen, *Chem. Ber.* 1959, **92**, 751.
185 R. Boyle*,"Considerations touching the Usefulness of Experimental Natural Philosophy"*, printed by H. Hall for R. Davis, 1663, Oxford.
186 R. Boyle, "*Experiments and Considerations Touching Colours, with Observations on a Diamond that Shines in the Dark"*, 1664, Oxford.
187 J. Waring, *Journal of Molecular Biology*, 1965, **13**, 269.
188 A. McIver, D. D. Young, A. Deiters, *Chem Commun*., 2008, **39**, 4750.
189 A. McIver, A. Deiters, *Org. Lett*., 2010, **12**, 1288.
190 L. Adriaennsens, L. Severa, T. Šálová, I. Císařová, R. Pohl, D. Šaman, S. V. Rocha, N. S. Finney, L. Pospíšil, P. Slavíček, F. Teplý, *Chem. Eur. J*., 2009, **15**, 1072.
191 D. K. James, J. M. Tour, *Topics in Current Chemistry*, 2005, **257**, 33.
192 J. J. Stapleton, T. A. Daniel, S. Uppili, O. M. Cabarcos, J. Naciri, R. Shashidhar, D. L. Allara, *Langmuir*, 2005, **21**, 11061.
193 Y. Li, J. Zhao, G. Yin, *Computationals Material Science*, 2007, **39**, 775.
194 J. K. Sørensen, M. Vestergaard, A. Kadziola, K. Kilså, M. B. Nielsen, *Org. Lett.*, 2006, **8**, 1173.
195 J. M. Tour, "*Molecular Electronics"*, 2003, World Scientific, Singapore.
196 U. F. Bunz, *Chem. Rev*. 2000, **100**, 1605.
197 C. Xu, A. Wakamiya, S. Yamaguchi, *J. Am. Chem. Soc*., 2005, **127**, 1638.
198 S. C. Yuan, S. L. Han, X. Ge, H. C. Wang, *Chinese Chemical Letters*, 2000, **21**, 97.
199 C. Wang, M. R. Bryce, A. S. Batsanov, L. M. Goldenberg, J. A. K. Howard, *J. Mater. Chem*., 1997, **7**, 1189.
200 A. Godt, M. Schulte, H. Zimmermann, G. Jeschke, *Angew. Chem.* 2006, **118**, 7722.
201 P. F. H. Schwab, M. D. Levin, J. Michl, *Chem. Rev*. 1999, **99**, 1863.
202 M. R. Pinto, B. M. Kristal, K. S. Schanze, *Langmuir*, 2003, **19**, 6523.
203 S. V. Rosokha, J. K. Kochi, *J. Am. Chem. Soc*. 2007, **129**, 828.
204 V. Maurizot, M. Yoshizawa, M. Kawano, M. Fujita, *Dalton Trans*. 2006, 2750.
205 P. T. Chiang, N. C. Chen, C. C. Lai, S. H. Chiu, *Chem. Eur. J*. 2008, **14**, 6546.
206 P. A. Malachesky, *Anal. Chem.* 1969, **41**, 1493.
207 H. W. Kroto, J. R. Heath, S. C. O'Brien, R. F. Curl, R. E. Smalley, *Nature*, 1985, **318**, 162.
208 M. S. Dresselhaus, G. Dresselhaus, P. C. Eklund, "*Fullerene Chemistry and Electrochemistry in Science of fullerenes and carbon nanutubes",* 1996, Academic Press, Los Angeles.
209 D. Dubois, K. M. Kadish, S. Flanagan, R. E. Haufer, L. P. F. Chibante, L. J. Wilson, *J. Am. Chem. Soc.* 1991, **113**, 4364.
210 M.M. Khaled, R.T.Carlin, P.C.Trulove, G.R.Eaton, S.S.Eaton, *J.Am.Chem. Soc.*, 1994, **116**, 3465.
211 W. Liu, X. Gao, *Electrochem. Commun.* 2008, **10**, 1377.
212 L. Pospíšil, J. Bulíčková., M. Hromadová, M. Gál, S. Civiš, J. Cihelka, J. Tarábek, *Chem. Commun.* 2007, **22**, 2270.
213 D. Heymann, *Fulleren Sci. Techol.* 1996, **4**, 509.
214 R. S. Ruoff, D. S. Tse, R. Malbotra, D. C. Lorents, *J. Phys. Chem.*, 1993, **97**, 3379.
215 Y.Zhang, W.Liu, X.Gao, Y.L.Zhao, M.Zheng, F.F.Li, D. L. Ye, *Tetrahedron Lett.* 2006, **47**, 8571.

216 L. Pospíšil, M. Hromadová, S. Filippone, A. Rassat, *Proceedings of 12th International Cyclodextrin Symposium*, Montpellier, France, 2004, 257.
217 F.Cecchet, S.Rapino, M.Margotti, T.DaRos, M.Prato, F.Paolucci, P.Rudolf,*Carbon*,2006,**44**,3014.
218 G. V. Andrievsky, M. V. Kosevich, O. M. Vovk, V. S. Shelkovsky, L. A. Vashchenko, *J. Chem. Soc. Chem. Commun.* 1995, 1281.
219 N. O. Mchedlov-Petrossyan, V. K. Klochkov, G. V. Andrievsky, *J. Chem. Soc. Faraday Trans.* 1997, **93**, 4343.
220 Y. Prilutski, S. Durov, L. Bulavin, V. Pogorelov, Y. Astashkin, V. Yashchuk, T. Ogul'chansky, E. Buzaneva, G. Andrievsky, *Mol. Cryst. Liquid Cryst.,* 1998, **324**, 65.
221 W. B. Ko, J. Y. Heo, J. H. Nam, K. B. Lee, *Ultrasonics*, 2004, **41**, 727.
222 J. Labille, A. Masion, F. Ziarelli, J. Rose, J. Brant, F. Vellieras, M. Pelletier, D. Borschenck, M. R. Wiesner, J. Y. Bottero, *Langmuir*, 2009, **25**, 11232.
223 P. Scharff, K. Risch, L. Carta-Abelmann, I. M. Dmytruk, M. M. Biliy, O. A. Golub, A. V. Khavryuchenko, E. V. Buzaneva, V. L. Aksenov, M. V. Avdeev, Y. Prylutskyy, S. S. Durov, *Carbon*, 2004, **42**, 1203.
224 G.V. Andrievsky, V.K.Klochkov, A.B.Bordyuh, G.I. Dovbeshko, *Chem. Phys. Lett.*, 2002, **364**, 8.